The HERMES recoil photon detector and the study of deeply virtual Compton scattering

De HERMES recoil fotondetector
en de studie van diep-virtuele Comptonverstrooiing

Promotor: Prof. Dr. Dirk Ryckbosch

Proefschrift ingediend tot het verkrijgen van de graad van
Doctor in de Wetenschappen: Natuurkunde
door
Charlotte Van Hulse

Contents

IV

1. Introduction

The picture of the internal spin structure of the nucleon (proton or neutron) is at present not complete. The nucleon is composed of elementary fermionic particles, the quarks, that interact through the exchange of gluons, the gauge bosons of the strong interaction (described by the theory of quantum chromodynamics). A proton (neutron) consists of 2 (1) up quarks and 1 (2) down quark. These quarks are called valence quarks; they determine basic properties of the nucleon such as its charge. The gluons, through which they interact, can split into quark-antiquark pairs, and these quarks, called sea quarks, can again annihilate into gluons. A nucleon can thus be seen to be made of valence quarks, dressed by a mixture of sea quarks that continuously originate from gluons and again annihilate into gluons.

Originally it was thought that the spin of the nucleon can be entirely attributed to the spins of its valence quarks. However, measurements at the EMC experiment showed in 1988 that the spins of the quarks (valence and sea quarks) account for a small fraction only of the nucleon spin, namely $14 \pm 9 \pm 21\%$ [1]. Following this, various experiments, one of which is the HERMES experiment at DESY in Hamburg (Germany), were constructed to pursue an advanced investigation of the origin of the nucleon spin. From these experiments, the contribution from the spins of the quarks is established to be around 30%. First results seem to indicate that also the spins of the gluons contribute a small fraction only. Thus, the orbital angular momenta of the nucleon's constituents is expected to be sizable.

Access to the quark orbital angular momentum is provided through the Ji relation, which relates so-called generalized parton distributions to the quark total angular momentum. Generalized parton distributions can be accessed through deeply virtual Compton scattering. In this process a lepton interacts with a quark in the nucleon via the exchange of a highly virtual photon. This photon is absorbed by the struck quark; subsequently the quark emits a real photon and returns back to the proton, thereby changing its momentum.

Deeply virtual Compton scattering has been studied at the HERMES experiment over the past years. The analysis was performed based on the kinematics of the scattered lepton and the real photon. The low momentum and angular distribution of the recoiling proton did not allow it to be detected, but through the reconstruction of its missing mass, it was possible to collect all necessary information. This method suffers, however, from a 14% background contribution, mainly originating from associated deeply virtual Compton scattering, i.e., deeply virtual Compton scattering where the proton does not stay in its ground state but is excited to a Δ^+ resonance. This Δ^+ decays either into a neutron and positively charged pion or into a proton and a neutral pion, which subsequently decays into photons. In order to reduce the background contribution, a recoil detector was installed in 2006. This detector consists of

three active detector components, two of which allow for the detection and reconstruction of protons and charged pions, whereas the third component, the photon detector, is able to detect photons.

The commissioning of the photon detector forms a major part of the here presented work. This detector and its performance are described in chapter 4. Preceding this chapter, chapter 2 treats the theoretical aspects related to generalized parton distributions and deeply virtual Compton scattering, and chapter 3 gives a description of the HERMES experiment. In chapter 5 the analysis of deeply virtual Compton scattering with the recoil detector is reported, as well as the capability of the recoil detector to isolate associated deeply virtual Compton scattering events. Finally, the summary and conclusions concerning the photon detector and the analysis of deeply virtual Compton scattering with the recoil detector can be found in chapter 6.

2. Deeply virtual Compton scattering and generalized parton distributions

In this chapter the motivation for the study of deeply virtual Compton scattering is discussed, and the theoretical ingredients needed for the understanding of the analysis are presented. To conclude, the study of deeply virtual Compton scattering at the HERMES experiment is placed in context.

2.1   Deeply virtual Compton scattering

The process under investigation in the present work is deeply virtual Compton scattering (DVCS) on a proton:

$$\gamma^*(q) + p(p) \rightarrow \gamma(q') + p(p'), \tag{2.1}$$

where a highly virtual photon (γ^*) interacts with a proton (p), producing in the final state a real photon (γ) and a slightly recoiling proton. More specifically, the photon's high virtuality allows it to penetrate into the proton and to interact with the proton's constituents. The symbols in parentheses in equation (2.1) represent the four-momenta of the respective particles.

In the generalized Bjorken limit, i.e., in the limit of large photon virtuality, $Q^2 \equiv -q^2 \rightarrow \infty$, with $x_B \equiv Q^2/(2pq)$ and $t \equiv (p - p')^2$ fixed, the amplitude of the DVCS process can be factorized into a convolution of a part describing the hard interaction of the virtual photon with a proton constituent, calculable in perturbation theory, and a soft non-perturbative part [2, 3, 4]. At leading order in $1/Q$ (leading twist) and in the coupling constant of quantum chromodynamics (QCD), α_s, the DVCS process can be described by the handbag diagram shown in figure 2.1. The non-perturbative part, represented by the blob, is expressed through matrix elements of gauge-invariant bi-local operators, i.e., gauge-invariant products of fields at separated space-time points. These matrix elements can be parametrized in terms of generalized parton distributions (GPDs), described in detail in the following section.

For the description of the DVCS process and the related quantities, it is natural to work
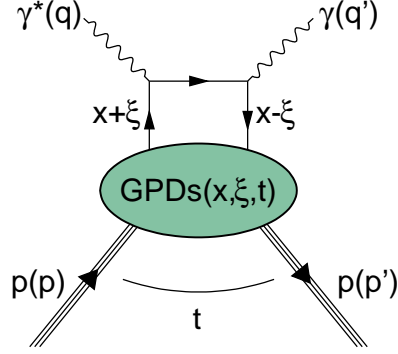
Figure 2.1: Handbag diagram for the leading-twist and leading-order contribution of the DVCS process. A second diagram is obtained by interchanging the quark-photon vertices.

with light-cone coordinates (see, e.g., reference [5] for detailed explanations), given by:

$$v^{\pm} = \frac{1}{\sqrt{2}}(v^0 \pm v^3) \text{ and } v_{\perp} = (v^1, v^2), \tag{2.2}$$

for any four-vector v. The handbag diagram can be seen in the frame where p and p' have large components along the positive z axis, with $P = (p + p')/2$ collinear with q, as the process where a quark carrying a momentum fraction $x + \xi$ of the proton's plus-momentum P^+ (or, equivalently in the infinite-momentum frame, longitudinal momentum) is taken out of the proton, and absorbs a virtual photon. The quark subsequently emits a real photon, acquiring a momentum fraction $x - \xi$, and returns back to the proton leaving it intact yet with a different momentum. The momentum fraction x ($\in [-1, 1]$) represents the average momentum fraction carried by the struck quark. The plus-momentum transfer to the proton is characterized by the 'skewness' ξ ($\in [-1, 1]$):

$$\xi \equiv -\frac{(q - q').(q + q')}{(p + p').(q + q')}, \tag{2.3}$$

$$\approx \frac{p^+ - p'^+}{p^+ + p'^+}, \tag{2.4}$$

$$\approx \frac{x_B}{2 - x_B}, \tag{2.5}$$

where the last two equalities apply in the generalized Bjorken limit. The transverse component of the momentum transfer is encoded in t, and is, as implied by the generalized Bjorken limit, small in comparison with Q. In the hard interaction, the in- and outgoing quarks (carrying momentum l) are treated as strictly collinear ($l_{\perp} = 0$) and on-shell ($l^- = 0$), resulting in helicity-selection rules.

4

The handbag diagram shown in figure 2.1 represents the dominant contribution to the DVCS amplitude. It appears at leading twist and leading order in α_s. To higher order in α_s radiative corrections to the hard-scattering amplitude need to be taken into account as well as diagrams where the 2 partons attached to the soft blob are gluons. Effects entering at next-to-leading order in α_s are well under control. The hard-scattering coefficients have been calculated [3, 7, 8]; for references concerning the evolution kernels related to the non-perturbative amplitude, see subsection 2.2.1. Diagrams involving the interaction with more than 1 proton constituent are suppressed by powers of $1/Q$, except for the exchange of longitudinally polarized gluons (gluons with polarization A^+). The exchange of these gluons is, however, summed in the non-perturbative part. It appears under the form of a Wilson line in between the two quark-field operators of the matrix elements. Diagrams involving the exchange of any other additional particle appear at higher twist. We use here the definition of twist as the order in M/Q at which an effect first appears. In particular for GPDs, it denotes the order in M/Q at which an operator matrix element contributes. Twist-t effects arise at order $(M/Q)^{t-2}$, with twist 2 (leading twist) forming the dominant contribution. The exchange of a transverse gluon between the horizontal line of the hard-interaction part and the soft blob appears at twist 3. This probes a different structure of the hadron; it involves antiquark-gluon-quark operators. Twist-3 contributions also involve the handbag diagram from figure 2.1 evaluated beyond the collinear approximation, by Taylor expanding the hard-scattering amplitude one order further, i.e., in $l_\perp$. These contributions can be expressed in terms of twist-2 GPDs. They relate to derivatives with respect to an overall translation in transverse direction of the twist-2 operators. They form the so-called Wandzura–Wilczek (WW) contribution. They are sometimes denoted as kinematical twist-3 contributions, while the antiquark-gluon-quark correlations are then called genuine twist-3 contributions. In a similar way, one can also consider twist-4 terms. Here also target-mass corrections need to be taken into account. The decomposition of the DVCS amplitude has been performed up to twist 3 [9] at leading order, and aspects about next-to-leading order twist-3 corrections [10], and about twist-4 corrections [11] have been investigated.

At leading twist and leading order in α_s, the strict collinearity of the particles entering the hard scattering dictates that the helicities of the incoming and outgoing states of the hard interaction must balance in order to ensure conservation of angular momentum. Additionally, since the quark is considered massless, conservation of chirality equals conservation of helicity. Thus, at leading twist and leading order in α_s the helicity of the photon is conserved, so that the incoming virtual photon needs to be transversely polarized. When considering twist-3 contributions that involve the exchange of a transversely polarized gluon, transitions from a longitudinally to a transversely polarized photon appear. Indeed, the exchange of a gluon can account for a helicity change by 1 unit. Also in the WW approximation, diagrams involving photon-helicity flip appear, with the struck quark carrying orbital angular momentum along the collision axis. Photon helicity transitions of 2 units appear at leading twist and next-to-leading order in α_s, balanced by the exchange of 2 gluons. Non-zero transfer of transverse momentum to the proton, providing 1 unit of angular momentum, allows the latter process to occur for the spin-1/2 proton. Also at twist 4 and leading order in α_s such photon-helicity-flip transitions can occur: either from the WW contribution, where the quark carries 2 units of angular momentum, either from a combination of the WW contribution with a quark carrying 1 unit of angular momentum and the exchange of an additional gluon, or from the collinear

configuration through the exchange of 2 additional transversely polarized gluons, provided that factorization holds at this order.

2.2 Generalized parton distributions

2.2.1 Definition of generalized parton distributions

The matrix elements entering the non-perturbative part of the handbag diagram from figure 2.1 can be decomposed in terms of GPDs as [12]:

$$
\begin{aligned}
F^q & = \int \frac{dz^-}{4\pi} e^{ixP^+z^-} \langle p'|\bar{\psi}_q(-\tfrac{1}{2}z)W[-\tfrac{1}{2}z,\tfrac{1}{2}z]\gamma^+\psi_q(\tfrac{1}{2}z)|p\rangle_{z^+,z_\perp=0_\perp} \\
& = \frac{1}{2P^+}[H^q(x,\xi,t)\bar{u}(p')\gamma^+ u(p) + E^q(x,\xi,t)\bar{u}(p')\frac{i\sigma^{+\alpha}\Delta_\alpha}{2M_p}u(p)], \quad (2.6)
\end{aligned}
$$

$$
\begin{aligned}
\tilde{F}^q & = \int \frac{dz^-}{4\pi} e^{ixP^+z^-} \langle p'|\bar{\psi}_q(-\tfrac{1}{2}z)W[-\tfrac{1}{2}z,\tfrac{1}{2}z]\gamma^+\gamma_5\psi_q(\tfrac{1}{2}z)|p\rangle_{z^+,z_\perp=0_\perp} \\
& = \frac{1}{2P^+}[\tilde{H}^q(x,\xi,t)\bar{u}(p')\gamma^+\gamma_5 u(p) + \tilde{E}^q(x,\xi,t)\bar{u}(p')\frac{\gamma_5\Delta^+}{2M_p}u(p)], \quad (2.7)
\end{aligned}
$$

where the superscript q refers to the quark flavor, ψ_q to the quark fields, u to the proton spinors, γ and σ to the Dirac matrices, and $\Delta = p' - p$. For legibility, the spin dependence of the hadron states and the spinors is omitted. The quantity $W[-\tfrac{1}{2}z^-,\tfrac{1}{2}z^-]$ represents the Wilson line along the light-like path from $-(1/2)\,z^-$ to $+(1/2)\,z^-$. It reduces to unity in the light-cone gauge, i.e., $A^+ = 0$. This gauge is assumed in the following.

The four GPDs H^q, $\tilde{H}^q$, E^q, and $\tilde{E}^q$ defined here conserve parton helicity. The GPDs H^q and $\tilde{H}^q$ conserve proton helicity; E^q and $\tilde{E}^q$ flip proton helicity. The GPDs H^q and E^q correspond to the sum over parton helicities (unpolarized GPDs), $\tilde{H}^q$ and $\tilde{E}^q$ to the difference (polarized GPDs). At leading twist there are in addition four quark helicity-flip GPDs [13], denoted H^q_T, $\tilde{H}^q_T$, E^q_T, $\tilde{E}^q_T$. Access to these distributions is more challenging due to their chiral-odd nature. A promising channel to study these distributions is the exclusive production of two mesons [14, 15].

Regarding the gluon structure of the proton, eight GPDs appear at leading twist. Similarly to the quark GPDs, they are categorized as spin-dependent and spin-independent gluon helicity-conserving (helicity-flip) and proton helicity-conserving (helicity-flip) GPDs.

From time-reversal invariance it follows that GPDs are real valued. They are functions of x, ξ, and t. In addition they depend on Q^2 through QCD evolution. The evolution kernels are computed at leading order [16, 17, 2, 18] and next-to-leading order [19, 20] in α_s. Here and subsequently, their dependence on Q^2 is not explicitly written. Contrary to the GPDs that conserve parton helicity, the quark helicity-flip and gluon helicity-flip GPDs do not mix under evolution. Access to gluon helicity-flip GPDs provides thus a rather unique probe to study the gluon content of the proton.

2.2.2 Properties and the physics of GPDs

The properties and physics interpretation presented here mainly focus on the quark helicity-conserving GPDs, which are of primary importance when studying DVCS.

Since GPDs involve a different initial and final state, they represent probability amplitudes and not probability densities. Considering $\xi \geq 0$, a GPD in the region $\xi < x < 1$ corresponds to the amplitude for taking out a quark of momentum fraction $x + \xi$, changing its momentum to $x - \xi$, and inserting it back into the nucleon, as was already mentioned in section 2.1; in the region $-\xi < x < \xi$, it represents the amplitude for the emission from the initial proton of a quark with momentum fraction $x + \xi$ and of an antiquark with momentum fraction $\xi - x$; finally, in the region $-1 < x < -\xi$, we find the equivalent of the first region, but now considering the emission of an antiquark with momentum fraction $\xi - x$ and the absorption of an antiquark with momentum $-\xi - x$. In the first and third regions ($|x| > \xi$), the scale evolution of the GPDs is given by the DGLAP equations [21, 22, 23, 24], whereas in the region $|x| < \xi$ it is described by the ERBL equations [25, 26]. Therefore, the former regions are referred to as the DGLAP region and the latter is referred to as the ERBL region. An explicit decomposition of the GPDs defined in equations (2.6) and (2.7) in terms of creation and annihilation operators can be found in reference [12].

The Mellin moments of GPDs have the property of polynomiality, as a consequence of Lorentz invariance [27]. This means that the ξ dependence of the n'th Mellin moment of the GPD is given by a polynomial in ξ of order $n + 1$ at most:

$$\int_{-1}^{1} dx\, x^n\, H^q(x,\xi,t) = h_0^{q(n)}(t) + h_2^{q(n)}(t)\,\xi^2 + \ldots + h_{n+1}^{q(n)}(t)\,\xi^{n+1},$$

$$\int_{-1}^{1} dx\, x^n\, E^q(x,\xi,t) = e_0^{q(n)}(t) + e_2^{q(n)}(t)\,\xi^2 + \ldots + e_{n+1}^{q(n)}(t)\,\xi^{n+1}. \tag{2.8}$$

Because of time-reversal invariance, the polynomial contains only even powers of ξ. Thus the highest power in ξ is n for n even, and $n + 1$ for n odd. For the spin-dependent quark helicity-conserving GPDs analogous relations hold, except that the polynomial is at most of order n, thus n for n even, and $n - 1$ for n odd. For n odd, the coefficients $h_{n+1}^{q(n)}(t)$ and $e_{n+1}^{q(n)}(t)$ of the GPDs H and E are related as [12]:

$$e_{n+1}^{q(n)}(t) = -h_{n+1}^{q(n)}(t). \tag{2.9}$$

In the forward limit of $t = 0$ and $\xi = 0$, the GPDs H^q, $\tilde{H}^q$, and H_T^q reduce to the parton distribution functions (PDFs) $q(x)$, $\Delta q(x)$, and $\delta q(x)$:

$$
\begin{aligned}
H^q(x,0,0) = q(x), \quad & \tilde{H}^q(x,0,0) = \Delta q(x) \quad \text{for} \quad x > 0, \\
H_T^q(x,0,0) = \delta q(x) \quad & \phantom{\tilde{H}^q(x,0,0) = \Delta q(x)} \quad \text{for} \quad x > 0,
\end{aligned} \tag{2.10}
$$

and corresponding relations for antiquark distributions for $x < 0$. The spin-independent distribution $q(x)$ represents the probability to find a quark of flavor q with momentum fraction x in a proton in the infinite-momentum frame; the helicity distribution $\Delta q(x)$ represents the difference in number density of quarks of flavor q having the same and opposite helicity

as the target proton in the infinite-momentum frame. The transversity distribution $\delta q(x)$ only has a probabilistic interpretation in the basis of transverse spin eigenstates. It relates to the difference in number density of quarks with their spin aligned and anti-aligned with respect to the transverse spin of a fast-moving proton. The distributions $q(x)$ and $\Delta q(x)$ are well known, see, e.g., references [28] for $q(x)$ and [29] for $\Delta q(x)$. The extraction of the transversity distribution is more intricate due to its chiral-odd nature. A first extraction was possible based on the combination of data sets from several experiments [30]. As can be seen from equations (2.6) and (2.7), the GPDs E and $\tilde{E}$ are multiplied with Δ and thus vanish in the forward limit. The same holds for the quark helicity-flip GPDs.

For gluons only 2 GPDs are accessible in the forward limit:

$$H^g(x,0,0) = xg(x), \quad \tilde{H}^g(x,0,0) = x\Delta g(x) \quad \text{for} \quad x > 0, \tag{2.11}$$

and corresponding relations for $x < 0$. For the definition of the gluon GPDs, reference [13] is followed. Analogous probabilistic interpretations as for the quark distributions hold for the spin-independent $g(x)$ and spin-dependent $\Delta g(x)$ gluon distributions. The spin-independent distribution is well known; the spin-dependent distribution is much less constrained [28, 29]. It is clear that the gluon helicity-flip GPDs must decouple in the forward limit, since here a change of helicity by 2 units cannot be compensated by a spin-$1/2$ particle.

Integrating the quark helicity-conserving GPDs over x, one finds the elastic form factors:

$$\int_{-1}^{1} dx \, H^q(x,\xi,t) = F_1^q(t), \quad \int_{-1}^{1} dx \, E^q(x,\xi,t) = F_2^q(t), \tag{2.12}$$

$$\int_{-1}^{1} dx \, \tilde{H}^q(x,\xi,t) = g_A^q(t), \quad \int_{-1}^{1} dx \, \tilde{E}^q(x,\xi,t) = g_P^q(t), \tag{2.13}$$

with $F_1^q(t)$ and $F_2^q(t)$ the Dirac and Pauli form factors, and $g_A^q(t)$ and $g_P^q(t)$ the axial-vector and pseudo-scalar form factors for the quark of flavor q in the nucleon. These relations show that GPDs allow for a decomposition of the form factors in longitudinal momentum fraction x. In other words, GPDs allow to determine how many quarks with momentum fraction x contribute to the form factors.

Through the construction of impact-parameter dependent parton distributions (IPD-PDFs), it is possible to locate quarks in the transverse plane [32]. The position of the quarks is herewith defined with respect to the transverse center of longitudinal momentum $R_\perp$, i.e., the average of the positions of quarks and gluons weighted with their longitudinal momentum fraction:

$$R_\perp = \sum_{i=q,g} x_i r_{\perp,i}. \tag{2.14}$$

The IPD-PDF $q(x,b_\perp)$ is then constructed from the GPD H^q, taking $\xi = 0$, as:

$$q(x,b_\perp) = \int \frac{d^2\Delta_\perp}{4\pi^2} H^q(x,0,-\Delta_\perp^2) e^{-ib_\perp \Delta_\perp}, \tag{2.15}$$

where $t = -\Delta_\perp^2$ for $\xi = 0$. The IPD-PDF $q(x,b_\perp)$ represents the probability to find a quark of flavor q with longitudinal momentum fraction x and at a transverse distance $b_\perp$ with

respect to $R_\perp$. Analogously the Fourier transform of $\tilde{H}^q(x, 0, t)$ yields the spin-dependent IPD-PDF $\Delta q(x, b_\perp)$. For a proton polarized in a direction other than z, e.g., along the x axis, the GPD E describes the distortion of the spin-independent quark distribution in the direction along y:

$$q_X(x, b_\perp) = q(x, b_\perp) + \frac{1}{2\,M_p} \frac{\partial}{\partial b_y} \mathcal{E}^q(x, b_\perp), \tag{2.16}$$

where $q_X(x, b_\perp)$ is the spin-independent quark distribution for a proton with spin-polarization along the x direction and $\mathcal{E}^q(x, b_\perp)$ is the impact-parameter dependent distribution built from GPD $E(x, 0, t)$.

Another very important aspect of GPDs is their connection with the angular momentum of quarks, J^q. GPDs H^q and E^q allow access to the quark angular momentum through the Ji relation [33]:

$$J^q = \lim_{t \to 0} \frac{1}{2} \int_{-1}^{1} dx\, x\, [H^q(x, \xi, t) + E^q(x, \xi, t)]. \tag{2.17}$$

The angular momentum J^q can be decomposed into the helicity contribution and the contribution from orbital angular momentum:

$$J^q = \frac{1}{2}(\Delta q + \Delta \bar{q}) + L^q, \tag{2.18}$$

and allows to extract the quark orbital angular momentum L^q. The Ji relation also allows access to the gluon angular momentum, J^g:

$$J^g = \lim_{t \to 0} \frac{1}{2} \int_{0}^{1} dx\, [H^g(x, \xi, t) + E^g(x, \xi, t)], \tag{2.19}$$

or alternatively, J^g can be evaluated from the proton spin as: $J^g = \frac{1}{2} - \sum_q J^q$. A further gauge-invariant decomposition of J^g does not exist. Contrary to the quark helicity distribution, L^q and J^g do not have a partonic interpretation in terms of differences in number densities. Interactions prevent a clean separation into pure quark and gluon contributions.

A different decomposition of the proton spin exists [34]. Here, the proton spin is separated into the individual contributions from the quark helicity, the gluon helicity, the quark orbital angular momentum, and the gluon orbital angular momentum. In the light-cone gauge all quantities are interaction independent, and a clear interpretation in terms of number densities exists for each of the four terms. The quark helicity contribution from this decomposition coincides with the one in equation (2.18); the gluon helicity contribution corresponds to $\Delta g(x)$ from equation (2.11). However, for the determination of the orbital angular momenta no experimental channel has so far been identified.

2.2.3 Parametrization of GPDs

At present, the extraction of GPDs relies on phenomenological parametrizations. A functional form for GPDs that contains a certain number of free parameters is here assumed. The free parameters can be obtained from fits to measured cross sections or asymmetries. As an example, the parametrizations used in the VGG model [27, 35] are briefly discussed here.

GPDs can be represented in terms of double distributions [36, 37]. For GPD H^q this reads:

$$H^q(x, \xi, t) = \int_{-1}^{1} d\beta \int_{-1+|\beta|}^{1-|\beta|} d\alpha \, \delta(x - \beta - \alpha \xi) \, H_{DD}^q(\beta, \alpha, t) + \theta[1 - \frac{x^2}{\xi^2}] D^q(\frac{x}{\xi}, t). \quad (2.20)$$

For GPD E^q an analogous expression applies, except that the second term is preceded by a minus sign. This representation satisfies the polynomiality property, given in equation (2.8). The term $D^q(\frac{x}{\xi}, t)$ is the so-called D-term which generates the highest power in ξ for n odd [38]. Because of the step function $\theta[1 - \frac{x^2}{\xi^2}]$, it only contributes in the ERBL region. The spin-dependent GPDs $\tilde{H}^q$ and $\tilde{E}^q$ can also be represented by double distributions as in equation (2.20), but here the D-term does not contribute at all. The parametrized form of the D-term is obtained by expanding the term in a Gegenbauer polynomial, and using as values for the coefficients calculations from the chiral quark-soliton model [39].

The double distribution is further written as:

$$H_{DD}^q(\beta, \alpha, t) = h^{(b)}(\beta, \alpha) \, H^q(\beta, 0, t), \quad (2.21)$$

where $h^{(b)}(\beta, \alpha)$ is a profile function of the form:

$$h^{(b)}(\beta, \alpha) \propto \frac{[1 - |\beta|^2 - \alpha^2]^b}{(1 - |\beta|)^{2b+1}}. \quad (2.22)$$

The parameter b is a free parameter that controls the strength of the dependence of the GPDs on ξ. In the limit $b \to \infty$, they become independent of ξ. The parameter b can be chosen independently for sea quarks and for valence quarks.

As ansatz for $H^q(\beta, 0, t)$, a factorized form can be chosen, where the x dependence is modeled by the spin-independent PDF and the t dependence by the Dirac form factor, satisfying relations (2.10) and (2.13). This ansatz is however disfavored based on phenomenological and theoretically motivated considerations [40]. Alternatively, a Regge-based ansatz can be opted for [27]:

$$H^q(\beta, 0, t) = \frac{1}{|\beta|^{\alpha' t}} q(\beta), \quad (2.23)$$

with α' the slope of the Regge trajectory and $q(\beta)$ the spin-independent PDF.

The parametrization of GPD $\tilde{H}^q$ follows the same procedure. For GPD E^q the constraint from the forward limit is absent. Instead, a PDF is constructed from contributions from valence quarks, following the shape of $q(x)$, and sea quarks, which according to the chiral quark-soliton model is narrowly peaked around $x = 0$. Finally, GPD $\tilde{E}^q$ is assumed to only receive contributions from the pion pole, of the form $1/(m_\pi^2 - t)$, with m_π the pion mass.

2.3 GPDs and DVCS amplitudes

DVCS amplitudes can be expressed in a basis of so-called Compton Form Factors (CFFs). These CFFs are the convolution integrals, mentioned previously, of the hard-scattering kernels and GPDs, where the hard-scattering amplitude makes them complex functions. At

leading order in α_s, the CFFs $\mathcal{F} = \{\mathcal{H}, \mathcal{E}\}$ and $\tilde{\mathcal{F}} = \{\tilde{\mathcal{H}}, \tilde{\mathcal{E}}\}$ are written as:

$$\mathcal{F}(\xi, t) = \sum_q e_q^2 \int_{-1}^{1} dx\, F^q(x, \xi, t) \left(\frac{1}{\xi - x - i\epsilon} - \frac{1}{\xi + x - i\epsilon} \right), \qquad (2.24)$$

$$\tilde{\mathcal{F}}(\xi, t) = \sum_q e_q^2 \int_{-1}^{1} dx\, \tilde{F}^q(x, \xi, t) \left(\frac{1}{\xi - x - i\epsilon} + \frac{1}{\xi + x - i\epsilon} \right), \qquad (2.25)$$

$$(2.26)$$

where F^q refers to the GPDs H^q and E^q, and $\tilde{F}^q$ refers to the GPDs $\tilde{H}^q$ and $\tilde{E}^q$. The Q^2 dependence of the CFFs is here not explicitly written. At next-to-leading order in α_s also gluon GPDs enter the expression of the CFFs $\mathcal{F}$ and $\tilde{\mathcal{F}}$. Analogously, also twist-3 CFFs, written in terms of twist-3 GPDs, exist.

From the above equations the interplay between the longitudinal momentum fractions x and ξ in the DVCS amplitude becomes apparent. The simultaneous dependence of the hard-scattering kernel and the non-perturbative amplitude on the longitudinal momentum fractions x and ξ does not allow direct access to x and to the GPDs [6][1]. Instead, at present, GPDs are constrained based on phenomenological parametrizations.

A possibility to gain in the future more direct information about GPDs is provided by the study of double DVCS, i.e., DVCS where the final-state photon is also virtual, and subsequently decays into, e.g., a lepton pair [41].

2.4 Exclusive lepto-production of real photons

Deeply virtual Compton scattering can be accessed in the exclusive process:

$$e(k) + p(p) \rightarrow e(k') + p(p') + \gamma(q'), \qquad (2.27)$$

where a high-energetic lepton, positron in the present study, is scattered off a proton, with as a result a final state that consists exactly of the scattered lepton, recoiling proton, and real photon. Again, the quantities between brackets in equations (2.27) represent the four-momenta of the respective particles. The interaction of the electron with the proton is in good approximation mediated by the exchange of a single virtual photon (at the energies considered here).

Apart from the DVCS process, the exclusive reaction (2.27) also includes the Bethe–Heitler (BH) process. Here the real photon is radiated by the incoming or scattered lepton. The DVCS and the BH processes are depicted in figure 2.2. Since both processes have the same initial and final states, their contributions add coherently.

2.4.1 Kinematic variables

Variables needed to describe the DVCS process are reconstructed from the four-momenta of the particles appearing in equation (2.27).

---

[1]except at $x = \pm\xi$, as shown in subsection 2.4.3.
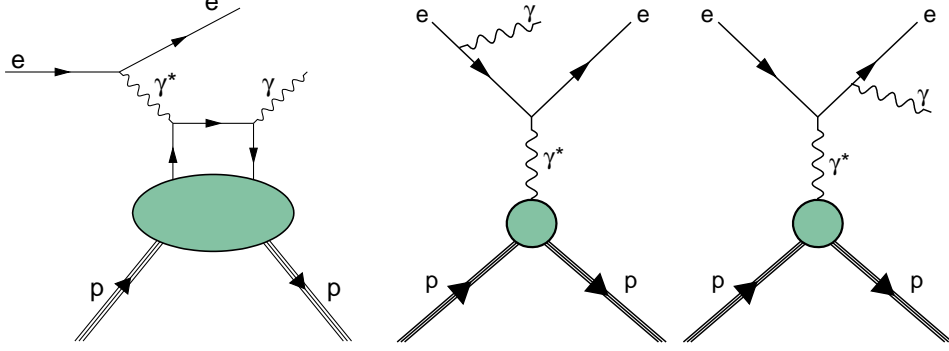
Figure 2.2: DVCS process (left) and BH process (center and right). For the DVCS process, a second diagram is obtained by interchanging the quark-photon vertices.

The photon virtuality Q:

$$Q^2 \quad \equiv \quad -q^2 = -(k - k')^2 \tag{2.28}$$

$$\overset{lab}{=} \quad 4EE' \sin^2\!\left(\frac{\theta}{2}\right), \tag{2.29}$$

can be calculated in the laboratory frame (lab) from the energy of the initial lepton E, the scattered lepton E', and θ, the angle of the scattered lepton with respect to the incoming lepton (= beam axis).

Another Lorentz invariant quantity is ν:

$$\nu \quad \equiv \quad \frac{pq}{M_p} \tag{2.30}$$

$$\overset{lab}{=} \quad E - E', \tag{2.31}$$

representing in the laboratory frame the energy transferred by the scattered lepton.

The variable y:

$$y \quad \equiv \quad \frac{pq}{pk} \tag{2.32}$$

$$\overset{lab}{=} \quad \frac{\nu}{E}, \tag{2.33}$$

represents in the laboratory frame the fractional energy transfer to the nucleon.

The Bjorken scaling variable is given as:

$$x_B \quad \equiv \quad \frac{Q^2}{2pq} \tag{2.34}$$

$$= \quad \frac{Q^2}{2M_p\nu}. \tag{2.35}$$
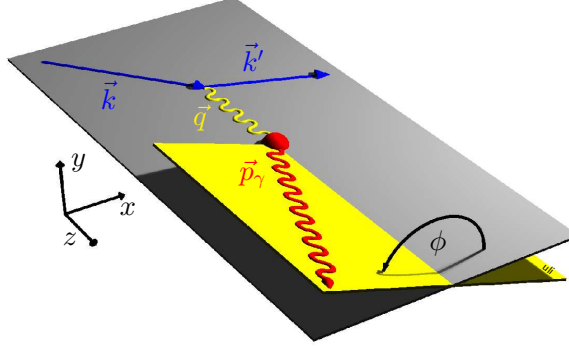
Figure 2.3: Azimuthal angle ϕ between the lepton-scattering plane and photon-production plane.

The squared invariant mass of the photon-nucleon system is defined as:

$$W^2 \equiv (p + q)^2 = M_p^2 + 2M_p\nu - Q^2. \tag{2.36}$$

The above variables enter the description of deep-inelastic scattering (DIS) processes, and are sufficient for the description of inclusive processes, where only the scattered lepton is reconstructed. For the description of the exclusive DVCS process, an additional invariant quantity is needed, namely the Mandelstam variable t:

$$t \equiv (p - p')^2 = (q - q')^2, \tag{2.37}$$

which can be calculated from the additionally detected real photon or the recoiling proton.

2.4.2 Cross section

The four-fold differential cross section of process (2.27) is given by:

$$\frac{d\sigma}{dx_B\, dy\, d|t|\, d\phi} = \frac{\alpha_{em}^3\, x_B\, y}{8\,\pi\, Q^2 \sqrt{1 + 4\,x_B^2\, M_p^2/Q^2}} \left| \frac{\tau}{e^3} \right|^2, \tag{2.38}$$

with α_{em} the fine-structure constant and e the charge of the lepton. The angle ϕ is the angle between the lepton-scattering plane, formed by the trajectories of the incoming and outgoing leptons, and the photon-production plane, determined by the virtual and real photons. The definition of the angle ϕ is illustrated in figure 2.3. The amplitude τ contains the coherent sum of the BH and the DVCS processes:

$$\tau^2 = |\tau_{BH}|^2 + |\tau_{DVCS}|^2 + \mathcal{I}, \tag{2.39}$$

with the interference term $\mathcal{I}$ given by:

$$\mathcal{I} = \tau_{DVCS}\tau_{BH}^* + \tau_{DVCS}^*\tau_{BH}. \tag{2.40}$$

13

The angular dependence of each term in equation (2.39) arises from the contraction of leptonic tensors, describing the $e-\gamma^*$ part of the interaction, and hadronic tensors, describing the $\gamma^* - p$ part. The terms can be decomposed in a finite sum of Fourier harmonics. For scattering on an unpolarized nucleon target, this decomposition reads [9][2]:

$$|\tau_{BH}|^2 = \frac{e^6}{x_B^2 \, y^2 \, t \, (1 + 4 \, x_B^2 \, M_p^2/Q^2)^2 \, \mathcal{P}_1(\phi) \, \mathcal{P}_2(\phi)} \left\{ c_0^{BH} + \sum_{n=1}^{2} c_n^{BH} \cos(n\phi) \right\}, \quad (2.41)$$

$$|\tau_{DVCS}|^2 = \frac{e^6}{y^2 \, Q^2} \left\{ c_0^{DVCS} + \sum_{n=1}^{2} c_n^{DVCS} \cos(n\phi) + \lambda \, s_1^{DVCS} \sin(\phi) \right\}, \quad (2.42)$$

$$\mathcal{I} = \frac{\pm e^6}{x_B \, y^3 \, t \, \mathcal{P}_1(\phi) \, \mathcal{P}_2(\phi)} \left\{ c_0^{\mathcal{I}} + \sum_{n=1}^{3} c_n^{\mathcal{I}} \cos(n\phi) + \lambda \sum_{n=1}^{2} s_n^{\mathcal{I}} \sin(n\phi) \right\}, \quad (2.43)$$

where $+\,(-)$ stands for a negatively (positively) charged lepton beam. The beam polarization is referred to by λ. The Fourier components are functions of x_B, t, and Q^2. The BH amplitude is real and calculable in quantum electrodynamics (QED). It depends on the Dirac and Pauli form factors, which are well measured at small t [42]. The quantities $\mathcal{P}_1(\phi)$ and $\mathcal{P}_2(\phi)$ represent the BH lepton propagators. They are of the form $J + K\cos(\phi)$. The coefficients belonging to the interference term are linear functions of the previously introduced CFFs. The coefficients entering the Fourier decomposition of τ_{DVCS}^2 are bilinear in the CFFs.

The coefficients $c_0^{\mathcal{I}}$, $c_1^{\mathcal{I}}$, $s_1^{\mathcal{I}}$, and c_0^{DVCS} are given in terms of twist-2 GPDs, with $c_0^{\mathcal{I}}$ appearing at twist 3, i.e., suppressed as $1/Q$; the coefficients $c_2^{\mathcal{I}}$, $s_2^{\mathcal{I}}$, c_1^{DVCS}, and s_1^{DVCS} are related to twist-3 GPDs; the coefficients $c_3^{\mathcal{I}}$ and c_2^{DVCS} are induced at twist 2 by gluon-helicity-flip GPDs, suppressed as α_s/π, and also contain twist-4 contributions from quark GPDs.

2.4.3 Beam-helicity azimuthal asymmetry

At leading twist the interference term vanishes after integration over ϕ, since $c_0^{\mathcal{I}}$ is kinematically suppressed as $1/Q$. The measurement of the cross section (2.38) integrated over ϕ thus allows to access the DVCS cross section, after subtraction of the BH cross section. At HERMES kinematics the BH cross section dominates the DVCS cross section by at least an order of magnitude [43], rendering the extraction of the DVCS cross section impossible. On the other hand, access to the interference term is possible through the measurement of cross-section differences or in order to avoid measurements of absolute cross sections, which require a good normalization, and to reduce the influence of the detector acceptance, through the measurement of asymmetries. The interference term also has the advantage that its Fourier coefficients are linear in the CFFs, whereas, as already mentioned, for the DVCS cross section the Fourier coefficients are bilinear.

The present work deals with the measurement of the beam-helicity asymmetry $A_{LU}(\phi)$:

$$A_{LU}(\phi) = \frac{d\sigma^{\rightarrow} - d\sigma^{\leftarrow}}{d\sigma^{\rightarrow} + d\sigma^{\leftarrow}}, \quad (2.44)$$

---

[2]Note that the angle ϕ from reference [9] is defined as $\phi_{[9]} = \pi - \phi$, resulting in opposite signs for the even sine and odd cosine coefficients.

using an longitudinally (L) polarized positron beam and an unpolarized (U) proton target. It is given as the ratio of the difference in normalized yields with positive ($\rightarrow$) and negative ($\leftarrow$) beam helicity to the sum of these yields.

Written in terms of the Fourier coefficients, the asymmetry reads:

$$A_{LU}(\phi) =$$

$$\frac{-K_{\mathcal{I}}\,\mathcal{P}(\phi)\displaystyle\sum_{n=1}^{2} s_n^{\mathcal{I}} \sin(n\phi) + K_{DVCS}\, s_1^{DVCS} \sin(\phi)}{\mathcal{P}(\phi)\left[K_{BH}\displaystyle\sum_{n=0}^{2} c_n^{BH}\cos(n\phi) - K_{\mathcal{I}}\displaystyle\sum_{n=0}^{3} c_n^{\mathcal{I}}\cos(n\phi)\right] + K_{DVCS}\displaystyle\sum_{n=0}^{2} c_n^{DVCS}\cos(n\phi)},$$

$$(2.45)$$

where we have implied that the measurement uses a positron beam. The factors K_{BH}, K_{DVCS}, and $K_{\mathcal{I}}$ refer to the kinematic prefactors appearing in equations (2.41), (2.42), and (2.43) respectively. The lepton propagators are combined into $\mathcal{P}(\phi) = \mathcal{P}_1(\phi)\,\mathcal{P}_2(\phi)$.

The numerator contains two terms with a $\sin(\phi)$ modulation, which experimentally can not be disentangled. Of these terms, only $s_1^{\mathcal{I}}$ is a leading-twist term, whereas s_1^{DVCS} involves a product of twist-2 and twist-3 CFFs. The $\sin(2\phi)$ modulation also appears at twist 3. In the denominator, the dominant contribution arises from the BH amplitude, and in particular from the c_0^{BH} coefficient. Considering only the dominant contributions, we can approximate the asymmetry as:

$$\begin{aligned}
A_{LU}(\phi) &\approx -\frac{x_B\,(1 + 4\,x_B^2\,M_p^2/Q^2)^2}{y}\,\frac{s_1^{\mathcal{I}}}{c_0^{BH}}\sin(\phi) \\
&\approx -\frac{x_B}{y}\,\frac{s_1^{\mathcal{I}}}{c_0^{BH}}\sin(\phi).
\end{aligned} \qquad (2.46)$$

(The last step is justified since the term between brackets in the first equation is close to unity.) The asymmetry has thus predominantly a $\sin(\phi)$ modulation. Note that the coefficients c_0^{BH} and $s_1^{\mathcal{I}}$ have different kinematic dependencies, so that effectively the asymmetry is in addition dependent on t and Q^2.

Within this approximation, the asymmetry can be related, through $s_1^{\mathcal{I}}$, to the imaginary part of the photon helicity-conserving DVCS amplitude $M^{1,1}$, as $A_{LU} \propto s_1^{\mathcal{I}} \propto \Im(M^{1,1})$, with

$$M^{1,1} = F_1(t)\,\mathcal{H}(\xi,t) + \frac{x_B}{2 - x_B}(F_1(t) + F_2(t))\,\tilde{\mathcal{H}}(\xi,t) - \frac{t}{4M_p^2}\,F_2(t)\mathcal{E}(\xi,t). \quad (2.47)$$

Here F_1 and F_2 represent the Dirac and Pauli form factors, respectively. The contributions from the CFFs $\tilde{\mathcal{H}}$ and $\mathcal{E}$ are kinematically suppressed with respect to the CFF $\mathcal{H}$ in the kinematic region covered by the HERMES experiment.

Separating the CFF $\mathcal{H}$[3] at leading order in α_s into its real and imaginary part:

$$\Re\mathcal{H}(\xi,t) = \sum_q e_q^2\,PV\int_{-1}^{1} dx\, H^q(x,\xi,t)\left[\frac{1}{\xi - x} - \frac{1}{\xi + x}\right], \qquad (2.48)$$

---

[3]An equivalent decomposition also applies for the CFFs $\tilde{\mathcal{H}}$, $\mathcal{E}$, and $\tilde{\mathcal{E}}$.

$$\Im \mathcal{H}(\xi, t) = \pi \sum_q e_q^2 \left[H^q(\xi, \xi, t) - H^q(-\xi, \xi, t) \right], \tag{2.49}$$

with PV Cauchy's principal value, one can see that at leading order in α_s the imaginary part of the CFF allows direct access to the GPD H^q at the points $x = \pm\xi$, the boundaries between the DGLAP and ERBL regions. At next-to-leading order in α_s the imaginary part of the CFF probes the DGLAP region, $|x| \geq \xi$. The real part of the CFF involves both the DGLAP and the ERBL regions, but appears as a convolution integral, already at leading order in α_s. Access to the real part of the amplitude is provided through the coefficient c_1^I, accessible via the extraction of the beam-charge azimuthal asymmetry.

2.5 Associated DVCS

The GPDs discussed so far describe the structure of the soft part of hard exclusive reactions where the nucleon stays in its ground state. For the description of processes where the nucleon is excited to a resonance state, e.g., $p \to \Delta$, transition GPDs need to be introduced. In this section we concentrate on the p–Δ^+ transition. The p–Δ^0 and p–Δ^{++} transition GPDs are related to the p–Δ^+ transition GPDs through isospin symmetry. There also exist transition GPDs to describe transitions from the proton to other single-baryon states, e.g., $p \to n$, or to continuum states, like $p \to p\pi^0$. The latter have been described and estimated in reference [44] in the limit of small pion momentum in terms of nucleon GPDs.

The p–Δ^+ transition GPDs can be accessed in the hard exclusive process:

$$e(k) + p(p) \to e(k') + \Delta^+(p') + \gamma(q'). \tag{2.50}$$

The formed Δ^+ resonance decays mainly into $p\pi^0$, with a branching ratio of $\sim 67\%$, or into $n\pi^+$, with a branching ratio of $\sim 33\%$. Analogously to the elastic process, the process (2.50) receives contributions from associated DVCS, where the real photon originates from the hadron, and from associated BH, where the photon is radiated by the incoming or scattered lepton. The interference of the two associated processes shows again a characteristic angular structure [6], allowing access to transition GPDs through, e.g., the study of the beam-helicity azimuthal asymmetry [44].

The factorization theorem valid for the elastic DVCS process also remains valid for associated DVCS (and for transitions other than $p \to \Delta^+$) in the generalized Bjorken limit, provided that the invariant mass of the final hadronic state is small in comparison with Q^2, as is also implicit for elastic DVCS when referring to the Bjorken limit. For a complete description at leading twist of the quark distributions eight leading p–Δ^+ transition quark GPDs are needed [45], in accordance with the number of independent helicity transitions for the quark-hadron system [6]. Analogously to equations (2.6) and (2.7), they are defined through non-diagonal matrix elements of products of quark fields at light-cone separation. Four GPDs relate to the vector twist-2 operator and four to the axial-vector twist-2 operator.

As for nucleon GPDs, the transition p–Δ^+ GPDs are real valued. They contain information about the distribution of quarks with respect to their helicity state, their longitudinal momentum, and their transverse position. Their first moment in x relates them to transition form factors. For one of the vector transition GPDs the first moment vanishes, since

gauge invariance for the nucleon electromagnetic current operator leads to only three vector transition form factors [44]. The remaining three form factors are the magnetic-dipole, electric-quadrupole and Coulomb-quadrupole transition form factors. The spin-dependent quark transition GPDs relate to the axial-vector current $p \to \Delta^+$ transition form factors [27].

In the large N_c limit, i.e., in the limit of an infinite number of colors, the proton and Δ^+ appear as different excitations of the same object, namely the soliton [46]. In this limit, estimated to be accurate at the 30% level [44], three transition GPDs out of the seven transition GPDs with non-vanishing first moment are dominant: one spin-independent transition GPD and two spin-dependent transition GPDs. They relate to the proton GPDs as $E^u - E^d$, $\tilde{H}^u - \tilde{H}^d$, and $\tilde{E}^u - \tilde{E}^d$, respectively. In this limit associated DVCS allows to probe different flavor combinations of the nucleon GPDs, since elastic DVCS probes in general combinations of the type $\frac{4}{9}F^u + \frac{1}{9}F^d$, where F^q represents a generic proton quark GPD.

2.6 DVCS at HERMES

Various azimuthal asymmetries for the process $ep \to ep\gamma$ have been measured at the HERMES experiment. The first measurement was performed using a longitudinally polarized positron beam and an unpolarized hydrogen target, allowing for the extraction of the azimuthal beam-helicity asymmetry [47]. From measurements with a positron and electron beam, the beam-charge azimuthal asymmetry was extracted [48]. This asymmetry is, as already mentioned, sensitive to the real part of the photon helicity-conserving DVCS amplitude $M^{1,1}$ (see equation (2.47)), which is dominated by the CFF $\mathcal{H}$. The combination of measurements with a longitudinally polarized positron and electron beam allowed for the separation of the coefficients $s_1^{\mathcal{I}}$ and s_1^{DVCS} in equation (2.45) [49]. Also azimuthal asymmetries from data collected on a longitudinally polarized hydrogen target have been measured [51]. These are dominated by the GPD $\tilde{H}$. Finally, data collected on a transversely polarized proton target allowed for the extraction of asymmetries that are mainly sensitive to GPD E [50]. This GPD enters in combination with GPD H the Ji relation (2.17).

The $ep \to ep\gamma$ process was for all these measurements reconstructed from the photon and scattered lepton. The proton could not be detected due to its low energy and its angular distribution. Instead, the missing mass squared M_X^2 was reconstructed:

$$M_X^2 = (q + p - q')^2, \tag{2.51}$$

and appropriate constraints were placed on its value for the event selection. The resolution of the HERMES spectrometer, however, does not allow to separate the elastic DVCS and BH processes from the associated processes $p \to \Delta^+$ and continuum-state transitions. In order to reduce the background from associated production, and from other DIS processes, a recoil detector was installed around the target area to allow for the detection of the low-energetic final state particles. This detector is described in the following chapter, together with the HERMES spectrometer. In chapter 5 the elastic DVCS and BH processes are studied using the recoil detector, and signals from associated production $p \to \Delta^+$ are isolated. The latter also receive contributions from the continuum-state transitions.

3. HERMES experiment

The HERMES (HERa MEasurement of Spin) experiment at the HERA[1] storage ring at DESY[2] started data collection in 1995 with the aim of analyzing the quark-gluon spin structure of the nucleon, through the study of asymmetries. The first five years of data collection, using a longitudinally polarized lepton beam and longitudinally polarized gaseous targets, concentrated on the investigation of parton helicity distributions. More specifically, the analysis of semi-inclusive DIS events, i.e., where in addition to the scattered lepton one or more hadrons created in the interaction are reconstructed, provides sensitivity to the flavor of the struck quark, and resulted in the extraction of flavor-dependent quark helicity distributions. In a later period, a transversely polarized target allowed the collection of data needed for the understanding of the spin structure of a transversely polarized nucleon, which because of the relativistic nature of partons, differs from the spin structure of a longitudinally polarized nucleon. In the last two years of data taking, from 2006 until 2007, the polarized-target setup made place for the recoil detector, with data collection on an unpolarized hydrogen and deuterium target to improve the study of DVCS, by strongly reducing the contribution from background processes.

In the present chapter the HERMES experiment is described, with emphasis on the detector components of importance for the analysis reported in this work.

3.1   The HERA lepton beam

The HERA beam facility was operational until 2007. It consisted of two independent storage rings, sharing the same tunnel [52]. They were located at a depth of 15–30 m below the surface and had a circumference of 6.3 km. One storage ring circulated 920 GeV (820 GeV before 1998) protons; the other storage ring contained either electrons or positrons with an energy of 27.6 GeV. Before injection in the HERA rings, protons and leptons were processed by a series of linear accelerators and synchrotrons. The pre-accelerator system and the HERA configuration are depicted in figure 3.1. The PETRA storage ring formed the last stage of the pre-accelerator system and injected protons with an energy of 40 GeV and leptons with an energy of 12 GeV into the HERA rings. The counter-rotating lepton and proton beams were brought head-on into collision at two interaction points. The interaction points were situated at the north and south halls, where, respectively, the experiments H1 and ZEUS were

---

[1]Hadron Elektron Ring Anlage
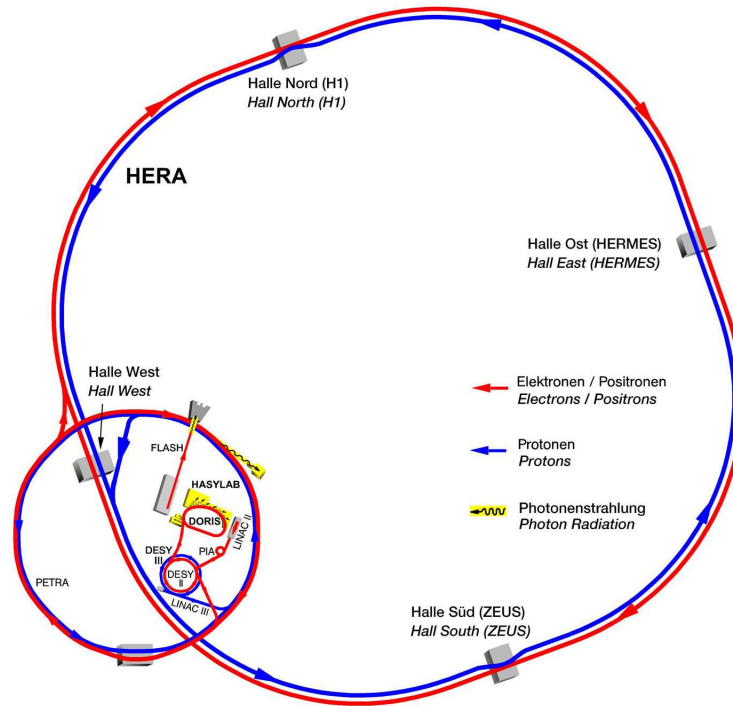[2]Deutsches Elektronen Synchrotron

Figure 3.1: Schematic representation of the HERA storage ring and the system of pre-accelerators. After processing and acceleration in the LINAC linear accelerators, DESY synchrotrons and the PETRA storage ring, electrons or positrons (red) with an energy of 12 GeV and protons (blue) with an energy of 40 GeV were injected in the HERA storage ring and further accelerated to an energy of respectively 27.6 GeV and 920 GeV.

located. These experiments, started up in 1992, measured the unpolarised structure of the proton with high precision, down to low values in x_B ($\sim 10^{-4}$) and over a large range in Q^2 ($10^0 \text{ GeV}^2 < Q^2 < 10^4 \text{ GeV}^2$). The east and west halls enclosed fixed-target experiments. The west hall contained the HERA-B experiment. This experiment collected data until 2003 for the analysis of CP violation in B-meson decay, by scattering beam-halo protons off a fixed wire target. The east hall was home to the HERMES experiment. The HERMES experiment, as already stated, made use of the lepton beam and of a gas target internal to the beam line.

The lepton beam was structured into 37 ps long bunches, separated from each other by a time period of 96 ns. A completely filled ring could contain 210 bunches, but only around 180 bunches were stored. The empty lepton bunches were paired with filled proton bunches and with empty proton bunches. This allowed the study of background events. The lepton-beam current at injection amounted to ~ 40 mA. Over a period of approximately 10 hours the beam current decreased exponentially to 15 mA, after which data collection continued for about 1 hour with the density of the HERMES target increased. The beam was subsequently dumped, and preparations for a new injection of leptons into the storage ring resumed. Such
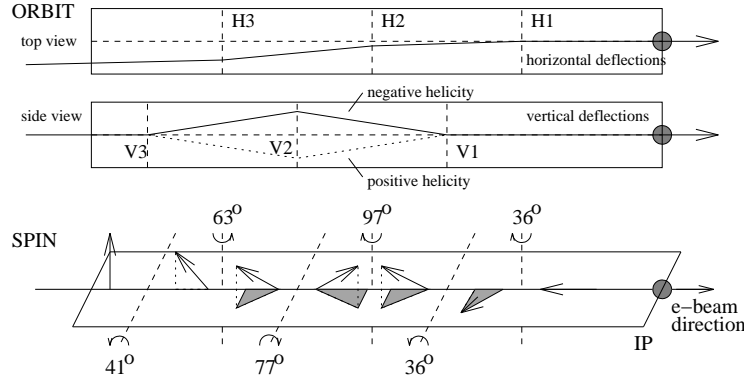
Figure 3.2: Illustration of the spin-rotation system installed upstream of the HERMES experiment. The upper two drawings show the deflection of the beam trajectory in the horizontal and vertical planes, and the lower drawing shows the associated spin orientation.

one cycle of data collection is called a fill. Since the life time of the proton beam largely exceeded the life time of the lepton beam, a refill of the proton beam line was necessary only every second or third lepton-beam refill.

Through a spin-flip asymmetry in the emission of synchrotron radiation in the magnetic fields of the guiding dipoles (the Sokolov-Ternov effect [53]), a vertical polarization of the positron (electron) beam $P(t)$, with spin states parallel (anti-parallel) to the magnetic field, was built up gradually over time, according to:

$$P(t) = P_\infty(1 - e^{-t/\tau}), \tag{3.1}$$

where the asymptotic polarization P_∞ and the rise-time constant τ are characteristic of the ring conditions. For a perfectly flat orbit, the theoretically maximal achievable polarization P_{th} is 92.4%, and the associated rise time τ_{th}, which depends on the radius of the storage ring and the beam energy, is 37 minutes for a HERA-type storage ring at lepton-beam energies of 27.5 GeV [54]. Various depolarization effects, e.g., from small misalignments of the magnets, substantially limit the polarization to lower values, and affect the rise time τ as $\tau = P_\infty(\tau_{th}/P_{th})$. For the data analyzed in the present work the average beam polarization is on the order of 40% with a rise-time below 20 minutes[3]. A 56 m long string of three pairs of horizontally and vertically bending dipole magnets, so-called spin rotators [55], placed upstream of the HERMES experiment rotated the vertical beam spin into a longitudinal beam spin, as depicted in figure 3.2; spin rotators downstream of the HERMES experiment performed the opposite spin rotation[4]. The longitudinal beam polarization was measured downstream of the HERMES interaction point by the longitudinal polarimeter, the LPOL [54]; the transverse polarization was measured downstream of the HERA-B experiment by the transverse polarimeter, the TPOL [56]. Both polarimeters measured signals from Compton

---

[3]Beam polarizations of up to 70% were achieved in previous years, with polarization values commonly between 50% and 60%.

[4]After 2001 also the experiments H1 and ZEUS were provided with spin rotators.
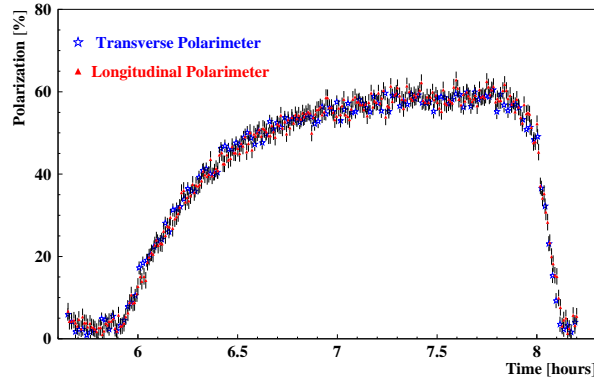
Figure 3.3: Example of the build-up of the beam polarization, as measured by the TPOL (blue) and the LPOL (red).

back-scattered photons from an intense circularly polarized laser beam. The TPOL made use of a spatial asymmetry for left and right circularly polarized laser light, whereas the LPOL was sensitive to an asymmetry in photon energy for photons with different helicities. The relative uncertainty on the beam polarization from the combined information of the LPOL and TPOL is on the order of 3% [57]. Figure 3.3 shows an example of the build-up of the beam polarization, measured by the LPOL and TPOL.

3.2 The target cell

Over the years of data collection various targets were used in the HERMES experiment in order to accommodate the different physics programs pursued. In the first year of data taking the target was filled with longitudinally polarized helium-3; subsequently data collection continued with longitudinally polarized hydrogen (1996–1997) and deuterium (1996–2000). After a shutdown period of one year during which the HERA storage ring and experiments were upgraded, a transversely polarized hydrogen target allowed data collection for the transverse-spin physics program until 2005. At various moments also data were collected with the three mentioned gas types unpolarized as well as with unpolarized helium-4, neon, nitrogen, krypton and xenon. The installation of the recoil detector in 2006 forced the dismantling of the polarized-gas system, and went along with data collection on unpolarized hydrogen and deuterium.

The target cell used in the last two years of HERMES operation consisted of an open-ended elliptical aluminum tube with outer diameters of 21.00 mm (horizontally) and 9.05 mm (vertically), and a wall thickness of 75 μm. The active length of the tube amounted to 15 cm, where a gas inlet located in the center allowed for the feed of hydrogen or deuterium gas. The diffusing gas atoms were pumped away at the outer ends by a very powerful pumping system. The tube was supported at its extremities by the scattering chamber and alignment pins, and laterally by 4 mm thick aluminum plates. To suppress temperature rises of the target
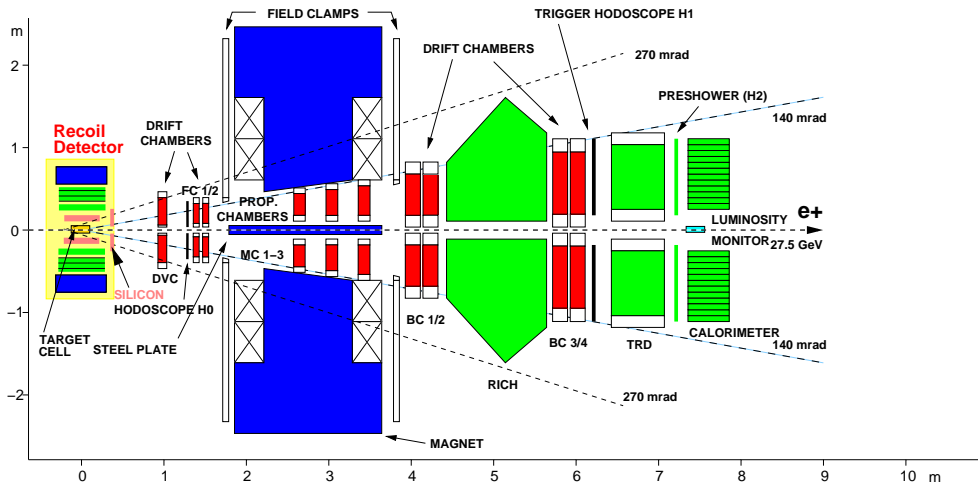
22

Figure 3.4: Side-view schematic representation of the HERMES spectrometer as constituted in the years 2006–2007.

cell related to the presence of the beam, these aluminum plates were water-cooled.

In order to allow for a reasonable life time of the lepton beam, the density of the gas injected had to be limited. During regular operation the target cell was filled with either hydrogen at a density of $0.5 \, 10^{15}$ nucleons/cm^2 or deuterium at a density of $0.1 \, 10^{16}$ nucleons/cm^2. When the lepton-beam current fell below 15 mA, the gas density was increased to $0.3 \, 10^{16}$ nucleons/cm^2 for hydrogen and $0.6 \, 10^{16}$ nucleons/cm^2 for deuterium [59].

3.3 HERMES spectrometer

The HERMES detector components were mounted on a large platform that, together with the electronic trailer (ET) containing the electronics and gas systems, could move on rails. This provided access within 24 hours for the HERA maintenance tram. A large concrete wall shielded the radiation zone from the remaining part of the hall, allowing access to the equipment stored in the ET during data collection.

For further reference, the HERMES right-handed coordinate frame is defined here. The z axis has its direction parallel to the beam line, oriented along the lepton-beam momentum. The y axis points upwards, and the x axis points then horizontally towards the outside of the HERA ring. The target-cell center is located at $(x, y, z) = (0., 0., 12.5)$ cm.

The HERMES spectrometer was designed with forward geometry to detect and reconstruct energetic particles originating from the beam interaction with the target nucleons. It consisted of two symmetric halves, above and below the horizontal plane, centered horizontally around the lepton beam line. The proton beam line ran parallel to the lepton beam line at a distance of 72 cm. A side view of the spectrometer configuration is shown in figure 3.4 with indication of its geometrical dimension. Also the recoil detector, surrounding the target cell, is depicted. This detector entity is described in a separate section.

The detector components depicted in red in figure 3.4 are the tracking detectors. Separated by the magnet, shown in blue, they are grouped into a front-tracking system, formed by two front chambers (FCs) and the drift-vertex chamber (DVC), and a back-tracking system, formed by four back chambers (BCs). They allowed for the reconstruction of the trajectories of charged particles and of the momenta of these particles, from their bending when passing the magnet. Contained inside the magnet three sets of proportional chambers provided tracking possibilities for low-energetic particles. Silicon detectors, installed in 2001, also contributed to the tracking of low-energetic particles. More specifically, they were constructed to increase the acceptance for Λ hyperons. Information from the latter two detector components is not used in the present analysis.

A very good discrimination between leptons, i.e., electrons or positrons, and hadrons is based on signals from the transition-radiation detector (TRD), the preshower, and the calorimeter. The ring-imaging Čerenkov (RICH) detector allowed for the distinction between kaons, protons, and pions. The hodoscopes H0, H1, the preshower and the calorimeter were used for the generation of trigger signals. As for neutral particles, more specifically photons, the calorimeter and the preshower were the only detectors capable of detecting them.

For the measurement of the luminosity, a luminosity monitor was inserted in between the two halves of the calorimeter after injection of the lepton beam. This detector, built of small calorimeter crystals, detected electrons from Møller scattering or positrons from Bhabha scattering off the electrons of the target atoms, as well as photons from the annihilation of positrons with the atomic electrons.

The spectrometer covered a vertical acceptance in scattering angle between ± 40 mrad and ± 140 mrad; the horizontal angular acceptance was limited to ± 170 mrad.

3.3.1 Tracking system

The dipole magnet

The dipole magnet provided a vertical magnetic field, with an integrated field strength of 1.3 T.m. An 11 cm thick steel plate mounted in the symmetry planes shielded both HERA beams as they passed through the dipole field. Additionally, a correction coil inside the lepton-beam shielding corrected for imperfections in the magnetic shielding and for fringe fields. Field clamps fixed in front and behind the magnet limited the fringe fields at the adjacent drift chambers to below 0.1 T.

Tracking detectors

The drift chambers of the front- and back-tracking systems consisted each of six planes, with alternative anode and cathode wires spanned between two cathode planes. Two planes had their wires orientated vertically, whereas the other four had their wires inclined pairwise by $30°$ and $-30°$. Two paired planes were offset with respect to each other by half the distance between 2 consecutive plane wires, in order to resolve tracking ambiguities. The front-tracking system was used for the reconstruction of the interaction point of the beam particles with the target atoms and for the determination of the scattering angles of the detected particles with respect to the lepton beam. The back-tracking system was used for the reconstruction of the particles' trajectories after their deflection by the large dipole magnet.

Track reconstruction

The HERMES reconstruction program (HRC) reconstructs tracks from charged particles [60].
It is based on a pattern-recognition fast tree-search algorithm. Once the front and back
straight tracks are reconstructed, they are combined for the determination of the particle's
momentum. On average, a momentum resolution of $\delta p/p \leq 2.6\%$ and an angular resolu-
tion of $\delta\theta \leq 1.8$ mrad are obtained. Since 2008 a second program, the HERMES tracking
code (HTC), provides an improved track reconstruction [61]. HTC is not a track-searching
algorithm; it uses the tracks found by the HRC code, and fits these tracks through an ad-
vanced procedure. Contrary to HRC, the used fit routine does not regard partial tracks as
straight sections with track slopes and momenta constant in position space, but using the
Kalman-filter method, works locally. It considers non-linear track propagation with track
slopes and momenta parametrized with a dependence on the position along the beam line.
This code takes effects related to multiple-scattering, inhomogeneity in (recoil-detector and
dipole) magnetic fields, and detector misalignment in a precise way into account, resulting in
a track-reconstruction with higher accuracy. An improvement on the order of 25% is observed
for the overall momentum resolution as well as for the angular resolution at low-momentum
values [62].

For the determination of the vertex several topologies are considered: either the inter-
section point from 2 or 3 tracks[5] is reconstructed, or the intersection point from a single or
multiple (up to 3) tracks with the lepton beam, taking into account its position and slope, is
reconstructed. For the present analysis, the intersection of a single track with the lepton beam
needs to be considered, as will be clarified in chapter 5. Once the vertex is determined, one
can chose to refit the tracks with this additional information or not. The former solution was
chosen for the study described here. The quality of reconstruction of tracks and vertices is
provided under the form of track probabilities and vertex probabilities, allowing the user to
decide if a track or vertex satisfies the necessary quality requirements.

3.3.2   Particle identification

For the discrimination of various particle types, the responses of four detectors are utilized.
The transition-radiation detector, the preshower, and the calorimeter allow to distinguish elec-
trons and positrons from hadrons; the ring-imaging Čerenkov (RICH) detector identifies pi-
ons, kaons, and protons. At momenta below 4 GeV, the latter detector also contributes to
the identification of leptons, but in view of this low threshold, it is not used in the present
analysis.

Transition-radiation detector

The transition-radiation detector exploits the property that relativistic charged particles cross-
ing media with different dielectric constants emit transition radiation at the boundary of these
media. Since the Coulomb fields induced by a traveling particle in media with different di-
electric constants differ, a transition field, observed as transition radiation, is created to ensure

---

[5]This limit is dictated by the low track multiplicity at HERMES, i.e., 1.4 tracks per event and the absence of
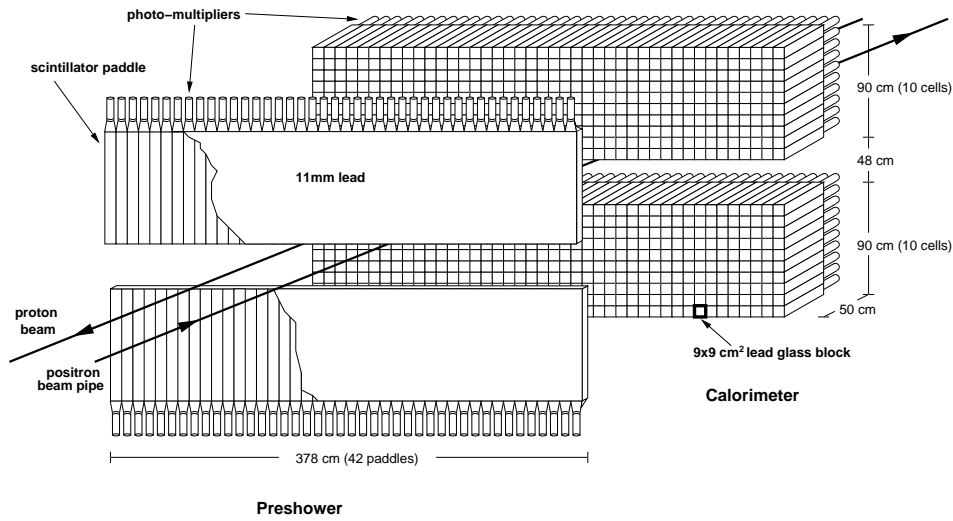analyses considering more than 3 tracks per event.

Figure 3.5: Schematic drawing of the preshower and the calorimeter.

continuity of the electromagnetic field. The energy of the emitted radiation scales with the Lorentz factor γ of the incident particle. Therefore only leptons produce transition radiation in the form of X-rays in the HERMES kinematic region.

The radiator of the transition-radiation detector was formed of loosely packed, pseudo-randomly arranged polyethylene/polypropylene fibers that had a diameter of around 20 μm. A subsequent multi-wire proportional chamber detected the radiation generated by leptons as well as the ionization signals from these leptons and from hadrons. On average, leptons deposited twice as much energy as hadrons. The transition-radiator detector consisted of a sequence of six such arrangements.

The preshower

The preshower was built of 42 scintillating paddles per detector half. They were preceded by an 11 mm thick lead plate sandwiched between 1.3 mm thick stainless-steel sheets (=2 radiation lengths). A schematic representation of the detector is shown in figure 3.5. The scintillators had a thickness of 1 cm and a width of 9.3 cm. The paddles were staggered horizontally by 3 mm in order to avoid insensitive areas, and were optically coupled via 25 cm long light-guides to photo-multiplier tubes. Traversing leptons initiated inside the lead plate electromagnetic showers, of which the charged particles were subsequently detected in the scintillating material. The large energy deposition of about 20–40 MeV allows to discriminate leptons from hadrons, since the latter loose energy, ~ 2 MeV, through ionization only.

The calorimeter

The electromagnetic calorimeter, also depicted in figure 3.5, consisted of an array of 2×420 lead-glass blocks. A block was 50 cm (=18 radiation lengths) long and covered an area of

$9 \times 9 \text{ cm}^2$. Čerenkov light created by charged particles was read out by photomultiplier tubes directly coupled to the calorimeter blocks. A cluster of 3×3 blocks contained 99% of the electromagnetic shower generated by leptons. These particles, contrary to hadrons, deposited all of their energy inside the calorimeter. A comparison of the deposited energy and the reconstructed momentum allows to distinguish hadrons from leptons.

Lepton-hadron separation

The responses of the various particle-identification detectors are combined into probabilities using a Bayesian probabilistic approach [64]. If a particle with a specific momentum and detector response is observed, the probability $\mathcal{P}_i$ for this particle to be of particle type i is given by:

$$\mathcal{P}_i = \frac{\phi_i \mathcal{L}_i}{\sum_{j=l,h} \phi_j \mathcal{L}_j}, \tag{3.2}$$

where the sum runs over all particle types, which in the present case are electrons or positrons ($j = l$) and hadrons ($j = h$). The parent distribution $\mathcal{L}_i$ represents the probability to observe a specific detector response for a particle of type i taking into account its momentum. Parent distributions are determined for each particle-identification detector from the data collected by imposing strong restrictions on the other particle-identification detectors. The flux factor ϕ_i is the prior probability that a particle with a given momentum is of type i. Using an iterative procedure, these fluxes are also obtained from experimental data.

From these probabilities PID values are constructed as:

$$\begin{aligned} \text{PID}' &= \log_{10} \frac{\mathcal{P}_l}{\mathcal{P}_h} & (3.3) \\ &= \text{PID} - \log_{10} \Phi, & (3.4) \end{aligned}$$

with $\text{PID} = \log_{10}(\mathcal{L}_l/\mathcal{L}_h)$ and $\Phi = \phi_h/\phi_l$. As is the case for the present analysis, the flux factor Φ can be neglected if sufficiently hard cuts on the PID value are applied. Additionally, the flux factor might show a momentum dependence, which then needs to be taken into account.

The PID values obtained for the calorimeter (PID_{cal}) and the preshower (PID_{pre}) are combined into $\text{PID2} = \text{PID}_{cal} + \text{PID}_{pre}$ and the PID values from the six modules of the transition-radiation detector are similarly summed into PID5. These PID values are used in the present analysis for the selection of leptons; their distribution will be shown in chapter 5. The efficiency for the identification of leptons amounts to 99% with a hadron contamination of less than 1%.

Detection of photons

The calorimeter and the preshower were the only detectors in the forward spectrometer capable of detecting photons. The calorimeter allows for the reconstruction of photon energies, since photons deposit practically all of their energy inside this detector. A fraction of photons initiated an electromagnetic shower in the preshower; whereas the remaining fraction only created the first electron-positron pair inside the calorimeter. The Čerenkov light generated

by the latter group of photons was as a consequence less attenuated, but on the other hand a larger fraction of shower particles leaked out at the downstream end of the calorimeter blocks. A combination of these opposite effects resulted finally in the measurement of a larger signal for this latter group of photons in comparison with equally energetic photons that generate a signal in the preshower detector. This is of importance for the reconstruction of the photon energy, as will be outlined in chapter 5. For photons creating a signal in the preshower, a photon-energy resolution $\delta E_\gamma / E_\gamma \leq 5\%$ is obtained.

The position of the photons in the calorimeter plane, transverse to the beam line, is determined as a weighted average over the 9 blocks of a calorimeter cluster, where the weight is a logarithmic function of the energies deposited in each block. The obtained transverse position resolution amounts to 0.5 cm [63].

3.3.3 Trigger system

Data collection in the HERMES experiment was based on a single-level trigger. Various triggers designed for a fast primary discrimination between a candidate physics event and background could initiate the readout of the HERMES detectors. In addition to this type of triggers there existed triggers that were not related to the recording of a physics event, but that were used for the calibration and monitoring of the detectors, for example, to initiate the read out of the responses of the preshower, calorimeter and hodoscopes to laser light injected in the HERA bunch-free zone.

When a trigger initiated the readout of the detector components, a new trigger could not be processed, resulting in a dead time of the spectrometer readout. For data collection in the years 2006 and 2007, the dead time was on average below 15%, but could at the start of certain fills amount to 25%.

The main physics trigger of interest (for the present analysis) is the so-called trigger 21, designed for the collection of candidate DIS events. The generation of this trigger was based on signals in the preshower and the calorimeter as well as in the hodoscopes H0 and H1. The hodoscope H1 was located in front of the TRD, as can be seen in figure 3.4. It was built of scintillating paddles following the same design as the preshower. The hodoscope H0 consisted of two scintillating plates, one per spectrometer half. Each plate was read out by 2 photo-multipliers. This detector was located in the front part of the spectrometer, distant from the other trigger detectors, so that timing restrictions allowed for the exclusion of trigger signals generated by particles originating from the proton beam. For the formation of trigger 21 the signals in each of the four detectors had to originate from the same detector half, and to arrive in coincidence with the bunch crossing signal from the HERA accelerator. In addition the sum of energy depositions in 2 adjacent columns of the calorimeter had to exceed $1.4\,\mathrm{GeV}$ during regular data collection, and $3.5\,\mathrm{GeV}$ at the end of a fill, when the target density was increased.

3.4 The recoil detector

The recoil detector consists of three active detector components, surrounding the target cell: a silicon-strip detector and a scintillating-fiber tracker to reconstruct protons and pions, and a
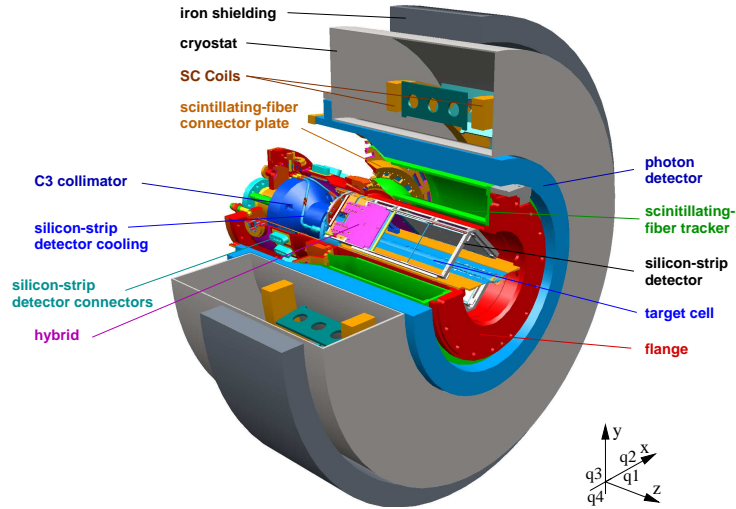
Figure 3.6: Schematic drawing of the recoil detector, with indication of its division into quadrants (q) in the HERMES coordinate frame.

photon detector built for the detection of photons, principally originating from the Δ^+ decay. The whole is mounted inside a 1 T superconducting solenoid. A schematic drawing of the recoil detector is given in figure 3.6.

3.4.1 Silicon-strip detector

The silicon-strip detector is placed within the beam vacuum, inside the scattering chamber. In this way the amount of material between the interaction point and the first active detector component is minimized. This allows for the detection of very low-momentum protons, as is desirable in view of the Ji relation (see equation (2.17)). The silicon-strip detector is constructed of 16 double-sided silicon-strip sensors. Each sensor is 300 μm thick and covers an area of 99×99 mm^2. The strip pitch amounts to 758 μm and the strips on either side of a sensor are placed perpendicularly to allow for a three-dimensional space-point reconstruction. The strips on the p-side are parallel to the beam direction; the strips on the n-side are perpendicular to the beam direction. Two silicon-strip sensors are glued into a ceramic frame and form a module. Modules are placed in diamond-shape around the target cell, with 2 modules per quadrant placed in parallel. According to this arrangement, the transverse area of all recoil detectors is labeled into quadrants. Quadrant 1 is defined as the region with azimuthal angle between $3\pi/2$ rad and 2π rad, quadrant 2 covers the region 0 rad to $\pi/2$ rad, and quadrants 3 and 4 follow with increasing azimuthal-angle values.

The signals from the silicon strips are transferred by Kapton flex foils to Helix chips. The readout chips and on-board electronics are mounted on the circuit board (hybrid in figure 3.6), which is also located within the beam vacuum. As a consequence they need to be actively cooled, which is done with -15° C ethanol. Each strip is read out twice. A charge-division

29

network couples a strip to one Helix chip directly and to another Helix chip through a 10 pF capacitor. With this setup a large dynamic range (1–70 MIPs) can be covered [66].

3.4.2 Scintillating-fiber tracker

The scintillating-fiber tracker is located outside the beam vacuum, around the scattering chamber surrounding the silicon-strip detector. It is formed of 2 concentric cylinders, each containing 2 layers of scintillating fibers parallel to the beam direction and 2 layers of fibers under an angle of $10°$ with respect to the beam line. The detector provides as such two space points for track reconstruction. The 4992 scintillating fibers of the detector are 1 mm in diameter and cover a length along the z axis of 25 cm. They are read out by 64-channel multi-anode PMTs.

3.4.3 Photon detector

The outer recoil-detector component is the photon detector. It contains three layers of alternating tungsten and scintillating material. The commissioning of this detector component and its role in the analysis of DVCS form the subject of the work presented here. The detector is extensively described in the following chapter.

3.4.4 Recoil-tracking system

Track reconstruction

The silicon-strip detector and the scintillating-fiber tracker both provide position and energy information. They can reconstruct protons with momenta between 0.125 GeV/c and 1.4 GeV/c. The reconstruction method depends on the range of the reconstructed particle. Figure 3.7 shows the energy deposited by protons in the inner layer of the silicon-strip detector as a function of the energy deposited in the outer layer of the detector. As indicated in the figure, protons with momenta below 0.125 GeV/c are stopped in the inner layer. Higher-energetic protons, with momenta up to 0.145 GeV/c reach the outer layer, but are stopped within. Finally, protons with momenta above 0.145 GeV/c punch through the outer layer. The low-energetic branch of this group is stopped in the scattering chamber, whereas protons with momenta above ~ 0.2 GeV/c reach the scintillating-fiber tracker.

Tracks reconstructed by the recoil detector are assumed to originate from the interaction point of the beam with the gas atoms. The vertex position in the transverse plane is taken equal to the beam position. With the recoil-tracking system, the reconstruction of protons and negatively or positively charged pions is at present considered, since these are the charged particles that are predominantly present. In the primary part of the tracking algorithm, first all tracks formed of 4 space points, i.e., 2 in the silicon-strip detector and 2 in the scintillating-fiber tracker are searched for, fit, and accepted if the fit is reasonable. The fit function here takes only the coordinate information from the space points into consideration. Subsequently, all tracks formed of 3 space points that do not belong to 4-space-point tracks are searched for and processed in an analogous way. Finally, combinations of 2 space points in the silicon-strip detector are considered, omitting space points used to construct 4-space-point tracks.
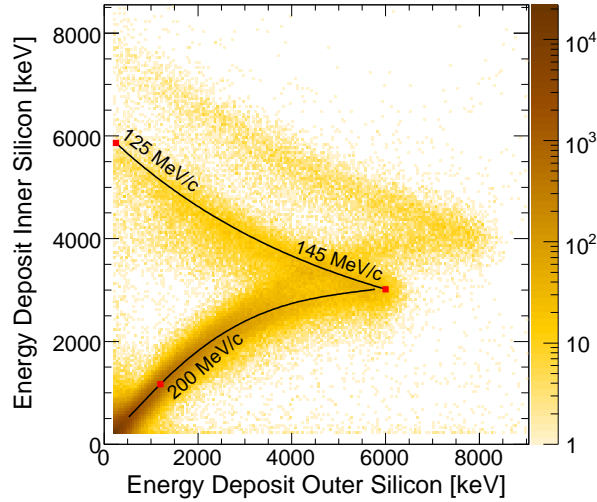
Figure 3.7: Energy deposition in the inner silicon-strip-detector layer as a function of the energy deposition in the outer silicon-strip-detector layer by protons (following the black curves) and deuterons (distinguishable in the band at higher energy-deposition values). The black curves are the result of a GEANT4 simulation. The figure is taken from reference [67].

Tracks formed of only 2 space points can be reconstructed in 2 ways. Either the total energy deposited in the silicon-strip detector is summed for the determination of the proton momentum, taking into account energy losses in passive materials, such as the target cell and the flex foils, or the track is reconstructed through a χ^2 fit from its deflection in the magnetic field, assumed to be homogeneous[6] [68]. Here the fit function not only considers information from position coordinates, but also from the energy depositions in the silicon-strip detector, and takes into account multiple scattering and energy losses in passive materials. This method also takes into consideration that protons can be stopped inside the silicon-strip detector. Track reconstruction based on the former method is labeled as the 'stopped-proton' hypothesis, whereas the latter is labeled as 'proton hypothesis'. If for the former reconstruction method, the track is not likely to be a proton stopped inside the silicon-strip detector, as determined from the data points shown in figure 3.7, this track reconstruction is not included in the track-reconstruction output. For the proton hypothesis, the χ^2 value of the fit needs to lie below 10^6, with the idea that at a later stage a stricter constraint is placed on this value by the analyzer, if necessary.

For particles reaching the scintillating-fiber tracker, i.e., for tracks formed of 3 or 4 space points, the track is not reconstructed with the stopped-proton-hypothesis method. In addition to the track reconstruction according to the proton-hypothesis, the track reconstruction from the primary part of the tracking algorithm, which considers only space-point coordinate

---

[6]A detailed mapping of the magnetic field of the recoil-detector magnet exists. However, studies on a Monte-Carlo simulation showed that the assumption of a homogeneously distributed magnetic field does not lead to significant reduction in accuracy of the momentum reconstruction.

information, is provided. This tracking method is labeled 'pion hypothesis', since it is appropriate for the parametrization of pions, which on average always reach the scintillating-fiber tracker and do not deposit large amounts of energy in the detectors[7]. After identification of the particle type, the appropriate track parametrization can be chosen.

For protons a momentum resolution of $\delta p/p \sim 2\%$ is obtained at momenta of 0.125 GeV/c and then gradually increases with increasing momentum to about 15% for protons with momenta of 1 GeV/c. The pion-momentum resolution is on the order of 10% throughout this same momentum range.

Particle identification

Tracks with less than 3 space points are assumed to be protons. For longer tracks, particles reconstructed with negative charge are readily identified as negatively charged pions, whereas the identification of positively charged particles is based on PID values, in a way similar to particle identification by the forward spectrometer [69]. The PID values are determined from tracks reconstructed with the pion hypothesis. At present, the flux factors are not provided. At most 6 PID values can be used: 1 for each layer of the silicon-strip detector, and 4 for the scintillating-fiber tracker, namely, for the parallel and stereo layers of the inner and outer barrels.

The PID distributions and their momentum dependence will be shown in section 4.11.

3.5 Data processing

When a trigger was generated, the data-acquisition system (DAQ) collected the information from all detector components and stored it into a file. Consecutive events were written to this file until the file attained a size of 500 Mb, after which the file was closed and a new file was opened. The data written to one file constitute a run. Parallel to the acquisition of event-level data, also data about the status of the experimental apparatus, e.g., beam parameters, detector temperatures, high-voltage levels, were stored. This forms the so-called slow-control data. It was recorded on a time basis of 10 s. This time period defines a burst.

The information stored in a run file is subsequently processed offline by the HERMES decoder (HDC). Using mapping and calibration information, the electronic output of each detector component is decoded into energy depositions, hit positions, and timing information. This output is subsequently processed by the HRC program to reconstruct tracks and photon clusters in the forward spectrometer and by the external tracking code, XTC, for the reconstruction of tracks and photon clusters in the recoil detector. Finally, this information is compacted and merged with the slow-control data into micro-data summary tables (μDSTs), which constitutes the output format used in the analysis. The whole procession chain is repeated at least twice, since the information needed for the calibration of detectors is determined from the actual collected data.

---

[7]It was checked that the consideration of multiple scattering into this fit procedure does not influence the track reconstruction, and thus multiple scattering is not taken into account for the pion hypothesis.

4. The photon detector

In this chapter the commissioning of the photon detector is explained and its performance is shown. This is preceded by a detailed description of the detector.

4.1 Description of the photon detector

As described in chapter 2, the main purpose of the photon detector is the detection of photons originating from π^0 decay in associated production. The photons have a uniform azimuthal distribution, a polar-angle distribution peaked at 0.8 rad, and their energies range up to ~ 500 MeV.

At those energies it is possible to detect the photons, using the fact that when passing through heavy material they create electron-positron pairs, which subsequently can be detected in a sensitive detector component. The probability for this pair creation starts to dominate other interaction mechanisms (mainly Compton scattering) at a photon energy of about 10 MeV, then slightly increases with increasing photon energy (while the probability for Compton scattering decreases rapidly), and reaches a constant, maximum value at photon energies of ~ 1 GeV. As the creation of electron-positron pairs occurs in the electric field of the nuclei, and to a lesser extent in the field of the atomic electrons, the probability for it increases with the atomic number of the material.

Considering the distribution of the photons as well as financial and geometric constraints — the photon detector had to fit into the small space between the recoil-detector magnet and the recoil scintillating-fiber detector — the best choice for the photon detector consists of a cylindrical volume of subsequent layers of tungsten as a converter and plastic scintillator material for the detection of the charged leptons.

4.1.1 Particle creation in tungsten

Interaction probability

The probability that an incident photon results in at least one detectable charged particle depends on the amount (and type) of converter material. On the one hand, a large layer of converter material increases the probability for pair production, but on the other hand, it also increases the probability that the created charged particles are absorbed in the converter before they emerge. It results thus that multiple thin layers of tungsten and scintillator material lead to an optimum detection efficiency. From a Monte-Carlo simulation, the best configura-

tion for the detection of π^0-decay photons, keeping in mind the above-mentioned constraints, was determined to consist of three tungsten layers, with a thickness of 6 mm for the inner layer, and 3 mm for each of the two following layers [70]. Each of the three layers is segmented longitudinally into 12 pieces to facilitate machining.
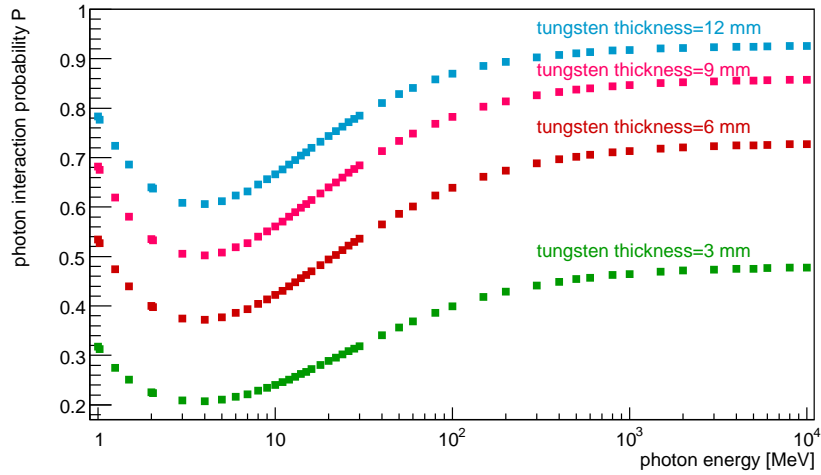

Figure 4.1: Photon interaction probability as a function of its energy, for different thicknesses of tungsten.

The interaction probability for photons P is given by $P = 1 - e^{(-t/\lambda)}$, with t the thickness of the layer under consideration, and λ the mean free path. The mean free path can be calculated as follows [71]:

$$\frac{1}{\lambda} = \frac{\sigma N_A \rho}{A}. \tag{4.1}$$

Here σ represents the total photon cross section [cm^2/atom], taking into account all possible processes , like pair production, the photoelectric effect, Compton scattering. It can be obtained from [72]. N_A is the Avogadro constant [mol^{-1}], ρ the density of the material, which for tungsten is 19.25 g/cm^3, and A the atomic mass, which for tungsten is 183.84 g/mol.

The total photon interaction probability as a function of photon energy for different tungsten thicknesses is shown in figure 4.1; the photons here under consideration have a probability of $\sim 85\%$ to interact. The total detection efficiency for photons in the photon detector will be partly discussed at the end of this chapter and in the following chapter.

Shower development

If a photon creates an electron-positron pair, these newly created particles will also interact with the converter material: at low energies mainly through the ionization and excitation of atomic electrons (collisional losses), and at higher energies mainly through Bremsstrahlung, being the emission of a photon in the electric field of nuclei, and to a lesser extent in the

34

field of atomic electrons. The energy loss rate for both processes is thus larger in dense material. The energy value at which the energy loss rate by collisional losses equals the energy loss rate by Bremsstrahlung is called the critical energy and can be approximated by $E_c = (800\,\text{MeV})/(Z+1.2)$, where Z represents the atomic number [73]. For tungsten ($Z = 74$) we obtain a value of ~ 10 MeV. From this point on, the energy loss by Bremsstrahlung rapidly dominates and increases with increasing lepton energy until it reaches an asymptotic value at lepton energies of ~ 1 GeV.

When an electron radiates a photon, the radiated photon will give rise to a new electron-positron pair or undergo Compton scattering. The newly created leptons can in turn radiate yet another photon. As such, at each step the number of particles increases, while their energy decreases. As the process goes on, more and more leptons fall into an energy range where radiation losses cannot compete with collision losses, until eventually the energy of the primary photon is completely dissipated. By measuring a sufficiently large fraction of the energy deposited by the charged particles, one is able to reconstruct the energy of the initial photon.

At this point it is convenient to introduce the concept of radiation length X_0 as it allows to describe the characteristic longitudinal dimensions of the high-energy shower (primary particle energy > 1 GeV)[1] in a material-independent way. This radiation length represents both the distance over which a high-energy electron looses all but $1/e$ of its initial energy and the distance that corresponds to 7/9th of the high-energetic photon mean free path. Tungsten has a radiation length of 3.5 mm [71]. It can also be calculated with an accuracy better than 2.5% via [71]:

$$X_0 = \frac{716.4A}{Z(Z+1)\ln(287/\sqrt{Z})}\rho. \tag{4.2}$$

For the photon detector this amounts to a total radiation length of 3.4: $1.71X_0$ for the inner layer and $0.85X_0$ for each of the outer layers.

The length over which the shower extends is well parametrized by $L(98\%) = t_{max} + 4\lambda_{att}$ [75]. This quantity represents the length for 98% longitudinal containment. The distance of the shower peak t_{max} is calculated within the framework of Rossi's 'approximation B' [74]:

$$t_{max} = 1.01(\ln\frac{E_0}{E'_c} - 0.5), \tag{4.3}$$

where E_0 represents the energy of the incident photon. The quantity E'_c here is the critical energy as defined by Rossi. It is the energy at which the collisional loss per radiation length of an electron equals the electron's energy. From [75] we obtain a value of $E'_c = 7.43$ MeV. For $E_0 = 300$ MeV, we obtain $t_{max} = 3.23X_0$, and for $E_0 = 120$ MeV, $t_{max} = 2.30X_0$. The center of gravity of the shower corresponds to $t_{med} = t_{max} + 1.7$. The quantity λ_{att} characterizes the slow exponential decay of the shower after the shower maximum. It is given by $\lambda_{att} = 3.4X_0$. We then finally obtain that $L(98\%) = 16.83X_0$ ($L(98\%) = 15.90X_0$) for 300 (120) MeV photons. The majority of the shower thus lies outside the photon detector.

Figure 4.2 shows the incident-energy distribution of photons leaving a signal in the photon detector. Two complementary Monte-Carlo simulations are used to analyze the distribution.

---

[1]The energies under consideration here are slightly lower, but for the aimed illustration purposes it remains meaningful to talk in terms of radiation lengths.
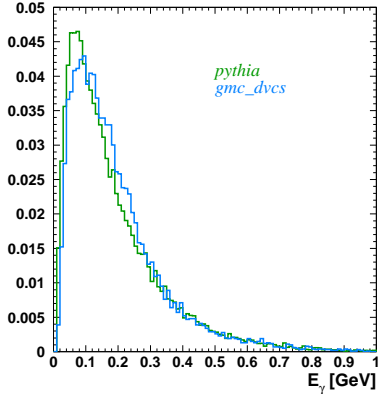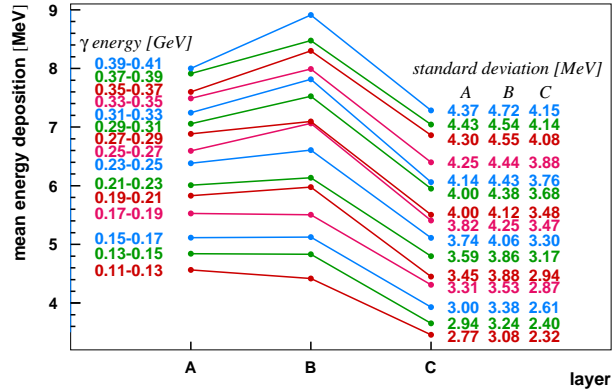
Figure 4.2: Photon-energy distribution.

Figure 4.3: Energy deposition of photons in each of the photon-detector layers.

The one labeled 'gmc_dvcs' originates from the gmc_dvcs generator, which simulates (part of) the processes of interest, namely elastic and associated BH and elastic DVCS[2]. The other distribution is based on a data sample created by the pythia generator, which generates a wide variety of processes, and gives a good description of the HERMES data. This generator does not include any of the processes simulated by gmc_dvcs though. For both generators, the observed photon-energy distribution is the same. Figure 4.3 gives the mean energy deposition per photon-detector layer for these photons if they generate a signal in each of the detector layers. In this figure only the pure energy deposition in the Monte-Carlo simulation is considered. The effect of a fluctuation in the number of produced scintillating photons in the scintillator or smearing due to instrumental effects is not included. The sample is sub-divided into several incident-photon energies. As can be seen, low-energy photons deposit most of their energy in the first layer, while higher-energy photons deposit most in the second layer. Taking into account the angle of incidence θ, photons with an energy around 120 MeV ($\langle\theta\rangle = 1.25$ rad), traverse $1.81X_0$ in the first tungsten layer, and $2.71X_0$ when also taking into account the second layer, while 300 MeV photons ($\langle\theta\rangle = 1.15$ rad) traverse $2.82X_0$ in the first two tungsten layers, and $3.76X_0$ in all three tungsten layers. The here observed distances for maximum energy deposition are thus in agreement with the values for t_{max} given by equation 4.3.

A qualitative estimate for the number of (charged) particles created in the detector can be obtained by considering the following very crude model [74]. Assume that each photon with sufficiently high energy ($E_0 \gg 10$ MeV) creates an electron-positron pair after traversing 1 radiation length of material. The initial photon energy is herewith equally shared between the two leptons. These leptons in turn will each radiate a photon if their energy is much larger than the critical energy. Again, the energy is equally shared between the lepton and the

---

[2]As the DVCS processes are subject to uncertainties due to their model dependence, they are not included when examining kinematic distributions.
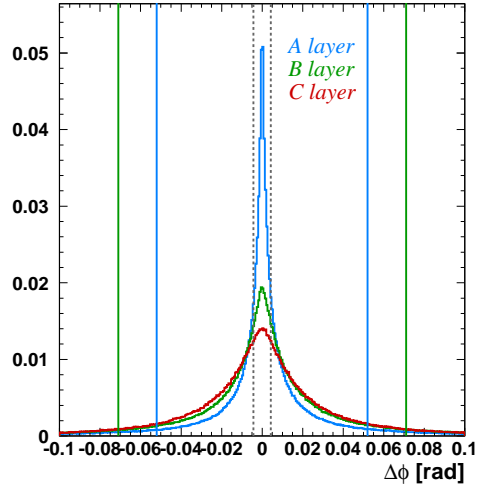
Figure 4.4: Angular spread of the photon-induced particle shower as observed in each of the scintillating layers.

radiated photon. Leptons with an energy smaller than the critical energy will be stopped, and we neglect Compton scattering.

Consider now a high-energy incident photon. After one radiation length we will have, according to the model, 2 charged particles; each has an energy of $E_0/2$. After a second radiation length, we again only have 2 detectable particles and 2 photons, each with an energy of $E_0/4$. After a third (and fourth) radiation length we will obtain 6 (10) charged particles with an energy of $E_0/8$ ($E_0/16$). Each of the charged particles will deposit on average a small amount of its energy in the plastic scintillators. As we can see from figure 4.1, the probability for pair production amounts to about 60% for the first tungsten layer. There is thus a high probability that the incident photon only converts in the second radiator layer, in which case we end up with 2 (6 for four radiation lengths) charged particles in the outer plastic scintillator. Additionally, the π^0-decay photons are low in energy, so the chances are high that one or several charged particles are stopped in one of the tungsten layers before reaching the scintillator. From this simple model it can be understood that the intrinsic fluctuations in energy deposition are large. This is also supported by figure 4.3, in which, for photons leaving a signal in each of the photon-detector layers, the standard deviation associated with the mean energy deposition is given. The fluctuations in energy deposition clearly are large, and an energy reconstruction of the incident photon is thus not possible. Additional factors contribute to fluctuations in energy deposition. These will be discussed in the section describing the Monte-Carlo implementation of the photon detector.

As the shower develops, its lateral spread increases. In the early, most energetic part of the cascade, this spread is characterized by the typical angle of Bremsstrahlung emission, which is proportional to the ratio of the electron's momentum and its mass, and by multiple

37

(Coulomb) scattering in the absorber. At this stage, 90% of the shower energy is contained in a cylinder of radius $r = 0.5X_0$. Multiple scattering increasingly influences the lateral spread with decreasing energy of the shower particles and causes a gradual widening of the shower.

The radius for containment of the total energy is $r = 2\rho_M$. The Molière radius ρ_M describes the lateral average deflection of electrons of energy E_c' after traversing one radiation length. It is given by $\rho_M = 21X_0/E_c'$. For tungsten this corresponds to 10.5 mm. Figure 4.4 represents the difference in azimuthal angle between incident photons (with $E_0 \leq 1$ GeV) interacting in the first converter layer and the charged particles observed in each of the scintillating layers. We can neglect the presence of scintillating material with respect to Bremsstrahlung and multiple scattering. The gray dashed line delimits the region corresponding to $0.5X_0$; the blue line corresponds to $2\rho_M$. As can be seen, the spread is narrow after the first converter layer, with a peak contained within $0.5X_0$, and then gradually increases with increasing amount of converter material.

4.1.2 Detection of charged particles in the scintillators

The measurable signal created in the plastic scintillator by the secondary electrons and positrons consists of scintillation light, resulting from the excitation of atomic electrons. As the charged leptons cross the scintillator, they will mainly interact via collisional losses, while Bremsstrahlung is suppressed due to the low atomic number of the scintillating material ($Z = 3.38$). Indeed, the ratio of specific energy loss by radiation and collisions is given approximately by [76]:

$$\frac{(dE/dx)_r}{(dE/dx)_c} = \frac{EZ}{700}, \tag{4.4}$$

with E the lepton energy expressed in MeV. For tungsten we obtain 15.9 for 150 MeV electrons, for the scintillator material we obtain 0.72.

Not only signals generated by photons, but also signals created by protons and pions are part of the output spectrum of the photon detector. These charged particles interact primarily through collisional losses with the atomic electrons both in the converter and in the scintillator, at a rate that is material-type and velocity dependent. Their passage through the scintillating strips creates thus also scintillating light that is subsequently read out.

Scintillation mechanism

The plastic scintillator material is of the type BC-408 from the manufacturer Saint-Gobain Corporation [77]. The base consists of polyvinyltoluene, represented in figure 4.5. The benzene ring contained in polyvinyltoluene forms the basis for the scintillation phenomenon. The ground state configuration of the carbon atoms is $1s^2 2s^2 2p^2$, but when binding to form the benzene ring, the configuration becomes $1s^2 2s 2p^3$. Three of the valence electrons hybridize into the (sp^2) configuration, so that their wave functions lie in the same plane at an angle of $120°$ from each other (see figure 4.6). These electrons form σ bonds with other hybridized carbon electrons: their respective wave functions overlap along the line joining the carbon atoms. The fourth electron (in a p-orbital) forms π bonds: its wave function overlaps sideways with an other π-electron wave function. The double bonds of the benzene molecule are
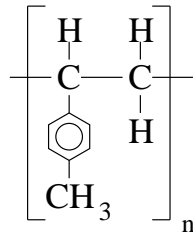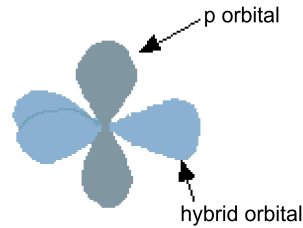
Figure 4.5: Polyvinyltoluene.

Figure 4.6: Angular wave functions in sp^2 hybridization.

composed of one σ and one π bond. There are therefore only three double bonds within the benzene ring, shared equally among the six carbon atoms into a resonant hybrid structure.

It are the π electrons that form the basis for the scintillation mechanism. Their energy states are quantized into a series of singlet (S_{ij}) and triplet (T_{ij}) states, depicted in figure 4.7. Each principal level, S_{i0} (T_{i0}), is accompanied by vibrational sublevels, S_{ij} (T_{ij}). The first excited principal level, S_{10}, lies a few eV above the ground state, S_{00}. The vibrational levels are separated typically by ~ 0.15 eV, which is large compared to the thermal energies ~ 0.025 eV, so that at room temperature most molecules populate the lowest vibrational S_{0j} states.

When a π electron is excited into a higher $S_{i>1j}$ state by the passage of a charged particle, it will de-excite to the S_{1j} levels through a non-radiative transition on a time scale of $\sim 10^{-12}$ s, followed by a radiative transition to the ground states S_{0j} on a time scale of $\sim 10^{-8}$ s, called fluorescence. A transition from an excited S_{1j} state to an excited T_{1j} state is also possible. This will be followed by a slow, $\sim 10^{-4}$ s, radiative decay to the ground states, known as phosphorescence and characterized by longer-wavelength photons due to the difference in relative energy levels. Finally, there is also a small probability to pass from the triplet T_{1j} state to an excited singlet S_{1j} state, followed by a fast radiative decay. The radiated photon has the same wavelength as the fluorescent transition, but the process occurs on a time scale of $\sim 10^{-6}$ s, hence its name delayed fluorescence, because of the low probability for the triplet-singlet exchange. This process probably forms a major component of the tail in the scintillation decay curve.

From this description, one would expect a photon-emission spectrum with a vibrational substructure, corresponding to all individual S_{1j}-to-S_{0j} transitions. However, for typical molecules in a solvent, there are many unresolved substates which result in a broad, smeared-out emission spectrum. A typical example is given in figure 4.8.

Apart from the excitation of π electrons, the passage of a charged particle can also cause the ionization of these electrons as well as excitation and ionization of other electron groups, like σ electrons. The ionization of π electrons, followed by ion recombination, seems to be responsible for the population of triplet states (and some singlet states), and probably leads to most, if not all, of the slow component in the scintillation process. The excitation of other electron groups is dissipated thermally; their ionization seems to be the main cause for radiation damage [78] .

Although polyvinyltoluene is an inherent scintillating material, it will release only a small
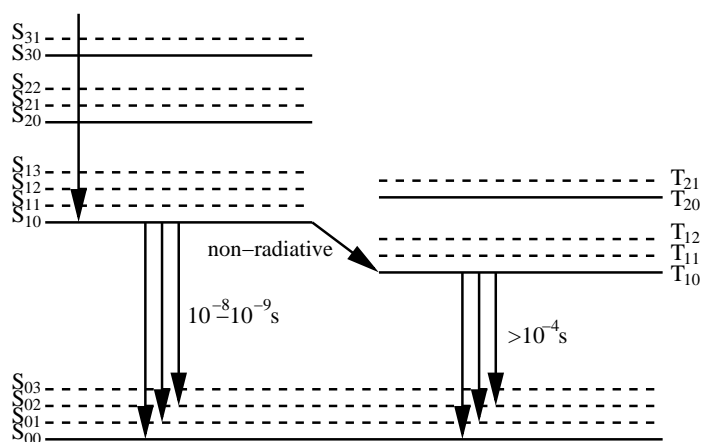
Figure 4.7: Energy levels of π electrons.

fraction ($\sim 3\%$) of the excitation energy under the form of fast fluorescent light. Therefore, it is, as most of the practical organic scintillators, doped with an efficient fluorescent emitter. This fluor has preferably a high fluorescence quantum yield, a fast decay time, and an absorption spectrum that matches the emission spectrum of the solvent. In addition it must be sufficiently stable, soluble, and chemically inert.

The passage of a charged particle will cause the excitation of, mainly, the base material within 0.5 ns. The excitation energy of the base molecule will then be transferred many times, via electron exchange, from one base molecule to another on a time scale of $\sim 10^{-12}$ s before being finally transferred to the fluor [79].

At very low concentration of the solute ($\sim 0.01\%$ by weight), the excited base material will de-excite by the emission of a photon. This photon can subsequently be absorbed by a fluor, which then in turn de-excites through the emission of another photon. However, when an atom is excited, its attraction to the neighboring atoms of the molecule is reduced and, as such, its equilibrium state occurs at greater interatomic spacing. The energy levels for the ground state and excited state are represented in figure 4.9. When a fluor absorbs a photon, the electronic transition takes place on a time scale that precludes any change in interatomic spacing during this transition (Franck-Condon principle). The newly created state corresponds to a high vibrational state of the equilibrium excited state (B' in figure 4.9). A radiationless transition to the minimum of the excited state (B) will follow on a very short time scale. From this point a radiation transition will occur to one of the substates above the ground state (A'), followed finally by a radiationless decay to the ground state (A). The emitted photon thus has a longer wavelength than the absorbed photon. This shift in wavelength is quantitatively expressed as the Stokes shift.[3] It will prevent the emitted photons from being absorbed by the solvent and the fluor, and is hence desired to be as large as possible. As explained before though, the emission and absorption spectra are not sharp lines but smeared out due to the presence of many substates. This will cause the emission

---

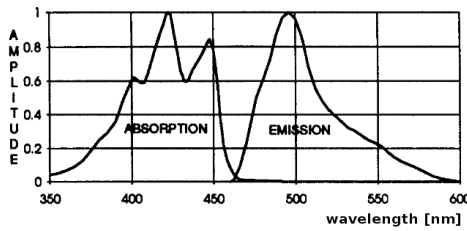[3]This same principle also applies of course to the base material.

Figure 4.8: Emission and absorption spectra of the BC-91A wavelength-shifting fibers [82].
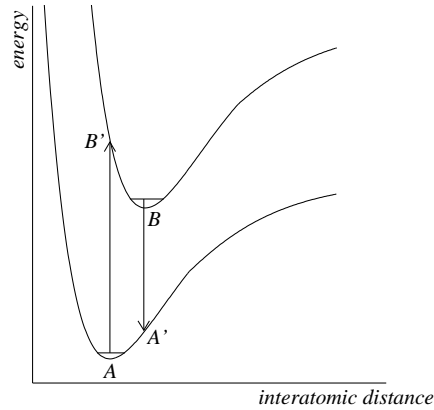
Figure 4.9: Illustration of the Stokes' shift related to the absorption and emission of a photon.

and absorption spectra to have a small overlap so that absorption of secondary photons is still possible. An example of an emission and absorption spectrum is given in figure 4.8.

At high concentration of the solute ($\sim$ 1% by weight), as distances between an excited base unit and a fluor molecule, d, are reduced to 10^{-8} m, the main energy transfer mechanism between the base and the fluor is not the radiation of a photon, but a non-radiative dipole-dipole interaction, known as Förster transfer [83], whose transition probability scales as d^{-6}. It turns out that this process is also proportional to the overlap between the emission spectrum of the solvent and the absorption spectrum of the solute. This strong dipole-dipole coupling causes a sharp increase in light yield, as the fluorescent light is now mainly emitted by the fluor which has a high fluorescence quantum yield, as well as an improvement in the speed of light emission, up to an order of magnitude. As an example, the decay time of undoped polyvinyltoluene is 11.8 ns, while for the BC-408 scintillator it is decreased to 2.1 ns.

For most practical plastic scintillators, the addition of a primary fluor at high concentration ($\sim$ 1% by weight) will be supplemented with a secondary (and sometimes tertiary) fluor at low concentration ($\sim$ 0.05% by weight) to increase the attenuation length. The light emitted by the primary fluor can namely be reabsorbed by the solvent or by the fluor itself. Although the amplitude of the absorption spectrum is several orders of magnitude smaller at the tail than at the peak, this residual is sufficient to absorb the emitted photons over a macroscopic scale and hence creates a limit to the concentration of the primary fluor. On the one hand, the low light-output efficiency from the solvent requires a substantial amount of primary fluor in order to facilitate efficient energy transfer by non-radiative dipole-dipole interaction, but on the other hand, a too high concentration increases self-absorption. By adding a small concentration of an appropriate secondary fluor, the dominant energy-transfer mode to this fluor is radiative, and the light emitted by the primary fluor can be absorbed by
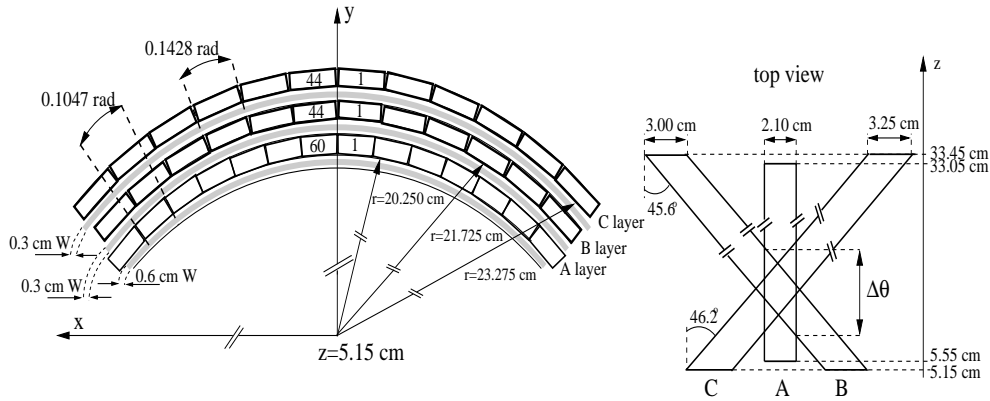
41

Figure 4.10: Geometrical description of the photon detector in the HERMES coordinate frame. The strip numbering is also indicated. For clarity, the picture is not up to scale.

the secondary fluor and shifted to longer wavelengths. The small concentration of secondary fluor limits self-absorption to an acceptable level, while maximizing light output. As such, bulk attenuation lengths can be increased from several millimeters, for a pure plastic base, to a few centimeters, for a base doped with a primary fluor, to finally a few meters, when doped with a secondary fluor.

Scintillator strips for the photon detector

Each scintillator layer of the photon detector is segmented into strips. The inner layer (A layer) has 60 strips, of trapezoidal shape for a maximal coverage. The strips are 1 cm thick, 2–2.1 cm wide and 27.5 cm long. They are laid out parallel with respect to the beam line. The subsequent layers have 44 strips oriented under an angle of $+45.6°$ for the second layer (B layer) and $-46.2°$ for the third layer (C layer) in order to reconstruct the position of the decay photons. The overlap between 1 parallel and 1 stereo layer results in a polar-angular resolution $\Delta\theta/\sqrt{12}$ of about 2.7°. The stereo strips are fabricated out of rectangular straight blocks of 1×2.1 (1×2.25) cm^2 for the second (third) layer, then bent, twisted and cut into their final shape. This results in an effective cross section of 1.00×3.00 (1.00×3.25) cm^2. The strips cover a length along the beam line of 28.3 cm. A schematic drawing of the photon detector is depicted in figure 4.10. As can be seen in figure 4.4, the lateral spread of a shower is contained in one strip. The blue (green) vertical line in this figure corresponds to one strip pitch in the A (B and C) layer, which equals 0.1047 (0.1428) rad.

On average 1000 photons per 100 keV of energy deposition are created in the scintillator [84]. Their wavelength ranges from 400 to 470 nm, with a maximum at 425 nm. Because of lack of space and the presence of the magnetic field, photomultiplier tubes (PMTs) used for the readout of the photon detector are not connected directly to the scintillating strips. Instead, 1.5 mm thick wavelength-shifting fibers are used to redirect and guide the scintillation light from the strips over to 2 m long clear light guides that transport the light to the PMTs. The fibers (clear light guides) are of the type BCF-91A (BCF-98) from the same
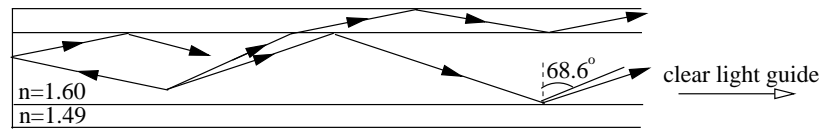
Figure 4.11: Light propagation in the wavelength-shifting fibers

manufacturer as the scintillator strips.

As can be seen in figure 4.8, the absorption spectrum of the wavelength-shifting fibers matches the emission spectrum of the scintillating strips well. Light that escapes the photon-detector strips can be absorbed by a fluor in the wavelength-shifting fibers. This light is then re-emitted isotropically at longer wavelengths, shifting the light from blue to green. The base material of the fiber core consists of polystyrene with an index of refraction of 1.60. It is surrounded by a thin, 50 μm thick, layer of acrylic with an index of refraction of 1.49. Light hitting the core-cladding interface under an angle, with respect to the normal, larger than the critical angle, $68.6°$ in the present case, undergoes total internal reflection, as illustrated in figure 4.11. As such, the light is guided to the clear light guides. These consist of pure polystyrene and will thus guide the light with minimal absorption to the PMTs. Light emitted by the fluor under smaller angles will be lost, apart from a small fraction that is trapped in the cladding by undergoing substantial reflection at the cladding-core interface and total internal reflection at the cladding-air interface. This light also can contribute to the final signal.

As the critical angle depends on the ratio of the low index of refraction to the high index of refraction, air, instead of cladding material, would increase the amount of light being totally reflected. However, impurities would degrade the core surface and cracks could penetrate into the bulk of the core [85]. These effects enhance light losses strongly, so that cladding is largely preferred. The amount of light trapped in fibers, the trapping efficiency, ranges from 3.4% to 7% for single-clad fibers.

Two round, 0.6 m long, wavelength-shifting fibers are glued with BC-600 optical cement in a groove along each side of a strip. Other configurations, e.g., using four strips glued on one surface of the strips, were also investigated, but did not give as good results [70]. Tests were performed to check if the bending of the fibers would result in an attenuated light output. No signs of additional light losses were observed.

Figure 4.12: Picture of the photon detector during its assembly.

To increase the light yield, the strips are covered with BC-620 reflective paint and the

43

wavelength-shifting fibers are mirror coated at their extremity. Their other end is connected to the clear light guides by means of an optical connector. The light attenuation length of the strips, wavelength-shifting fibers, and clear light guides amounts to 280 cm, 362.5 cm, and ≥ 860 cm, respectively. This allows the installation of the PMTs at a distance where the influence of the magnetic field is not so strong.

Figure 4.12 shows a picture of the photon detector during its construction. The painted strips of the outer layer, oriented under a stereo angle, are clearly visible. The wavelength-shifting fibers, with their green light output, are connected to the optical connector, as can be seen in the picture. Not shown are the clear light guides that are connected to the depicted optical connectors. For the final assembly care was taken that the detector is completely light tight by covering it with black foil and black paint.

4.1.3 External monitoring devices

To monitor the stability of the photon-detector response, a gain-monitoring system is installed. It consists of light injected at the downstream end of the photon detector. The light is created by a group of 20 blue light emitting diodes (LEDs), thus light with approximately the same wavelength as the light emitted by the photon-detector strips, and transported over several clear fibers to three optical connectors. The inner part of these connectors consists of a reflective layer to homogeneously distribute the light. This light is then transferred by light guides to the downstream extremity of each photon-detector strip, guided through the scintillating strips, absorbed by the wavelength-shifting fibers, and subsequently read out. The optical connectors and the fibers, painted in black, that bring the light over to the strips are visible in figure 4.12.

Two fibers illuminated by the LED device are connected to an additional 'reference' PMT, instead of to the photon detector, in order to check the stability of the LEDs' light output. The stability of this PMT is in turn monitored by a signal originating from a radioactive source: emitted α-decay particles incident on a crystal create very stable light pulses, and thus provide a reliable reference signal.

Figure 4.13 shows the response of the α source and of the LED light injected in the photon detector and in the 'reference' PMT over a period of 1 month. A good stability of the photon detector as well as of the reference PMT can be observed. Fluctuations in the response of the photon detector can be correlated with fluctuations in the light output from the LEDs. After correction for the fluctuations in the LED system, the photon-detector response is stable within 1%.

4.1.4 Photon-detector readout

The readout of the clear light guides is performed by 6 Hamamatsu 64-channel multi-anode H7546 PMTs [86]. Two PMTs read out one photon-detector layer. The cathode is sensitive to wavelengths from 300 to 650 nm, with a maximum at 420 nm. This matches the emission spectrum of the wavelength-shifting fibers reasonably well. The cathode pixel size is 2×2 mm^2, which allows the connection of one fiber per pixel. Fibers originating from the same strip are connected to two neighboring pixels, while fibers originating from adjacent strips are never connected to adjacent pixels on the PMT. Additionally, the mapping of the pixels
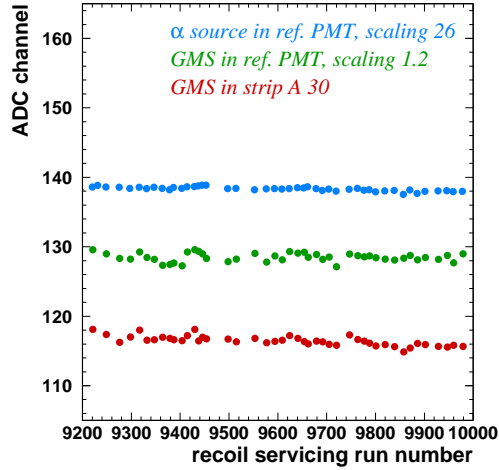
Figure 4.13: Gain-monitoring system response in terms of ADC channels: α source (blue), LED light in reference PMT (green), and LED light in photon-detector strip (red). The signal from the reference PMT is scaled down.

takes as much possible advantage of the free space provided by the 88 pixels to which no light guides are connected. These pixels are also grouped per 2, and read out. This layout minimizes crosstalk on the PMT cathode, and separates signals originating in the PMT from signals created in the photon-detector strips.

Since the PMTs can only function properly in a magnetic field not exceeding 0.5 mT, they are, each individually, surrounded by two 0.2 mm thick μ-metal sheets and placed in a soft-steel case of 14 mm thickness [87]. Per group of three they are then disposed in an additional soft-steel box. The two boxes are installed at a distance of 1.5 m from the magnet, where the magnetic field is of the order of 20 mT. After the installation of the photon detector, signals from cosmic particles and LED light, measured with magnet on and off, were compared and no differences were observed.

The signal from the PMTs is transferred to a patch panel, and from there to a 'transmitter'. In the transmitter, signals originating from the same strip are summed together, slightly amplified, and transported as a differential signal over 30 m long flat cables to the 'receiver', located in the electronic trailer. The receiver converts the signals back to non-differential signals, amplifies them, and sends them over 70 m of flat cable to 6 charge-integrating analog-to-digital converters (ADCs), one per PMT. Also here, to allow for crosstalk correction, care is taken that channels adjacent in the flat cables are never neighboring pixels in the PMT or adjacent strips in a photon-detector layer.

The digital signal is subsequently processed by the DAQ, and stored in EPIO format. The readout chain is depicted in figure 4.14.

Although the time between 2 HERA bunches amounts to 96 ns, the gate width for the readout of the ADCs is set to 250 ns. As can be seen in figure 4.15, the photon-detector
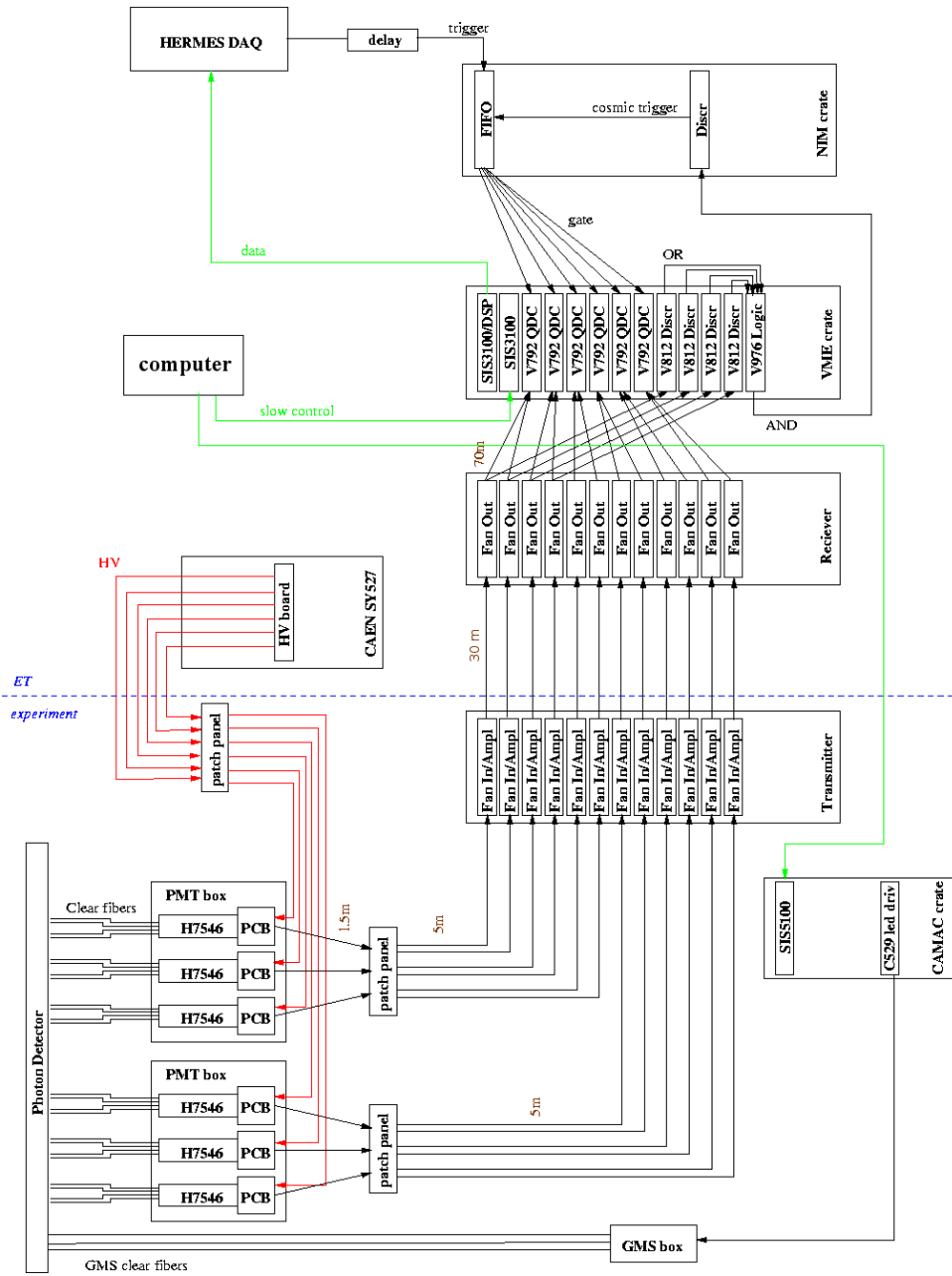
Figure 4.14: Photon-detector readout chain. The first series of readout components, up to the transmitter, are located in the experimental enclosure. From the transmitter, the signals are then transferred via 30 m long cables to the electronic trailer (ET), where they are processed by the receiver, and after delay, digitized by the charge-integrating ADCs (QDCs).
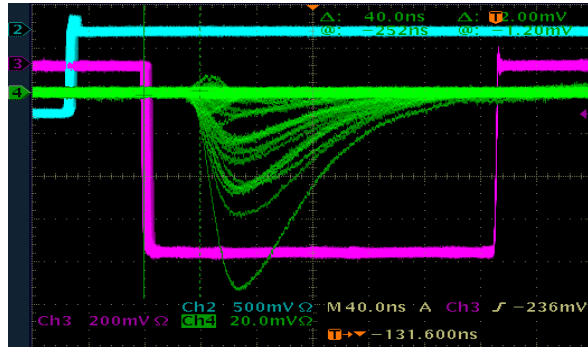
Figure 4.15: Photon-detector signal (green) and gate (magenta) during data taking.

signal is $\sim$ 200 ns long. Additionally, differences of up to 17 ns in travel time have been measured for channels from the same flat cable. Finally, since the ADC starts digitizing 15 ns after the arrival of the gate signal, a gate width of 250 ns is considered safe. No problems concerning bunch overlap are expected, as the event rate is low.

4.1.5 Photon-detector offline data processing

As explained in chapter 3, the offline processing of the data occurs in different steps. In this subsection, the treatment of the photon-detector data at each of these steps is described.

HDC

The information from the ADCs, stored in EPIO format, is decoded and converted into energy units and photon-detector strip numbers [88].

For each ADC channel present in the data stream, the corresponding strip and layer number is determined from the information stored in mapping files. After subtraction of the mean pedestal value, ADC values are converted into energy values. The appropriate conversion factor is obtained from the calibration of a preceding data production. The calibration procedure for the photon detector is explained in a following section.

Finally, each strip number, layer number, ADC value, and energy value is stored for each event in a separate table, dedicated to the photon detector.

Figure 4.16 shows the ADC spectrum of a photon-detector strip after the processing of the photon-detector signals by HDC. The sharp peak around ADC channel 250 corresponds to half the pedestal, which is part of the readout signal. The largest photon-detector signals are located around ADC channel 4500. With the ADC range extending to 8192 channels, this lies far away from the overflow region.

XTC

The hits from the silicon-strip detector and scintillating-fiber tracker are combined into tracks. For the photon detector, hits are combined into clusters and, if applicable, linked to a track.
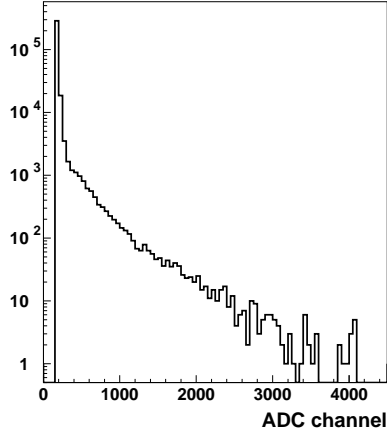
Figure 4.16: ADC spectrum of a photon-detector strip after processing by HDC.

First, all hits originating from the HDC tables are sorted out: hits with negative energy value or ADC value below threshold (2σ above pedestal) are discarded as well as signals induced by crosstalk in the flat cables [89].

In a second step, signals originating from neighboring PMT pixels are grouped together into clusters [90]. For this, first the local maxima on the photomultiplier are determined. A pixel is considered a local maximum if for none of its neighboring pixels — 8 for pixels not located at the edge of the cathode — a higher signal is recorded. Then, the non-local maxima are examined. A non-local maximum is considered a crosstalk hit if it has an energy value lower than a certain threshold value, and if it corresponds to a photon-detector strip that has no adjacent strips for which a signal is recorded. If one of these two conditions is not satisfied, the non-local maximum is promoted to a local maximum. Finally, the energy of the crosstalk hits is added to that of the local maximum. If a cross-talk hit is associated with several local maxima, its energy is shared between them, proportionally to the energy value of each of the associated local maxima.

In a third step, neighboring strips in each of the photon-detector layers are combined into clusters [91]. Also here, first the local maxima are determined. A local maximum is formed by a strip that has a signal higher than its 2 adjacent strips. Then, the energy of the non-local maxima are added to that of the local maximum. If a non-local maximum belongs to two local maxima, its energy is distributed between the local maxima. The energy fraction of the non-local maximum added to the signal of one of the local maxima, denoted here as local maximum 1, is given by:

$$\frac{E_{max,1} e^{-d_1}}{E_{max,1} e^{-d_1} + E_{max,2} e^{-d_2}}. \tag{4.5}$$

The quantity $E_{max,1}$ ($E_{max,2}$) represents the energy of local maximum 1 (2), and d_1 (d_2) is the distance, in units of strip number, between the non-local maximum and local maximum 1
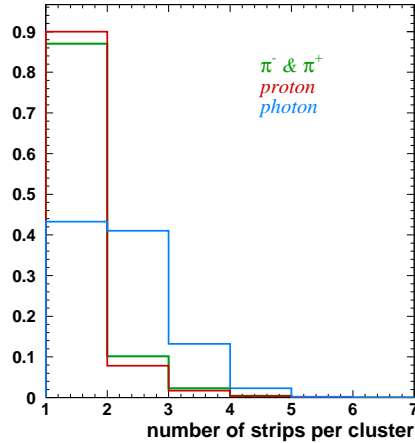
Figure 4.17: Number of strips contributing to the formation of a cluster.

(2).

The energy contribution from each of the individual strips is also used to determine the energy-weighted azimuthal angle and strip number of each cluster. The azimuthal angle is defined as the angle corresponding to the cluster center at the upstream end of each of the layers.

It has been shown [92] that the clustering algorithm works well with respect to the localization of the cluster maxima, and the reconstruction of the energy deposition. Some problems in the determination of these two quantities arise, however, when cluster maxima are separated by less than 3 strips. As can be seen in figure 4.17 (and anticipated from figure 4.4), the cluster width amounts, in most of the cases, to 1 strip for pions and protons, and to 1 or 2 strips for photons (although cluster widths of up to 7 strips have been recorded). Thus problems arise at the limit of overlapping clusters.

Figure 4.18 represents the opening angle between two π^0-decay photons leaving a signal in the photon detector, as a function of the π^0 momentum; figure 4.19 shows the corresponding momentum distribution of the neutral pion. The distributions are obtained from data generated by the gmc_dvcs and pythia generators. As can be seen in these figures, the average opening angle between two photons originating from π^0 decay is large, thus the probability for overlapping clusters low. Also, in view of the analysis of DVCS events, the occurrence of overlapping clusters is expected to be limited, as for this analysis the dominant event topology is restricted to 1 charged particle and at most 2 photons, originating from the background process, in the photon-detector acceptance.

From the reconstructed clusters in each layer, only those with energy values above 1 MeV are stored. The justification for this threshold value is given in one of the following sections.

In a fourth, and last step, clusters are associated, if applicable, with tracks reconstructed by the scintillating-fiber tracker and the silicon-strip detector.

The intersection of a charged particle's track with the photon detector can be calculated
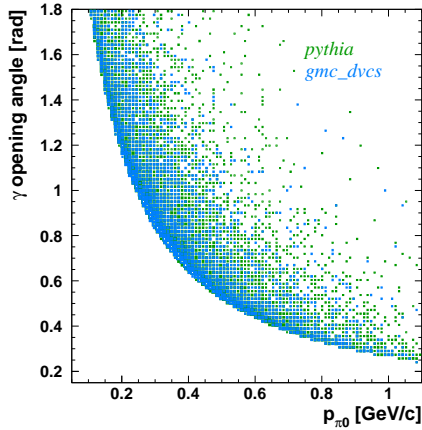
Figure 4.18: Opening angle of π^0-decay photons as a function of the π^0 momentum.
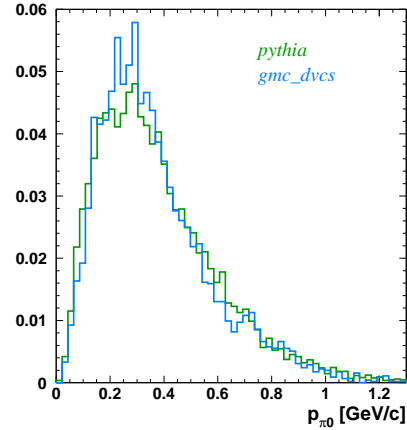
Figure 4.19: Momentum distribution of π^0s.

as the intersection of a helix, describing the particle's path, with a circle, formed by one of the photon-detector layers. For this calculation the magnetic field is assumed homogeneous, and multiple scattering and energy losses are neglected. This last aspect is most relevant for low-momentum protons, but these do not form a large fraction of the protons reaching the photon detector. Also, as explained in the previous chapter, for one same track, several track-parameter values are provided according to each of the track hypotheses: stopped proton, non-stopped proton or pion. After the determination of the particle's type, the correct track parameters can be selected. However, at this stage of the data chain no particle identification is provided, so that for any track the parameters corresponding to the pion hypothesis are used.

Figures 4.20 and 4.21 show the results of the calculation on pure Monte-Carlo information level in each of the photon-detector layers. For all hits generated in a photon-detector layer by the impact of a traversing particle, the Monte-Carlo simulation provides the corresponding hit coordinates, from which then an energy-weighted azimuthal angle and z position can be determined. From the track parameters of the generated Monte-Carlo track, the position of impact of a particle in each of the layers can be calculated. The difference in azimuthal angle between the hit information and track information is shown in figure 4.20 for positive and negative pions, and for protons. Clearly, the influence of the magnetic field is visible, resulting into a shift in opposite direction for oppositely charged particles, and more pronounced for protons due to their lower energy. The accuracy of the method is, however, evidently satisfying, as the difference is smaller than 1 strip pitch, indicated by the blue (green) line for the parallel (stereo) layer. The accuracy of the z-coordinate determination is shown in figure 4.21 for negative pions and for protons. Also here the results are satisfying, and as for the determination of the azimuthal angle, a wider spread as a function of number of crossed (tungsten) layers is observed.

To understand the results of the calculation on reconstructed track and cluster level, first

Figure 4.20: Difference in azimuthal angle between hit position in the photon detector and hit position calculated from track parameters.

the differences in track parameters between the generated Monte-Carlo track and recon-structed track are compared. The comparison here is based on a sample generated by a Monte-Carlo background generator that simulates, per event, one single particle of a prede-termined type, and does not include detector inefficiencies, misalignment, or miscalibration issues, so that depending on the severity of these aspects, distributions might look different for experimental data. The here described method has been applied to analyze experimental data as well, and as will be shown, the influence of detector inefficiencies is sometimes visible, but not always hindering; work is in progress to reduce the effect of detector inefficiencies on
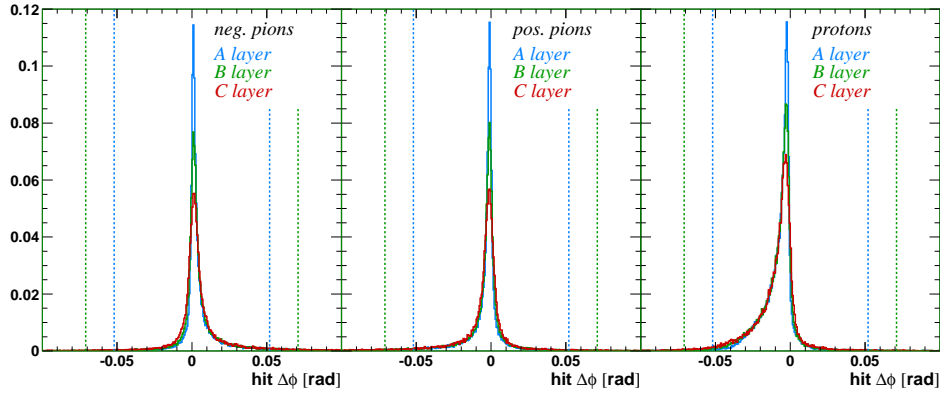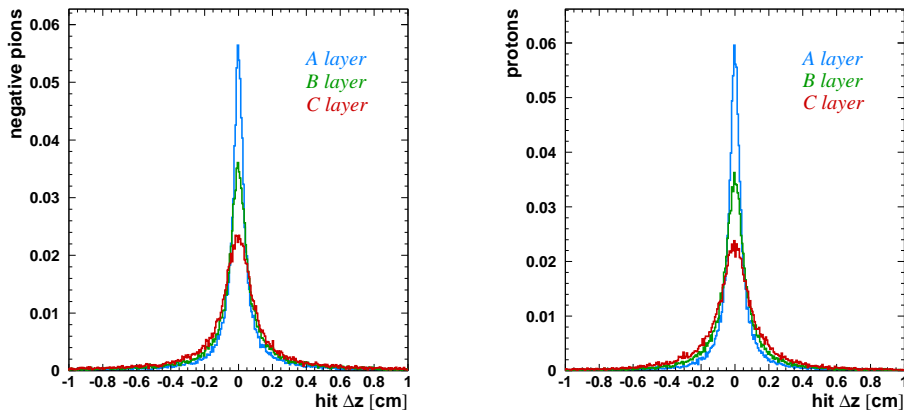

Figure 4.21: Difference in z coordinate between hit position in the photon detector and hit position calculated from track parameters.

51
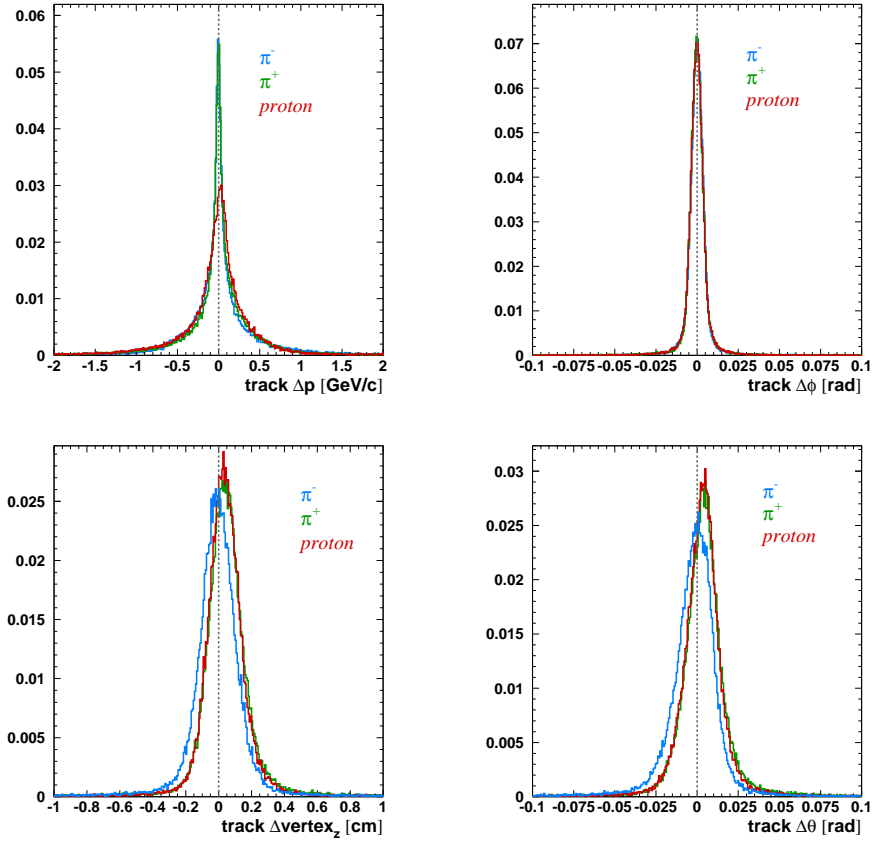
Figure 4.22: Difference between Monte-Carlo generated and reconstructed momentum (top, left), azimuthal angle (top, right), z-vertex coordinate (bottom, left) and polar angle (bottom, right).

track reconstruction.

Figure 4.22 represents the difference in momentum, azimuthal angle, z-vertex position, and polar angle between the Monte-Carlo generated track and the track reconstructed by the recoil detector for positive and negative pions, and for protons. As can be seen, the accuracy of the azimuthal angle determination is very good for all three particle types. Also the momentum reconstruction is very satisfactory. The effect of neglecting energy depositions, resulting from the use of the pion track hypothesis, is visible for protons: the reconstructed momentum is slightly lower than the generated one. A small shift in the reconstruction of the polar angle and the z-coordinate of the vertex is present for positive particles. This will have a small influence on the determination of the z coordinate of the track-layer intersection, and consequently on the determination of the azimuthal angle for the stereo layers.

52
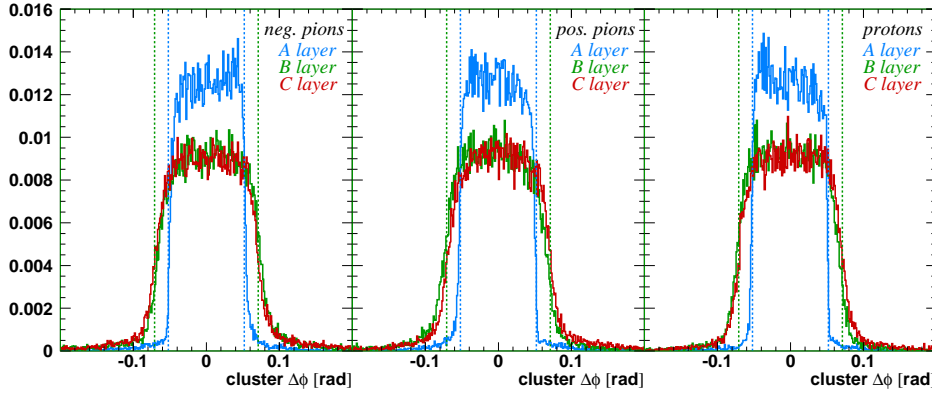
Figure 4.23: Difference between the azimuthal angle of a photon-detector cluster and the angle determined from the reconstructed track parameters.

Finally, the difference between the azimuthal angle from a photon-detector cluster and the angle obtained from the reconstructed track parameters is shown in figure 4.23, together with the respective strip pitch. The distribution is well centered around zero and the width only slightly exceeds a strip pitch. A photon-detector cluster is associated with a track if the difference in azimuthal angle is less than 1 strip pitch and if the z coordinate of the intersection is comprised between certain boundaries, which are slightly larger than the length of the individual layers, due to the limited resolution and a tiny residual misalignment, as will be discussed later. These cuts provide a good efficiency in the use of the photon detector as a detector able to reject events in which a photon is present, as will be shown in the last section of this chapter and in the following chapter.

The average strip number and energy of the clusters are stored, together with the information of the tracks and of the other two recoil detector components, as well as the same information present at the output of HDC. This allows easy access to all the needed information for detector studies and calibration.

The photon-detector geometry should also allow for the reconstruction of space points, however, depending on the amount and type of particles present in the event, it can turn out to be a difficult task. Since the angle of inclination of the stereo layer is large, 1 strip from the stereo layer crosses 14 strips from the parallel layer, which is nearly a quarter of the detector. Therefore, it may become complicated to distinguish accidental strip crossings from crossings related to the actual impact of a particle. Also, the possible inefficiency of a layer, or the fact that certain particles do not reach the outer layer(s) or only interact after the first layer, increases the complexity of the problem.

An example of an event with such a complex configuration is shown in figure 4.24. This picture, obtained from a Monte-Carlo simulation, represents all strips in which a signal is recorded, color-coded according to the particle that created the signal, and drawn along the azimuthal-angle and z axis. The π^+ is correctly reconstructed by the tracking code, and the corresponding clusters in the photon detector are correctly assigned as belonging to this
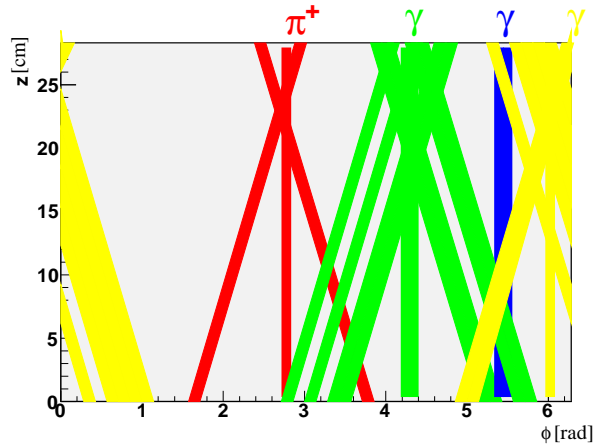
Figure 4.24: Example of an event for which many particles are observed in the photon detector. For each particle the corresponding strips in which a signal is recorded are represented, and color-coded accordingly.

track. This leaves us with the disentanglement of the 3 photons. The clustering algorithm will reconstruct more clusters than actually present. Indeed, for clusters formed by non-directly adjacent strips, several local maxima are found, and thus several individual clusters are reconstructed, although they all originate from the same particle. Then, at the level of space-point reconstruction, even if one would allow several clusters from a same layer to be combined as one, it seems very difficult to decide if part of the original 'green' cluster from the B layer (under an angle of $+45.6°$) and the 'yellow' cluster from the C layer belong to the crossing with the 'blue' photon or to the crossings they actually originate from, or if part of the original 'yellow' cluster from the B layer might be combined with the 'blue' photon cluster. The amount of deposited energy also does not always help, as depending on the photon's energy (or the fact that it is stopped in a certain layer), it will deposit more or less energy in one layer compared to the other.

Although this event represents an extreme and rarely occurring topology, it illustrates that depending on the type of events one wishes to analyze the space-point algorithm might be more or less complex. Therefore, this point is left open until the analysis of DVCS events with the recoil detector, presented in the next chapter.

μ**DSTs**

This last part of the data-production chain only stores the information necessary to the analyzer. It includes the track parameters and the information from clusters to which no track is assigned. At this stage also particle identification is provided in terms of PID values.
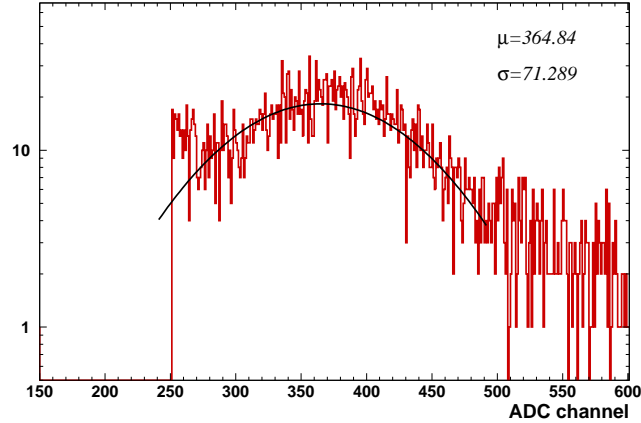
Figure 4.25: Signal of cosmic particles in a strip of the photon detector.

4.2 Test experiment

Before the installation of the recoil detector in the HERMES experiment, data were taken with the recoil detector in a test area in the East Hall. From end of March 2005 until beginning of September from that same year, signals from cosmic particles were detected and analyzed in order to gain a better understanding of the different recoil-detector components. In total, over 100 million cosmic events were collected. During this period also the gain-monitoring system was operational and fine tuned.

The trigger for the detection of cosmic particles is formed by a signal above threshold in the lower half of one of the photon-detector layers[4]. The signals originating from cosmic particles can then be isolated by requiring a hit, 11σ above pedestal, in 2 diagonally opposite strips or in 2 strips opposite to each other with respect to the $y = 0$ plane. Since the angular distribution of cosmic particles follows a $\cos^2 \theta$ distribution, the first selection yields nearly no events for diagonally opposite strips around $y = 0$, while it restricts the variation in path length for strips closer to the zenith, and thus for these strips improves the quality of the observed signal. The fit of a Gaussian distribution to the obtained spectrum provides a preliminary calibration of the photon detector, used as input for the first HDC production.

An example of a signal from cosmic particles is given in figure 4.25. The mean pedestal value is located around 200 ADC channels, has a width of 3 to 4 ADC channels, and is extremely stable, which results in an observed signal clearly separated from the pedestal.

The signals from cosmic particles also allow for an estimate of the efficiency of the individual photon-detector strips. To this effect, information from the outer layers of the scintillating-fiber tracker is included. The fiber with highest ADC signal is searched for in

---

[4]Sometimes a coincident signal between two diagonally opposite strips in each of the halves of a layer was required, but due to the restricted number of logic units, this configuration did not allow for a full coverage of the detectors.

Figure 4.26: Difference in azimuthal angle between hit position in the photon detector and hit position calculated using the scintillating-fiber tracker for the lower A (left) and lower C (right) layer. The vertical lines delimit 1 strip pitch.
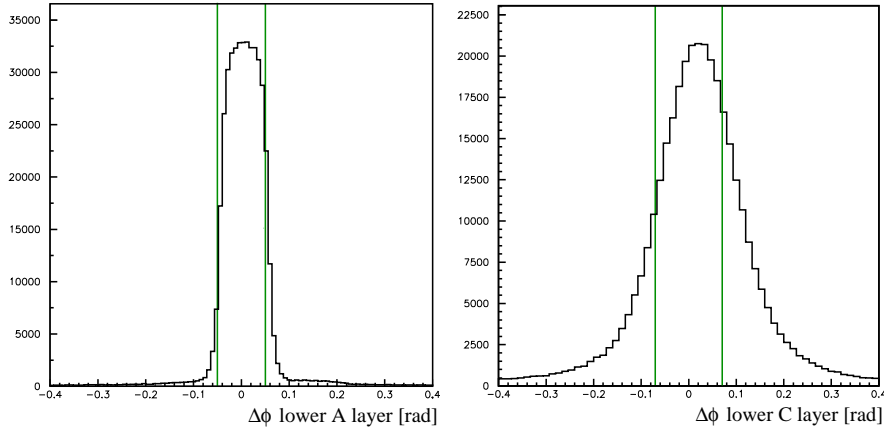
the upper and lower half of the tracker's outer parallel layer. For each of these two fibers, the stereo fiber with highest signal, and crossing the parallel fiber, is selected. The fibers from the parallel layer allow to determine in which A-layer strips a signal is expected; for the B and C layers, the z coordinate of the crossing point between two fibers needs to be included. Then, the lower and upper halves of each photon-detector layer are scanned for the strips with highest signal. The difference in azimuthal angle (again with respect to the upstream end of the photon detector) between the strip that fired and the one determined using the scintillating-fiber tracker is shown in figure 4.26 for the lower half of the A layer (left) and of the C layer (right). The vertical lines correspond to one strip pitch. Although a small misalignment is observed, the A layer is relatively well aligned with respect to the scintillating-fiber tracker. For the stereo layer, a larger deviation and spread in alignment is observed, which can be understood, as the exact position of the photon-detector strips and the tracker's fibers was unknown, and a small shift in fiber position has a large influence on the determination of the z coordinate. Nevertheless, this does not prevent a first determination of the photon-detector efficiency.

For the study of the efficiency of a layer, an event is accepted if for the layer halves not under study, the strips determined using the scintillating-fiber tracker correspond to the strips in which a signal is recorded. For strips from the layer under study, three situations are investigated. In the first case, the strip determined using the scintillating-fiber tracker is required to indeed have detected a cosmic particle; in the second case, the condition is relaxed to one of its two direct neighbors; in the last case, also its two indirect neighbors are taken into account. The result is shown in figure 4.27, where the first case corresponds to the blue symbols, the second case to the green symbols, and the last case to the red symbols. As expected, the obtained A-layer efficiencies do not vary too much for the three considered cases. For the stereo layers, the effect of the misalignment is clearly visible, affecting even
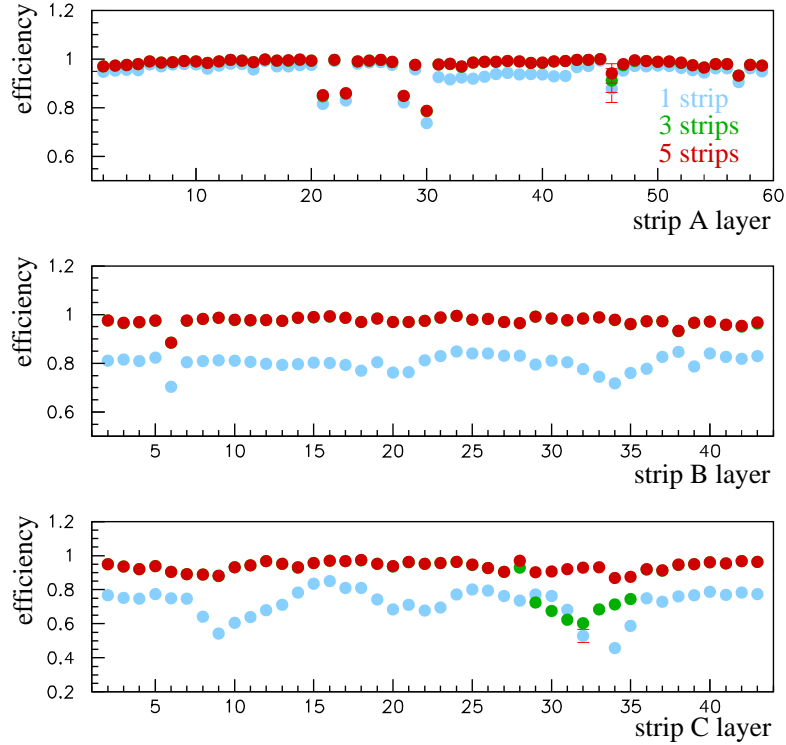
Figure 4.27: Efficiency of the photon-detector strips, determined from cosmic signals.

more the outer layer. Nevertheless, these results already give a satisfying impression of the detection efficiency of minimum-ionizing particles, i.e., particles that have their mean energy-loss rate at the minimum.

4.3 Implementation of the photon detector in the HERMES Monte Carlo

Monte-Carlo simulations at HERMES are based on GEANT3 [80]. Events are generated by a generator, e.g., gmc_dvcs or pythia. Once particles are generated, control is turned over to GEANT, which tracks particles in steps through the detector volumes.

The geometry of the HERMES detector is described in the geometry file. This file contains the description of each detector volume, the material each volume consists of, and a flag to tag sensitive detector components so that energy depositions in these components are saved by a user-written routine for further processing. The photon detector is described as consisting of 3 cylinders of tungsten and 3 cylinders of scintillating material, each of the appropriate thickness and length. The scintillators are sensitive detectors, and thus tagged as

active, while the tungsten layers are tagged as passive.

Additional parameters are associated with each detector volume. One type of parameters consists of flags that enable or disable certain physics processes or the generation of secondary particles, if applicable. The following processes are enabled in all components of the photon detector: pair production, Compton scattering, photoelectric effect, δ-ray production, positron annihilation, Bremsstrahlung, hadronic interactions (using the GHEISHA package [81]), muon-nucleus interactions, continuous energy loss with generation of δ-rays above a certain threshold and restricted Landau fluctuations below, decay of particles, and multiple scattering.

The other parameters are threshold values below which a particle is considered to be stopped. These threshold values can be set individually for different types of particles: photons, electrons and positrons, neutral hadrons, charged hadrons, muons, and one can choose separate thresholds for electron Bremsstrahlung, muon and hadron Bremsstrahlung, δ-rays by electrons, δ-rays by muons, and direct-pair production by muons. For the photon detector, the threshold value is set to 100 keV for all particles in the scintillator and tungsten material.

GEANT tracks each generated particle traveling through the detector volumes in steps. At the beginning of each step, the step size is determined. GEANT calculates the distance to the interaction point for each of the physics processes mentioned above, based on known probability distributions and a random-number generator. The smallest of these distances determines the step size. Additional factors can reduce this step size. If a particle crosses a volume boundary within the originally determined step size, the step size will be restricted to the distance to the volume boundary. A specified maximum step limit, a maximum angular deviation in a magnetic field, a maximum continuous energy loss, or a limit imposed by the validity of the Molière formula for multiple scattering also can reduce the step size. Finally, if the particle's energy falls below the set energy threshold, the particle is considered to be stopped and its effective step size is also reduced. Once the step size is determined, GEANT transports the particle over the corresponding distance, and adjusts the particle's trajectory and energy according to the mechanism in effect. If applicable, secondary particles are generated, and once the tracking of the primary particle throughout all detector volumes is completed, these secondary particles can also be tracked.

After each step, the user-written routine is called. It puts secondary particles on the tracking stack for future tracking and stores hit information for active detector volumes. Once a particle is stopped or has left the detector volume, the hit information corresponding to the crossed detector volume is stored in output tables. This hit information consists of the total energy deposited by the particle in that volume, its coordinates at the entrance of the detector volume, and its average hit position in the detector. Finally, a link to the track from which the hit originates is created.

Track information is stored for primary tracks only. A primary track is either a track generated at the beam-target interaction point or a track from a secondary particle if this particle has a momentum above a set threshold. This threshold can be chosen by the user. In most productions, it is set to 100 MeV. Hits originating from secondary particles with lower momenta are thus associated with the primary track the secondary particles originate from, and are distinguishable from hits directly generated by primary tracks by the value of $iStak$. Hits directly originating from the primary track have $iStak = 0$, while hits from secondary tracks have a larger value, depending on the track's position in the tracking stack.

58
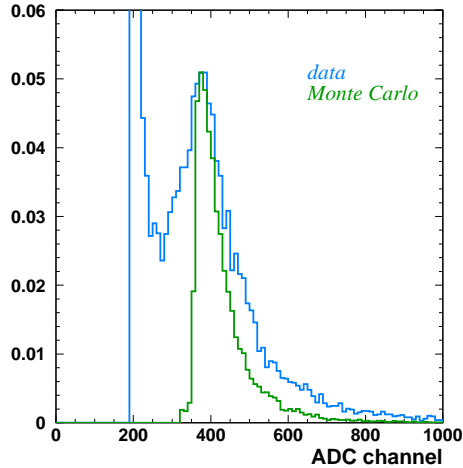
Figure 4.28: ADC spectrum from cosmic particles for experimental data and a Monte-Carlo simulation that does not include the full detector smearing.

At the end of each event, the digitization routine for each detector is called. Its purpose is to simulate the actual response of the detector. GEANT only provides pure energy depositions, not including any fluctuations related to the intrinsic detector response or instrumental effects. The output of this routine is designed to reproduce experimental data after their processing by HDC.

The photon-detector scintillators are modeled in the geometry file as cylinders without any subdivision into strips. In the digitization routine, the strip number corresponding to a hit is determined from the hit position. The energy depositions of all hits belonging to the same strip are summed together. When doing so, one takes into account the geometry of the strips: if a particle crosses the edge of a strip, it does not traverse as much material as when crossing a continuous cylinder. The average hit position and the coordinates at the entrance of the scintillator allow to determine the amount of material a particle encounters when traversing a strip. For particles that are not stopped in the scintillator, the deposited energy is corrected for the actual path length. No difference in energy deposition was, however, observed when this correction is applied or not.

In a subsequent step, the energy is converted into an ADC value, with a common conversion factor for all strips belonging to the same PMT. This ADC value is smeared according to a normal distribution with a width of 3.7 ADC channels, the average of all measured pedestal widths. The obtained ADC spectrum is compared to experimental data in figure 4.28 for signals from cosmic particles. No special event selection to isolate signals is performed. Data are plotted for any cosmic particle impinging on the photon detector, regardless if the particle crosses the strip under investigation or not[5]. Clearly, the width of both distributions differs

---

[5]The reason that signals from cosmic particles are not extracted as described in the previous section is due to the fact that originally a cosmic generator, generating muons from a plane above the detector, was not available, and

strongly; additional factors contributing to the spread of the distribution need to be taken into account.

As mentioned, GEANT only provides energy depositions, but does not simulate any fluctuation in the number of scintillating photons that actually contribute to the readout signal. The number of scintillating photons created by the passage of a charged particle in the photon-detector strips is subject to statistical fluctuations, and this affects the energy resolution. The efficiency and the variation in efficiency with which the photons are collected at the PMT cathode also have an influence on the resolution. Here, the attenuation of light in the strips, wavelength-shifting fibers, and clear light guides is a contributing factor. Also, depending on the point of impact of a traversing particle, the distance traveled by the generated photons until the upstream end of the detector varies, thus affecting the variation in number of collected photons. The trapping efficiency in the wavelength-shifting fibers also plays a role. It depends on the position at which light is emitted by the fluor [82]: it ranges from 3.4% for events occurring at the fiber axis to $\sim 7\%$ for events near the core-cladding interface. Any imperfection in the bulk material or at the surface of the strips, wavelength-shifting fibers, and clear light guides as well as a non-optimal connection between the strips and the wavelength-shifting fibers, the wavelength-shifting fibers and the clear light guides, and the clear light guides and the photocathode also contribute to a decrease in energy resolution. Finally, the quantum efficiency of the photocathode and a non-uniformity in light collection at the cathode also affect the energy resolution.

As values for the individual contributing factors are not available, a global approach, including the effect of all possible factors at once, is used in the tuning of the Monte-Carlo simulation. The tuning was done on ADC spectra[6] by adjusting the width of the cosmic spectrum from Monte-Carlo data to the width of the spectrum from experimental data. The starting point is the article [93], in which the response of a PMT is modeled as a Gaussian distribution with mean μQ_1 and standard deviation $\sqrt{\mu(\sigma_1{}^2 + Q_1{}^2)}$ for large μ and negligible noise intensity. Here, Q_1 represents the average charge at the PMT output when 1 photoelectron is collected at the first dynode, σ_1 is the corresponding standard deviation, and μ is the mean number of photoelectrons collected by the first dynode. This mean number of photoelectrons is a product of the mean number of photons hitting the photocathode and the quantum efficiency of the cathode.

For the simulation of the photon-detector response, the values used for Q_1 and σ_1 originate from measurements done prior to the installation of the photon detector [87], using different amplification and readout electronics, and thus can not be taken as correct for the final setup. As no other values are available (with the current setup it is not possible to observe the single photoelectron peak), the values obtained prior to the installation are nevertheless used, and combined into one common average value for all PMTs. Thus, since the values of Q_1 and σ_1 are unknown, this approach does not allow for the extraction of μ.

The value of μ corresponding to an energy deposition E is given by $\mu = \mu_{ref} \frac{E}{E_{ref}}$, where μ_{ref} represents the number of photoelectrons hitting the first dynode (if the correct values of

---

only a muon generator that generates muons originating from the target cell could be used. The comparison of this generator with data did not give satisfactory results, as the tails of the deposited-energy spectra were underestimated. Once the cosmic generator was available, checks were carried out again and the results, as will be discussed, updated.

[6]In retrospect, a better approach consists in relying on the preliminary calibration, obtained from cosmic particles, and tuning energy spectra instead of ADC spectra.
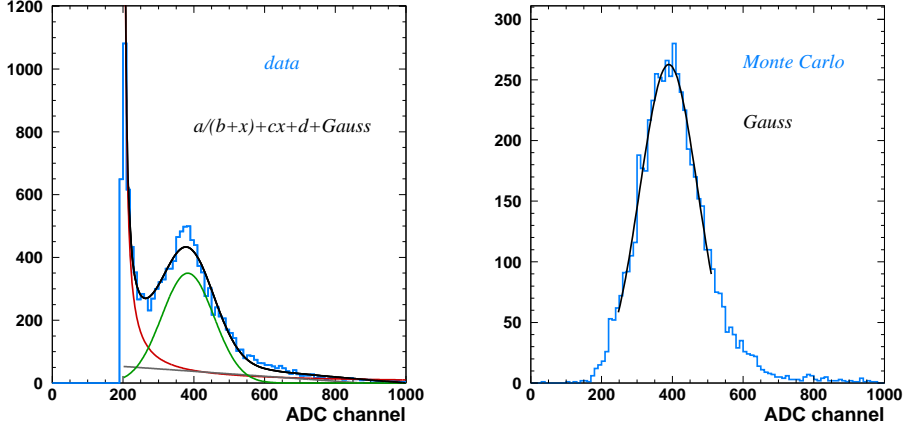
Figure 4.29: Fit of the energy-deposition distribution from cosmic particles for experimental data (left) and simulated data (right).

Q_1 and σ_1 are known) for a reference energy deposition E_{ref}. To determine the value of μ_{ref}, ADC spectra for strips located around $x = 0$ are analyzed. A cosmic particle passing through these strips traverses on average 1 cm of scintillating material, which corresponds to an energy deposition of ~ 2 MeV. The strip with ADC gain closest to the average gain of all strips belonging to the same PMT is then selected. The spectrum from experimental data is fit, taking into account the presence of the pedestal, with the following function $f(x)$:

$$f(x) = G(x; \nu, \sigma) + \frac{a}{b + x} + cx + d, \tag{4.6}$$

where $G(x; \nu, \sigma)$ represents a Gaussian distribution with mean ν and standard deviation σ. The result of the fit is shown in figure 4.29 (left). Analogously, Monte-Carlo spectra obtained for different values of μ_{ref} are fit with a Gaussian distribution, as depicted in figure 4.29 (right). Subsequently, the standard deviations of the Gaussian distributions from experimental data and Monte-Carlo data are compared for each of the three detector layers, and the value of μ_{ref} corresponding to the best overall agreement is chosen as the reference value for an energy deposition of 2 MeV. The resulting cosmic spectra for experimental and Monte-Carlo data are compared in figure 4.30.

After the smearing of the ADC value by the product of $\sqrt{\mu(\sigma_1{}^2 + Q_1{}^2)}$ and a randomly generated number distributed according to the standard normal distribution, the discrete ADC value is converted back into energy, and finally this obtained energy-deposition value, ADC value, strip number, and layer number are stored in a table, and for each entry, a link to the table containing the hit information is created.

The comparison between experimental data and Monte-Carlo data in terms of energy deposition is shown in figure 4.31 for signals from negative pions with momenta above 0.5 GeV/c, which are minimum-ionizing particles. The energy depositions are normalized to path length. The energy spectra are fit with a convolution of a Landau and a Gaussian

61
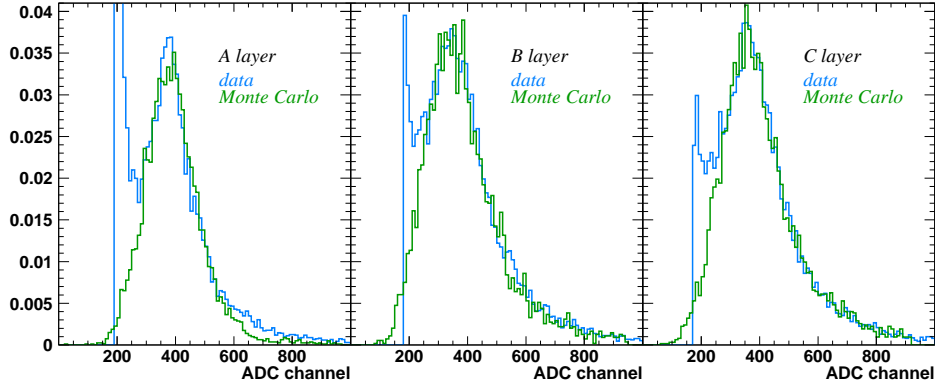
Figure 4.30: Comparison between the energy deposited by cosmic particles in each of the photon-detector layers for experimental data and Monte-Carlo data.

distribution (as described in the section treating the photon-detector calibration). The mean from this fit function is calculated, and the width σ is taken as $\sqrt{\sigma_L{}^2 + \sigma_G{}^2}$, where σ_L (σ_G) represents the width of the Landau (Gauss) distribution. The figure on the left-hand side shows the ratio of the mean from experimental data and from simulated data as a function of strip number for each of the layers; the figure on the right-hand side shows the ratio of the width. For certain strips no data are available due to a combination of the geometry of the
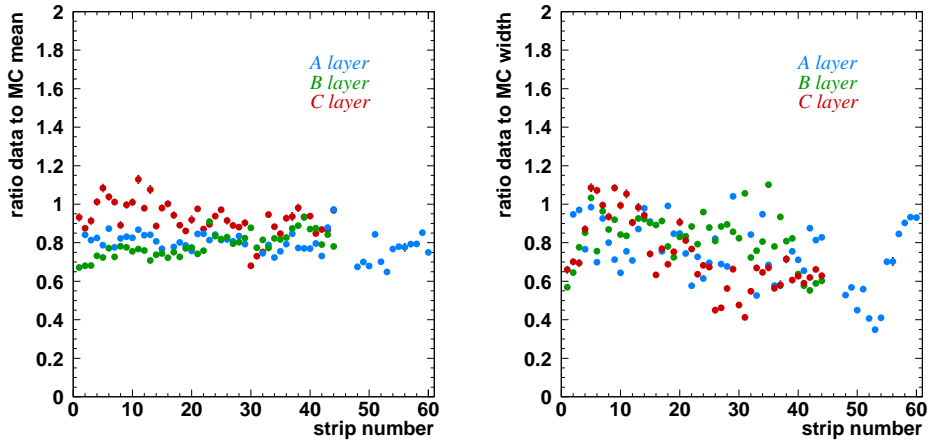
Figure 4.31: Comparison between experimental and Monte-Carlo data for signals from negative pions with momenta above 0.5 GeV/c: ratio of the mean energy deposition (left) and ratio of the width of the energy distribution (right).
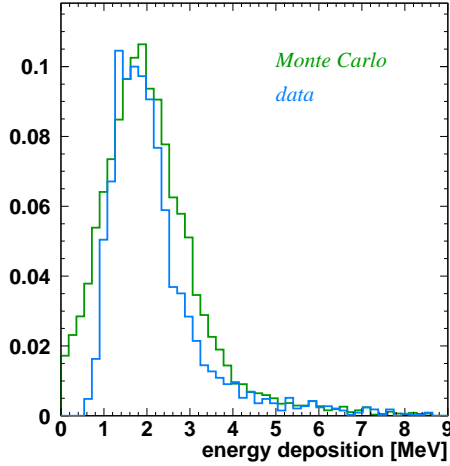
Figure 4.32: Comparison between energy-deposition spectra from experimental data and Monte-Carlo data for signals from negative pions with momenta above 0.5 GeV/c.

silicon-strip detector (gaps in between the different modules) and the bending of the negatively charged particles in the magnetic field. As explained further, the gains of strips 46–54 from the A layer are underestimated due to inefficiencies of the tracking detectors. This also partly affects strips 40–44 and 1–3 from the B layer and strips 27–35 from the C layer. As the value of μ_{ref} is common to all strips, but an individual gain factor for each group of strips belonging to the same PMT is implemented in the Monte-Carlo simulation, the effective smearing of the energy distribution is slightly different depending on the PMT. This is also visible in figure 4.31. On average, however, it is clear that the Monte-Carlo simulation underestimates the energy resolution of the photon detector.

Since the value $\sqrt{\mu_{ref}(\sigma_1{}^2 + Q_1{}^2)}$ is adjusted using σ_1 and Q_1 from a setup in which the one-photoelectron peak is visible, thus corresponding to a large value of Q_1, while in the current setup the real value of Q_1 is small (the one-photoelectron peak cannot be observed), the here determined value of μ_{ref} is underestimated. However, it is this quantity that encodes the energy resolution, while Q_1 only represents the gain of the PMT. Another factor that possibly contributes to an overestimation of the width stems from the light attenuation in the strips and wavelength-shifting fibers. Cosmic particles are distributed over the full length of the strips, while pions from experimental data are mainly hitting the downstream end of the photon detector, thus their signals are less affected by a variation in attenuation as a function of impact position.

Although the mean energy deposition in the Monte-Carlo simulation lies around 2 MeV, and the experimental signals are calibrated at 2 MeV, the ratio of the means, shown in figure 4.31, lies on average below 1. This can be understood with the help of figure 4.32, where
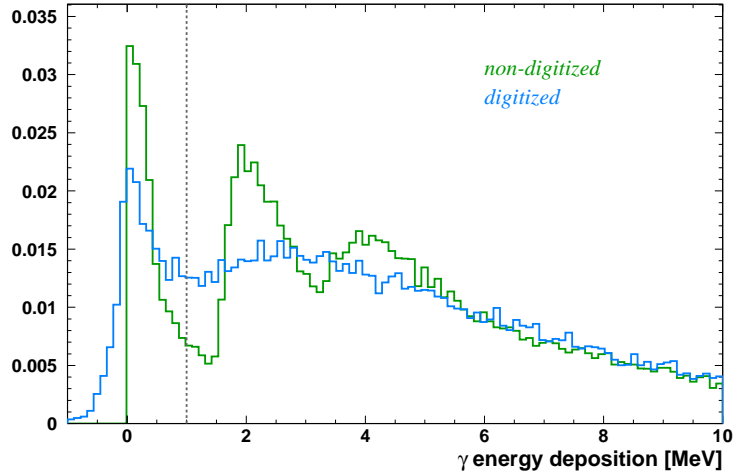
Figure 4.33: Comparison between the energy deposition from photons for a non-digitized and digitized Monte-Carlo simulation.

the energy depositions, normalized to path length, are shown down to 0 MeV[7] for experimental and simulated data. The mean values considered for figure 4.31 are calculated from the Landau-Gaussian convoluted functions fit to these energy distributions. For the calculation, values below 0 MeV are, however, disregarded. This is justified for experimental data. As can be seen in figure 4.32, the energy distribution for experimental data indeed converges to 0 at energy depositions equal to 0 MeV, while for the Monte-Carlo simulation, there is a non-negligible amount of entries below 0 MeV. This causes the mean of the Monte-Carlo spectrum to be effectively shifted towards higher values.

The experimental data shown here are based on a first calibration iteration, using signals recorded in terms of ADC values. This does not include yet any crosstalk contribution on PMT level. As will be shown, this correction is non-negligible and can contribute to an additional improvement of the energy resolution. The inclusion of the cross-talk contribution is possible in a next calibration iteration, based this time on energy depositions. Once this calibration is available, a tuning of the energy-deposition distribution of the Monte-Carlo simulation will subsequently be done, possibly including the effect of light attenuation in the strips and wavelenght-shifting fibers.

As it is not the aim of the photon detector to reconstruct energy depositions with high precision, the agreement between experimental and simulated data is sufficient at this stage. The overestimation of the width has an influence, however, when considering the number of detected particles per event. The number obtained from the Monte-Carlo simulation is underestimated. This is most important when studying the capability of the photon detector

---

[7]The data selection here does not allow to show energy depositions from experimental data truly down to 0 MeV, but this does not alter the argumentation. In section 4.8 an ADC spectrum and the fit function are depicted, which clearly show that around 0 MeV practically no entries are observed.

to reject events in which photons are present. However, since on average photons have a larger energy deposition than minimum-ionizing particles, the effect of the overestimated width is reduced. As an illustration, figure 4.33 depicts the energy deposition from π^0-decay photons for a digitized and non-digitized Monte-Carlo simulation. In the non-digitized Monte-Carlo simulation peaks stemming from the energy distribution from one electron or positron and an electron-positron pair are clearly visible, while in the digitized Monte-Carlo simulation they are not visible anymore. The first peak, corresponding to the energy deposited by very low-momentum electrons and positrons, emerging from the tungsten and stopped in the scintillator layer, is still visible in the digitized Monte-Carlo simulation, but less pronounced compared to the non-digitized simulation. The difference in number of entries above 1 MeV between the digitized and non-digitized Monte-Carlo simulations amounts to 2%. In a large fraction of events photons generate a signal in more than 1 layer, thus when examining the capability of the photon detector to reject events in which photons are present, the influence of the overestimation of the width is reduced to less than 2%.

4.4 Installation of and data taking with the photon detector

Preparations for the installation of the recoil detector started half November 2005. These included the removal of the atomic beam source, which provided a polarized hydrogen target, the insertion of an additional collimator, and the installation of a new, 25 cm shorter target cell. Beginning of February 2006 all adjustments and the installation of the recoil detector were completed. Data taking started less than three weeks later, with only the scintillating-fiber tracker operational. Data were collected by scattering an electron beam from an unpolarized hydrogen or deuterium target. A month later, however, the target cell was damaged, most likely due to a missing RF-coupling. A new target cell was installed, but sustained damage during its installation. Data taking with this target cell produced a huge amount of radiation in the neighborhood of the readout chips of the silicon-strip detector, which led to their damage. Subsequently, the silicon-strip detector had to be dismantled, involving a partial dismantling of the other two recoil-detector components, and repaired. In June of that year the recoil detector was re-installed, and data taking with a positron beam started. By August the timing of the photon detector was correctly adjusted, and in September also the fine tuning of the silicon-strip detector was completed. From this date on, data taking with the recoil detector went smoothly, with a 95% data-taking efficiency, until the shutdown of the storage ring on June 30, 2007. Over the period of these 10 months, a total of 28 M DIS events on hydrogen target and 7 M on deuterium target were collected with an operational recoil detector. The photon-detector commissioning and the analysis of DVCS events are based on this data sample.

During data taking the photon detector showed a very stable behavior and collected data with a 99.6% efficiency. The ADC signal from each of its strips was stored if its value lay above the respective mean pedestal value. As at the start of data taking a working tracking algorithm was not available, thus slightly complicating the monitoring of the photon detector, and as the load from the photon-detector output was small in comparison with that from the other recoil-detector components, it was considered desirable to set the threshold for the detector readout at the mean pedestal value. The raw ADC spectra of each strip were
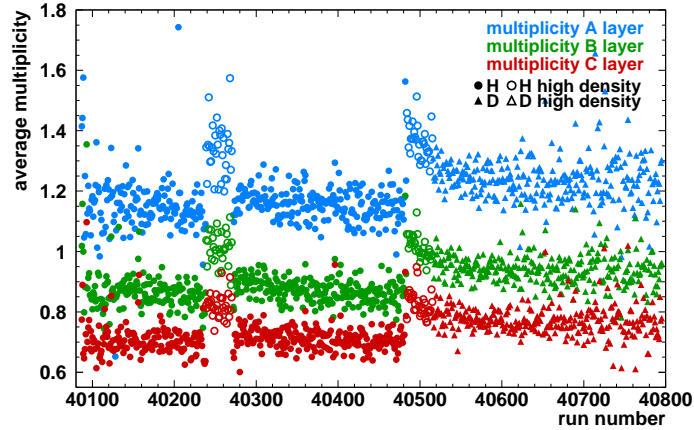
Figure 4.34: Hit multiplicity as a function of run number in each of the photon-detector layers.

controlled twice a day to check for a bad connection of cables or a possible change in pedestal or signal position. Additionally, the shift crew monitored the average number of entries for each strip, their average ADC value, and the number of hits per event in each detector layer over a 1–2 hour time period. Each 2–3 hours data taking was interrupted shortly to read out the pedestal signals from all recoil-detector components. After each fill, signals from the gain-monitoring system were collected. Finally, on a weekly basis, the hit multiplicity for DIS events, pedestal values and the signal from the gain-monitoring system were checked to detect effects varying slowly in time. An example of the hit multiplicity as a function of run number is shown in figure 4.34. As can be seen, the average hit multiplicity is low, and decreases towards the outer layer. A higher hit multiplicity is observed when collecting data on a deuterium target (filled triangles), or when the density of the injected gas is increased (open symbols) at the end of a fill.

4.5 Detection of elastically scattered protons

The first observed physics channel in the photon detector originates from elastically scattered protons. By requiring the detection of exactly one particle in the forward spectrometer, and selecting only those events for which this particle is a positron with sufficiently high momentum, the signal originating from the recoiling proton can be distinguished in the photon detector. This is illustrated in figure 4.35, which depicts the ADC spectrum of a photon-detector strip for various lepton momenta. For lepton momenta above 26 GeV/c, the proton signal becomes visible. A clearer signal can be obtained by imposing additional constraints on the azimuthal angle of the scattered lepton.

Figure 4.36 represents the azimuthal angle of the scattered lepton if the ADC value of the strip here under consideration is larger than 300. A peak, corresponding to elastically

Figure 4.35: ADC spectra of a photon-detector strip for various lepton momenta.

scattered leptons, is clearly visible. The gray vertical lines delimit the expected angular range covered by the scattered lepton, i.e., diametrically opposite to the range covered by the photon-detector strip in case of elastic scattering and without taking into account the bending of the proton in the recoil-detector magnetic field. Since the presence of the magnetic field needs to be taken into account as well as a possible misalignment between the photon detector and the spectrometer, events delimited by the red vertical lines are selected and considered to
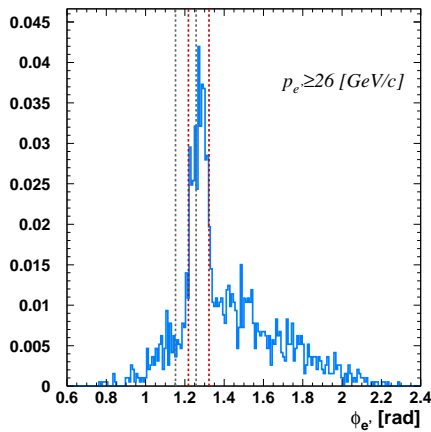
Figure 4.36: Azimuthal angle of the scattered lepton for ADC values above 300.
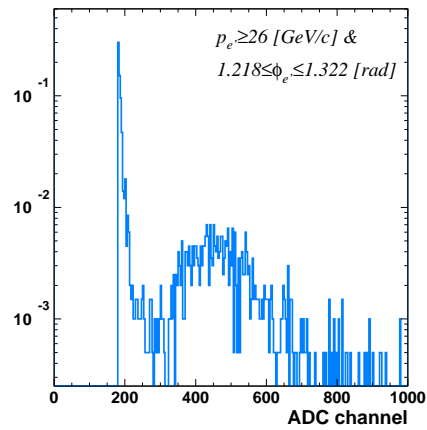
Figure 4.37: ADC spectrum of a photon-detector strip for lepton momenta above 26 GeV/c and restricted lepton azimuthal angle.

originate from elastic scattering. The ADC spectrum corresponding to this selection is shown in figure 4.37. The result is a cleaner signal from elastically scattered protons.

This detection of elastic protons showed for the first time that the events observed by the photon detector are in coincidence with the events observed by the forward spectrometer.

4.6 Alignment of the photon detector

The photon detector was in a first step aligned as a whole with respect to the recoil-detector magnet, prior to its installation in the experiment. While the photon detector was bolted to the magnet, it was possible to adjust its position, on the basis of two positioning marks located at its outer ends. This alignment was done with a precision on the order of 200 μm. Beginning of 2006, the magnet and the photon detector were installed as a single unit in the HERMES experiment. The magnet was then aligned with respect to the beam axis and the pump cross, with an accuracy of around 200 μm.

In a second step, once the correct position of the silicon-strip detector and the scintillating-fiber tracker were determined, the photon detector was aligned with respect to these two detector components, using reconstructed tracks from particles originating from the interaction of the positron beam with the proton target. The construction precision of the photon detector is claimed not better than 1 mm for the positioning of the individual strips and the relative alignment of the layers along the cylindrical surface, and not better than 0.5 mm for the radius of each layer [94]. Since also the analysis of data showed an unsatisfactory alignment of the photon detector, the following alignment procedure was opted for: first the orientation of each strip of the B and C layer is measured with respect to the beam line and averaged over all strips from the same layer; secondly the x and y coordinates of the center of each layer as well as the layers' azimuthal orientations are determined; finally the measurement of the strip orientation is repeated to check for a possible correlation between the two distinct alignment procedures.

For the alignment of the photon detector, the design value of the radius of each of its layers is assumed sufficiently accurate by construction. The photon detector is also assumed not to be inclined with respect to the beam axis. Considering the low θ resolution of the photon detector (see figure 4.10), the small amount of available space between the magnet and the scintillating-fiber tracker, the fixation of the photon detector to the magnet, and results from survey measurements, this assumption is reasonable. The survey measurements [95] have determined that the slope between the photon detector and the beam axis amounts to $0.264 \pm 0.001°$, a value far below the θ-resolution of the photon detector.

The determination of the position of the photon detector along the beam axis will be shown in the last section of this chapter. It concerns here not the determination of the exact position of the photon detector along the beam line, but rather an effective position tuned to optimize the rejection of events in which photons are present.

4.6.1 Measurement of the strip orientation

The strip orientation of the B and C layer is determined using tracks from negative pions, with momenta above 0.4 GeV/c. As described in subsection 4.1.5, the intersection of a parti-
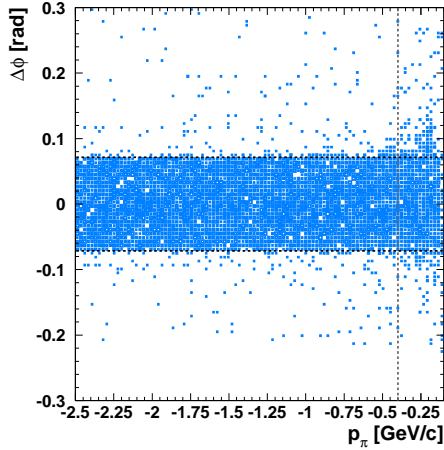
Figure 4.38: Difference between the azimuthal angle of a photon-detector strip and the angle determined from the reconstructed π^--track intersection as a function of the particle's momentum. The negative momentum values refer to the negative charge of the here considered particles.
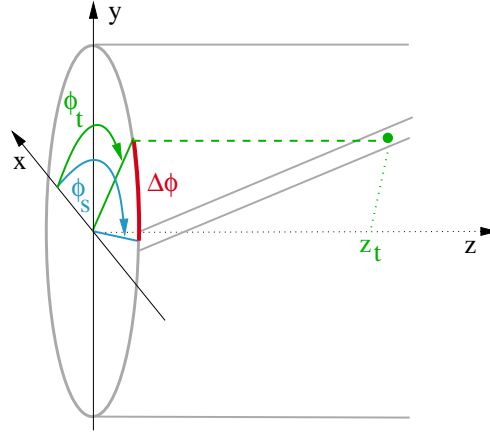
Figure 4.39: Illustration of the procedure for the measurement of the strip orientation.

cle's track with the photon detector, taking into account the presence of the magnetic field, can be determined with good precision. Figure 4.38 shows for negative pions in a Monte-Carlo simulation the difference in azimuthal angle between the center of a strip and the intersection point of a track with a photon-detector layer translated along the strip orientation to the upstream layer end, as a function of the particle's momentum. The horizontal dashed lines delimit the region covered by one strip. The data points are well confined in this region. However, as can be seen, for low momenta the hit-position determination is less accurate than for higher momenta. On the other hand, the amount of statistics decreases strongly with increasing pion momentum [8]. The combination of these two arguments leads to the selection of tracks with momenta larger than 0.4 GeV/c, indicated by the gray line in figure 4.38.

At the time the alignment of the photon detector was analyzed, the selection procedure for positive pions, using PID information from the other two recoil-detector components, did not generate enough statistics for the strips located in quadrant 2. As already stated, for negative pions no particle identification is needed, since the occurrence of other types of negatively charged particles is strongly suppressed. In addition, studies on a Monte-Carlo simulation did not show that the inclusion of data from positive pions leads to a significant improvement in accuracy for the measurement of the strip orientation. It was then decided that it is preferable

---

[8]This is not visible in figure 4.38, as the figure is produced with data from a Monte-Carlo background generator, but will be shown in the section describing the photon-detector calibration.
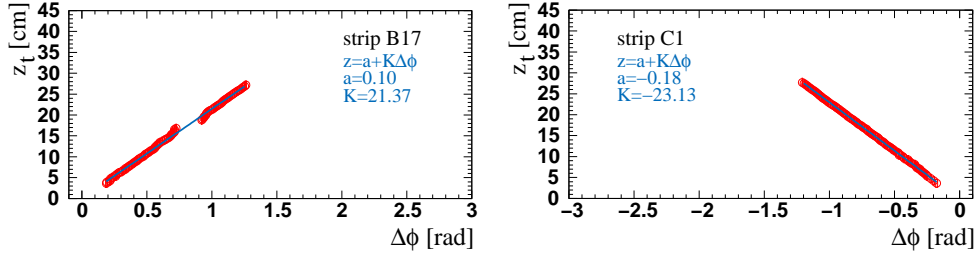
Figure 4.40: Fit of the distance z_t as a function of $\Delta\phi$ for a strip from the B layer (left) and a strip from the C layer (right).

to treat the photon detector in the same way, and thus only tracks from negative pions are used.

The procedure for the measurement of the strip orientation is illustrated in figure 4.39. The azimuthal angle, ϕ_t, and the distance along the beam line, z_t, of the intersection of a track with a photon-detector layer, represented by the green circle in figure 4.39, are calculated from the track parameters. The distance z_t is measured with respect to the upstream end of the photon-detector layer under consideration. The strip number corresponding to this intersection is also determined. In a subsequent step, the strip in the photon-detector layer with a signal 30σ above pedestal, closest to the track intersection, and within a distance of 3 strip pitches is searched for. The difference between the azimuthal angle of the center of this strip measured at the upstream end of the layer, ϕ_s, and ϕ_t is stored as $\Delta\phi$, together with the value of z_t. Finally, the length of the photon-detector layer along the beam line is divided into 100 bins, the $\Delta\phi$ distribution is projected in each of these bins, and the resulting data points are fit with a straight line $z_t = a + K\Delta\phi$. Ideally, the constant a should be equal to 0 cm. From the measured data, one obtains, after the alignment of the photon-detector layers, an averaged value of $a = -0.08 \pm 0.02$ cm for the B layer and $a = -0.11 \pm 0.08$ cm for the C layer. A value for a different from 0 cm can point to a misalignment of the layers along the beam line, a residual misalignment of the layers in azimuthal angle, or along the x and y axis. The misalignment in azimuthal angle or along the beam line does not influence the value of K, whereas for a displacement along x and y the situation is more intricate. However, regarding the latter case, the value of a is close enough to 0 cm for the present purpose.

An example of the fit procedure, applied to experimental data, is shown for a strip from the B layer (left) and a strip from the C layer (right) in figure 4.40. The absence of data points between 0.75 rad and 0.90 rad for the shown B-layer strip corresponds to the gap in between two modules of the silicon-strip detector. The acceptance gap artificially modifies the strip orientation in its neighborhood. Indeed, as in the lower z_t region in front of the acceptance gap, the strip half corresponding to $\phi_t > \phi_s$ is intersected by reconstructed tracks, while the other half, with $\phi_t < \phi_s$, is not, the $\Delta\phi$ value is biased towards lower values. Since at the other side of the gap a bias in the opposite direction is created, the effect of the acceptance gap is relatively well averaged out.

As for the determination of the strip intersected by the track, the strip orientation itself is used, an iterative procedure is needed. Initially, a value for the strip orientation K larger
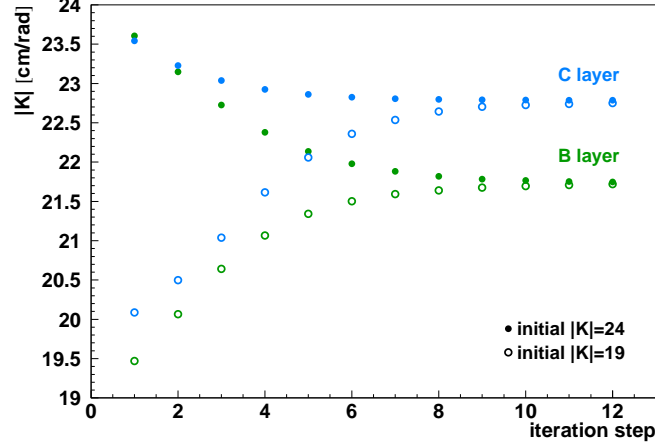
Figure 4.41: Obtained strip orientation K at each iteration step for the B (green) and C (blue) layer.

than the design value is chosen, and the above described procedure is applied to obtain a new value for K. This new value then serves as input for the next iteration step. This is repeated until the value of K converges. The same iteration procedure is executed a second time, but now choosing as initial input value for K a value smaller than the design value. Studies on Monte-Carlo data have shown that 12 iterations in each direction are largely sufficient for the strip-orientation value to converge. The difference in K value between the penultimate and ultimate iteration step is at most $2.7\ 10^{-3}$ cm/rad, corresponding to a difference in strip orientation of $\theta_s = 0.0035°$[9], a value far below the precision of the whole procedure itself. Studies on Monte-Carlo data have revealed a precision in determination of strip orientation better than $0.5°$: for the B layer an underestimation of $0.16°$ ($0.17°$) was observed for π^- (π^+), while for the C layer an overestimation of $0.41°$ ($0.35°$) for π^- (π^+) was observed. The results from the various iteration steps are depicted in figure 4.41 for experimental data. For one iteration the initial input value for $|K|$ was set to 19 cm/rad, while for the other iteration the initial value was set to 24 cm/rad. The data points do not converge as rapidly as in the Monte-Carlo simulation. However, the difference between the last and second last step, and the difference between the last step of both iterations do not exceed $0.05°$, which is certainly sufficiently accurate. The strip orientation values shown here are obtained after the alignment of the photon-detector layers. They amount to $45.64°$ for the B layer, compared to $44.58°$ according to the technical specifications, and $-46.24°$ for the C layer, compared to $-46.55°$ according to the technical specifications. The distribution of the strip orientation of all individual strips belonging to the same layer has a standard deviation of $0.5°$. The difference in measured values before and after the alignment of each layer amounts to $-0.054°$

---

[9]The relation between the strip orientation K, expressed in [cm/rad], and the strip orientation θ_s, expressed in [deg], is given by: $\tan\theta_s = R/K$, with R the radius of the layer under consideration.

for the B layer and $0.227°$ for the C layer, thus the strip-orientation measurement does not seem influenced by the alignment procedure of the individual detector layers.

4.6.2 Alignment of the photon-detector layers

For the alignment of the photon-detector layers three free parameters are adjusted: the position of the layer center along the x and y axis, and a rotation in azimuthal angle, ϕ. The alignment is based on tracks from pions with momenta larger than 0.4 GeV/c. Not only negatively charged pions are considered, but also positively charged pions. An example of PID distributions used for the identification of positively charged pions and their momentum dependence is shown in section 4.11. Monte-Carlo studies have shown that the difference in alignment parameters determined using positively charged pions and negatively charged pions does not exceed 0.035 cm in center position and $0.28°$ in ϕ; the same alignment procedure applied to data yields differences of 0.26 cm in center position and $0.73°$ in ϕ. Since for the alignment of the photon-detector layers it was possible to collect a sufficient amount of data with positive pions, it was considered desirable to use both pion types.

The alignment procedure is based on the minimization of χ^2, with:

$$\chi^2 = \sum_i \frac{(\phi_{s,i} - \phi_{tr,i}(x,y,\phi))^2}{\sigma^2},$$ (4.7)

where the sum runs over all events selected for the alignment procedure. The angle ϕ_s represents again the azimuthal angle of the strip center, measured at the upstream end of the layer under consideration. The angle $\phi_{tr}(x,y,\phi)$ represents the azimuthal angle of the intersection of a track with the layer under consideration translated to the upstream end of the layer in a direction parallel to the strip orientation; the variables (x,y) and ϕ represent the fit parameters, namely the center position and azimuthal orientation of the layer under consideration. The error σ is taken as the strip pitch divided by $\sqrt{12}$. The selection of events is again based on the search of the strip closest to the track intersection, within a distance of 3 strip pitches, and with ADC signal 30σ above pedestal.

layer	x [cm]	y [cm]	ϕ [deg]
A	0.15 ± 0.01	0.02 ± 0.01	-1.99 ± 0.02
B	0.32 ± 0.01	0.07 ± 0.01	-4.39 ± 0.02
C	-0.05 ± 0.01	0.39 ± 0.01	0.12 ± 0.02

Table 4.1: Alignment parameters of the photon-detector layers.

Tests on a Monte-Carlo simulation revealed the alignment procedure to be very stable, and to yield satisfying results. One test is based on the photon-detector layers centered around $(x,y) = (0,0)$ cm, while in another test the layers are offset in (x,y) by $(2,3)$ cm. In neither case a shift in azimuthal angle is introduced. The determined alignment parameters show a maximum deviation of 0.03 ± 0.01 cm[10] for the center position along an axis and

---

[10]observed for the B layer
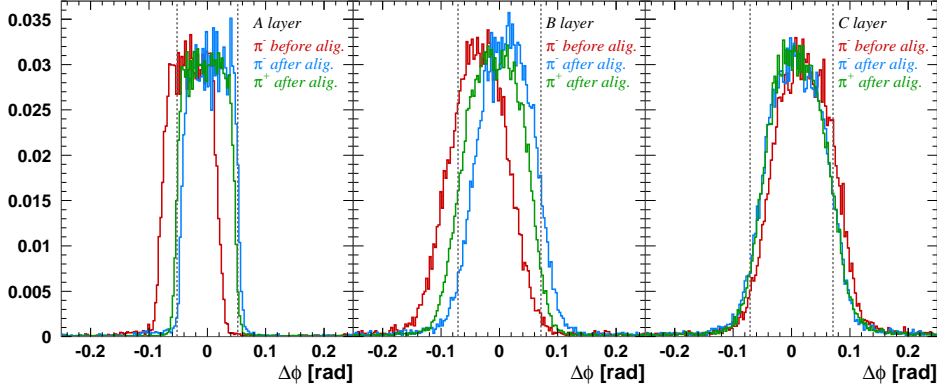
Figure 4.42: Distributions in $\Delta\phi$ before and after the alignment for the A layer (left), B layer (center), and C layer (right).

$0.16 \pm 0.02°^{11}$ for the orientation in ϕ.

The results, averaged over both pion charges, for the alignment of the photon-detector layers in the HERMES experiment are given in table 4.1. The values for each of the pion charges can be found in appendix A.

The effect of the whole alignment procedure is shown in figure 4.42 through the $\Delta\phi$ distribution, which represents the difference between the azimuthal angle of the strip center and the azimuthal angle of the track intercept translated along the strip orientation to the upstream end of the detector layer. The vertical dashed lines in the figure delimit one strip pitch. Before the alignment, the mean of the $\Delta\phi$ distribution for π^- amounts to $-1.69°$, $-2.01°$, and $1.17°$ for the A, B, and C layer respectively; after the alignment, the mean of the distribution for π^- (π^+) amounts to $0.24°$ ($-0.16°$), $0.55°(-0.50°)$, and $0.50°$ ($0.56°$) for the A, B, and C layer. The deviation from $0°$ is largest for the two outer layers. As the additional knowledge of the z-coordinate of the track intercept with the layer is needed for the B and C layer, and the track's polar angle and z-vertex position are known with less precision than the track's azimuthal angle, an additional bias can be introduced for the two outer layers. Moreover, the Monte-Carlo studies show that the strip orientation can not be determined better than $0.2°/0.4°$ for a perfectly aligned B/C layer, while the layer alignment is limited to $0.16°$ in ϕ and 0.03 cm in x and y for a precisely known strip orientation. A combination of these various factors can explain the magnitude of the observed shift for each of the three detector layers. This has to be supplemented with a small misalignment in θ of the detector with respect to the beam line and the non-homogeneity of the magnetic field, which is not taken into account. Although the above given arguments can explain the magnitude of the shift, they can not explain the difference in shift of the $\Delta\phi$ distribution between negatively and positively charged pions for the A and B layer. It can be understood, however, if the radii

---

[11] observed for the A layer
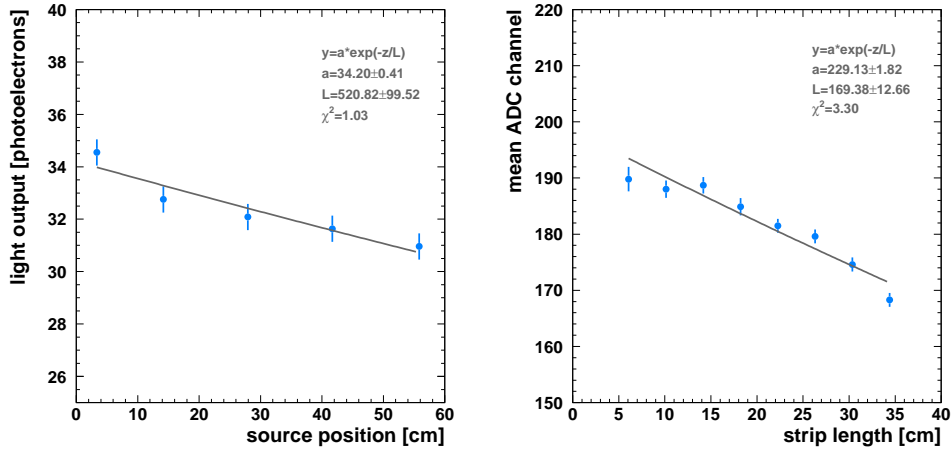
Figure 4.43: Measurements of the attenuation length of photon-detector strips with a ^{90}Sr source (left) and with signals from pions (right). The data points originating from the measurement with ^{90}Sr are reproduced from [70]; the errors on those data points are set to an artificially fixed value.

of both layers are underestimated. This of course also contributes to the magnitude of the shift. The inclusion of the layers' radii as free parameters in the layer-alignment procedure can reduce this shift. However, as the magnitude of the shift in either direction does not exceed the shift observed in the C layer, it was decided not to elaborate on this. The here obtained alignment results show a clear improvement at a level of accuracy in agreement with the accuracy needed for the photon detector.

4.7   Measurement of the strip attenuation length

The possibility to implement a correction for the attenuation of the scintillation light when it propagates through the strips and wavelenght-shifting fibers has been examined. As explained in section 4.1.2, the light signal created in a strip by the passage of a charged particle is attenuated more if the particle crosses the strip at a distance far from its readout end than when the particle crosses the strip close to its readout end. Knowing the z coordinate of the intersection of a particle with a photon-detector strip, it is in principle possible to correct for the attenuation of the light. The decrease in light amplitude along its travel distance, z, is described by $ae^{-z/L}$, where a represents the light amplitude at its point of origin, and L the attenuation length. Measurements of the combined attenuation length of a strip and its two wavelength-shifting fibers were performed with a ^{90}Sr source [70]. The source was placed at various positions along the strip, and the corresponding output signal was read out. The result of the measurement is shown in figure 4.43 (left) together with the fit of the function $ae^{-z/L}$. Although nothing guarantees a simple exponential behavior, since the measured configuration
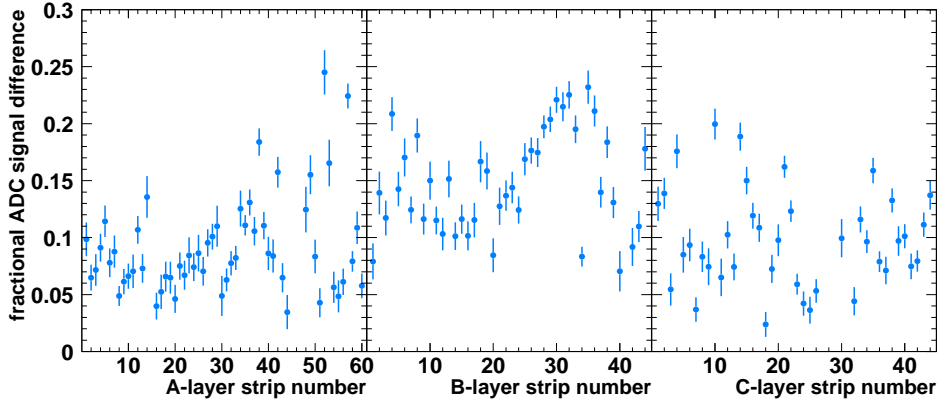
Figure 4.44: Fractional difference between the highest and lowest observed ADC signal for the A (left), B (center), and C layer (right).

consists of the combination of a strip and two wavelength-shifting fibers, and measurements of the attenuation length of a single wavelength-shifting fiber showed an increase in light output for a source placed at the fiber's end due to the mirroring of its extremity [70], the fit result shows that indeed the exponential fit function describes the data reasonably well.

To obtain the attenuation length of each of the individual photon-detector strips, measurements with pions, originating from the positron-proton interaction, are performed. Only pions within the restricted momentum range 0.45 GeV/c to 0.55 GeV/c are selected, and the ADC signal is analyzed as a function of the position of the pion's intersection with the strip. To this purpose, the strip length is divided into 10 bins, which corresponds to a bin width of 2.75 cm, 4.05 cm, and 4.09 cm for the A, B, and C layer, respectively. The first and last bin are not included in the analysis to avoid the influence of edge effects. The mean ADC signal, above pedestal, as a function of strip length is shown in figure 4.43 (right) for a photon-detector strip. The depicted measurement is representative for $\sim 20\%$ of the strips, while for the remaining 80% of the strips no exponential behavior is observed. The deviation from the expected behavior can be explained by the quality of the connection between the strip and the wavelength-shifting fibers.

In order to determine the importance of the correction for light attenuation, the difference between the highest and lowest ADC value, divided by the average ADC value, is examined for each strip. This fractional difference is shown in figure 4.44 for each of the three photon-detector layers. As the average fractional difference amounts to 11.1%, and the energy resolution of the photon detector is not crucial for protons and pions, while it is intrinsically low for photons, it was decided not to correct the output signals for the light attenuation in first instance.
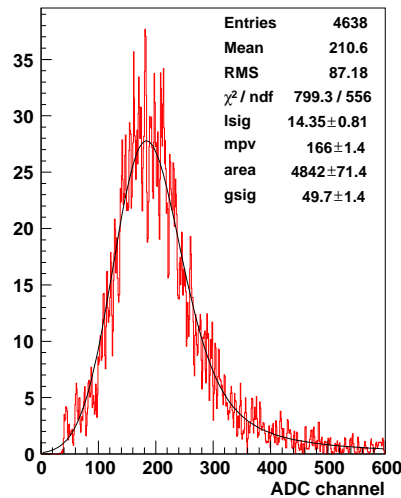
Figure 4.45: ADC spectrum for energy depositions by minimum-ionizing particles.

4.8 Calibration of the photon detector

The calibration of the photon detector is based on signals from charged pions. As already stated, pions in the energy range at which they are observed at the HERMES experiment mainly lose energy through collisional losses, i.e., through the excitation and ionization of the atomic electrons of the medium. The pions hereby undergo a large number of independent collisions wherein different amounts of kinetic energy can be transferred to the atomic electrons. Most of the time they lose a small fraction of their energy, although also collisions in which a larger amount of energy is lost are possible, yet less frequent. This way of interacting with the surrounding material results in an energy-deposition spectrum described by a Landau distribution: most of the energy depositions are small, but occasionally a collision involving a large amount of deposited energy is possible, leading to a long tail at higher energies.

However, as explained in section 4.3, several factors contribute to a decrease in resolution of the measured energy deposition. Since these factors are Gaussian distributed, the resulting energy-deposition spectrum is correctly described by a Landau-Gaussian convoluted function. A typical example of such an energy spectrum, together with the Landau-Gaussian convoluted fit function, is shown in figure 4.45, in units of ADC channels, for signals generated in a photon-detector strip.

The mean excitation and ionization energy loss per path length by heavy charged particles is well described by the Bethe–Bloch formula [71]. An instructive review of all factors contributing to the correct description of the energy-loss distribution can be found in [96]. Although the formula describes the energy-loss rate accurately, within a few percent, it can not be used directly for calibration. Indeed, the formula quantifies the energy loss, but not the energy deposition. These two quantities differ from each other, because of the occurrence of collisions in which an atomic electron receives a large amount of energy and subsequently

escapes the detector volume without depositing all of its energy. The Bethe–Bloch function can be modified to describe the energy deposition in the detector correctly, but this implies the tuning of an additional parameter, unique to each detector[12], and thus does not offer the ideal solution. Additionally, the mean energy deposition represents another inconvenience, mostly relevant for (very) thin detectors. As the mean of the energy distribution is weighted by very rare events with large single-collision energy deposits, a sufficiently large amount of data has to be collected in order to obtain a stable and reliable value for the mean. All these considerations do not affect the determination of the most probable energy-deposition, and thus lead to the conclusion that it is preferable to use the most probable value of the Landau distribution, obtained from the fit with the Landau-Gaussian convoluted function, instead of the mean value of this fit function.

The most probable energy deposition of a charged particle crossing a medium can be calculated using a modified version of Landau's equation [97, 98]. The formula for the calculation of the most probable energy deposition can be found in appendix B. The used formula is valid for[13]:

$$0.084\,x\,\frac{1-\beta^2}{\beta^4} < 0.01, \tag{4.8}$$

with x being the distance traveled by the particle inside the medium and β the relativistic speed. For a charged pion with momentum $\vec{p}$, and crossing the photon-detector strips under an angle of 1.13 rad, we obtain the following values for the left-hand side of equation 4.8: 0.067 for $|\vec{p}| = 200$ MeV/c, 0.024 for $|\vec{p}| = 300$ MeV/c, 0.013 for $|\vec{p}| = 400$ MeV/c, and 0.0078 for $|\vec{p}| = 500$ MeV/c. Thus, for low-momentum pions we exceed the limit of validity for the calculation of the most probable energy deposition.

In order to check the possibility to calibrate the photon detector using the most probable value, the accuracy of its determination is first evaluated on data from a Monte-Carlo simulation. The extracted most probable energy deposition in the A layer is shown in figure 4.46 as a function of the pion momentum, together with the corresponding theoretical value. In order to be insensitive to the dependence of the most probable energy deposition on the pion's path length inside the photon-detector strips, the results are extracted for a limited range in the pion's polar angle, namely between 1.07 and 1.19 rad (corresponding to a relative variation in path length of 6%). As can be seen in the figure, the agreement between the most probable value from theory, represented by the dark-blue symbols, and from a Monte-Carlo simulation in which the digitization of the photon detector is not simulated, represented by the blue and gray closed symbols, is very good. Even at lower momenta the agreement is reasonable for the data points represented in blue, while for the data points represented in gray, the agreement stays excellent. The difference between the blue and gray data points is related to the presence of tungsten in front of the scintillating layer, as will be explained below. However, for the values represented by the green closed symbols, corresponding to a Monte-Carlo simulation in which the photon detector is digitized, i.e., in which the decrease in energy resolution is simulated, the discrepancy with theory is large. The explanation for this is to be found in the Gaussian distribution that enters the convolution integral. The fit

---

[12]The parameter depends of course on the geometry and material of the detector, but also on the track- or cluster-reconstruction algorithm that determines which signals should be considered to originate from the same or a different particle.

[13]See appendix B.
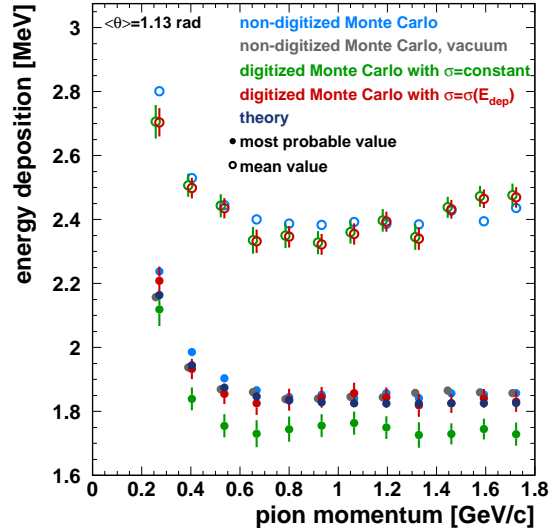
Figure 4.46: Monte-Carlo simulation of the most probable and mean energy deposition of pions in the photon-detector strips as a function of momentum. For reasons of clarity, the gray and open green symbols are slightly offset.

parameter σ of the Gaussian is here taken as constant. However, as explained in section 4.3, the energy deposition is smeared according to a Gaussian distribution with width proportional to $\sqrt{E_{dep}}$, where E_{dep} represents the energy deposited by the traversing particle. Replacing in the convolution integral σ by $\sigma'\sqrt{E_\mu}$, where E_μ represents the mean of the Gaussian, results in a correct extraction of the most probable value. The obtained result is also shown in figure 4.46 (red closed symbols). A more precise approach consists in replacing the parameter σ by $\sigma'\sqrt{E_\mu} + \sigma''$, where the first term accounts for the decrease in energy resolution related to the variation in number of photoelectrons collected in the photomultiplier, and the second term accounts for the decrease in resolution due to noise, as reflected by the pedestal. This last factor is also simulated in the Monte-Carlo simulation, but is negligible compared to the energy-dependent term, and thus its omission does not affect the extracted most probable value.

Also shown in figure 4.46 are the mean values obtained for the various Monte-Carlo simulations and parametrizations of σ. The mean value does not appear as a parameter of the Landau-Gaussian convoluted function, as the mean of the Landau distribution is not defined: the tail extends to infinity. Of course, for signals in detectors generated by particles, there is an upper limit given by the energy of the incident particle. The here shown mean values are calculated from the obtained fit function in the energy range 0 MeV to 9 MeV. For the digitized Monte Carlo, since the smearing procedure extends the energy depositions down to negative values (see figure 4.32), the lower boundary is extended to -2 MeV. As can be
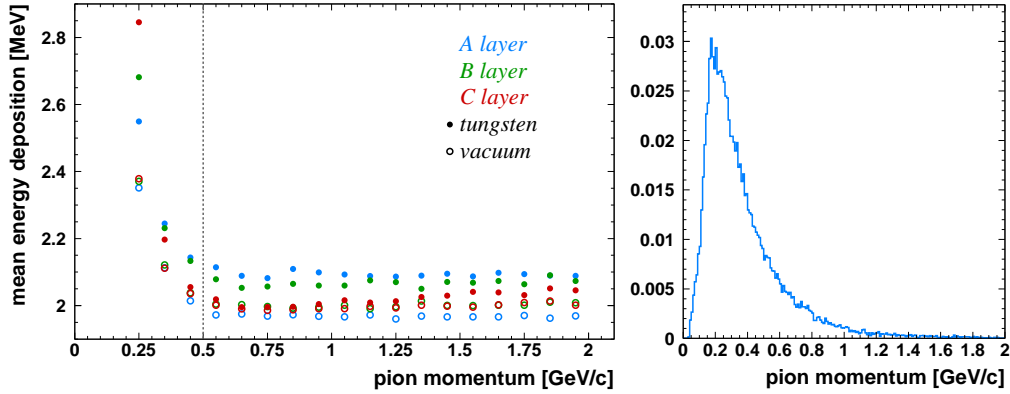
Figure 4.47: Mean energy deposition of pions in the photon detector as a function of momentum (left). Pion momentum distribution (right).

seen in figure 4.46, the value of the mean is not influenced by the choice of σ. The difference between the extracted mean value and the mean value of the energy-deposition spectrum amounts to less than 1% for the non-digitized Monte-Carlo simulation and to $\sim 1\%$ for the digitized Monte-Carlo simulation.

The extraction of the most probable value is a relatively elaborate procedure. This, in combination with the ignorance of the accuracy of the Monte-Carlo digitization at the time the calibration procedure was implemented and the fact that a good energy resolution is not crucial for the photon detector, led to the choice of the mean value, over the most probable value, as the calibration point for the first calibration iteration.

The mean energy deposited by minimum-ionizing particles in the BC-408 scintillating strips lies between 1.8 and 2.0 MeV/cm [100]. Pions with momenta around 0.6 GeV/c are minimum-ionizing particles in the scintillating plastic [71]. Since pions reaching the photon-detector strips first cross the inner recoil-detector components and, more importantly, tungsten, a dense material in which the rate of energy loss is large, their energy deposition can be different from the value quoted in reference [100]. The appropriate value for the energy deposition is therefore first examined on Monte-Carlo data. The mean energy deposited by pions, normalized to a path length of 1 cm, is shown in figure 4.47 (left) as a function of their momentum. The open symbols represent the mean value for the case that the tungsten layers are replaced by vacuum, while the closed symbols correspond to the correct description of the photon detector. The pions do indeed behave as minimum-ionizing particles in the above-mentioned momentum range for the case that no tungsten is present. For higher-momentum pions the energy deposition is relatively constant and equal to the energy deposited by lower momentum pions, while the Bethe–Bloch formula predicts an increase in energy loss. This observation is related to the creation of high-energy electrons that escape the detector strips without depositing all of their energy, as mentioned previously. The energy deposition in the A layer in the absence of tungsten lies between 1.8 and 2 MeV, as cited in [100]. For the subsequent layers, the mean energy deposition is systematically higher, since particles cre-
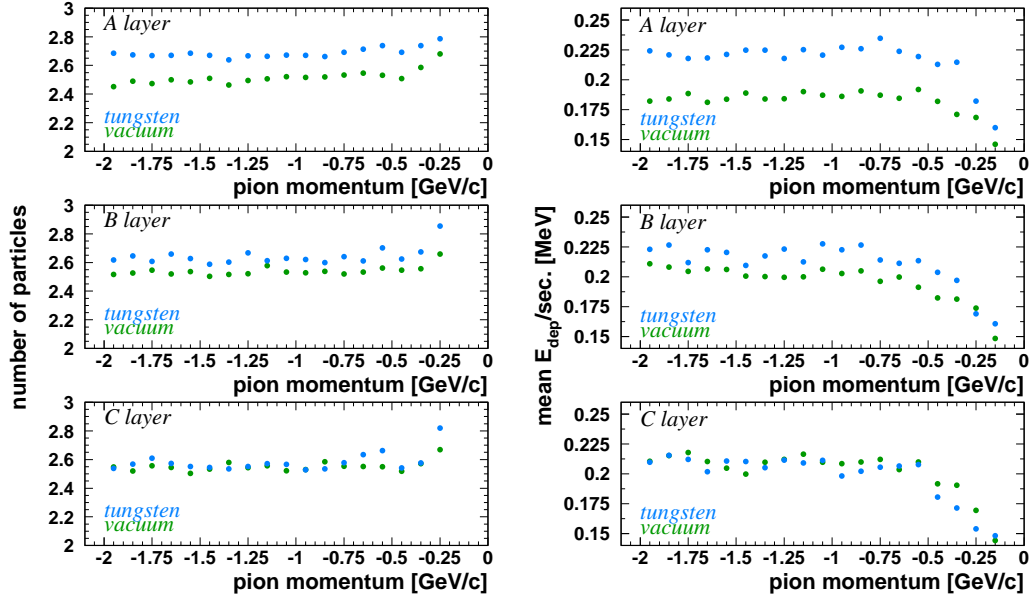
Figure 4.48: Number of particles, with kinetic energy above 100 keV, detected in each of the photon-detector layers (left), and average energy deposited per secondary particle in the photon-detector scintillators (right). The negative values of the pion momentum reflect the negative charge of the here considered pions.

ated in a lower-lying layer can escape this layer and deposit their energy in the next layer(s). This is indeed observed in figure 4.48, which displays the total number of particles[14], i.e., the traversing pion and the secondary particles it generates, present in the scintillating material as a function of the pion momentum, for each of the three layers. Also shown is the average energy deposited by the secondary particles. The vast majority of these secondary particles are ionized atomic electrons with an average energy of ~ 0.5 MeV. Most of them are created and stopped inside the scintillating material, and only a small fraction is created outside the scintillating strips. However, the number of particles belonging to this last category is larger in the presence of tungsten. This is especially the case for the A layer, preceded by a 6 mm thick tungsten layer. While these secondary particles do influence the mean energy deposited in the A layer, they do not influence the value of the most probable energy deposition for momenta above 0.6 GeV/c, as can be seen in figure 4.46. For the B layer, the 3 mm thick tungsten layer has less influence compared to the situation where only scintillating material is present, as secondary particles originating from the A layer are stopped inside the tungsten layer, and only newly created electrons inside this tungsten layer can influence the signal observed in the B layer. For the C layer, both configurations even out for pions with momenta above ~ 0.5 GeV/c. The pion momentum itself is not largely affected by the presence of the

---

[14]with kinetic energy above the 100 keV threshold implemented in the Monte-Carlo simulation, see section 4.3
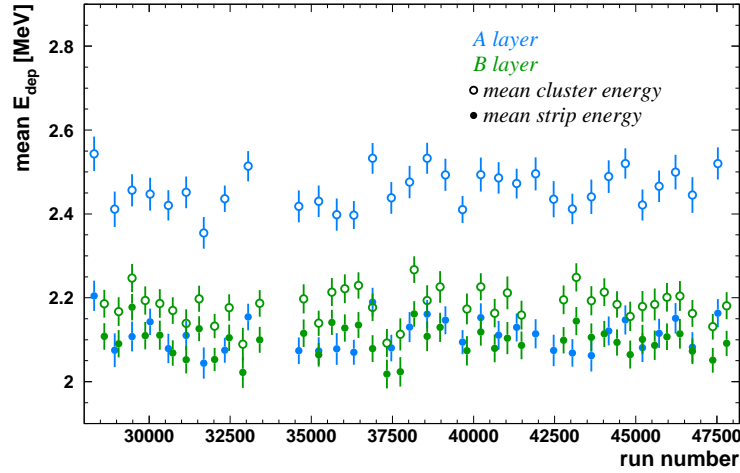
Figure 4.49: Mean energy deposition of pions with momenta above 0.5 GeV/c, after the calibration of the photon detector.

inner-lying material: the difference in momentum before the pion enters the photon detector and when it reaches the C layer amounts to 40 MeV/c in the case that tungsten is present and to 5 MeV/c in the case that no tungsten is present.

From the above considerations, and based on the momentum distribution of pions, which is mostly centered around low values (see figure 4.47, right), pions with momenta above 0.5 GeV/c are selected for the calibration of the photon detector, and their mean energy deposition is set to 2.1 MeV/cm for all three layers.

Pions selected for the calibration procedure are required to leave a signal in each of the modules of the silicon-strip detector and of the scintillating-fiber tracker in order to obtain a well reconstructed track. This condition is relaxed for tracks from quadrant 2, as in this quadrant both the silicon-strip detector and the scintillating-fiber tracker suffer from a substantial amount of dead channels or channels with a low detection efficiency. Signals generated by positively and negatively charged pions are used, as a combination of the track selection, the bending of the particles in the magnetic field and the gap in between two silicon modules causes photon-detector strips centered around this gap to only receive signals from pions of one charge. The selected tracks provided, at the time of the implementation of the calibration, useful signals in three of the four recoil-detector quadrants. For quadrant 2, however, pions with momenta above 0.5 GeV/c generated a larger signal than pions with lower momenta, and additionally the shape of the energy-deposition distribution seemed distorted. It was decided that reconstructed particles with momenta above 0.5 GeV/c could not be trusted for this quadrant, and that instead pions with momenta between 0.3 and 0.5 GeV/c should be used. The signals in the other three quadrants originating from pions with momenta in the range 0.3–0.5 GeV/c and above 0.5 GeV/c were compared and the ratio of their mean used as a scale factor that was applied to the signals from quadrant 2. After the finalization of the new
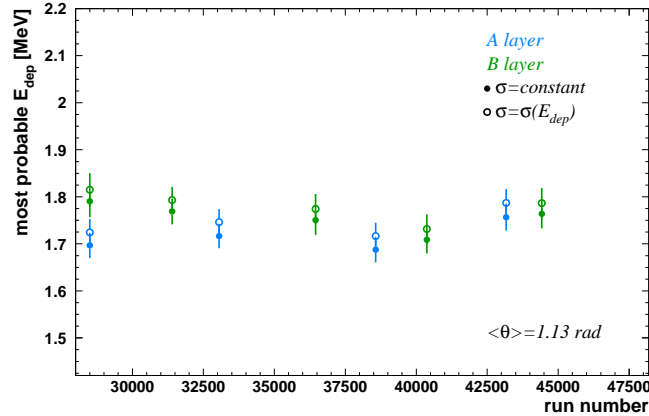
Figure 4.50: Most probable energy deposition of pions with momenta above 0.5 GeV/c, after the calibration of the photon detector.

data production, which includes the new photon-detector calibration and an improved track reconstruction, the result of the photon-detector calibration can be evaluated. The newly calibrated data show a stable energy-deposition signal over time, with a mean at 2.1 MeV/cm for all strips outside quadrant 2. An example of the mean energy deposition, normalized to path length, as a function of run number is shown in figure 4.49, represented by the closed symbols, for a strip from the A (blue) and B (green) layer. For strips in quadrant 2, the mean deposited energy lies 25% lower. An equal mean energy deposition is also observed when analyzing signals from cosmic particles, of which the selection only involves the photon detector. Since both independent methods provide the same result, it can be concluded that for the new data production the reconstruction of tracks in quadrant 2 is reliable, while for the previous data production it is inaccurate. A new calibration iteration will thus result in a correctly calibrated quadrant 2.

Another reason for a new calibration iteration is related to the clustering algorithm on PMT level, as explained in subsection 4.1.5. The clustering algorithm provides a correction for light leakage on the PMT cathode. Depending on the amount of crosstalk, this correction can be more or less substantial. The mean energy deposition corrected for crosstalk is also shown in figure 4.49, represented by the open symbols. As can be seen, for certain strips the crosstalk is small, but for other strips, as is the case for the here shown A-layer strip, the crosstalk correction contributes to an increase in signal by 15%. The signals corrected for crosstalk will be used as input in the next calibration iteration.

Finally, the most probable energy deposition is shown in figure 4.50 for pions with polar angle between 1.07 and 1.19 rad. The shown values are once obtained with a constant σ for the Gaussian distribution, and once with an energy-dependent σ. The resulting values are lower than those extracted from the Monte-Carlo simulation and the theoretical calculation. Contrary to the Monte-Carlo simulation, for which the smearing of the energy distribution is overestimated, a constant term might also be of importance to correctly describe the experi-

mental data, thus taking $\sigma = \sigma' \sqrt{E_\mu} + \sigma''$. Currently, this is not taken into account.

4.9 Possibility for particle identification.
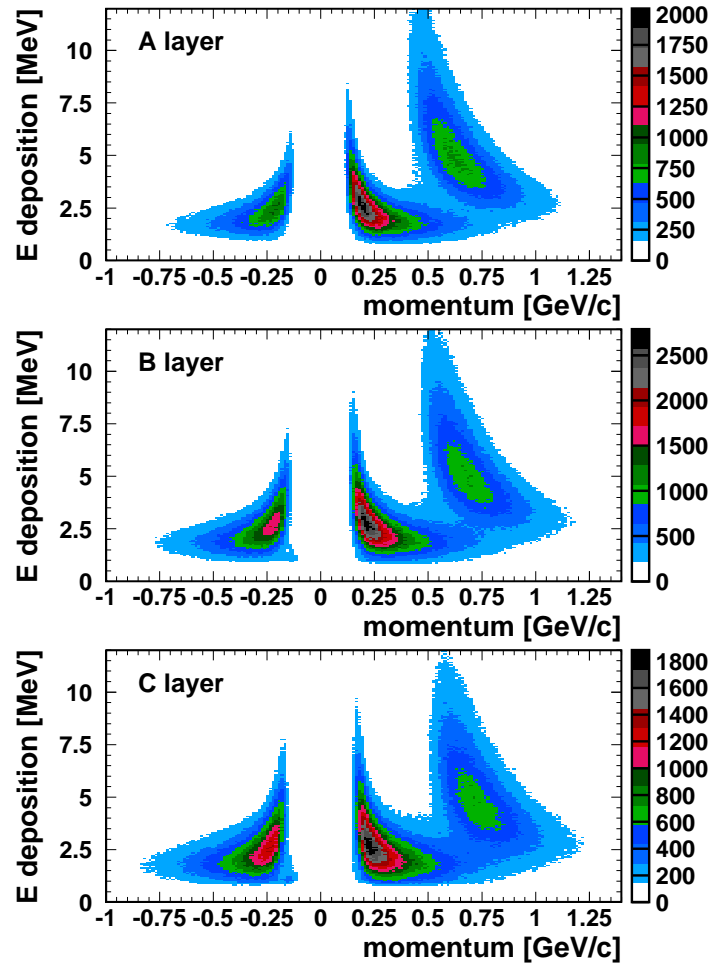
Figure 4.51: Energy deposition as a function of momentum in a quadrant of the A layer (top), B layer (center), and C layer (bottom).

With the photon detector calibrated, its ability to discriminate pions and protons produced in the HERMES experiment can be investigated. Figure 4.51 shows the energy deposition, normalized to path length, in a quadrant of the A, B, and C layer as a function of the momen-

83
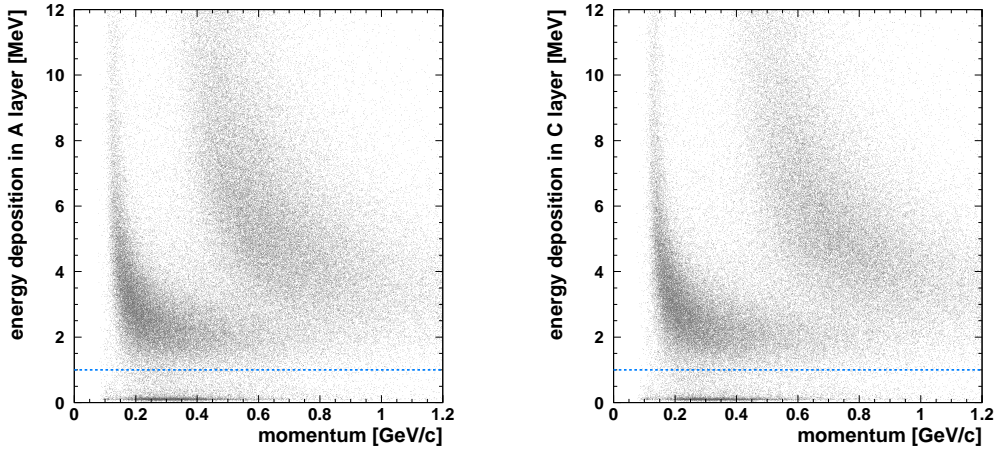
Figure 4.52: Energy deposition, not normalized to path length, as a function of momentum in a quadrant of the A layer (left) and C layer (right). The B layer shows a behavior similar to the A and C layer. The blue line represents the 1 MeV threshold.

tum of the detected particles. On the left-hand side of the figure, the signals from negative pions can be distinguished, and on the right-hand side, protons, corresponding to the higher energy signals, and pions are visible. The silicon-strip detector is able to separate protons from pions for momenta up to 0.70 GeV/c, and the scintillating-fiber tracker is effective for momenta up to 0.55 GeV/c. From figure 4.51 one can see that the photon detector can contribute to particle identification for momenta up to 0.7 GeV/c, with a lower momentum-threshold for the detection of protons at around 0.45 GeV/c for the A layer, 0.5 GeV/c for the B layer, and 0.55 GeV/c for the C layer. The separation between protons and pions becomes, however, less pronounced for the outer layers; this is especially true for the C layer. Nevertheless, all three layers are useful for particle identification in the momentum range not covered by the scintillating-fiber tracker.

4.10 Determination of the energy-deposition threshold

A series of studies on the noise level in the photon detector were performed by analyzing the hit multiplicity in the detector for events collected using a randomly generated trigger with several configurations for the lepton beam and target cell [101]. A first set of data were collected with an empty target cell and in the absence of the lepton beam, but with the HERA proton beam passing through the HERMES spectrometer. A second set of measurements were performed with an empty target cell and both the proton and lepton beam passing through the experiment. Finally, for the third set of measurements, the target cell was filled with hydrogen and both beams were circulating through the accelerator. The magnitude of the lepton-beam current was not the same for all measurements. The measured hit multi-
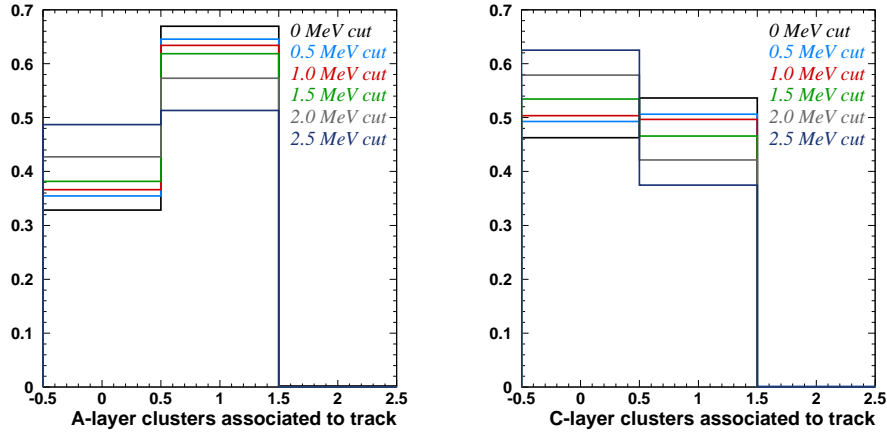
Figure 4.53: Number of A-layer (left) and C-layer (right) clusters, above the cited threshold, associated with a track. The results for the B layer are similar to the results for the A and C layer.

plicity is lowest, but not negligible, when only protons are passing through the HERMES experiment[15]. The noise level measured with an empty target cell and a lepton-beam current of 35 mA equals the noise level measured with a filled target cell and a beam current of 28 mA, and lies 40% higher than the noise level measured with a filled target cell and a beam current of 15 mA. Also follows from these measurements that a minimum threshold of 3.5–4.0 σ above pedestal, with σ the pedestal width, is required for the selection of clean signals, leading to a hit multiplicity of less than 0.1 'noise' hits per event in a layer. For the most noisy strips, this cut corresponds to a minimal energy-deposition threshold of 0.5 MeV. Analogous conclusions can be drawn from figure 4.52, which shows for the inner and outer photon-detector layers the energy deposition as a function of particle momentum, but contrary to what is shown in figure 4.51, uncorrected for angle of incidence and with a lower threshold of 2σ above pedestal.

In order to quantify the influence of an energy-deposition threshold, the number of clusters, with energy above this threshold, associated with a track is examined for events in which the scattered lepton is observed in the spectrometer. The results are shown in figure 4.53 for the A and C layer. The difference in number of clusters between a 0.5 MeV and a 1.0 MeV threshold only amounts to 2%. Since at the time the study was performed, the quality of the data was not well understood, especially the behavior in quadrant 2, a rather conservative energy threshold of 1 MeV was opted for[16].

---

[15]When looking at the photon-detector output with an oscilloscope for an empty target cell and in the absence of a lepton beam, the presence of a passing proton bunch was clearly visible. The collection of data with the gain-monitoring system was also not possible in the presence of protons in the beam line, and thus only took place in between fills.

[16]Subsequently a new xtc and μDST production were completed, including also changes to the track-reconstruction and particle-identification algorithms. Results based on these productions are shown in sections 4.6

To determine the effect of the energy threshold on the detection of photons, a study on Monte-Carlo data is performed. The data are generated with the pythia and gmc_dvcs generators, and only photons originating from the decay of neutral pions are analyzed. From the photons interacting in the photon-detector material 3.6% (4.7%) are lost for data generated with gmc_dvcs (pythia) when a lower threshold of 0.5 MeV is applied on cluster level, while the 1 MeV threshold corresponds to a loss of 6.6% (8.5%) of the photons. In view of the main design goal of the photon detector, namely the rejection of events in which a π^0-decay photon is present, the more important quantity to analyze is the number of events in which no photon at all is detected. Compared to the absence of a lower threshold, a 0.5 MeV cut increases the number of these events by 2.2% (3.5%), while a 1 MeV threshold increases the number of these events by 3.9% (6.3%). The here quoted numbers are slightly overestimated, however, since the Monte-Carlo simulation underestimates the photon-detector energy resolution.

4.11 Efficiency of the photon detector

The efficiency of the photon-detector strips in detecting signals from pions and protons is presented in the following. For its determination, the intersection of a reconstructed track with each of the photon-detector layers is calculated first. Subsequently, if in the two photon-detector layers not under study a signal within a distance of 1.5 strip pitches from the track intercept is observed, the remaining layer is examined. In case this layer contains a cluster that is not more than 1.5 strip pitches away from the intersection point of the track, the strip corresponding to this intersection point is considered efficient; in the opposite case the strip is considered inefficient. The presented efficiencies are extracted on cluster level, thus affected by the 1 MeV threshold and the PMT-clustering routine.

The tracks selected for the study of the photon-detector efficiency are required to be reconstructed from 2 space points in the silicon-strip detector and 2 space points in the scintillating-fiber tracker, in order to suppress the presence of erroneously reconstructed tracks. This condition is released for tracks originating from quadrant 2. Here, a space point in the outer layer of the scintillating-fiber tracker is not mandatory, since this part of the detector is inefficient. Although the n-side strips of both outer silicon-strip-detector sensors from this quadrant are also broken, the p-side strips still generate a useful signal, forming a space point that provides a loose constraint for the track reconstruction. The selected tracks are in addition only considered if their intersection point with the photon-detector layers lies more than 2.5 strip pitches away from the intersection points of other possibly reconstructed tracks. This condition aims at a further reduction of incorrectly reconstructed tracks. For tracks identified as pions, the momentum is required to lie between 0.2 GeV/c and 0.7 GeV/c, where the choice for the lower-momentum boundary is dictated by the limited penetration of pions in the tungsten layers, and the upper-momentum boundary arises from the limitation in particle identification. The momentum range for protons is restricted to 0.5 GeV/c–0.7 GeV/c, since lower-momentum protons do not reach the (outer) photon-detector layers.

In order to identify positively charged pions and protons, the PID values provided for each of the subcomponents of the recoil tracking detectors are used. The sum of these PID values is shown in figure 4.54 for tracks from quadrant 3, for experimental data collected

(figure 4.42), 4.8, 4.9, 4.11 and the following chapter.
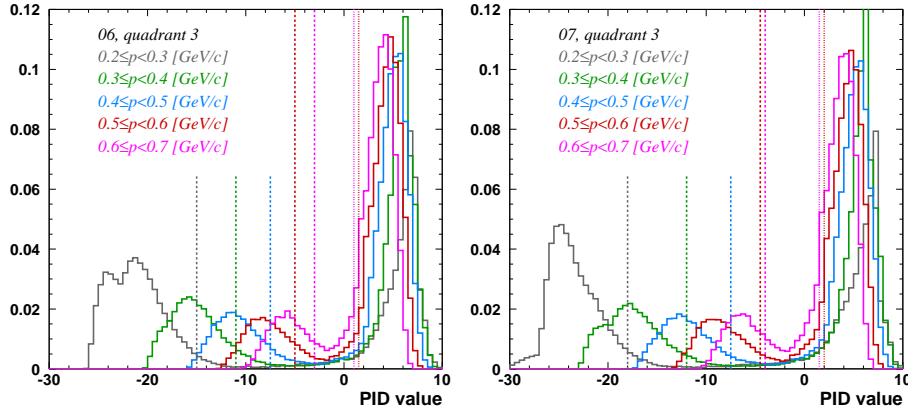
Figure 4.54: PID distributions from data collected in 2006 (left) and 2007 (right), subdivided in various momentum intervals for positive particles detected in quadrant 3. PID values located on the left (right) of the dashed (dotted) vertical lines correspond to the selection of pions (protons).

in 2006 (left) and in 2007 (right). Positive PID values correspond to protons; negative PID values are most representative for positively charged pions. The PID values are presented for 5 momentum intervals, ranging, in subdivisions of 100 MeV, from momenta of 0.2 GeV/c to 0.7 GeV/c. A strong momentum dependence can be observed together with small differences between the two years of data taking. Not shown here is the presence of a quadrant dependence. The minimum of the PID distribution is expected to be centered around zero if the same amount of protons and pions are detected, as is approximately fulfilled, e.g., for the momentum range between 0.2 GeV/c and 0.3 GeV/c. In the here presented distributions the minimum is, however, located at negative values. The reason for this shift is at present unknown. A reconstructed positively charged particle is identified as a pion if its PID value lies below the momentum-dependent value indicated by the dashed vertical line in figure 4.54. Particles with PID values above the value indicated by the dotted lines are considered to be protons. The cuts on the PID values are adjusted for each quadrant individually.

The time dependence of the efficiency of the photon-detector A-layer strips is shown in figure 4.55 for negatively charged pions with momenta between 0.6 GeV/c and 0.7 GeV/c. The data collected in 2006 are subdivided into 2 time periods; the data collected in 2007 are subdivided into 4 time periods. The efficiency shows a very stable behavior over time. A difference between the years 2006 and 2007 is, however, observed for quadrant 2. This is related to the calibration, described in section 4.8. The decrease in statistics for the strips 33–42 originates from the lower pion-detection efficiency of the silicon-strip detector in this quadrant. The efficiency of the strips centered around the gap between two modules of the silicon-strip detector are not shown, since not enough data can be collected with the present event selection[17]. This is also valid for the strips located in the first half of quadrant 2. Less

---

[17]The efficiency of a strip is only shown if at least 100 entries satisfy all data-selection criteria, except the one
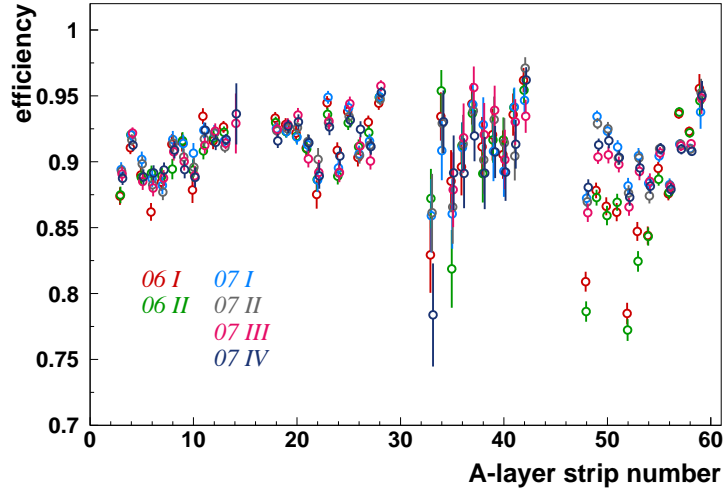
Figure 4.55: Time dependence of the efficiencies of the photon-detector A-layer strips.

strict conditions on the track selection increase the statistics, but also deteriorate the quality of the selected sample. At this stage, the quality of the data sample is preferred over the gain in statistics. Regarding time dependence, the B and C layer show the same behavior as the A layer. Their efficiencies for various time periods are shown in appendix C.

The momentum and particle-type dependence of the detection efficiency is shown in figure 4.56 for the A (top), B (center), and C (bottom) layer (for data collected in 2007). The efficiencies for negatively charged pions are shown on the left-hand side; those for protons (squares) and positively charged pions (circles) are shown on the right-hand side. The various colors are representative for the different momentum ranges. As can be seen, on average no difference in detection efficiency for positively and negatively charged pions is observed in the A and B layer. For strips located around the gap in between 2 silicon-strip modules, the detection efficiency is different for both particle types, as, e.g., for A-layer strips 3 and 58. This is related to the bending in opposite direction of the positively and negatively charged particles in the magnetic field together with the track selection. Positively charged pions reaching, e.g., A-layer strip 58 are reconstructed in the silicon-strip detector from strips close to the edge of the sensor, whereas negatively charged pions are reconstructed from strips located further away from the sensor edge. These edge effects can influence the quality of the reconstructed track. The same principle also applies to the difference in efficiency as a function of momentum for the photon-detector strips located around the gap: considering again A-layer strip 58, high-momentum negatively charged pions are reconstructed from silicon strips located closer to the sensor edge in comparison with low-momentum pions. As an illustration, pions with a transverse momentum of 300 MeV/c are bent in azimuthal direction by an angle equivalent to 1 A-layer strip pitch when reaching this photon-detector layer,

related to the layer under study.
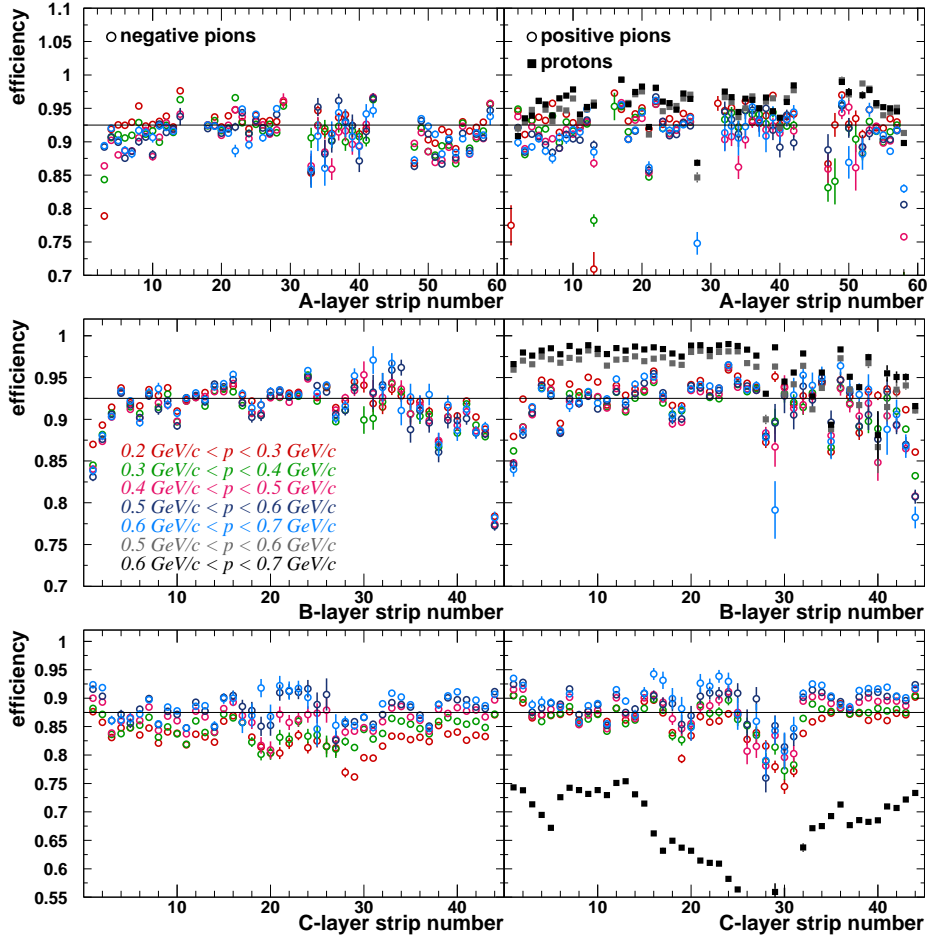
Figure 4.56: Detection efficiency of the A (top), B (center), and C (bottom) layer for negatively (left) and positively (right) charged pions, and for protons (right), as a function of momentum.

whereas pions with a transverse momentum of 100 MeV/c are bent away by the equivalent of 3 strip pitches. Apart from these edge effects and not considering the problematic region of quadrant 2, which affects A-layer strips 46–50 and B-layer strips 1–3 and 38–44, the detection efficiency shows no dependence on neither the momentum nor the type of the pions. It is for both layers around 92%.

The detection efficiency of the C layer is on average lower. This can, however, not directly be attributed to the intrinsic detection efficiency of the layer, but rather, at least partially, to the limited penetration of the selected particles, especially low-momentum particles. Because

of the absence of an active detector component behind the C layer, it is not possible to check if the selected particles indeed reach the C layer or if they are stopped before. The intrinsic detection efficiency of this layer can thus not be measured in a straight-forward way. Yet, it would be possible to compare the here obtained results with results from a Monte-Carlo simulation, and to extract from this the intrinsic detection efficiency. This has at present not been investigated. Independently, the difference in efficiency for positively and for negatively charged pions, most prominent at low momenta, is not expected. It could be related to the particle-identification criteria used for the selection of positively charged pions. It was checked that the requirements on particle identification do not give rise to a difference in reconstructed-momentum distribution for the positive and negative pions. Regarding the strips 26–31, which are mainly located in quadrant 2, a combination of proton contamination, non-optimal calibration, and possibly track reconstruction[18] could explain the lower observed efficiencies.

Since the protons observed here have a smaller range than the pions, their detection efficiency in the C layer lies well below that for pions. On the opposite, in the A and B layer the proton-detection efficiency lies above the pion-detection efficiency, as the protons generate larger signals than the pions do. Because the selected protons are required to reach the C layer, they generate on average larger signals in the B layer than in the A layer. This explains the difference in proton-detection efficiency for these two layers. No momentum dependence is observed for the A layer, whereas the efficiency of the B layer for protons in the momentum range 0.5 GeV/c–0.6 GeV/c lies below that for protons in the momentum range 0.6 GeV/c–0.7 GeV/c. Although protons with momenta around 0.5 GeV/c reach the B layer, there is a non-negligible probability that some are stopped in the tungsten layer located in front. This in combination with a noise hit in the C layer results effectively in a lower measured efficiency. As for the lower proton-detection efficiency of B-layer strips 28–44 in comparison with the other B-layer strips, the reason is not clear. Particle identification might have an influence. Also, there might be an effect related to track reconstruction, mainly then for (the first half of) quadrant 2, where the tracking detectors are less efficient. This would affect B-layer strips 1–3 and 38–44, for which also the pion-detection efficiency is lower. Yet, for these strips, the effect can also be attributed to the imperfect calibration. Also for the strips from the C layer covering quadrant 1, i.e., from strip 18 to 26, and quadrant 2 a lower proton-detection efficiency is observed. No such effect is visible for the A layer. The selection of signals for this layer is of superior quality because of the requirement of a signal in the successive two layers.

In conclusion, the detection efficiency of the photon detector for charged particles lies appreciably high in view of its usage, is constant over time, and relatively homogeneous (possibly influenced by the PMT clustering) in the regions where the measured efficiency is believed to represent the intrinsic efficiency.

---

[18]It was stated in section 4.8 that for the new production the tracks from quadrant 2 are reliable for the photon-detector calibration. This does not necessarily exclude that the track reconstruction in quadrant 2 is of lower quality than in the other quadrants. This in consequence would affect the measurement of the photon-detector-strip efficiencies.

4.12 The identification of cluster signals from neutral and charged particles

In this section the capability of the photon detector to correctly assign a signal as originating from a charged particle or a neutral particle is examined on Monte-Carlo data, generated with the pythia and the gmc_dvcs generators. The identification criteria are investigated on cluster level. As explained in section 4.1.5, the reconstruction of space points is not trivial and can be very elaborate, depending on the event topology. The space-point reconstruction might prove not to be a real benefit for the analysis of DVCS because of the event topology, with in addition the fact that the photons observed for this analysis do not necessarily leave a signal in more than one photon-detector layer. Thus, a first approach consists in the development of criteria based on cluster level.

The distribution of the difference between the azimuthal angle of the strip center and the azimuthal angle of the intersection point of a track with a photon-detector layer translated along the strip orientation to the upstream layer end, as shown in figures 4.23 and 4.42 for charged pions and protons, together with the limited spread of a photon signal, as shown in figures 4.4 and 4.17, leads to a first selection criterion. A cluster signal is considered to originate from a charged particle if the difference between the two above mentioned azimuthal angles does not exceed 1 strip pitch. In the opposite case, or if no track is found, the cluster signal is assigned to a neutral particle. For the selection of elastic DVCS events, the latter situation corresponds to the rejection of the investigated event, as it is considered to originate from a background process, mainly associated production.

An additional constraint can be placed on the z coordinate, z_t, of the intersection point of a track with a photon-detector layer, i.e., it can be required that this quantity, calculated from the reconstructed-track parameters, lies within certain boundaries. The z_t coordinate is determined with respect to the mean radius of a layer, and thus is allowed to exceed the position of the downstream end of a layer by 0.7 cm for particles originating from the far upstream end of the target cell and crossing the photon-detector layer under a shallow angle, i.e., not traversing the layer over its full thickness. Taking also the finite resolution in z_t into account, shown in figure 4.21, a track is considered in the photon-detector layer acceptance for a value of z_t being ~ 1 cm larger than the position of the downstream end of the detector layer. This is in accordance with the Monte-Carlo distribution of z_t, shown in figure 4.57 for negative particles leaving a signal in a photon-detector layer. The distribution rises with increasing z_t, as most of the simulated particles are created under a forward angle, and then shows an abrupt fall off around the end of the photon-detector layer, marked by the dotted vertical line on the right side. Since the number of backward created particles is small, the same effect is not clearly observed at the upstream end of the photon detector. The figure shown here only represents the distributions in z_t for negative pions, but the results for protons and positive pions are similar. The shape of the distribution is also independent of the particle's momentum. The various histograms in figure 4.57 represent the distribution in z_t determined from generated Monte-Carlo tracks (green), reconstructed Monte-Carlo tracks with a signal in each subcomponent of the tracking detectors (blue), and from reconstructed Monte-Carlo tracks with a signal in at least three of the four subcomponents of the tracking detectors (dark blue). Apart from small differences, all distributions show the same behavior:

91
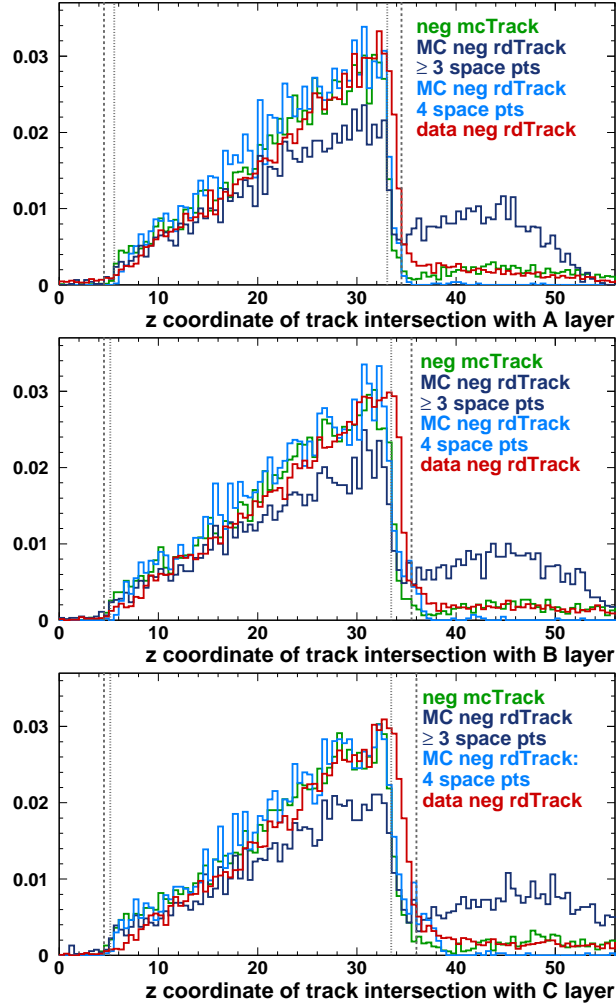
Figure 4.57: Position along the beam line of the track intersection with the photon-detector A layer (top), B layer (center), and C layer (bottom). Each of the distributions is normalized to unity. The vertical dotted lines delimit the position, according to the technical drawings, of the photon-detector layers; the dashed lines delimit the effective photon-detector acceptance (see text).

a well pronounced falling edge around the end of the respective photon-detector layers and a small number of events past that edge. The origin of the latter events is explained further in this section.

The same analysis is performed on experimental data. In order to select a clean track sam-

ple, only negatively charged particles with a track reconstructed from signals in each of the four (three for tracks originating from quadrant 2) subcomponents of the tracking detectors are selected. The obtained z_t distribution, represented by the red curve in figure 4.57, shows a behavior similar to the distribution extracted from the Monte-Carlo simulation, but the sharp falling edge is displaced. Also, a small increase of the distribution past the fall-off edge is observed in comparison with the reconstructed 4-space-point tracks from the Monte-Carlo simulation, because for the track reconstruction of experimental data only 3 space points are required in quadrant 2 and possibly also because of the absence in the Monte-Carlo simulation of inefficiencies. The shift of the fall-off edge points to a misalignment along the beam line of the photon detector with respect to the tracking detectors. Based on the z_t distribution from experimental data, the values of z_t for which the intersection of a track with a photon-detector layer is considered to lie within the acceptance are chosen to be 4.5–34.5 cm for the A layer, 4.5–35.5 cm for the B layer, and 4.5–36.0 cm for the C layer. They correspond to the dashed vertical lines in figure 4.57. These same values are also used in the subsequently explained part of the analysis of Monte-Carlo data, which is not totally accurate, but since the influence of the constraint on z_t is small, and the additional gain in events due to the displacement of the boundaries is small, the error can be neglected.

The assignment of a particle as the origin of a generated cluster signal is based on Monte-Carlo information extracted as follows. As explained in section 4.3, a primary particle crossing a detector volume, for example a tungsten layer, can generate secondary particles. If a secondary particle has a momentum above a set threshold, in most productions 100 MeV, this particle is considered a primary particle and its track information is stored. If this particle then generates a signal in, e.g., a photon-detector strip, the Monte-Carlo simulation links this signal to the secondary particle. In case the secondary particle has a momentum below threshold, the observed signal is linked to the original primary particle. However, for the former case, it is meaningless to consider the secondary particle as the original particle if it concerns, for example, a pair-produced electron in a tungsten layer. Yet, since a link from this secondary particle to its parent track exists, the primary particle can be traced down. In the present analysis, the first stable particle at the origin of the chain is identified as the primary particle[19]. This definition excludes, for example, neutral pions. As neutral pions decay practically instantaneously, these pions are modeled as virtual, and not as stable, particles in the simulation. The resulting decay photons, however, are modeled as stable particles, and according to the here utilized identification criterion, they will be considered as the original particles responsible for the generation of a signal in the photon detector. On the other hand, K_S^0 particles are modeled as stable particles in the Monte-Carlo simulation. However, they decay relatively fast, and generate secondary charged particles, reconstructed by the tracking algorithm. Although the signals generated by these decay particles should be considered as originating from charged particles, they will be identified as originating from neutral particles. One thus needs to interpret the results of the analysis with caution. The sample of signals erroneously identified by the photon detector as originating from charged or neutral particles is, however, analyzed and explained in the following, and the contribution from decaying particles clarified.

---

[19]The convention for the treatment of very fast-decaying particles is not followed consequently for the gmc_dvcs generator. Some of these particles, like η and Σ^0, are labeled as stable in the Monte-Carlo simulation. They were, however, identified and their decay products were taken as the primary stable particles.

As mentioned previously, the study of the capability of the photon detector to discriminate signals generated by charged particles from signals generated by neutral particles is solely based on cluster level. Also, only clusters for which a signal above 1 MeV is observed are considered. The number of cluster signals correctly identified as originating from a neutral particle amounts to 98% (96%) for data generated with gmc_dvcs (pythia); the number of cluster signals correctly identified as originating from a charged particle amounts to 78% (67%). The results are summarized in table 4.2. The constraint on z_t has only a minor positive influence (0.9%) on the selection of neutral particles, while it has a negative, but even smaller, influence ($< 0.5\%$) on the identification of charged particles. The identification of neutral particles has a rather high efficiency, while for charged particles it is not optimal. However, as explained, care has to be taken in the interpretation of these results. In the following two subsections the reason for the incorrect assignment of neutral and charged particles is analyzed. For the misidentified clusters originating from neutral particles no constraint is placed on z_t; for the study of clusters originating from charged particles the constraint on z_t is applied.

	pythia without z_t cut	pythia with z_t cut	gmc_dvcs without z_t cut	gmc_dvcs with z_t cut
neutral, correct id.	95.34%	96.24%	97.40%	98.25%
neutral, incorrect id.	4.66%	3.76%	2.60%	1.75%
charged, correct id.	66.98%	66.51%	77.63%	77.55%
charged, incorrect id.	33.02%	33.49%	22.37%	22.45%

Table 4.2: Identification of cluster signals from neutral and charged particles.

4.12.1 Incorrectly identified neutral particles

The sample of misidentified clusters associated with a neutral particle can be subdivided into three categories. The distinction between the first and other two categories is based on the comparison of the first stable particle, defined above, associated with a cluster with the first stable particle associated with a reconstructed track. The original stable particle associated with a reconstructed track is traced down in a way similar to the original stable particle associated with a photon-detector cluster. The link between the last primary particle of the particle chain and the reconstructed track is provided through the space points that form the track.

The first considered category of misidentified photon-detector clusters consists of clusters that are associated with the same particle as are the reconstructed tracks. This group forms 47.79% (78.44%) of the misidentified clusters, for data generated with gmc_dvcs (pythia). For 99.1% (98.5%) of these clusters, only one particle is found to be at the origin of the generated signal. For the other two categories, the particle associated with the reconstructed track is different from the particle associated with the photon-detector cluster. A further distinction is based on the number of particles crossing the cluster. For the second group of clusters two particles are linked to the same cluster, whereas for the third group only one
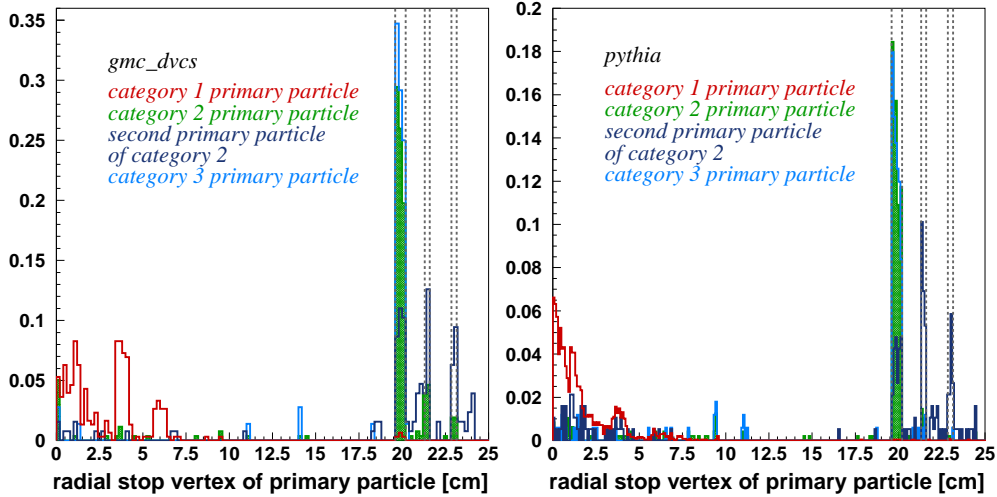
Figure 4.58: Transverse distance from the beam axis of the stop vertex of neutral primary particles linked to misidentified photon-detector clusters, for data generated with gmc_dvcs (left) and data generated with pythia (right). The vertical lines delimit the position of the photon-detector tungsten layers. Each histogram is normalized to unity.

particle is associated with the cluster, The population of clusters linked to more than two particles is only on the order of 0.1%, and will thus be ignored. The second group forms 40.82% (15.97%) of the misidentified clusters and the third group 11.39% (5.59%).

The origin of contamination for the first group of misidentified clusters can be understood from the position, transverse to the beam axis, at which the primary original particle is stopped due to interaction with material or its decay. This position is depicted in figure 4.58 for particles from each category. As can be seen, contrary to the particles from the other categories, all particles from the first category are stopped between the target cell and the silicon-strip detector. The different types of particles present in this group are mainly γ with 62.25% (16.96%), Λ^0 with 19.54% (15.86%), and K_s^0 with 11.26% (57.46%). It is to be noted that the tracking algorithm assumes all particles to originate from the beam-proton interaction point, and does not reconstruct secondary vertices. Thus, charged particles that originate from a K_s^0 or a Λ^0 that decays close to the target area have a higher chance to be reconstructed (with better accuracy). It is clear that the signals from the here considered clusters should be considered to originate from charged particles, and thus do not form a real sample of misidentified cluster signals.

The primary particles of the second category consist nearly exclusively of photons, while the second particle linked to the cluster is found to be most of the time a proton in case of data generated with the gmc_dvcs generator, and a pion in case of data generated with the pythia generator. This second particle is in 97% of the cases the primary original particle to which the reconstructed track is linked. As such, this group of clusters is unavoidably misidentified.
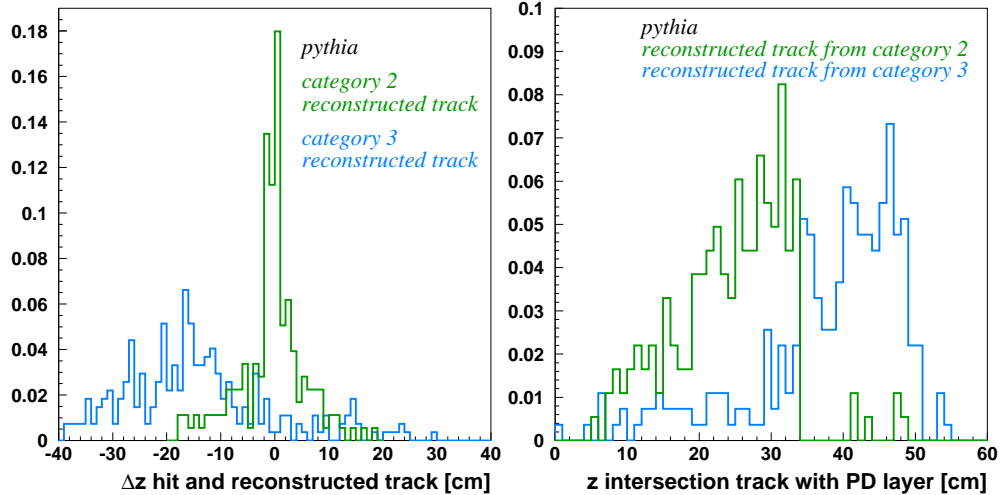
Figure 4.59: Difference between the energy-weighted z position of the signal in a cluster and the z coordinate of the intersection of a reconstructed track with a photon-detector layer (left), and the position along the beam-line of the intersection of a reconstructed track with a photon-detector layer (right). Each histogram is normalized to unity.

As for the third group, the generated cluster signals originate from photons that mainly interact in the first tungsten layer of the photon detector. The charged particle, to which the cluster is erroneously linked, is mainly reconstructed from three space points: two from the silicon-strip detector and one from the inner scintillating-fiber tracker. This statement is especially valid for data generated with the pythia generator. For data generated with gmc_dvcs, only a small excess in tracks reconstructed from three space points is observed. While the distribution of the difference between the azimuthal angle of the cluster center and the azimuthal angle of the track intersection with the photon-detector layer, translated along the strip orientation to the upstream layer end, shows no difference for clusters from category 2 and 3, a clear difference in the distribution of Δz is observed, as shown in figure 4.59 (left). The quantity Δz represents the difference between the energy-weighted z coordinate of all hits recorded in the cluster under investigation and the calculated z coordinate of the intersection point of the charged particle with the photon-detector layer. As can be seen, for clusters from category 3 it is a mere coincidence that the clusters are linked, via the selection criterion on the azimuthal angle, to reconstructed tracks. If the crossing of clusters from two different layers were reconstructed, the consideration of the z coordinate of the crossing would result in a correct assignment of the origin of the signal. Since most of the charged particles linked to clusters from category 3 intersect the photon-detector layer outside its acceptance, as can be seen in figure 4.59 (right), the imposed boundaries on z_t, defined above, correctly identify the signal. For data generated with gmc_dvcs this effect is less pronounced.

We can conclude that if a signal from a neutral particle is detected in a photon-detector

cluster, the signal will be identified as originating from the neutral particle with a high efficiency. The identification efficiencies of neutral particles given in table 4.2 are slightly underestimated. The deduction of misidentified clusters from the first category and the constraint on z_t result in an identification efficiency of about 99% for data generated with gmc_dvcs and pythia.

4.12.2 Incorrectly identified charged particles

For only 15.21% (24.29%) of the misidentified clusters belonging to a charged particle, the track of the particle is effectively reconstructed by the tracking algorithm, when considering data generated with gmc_dvcs (pythia). The effective reconstruction of the track of a particle refers here to the existence of a link between a reconstructed track and the Monte-Carlo primary particle directly responsible for the generation of signals in the tracking detectors (thus not necessarily the original generated stable particle). A reconstructed track is linked to a Monte-Carlo particle if each space point used to form the track is linked to the same simulated particle, and if the track is reconstructed from at least three space points or if the track consists of exactly two space points in the silicon-strip detector. For 84.79% (75.71%) of the incorrectly identified clusters, the Monte-Carlo particle is not found to be reconstructed by the tracking algorithm, and these clusters are thus unavoidably misidentified[20]. In comparison, for 99.74% (99.73%) of the correctly identified clusters associated with a charged particle, the track of the charged particle is reconstructed by the tracking algorithm. The type of particle associated with misidentified clusters consists mainly of protons (67.15%) and pions (31.76%) for data generated with gmc_dvcs, and of pions (83.33%), protons (8.25%), and kaons (6.04%) for data generated with pythia.

In the following we will only concentrate on the misidentified clusters for which the associated charged particle is reconstructed by the tracking algorithm. A classification of this group of misidentified clusters is based on the position at which the original primary particle associated with the cluster is stopped. The location of this 'stop vertex' is shown in figure 4.60 (left) in terms of its transverse distance from the beam line as a function of its position along the beam line. Also for correctly identified clusters, the stop vertex inside the area considered is shown on the right hand-side of the figure. From the particles reconstructed by the tracking algorithm and associated with a misidentified cluster 97.82% (97.10%) are stopped inside the area depicted in figure 4.60. For particles associated with a correctly identified cluster, only 29.26% (25.93%) have their stop vertex inside the considered area. From these particles, only a small fraction 1.57% (14.96%) is stopped inside material located in front of the photon detector, and for data generated with pythia, it concerns here mainly the region surrounded by the silicon-strip detector. The particles associated with misidentified clusters, however, interact much more often with material components situated outside the scattering chamber. The stop vertices of particles linked to misidentified clusters are grouped in figure 4.60 into 6 regions. The data are generated with the pythia Monte-Carlo generator. For data generated with gmc_dvcs the same interaction regions are visible, but the population in each region is differently distributed (see table 4.3). Region 1 corresponds to the position of the flange of

---

[20]Some of the simulated particles can still be reconstructed by the tracking algorithm, but are not linked to the reconstructed track. However, it is clear that these particles only form a minority when comparing to the number of simulated particles provided with a link to a reconstructed track for the group of correctly identified clusters.
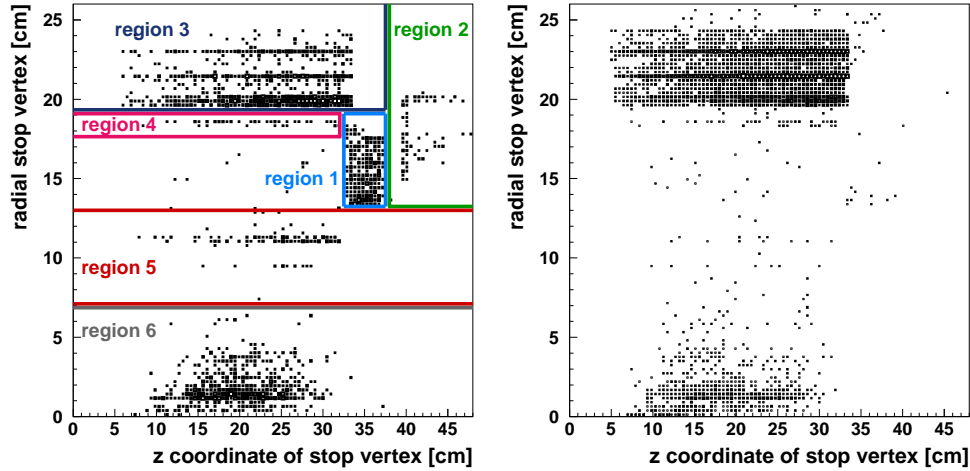
Figure 4.60: Transverse distance from the beam line of the stop vertex of reconstructed charged particles as a function of its z coordinate along the beam line, for misidentified clusters (left) and correctly identified clusters (right). The data shown here are generated with the pythia generator.

the pump cross and of the 'end cap' of the scintillating-fiber tracker, which is attached to the flange; in region 2 the holding structure of the lambda wheels is visible; region 3 corresponds to the location of the photon detector, where particles interact principally in the tungsten layers; region 4 contains the outer barrel of the scintillating-fiber tracker; region 5 contains the inner barrel of the scintillating-fiber tracker, located at a distance of 10.9 cm to 11.3 cm from the beam line, as well as the wall of the scattering chamber, at a distance of 9.5 cm; finally, region 6 encompasses the target cell and the silicon-strip detector. The fraction of misidentified clusters in each region, with respect to the total amount of misidentified clusters associated with a particle stopped inside the area represented in figure 4.60, is given in table 4.3.

	pythia	gmc_dvcs
region 1	13.64%	4.00%
region 2	2.78%	0.84%
region 3	43.19%	84.91%
region 4	1.67%	2.46%
region 5	5.68%	3.96%
region 6	32.25%	3.32%

Table 4.3: Distribution of misidentified clusters according to the position of the stop vertex of the associated charged particle. For the definition of the various regions, see figure 4.60.

Although the photon detector records signals from the primary particles stopped in re-

gions 1 and 2, the particles themselves never reach the photon detector. Instead, the secondary particles originating from the interaction of the primary particle with material located inside regions 1 and 2 are back scattered and generate signals in the photon detector. These types of events also explain the origin of signals outside the photon-detector acceptance along the beam line, shown in figure 4.57. For the considered group of misidentified clusters, the constraint imposed on z_t has only a small influence. Removing the constraint recovers merely 10% of the misidentified clusters, because also in the azimuthal angle of the track intersection with the photon detector any correlation is lost. The misidentification of clusters associated with the interaction of a particle in region 1 or 2 forms an advantage for the study of elastic DVCS events, where it leads to the rejection of the event, since back-scattered particles can also generate signals in the outer layer of the scintillating-fiber tracker, and the combination of these signals with the signals generated by the primary particle in the silicon-strip detector and the inner layer of the scintillating-fiber tracker can lead to an erroneous reconstruction of the event topology.

For all other regions shown in figure 4.60, the interaction of the primary particle with material results in a broader distribution of the difference, $\Delta\phi$, between the azimuthal angle of the cluster center and the azimuthal angle of the track intercept with the photon detector, translated along the strip orientation to the upstream layer end. Understandably, the width increases with the distance from the interaction point to the photon detector. Some of the misidentified clusters can be recovered by extending the allowed range of the difference in azimuthal angle from 1 strip pitch to 2 strip pitches. Table 4.4 summarizes the effect of this alternative selection criterion. Although the fraction of misidentified clusters associated with a neutral particle increases by only 1%, while the fraction of misidentified clusters originating from the passage of a charged particle decreases by 2–3% with the constraint on $\Delta\phi$ extended to 2 strip pitches, the 1 strip pitch constraint is opted for in the analysis of DVCS. The reason is two-fold. The photon detector's main design goal is the rejection of events in which a photon is present. In that respect, a cleaner sample of events is preferable over a small gain in statistics. Additionally, apart from the broken n-side of one module of the silicon-strip detector, the inefficiencies of the scintillating-fiber tracker and silicon-strip detectors are not yet implemented in the Monte-Carlo simulation. Inefficiencies result in a lower track-reconstruction efficiency, but also influence the quality of the reconstructed tracks. As explained in section 3.4, the tracking algorithm first searches for all tracks reconstructed from signals in each of the four tracking-detector subcomponents. In a next step, all tracks reconstructed from a signal in two or three of the subcomponents are searched for, not considering

	pythia 1 pitch	pythia 2 pitch	gmc_dvcs 1 pitch	gmc_dvcs 2 pitch
neutral, correct id.	96.24%	95.27%	98.25%	97.52%
charged, correct id.	66.51%	69.46%	77.55%	78.98%

Table 4.4: Fraction of correctly identified clusters for a 1-strip-pitch and 2-strip-pitch cut on the difference in azimuthal angle between a cluster center and the intersection of a track with a photon-detector layer translated along the strip orientation to the upstream layer end.

anymore the signals used in the previous step. The tracks reconstructed from two or three signals can, however, have several space points in common with each other. The presence of detector inefficiencies increases the amount of tracks formed out of two or three space points, and thus also the amount of inaccurately reconstructed tracks, originating from a fortuitous combination of space points. The degree to which erroneously reconstructed tracks would influence the correct identification of particles leaving a signal in the photon detector is not known.

In summary, one can conclude that the proposed selection criterion on the difference in azimuthal angle between a cluster center and the intersection of a track with a photon-detector layer translated along the strip orientation to the upstream layer end together with the constraint imposed on z_t allow for a good identification of signals generated by neutral particles. As for the identification of signals from charged particles, the proposed constraints misidentify 22.45% (33.49%) of the clusters. Taking into account that for a large number of these clusters, the track of the particle is not reconstructed, the selection criteria lead to an incorrect identification of the clusters of around 3% (8%) when the particle is reconstructed by the tracking algorithm. The here considered study does not involve the simulation of detector inefficiencies (apart from the broken n-side of a silicon module). It also only considers photon-detector clusters for which a signal above 1 MeV is recorded, and is thus insensitive to particles depositing less energy. The capability of the photon detector to reject DVCS events originating from associated production is presented in the following chapter.

5. Analysis of elastic and associated deeply virtual Compton scattering

This chapter contains a description of the steps undertaken towards the analysis of elastic and associated DVCS events using information from the recoil detector, within the current status of understanding of this detector. First the analysis of elastic DVCS is covered, then the study of associated DVCS events is described. For the sample of associated production only the channel $\Delta^+ \to p\pi^0$ is considered.

5.1 Data sample and data quality

As already indicated in the previous chapter, the results shown here are based on the analysis of data collected at the HERMES experiment from September 2006 until end of June 2007. The data originate from the scattering of a positron beam off an unpolarized hydrogen target. During the mentioned time period also data on a deuterium target were collected, but these are not included in the present analysis.

In order to ensure the quality of the data, requirements are imposed on the individual detector components and data-taking conditions relevant to the presented study. These requirements are encoded in a bit pattern and compared on burst level with information dedicated to data quality. In the present case, the imposed constraints lead to the bit pattern 0x3c1e1bd8, which includes following criteria:

- the burst is not the first burst of a run and has a reasonable length

- absence of high-voltage trips in the tracking chambers

- good tracking efficiency

- reasonable beam current and regular measurement of the beam polarization within a time period of maximum five minutes

- operational TRD

- absence of non-operational calorimeter and preshower components

- particle identification provided

- recoil-detector magnet ramped up

The bit pattern also encodes the requirement of an operational silicon-strip detector and scintillating-fiber tracker. However, these requirements are currently not implemented in this data-quality frame work. The 0.4% of data for which the photon detector was not entirely operational are discarded from the data sample.

Additional constraints, not encoded in the bit pattern, are imposed on burst level. They consist of a lower limit on the beam energy, add a requirement for the performance of the TRD, ensure the lifetime of the data-acquisition system to be reasonable, guarantee an operational measurement of the beam polarization, and restrict the upper polarization value to 80%.

5.2 Event selection with the forward spectrometer

In this section the selection of DVCS events using information from the forward spectrometer only is described. The exclusive events are extracted in three steps. The first step consists of the identification of DIS events. From this sample, events containing no other particles than exactly 1 DIS lepton and 1 photon, as detected by the calorimeter, are selected, and constraints are imposed on the reconstructed photon. This category of events are called single-photon events. The last step then isolates exclusive events. The selection of exclusive events with the inclusion of the recoil detector is described in the subsequent section.

5.2.1 Selection of deep-inelastic scattering events

A primary requirement consists of the presence of trigger 21 in order to ensure a relatively homogeneous composition of the data collected over different time periods. As explained in subsection 3.3.3, this trigger is formed when a signal above threshold is measured in the hodoscopes H0 and H1, the preshower and the calorimeter. In addition, the signals in each detector have to originate from the same detector half. As the background originating from the proton beam, which is mainly rejected by the inclusion of H0, was reduced for the years 2006 and 2007 compared to previous years, and the efficiency of H0 was lower than the efficiency of the other detector components involved in the formation of trigger 21, it was checked if requiring a combination of triggers similar to trigger 21, but not involving H0, leads to a significant gain in statistics. The appropriate triggers for this study are trigger 18, formed by a signal in the upper halves of H1, the preshower and the calorimeter, and trigger 26, which is the analogue of trigger 18 but considers signals from the lower detector halves. Since the loss in number of DIS events obtained when requiring the presence of trigger 21 only amounts to 0.4%[1] in comparison to the number of DIS events obtained when requiring a combination of trigger 18 and 26, trigger 21 is considered to be the appropriate choice.

---

[1]This value does not give an indication of the H0 inefficiency, as contrary to the situation for trigger 21, periods exist during which triggers 18 and 26 are prescaled and thus not included for the data analysis. The percentage of times that these triggers are prescaled lies below 2%.
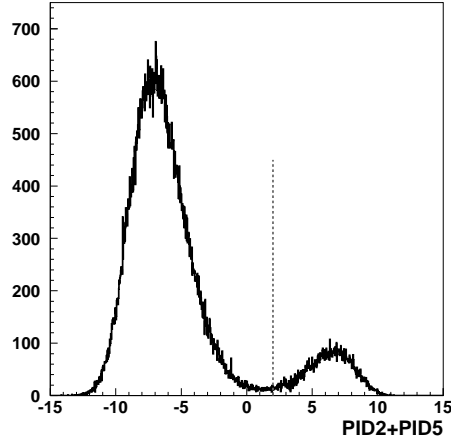
Figure 5.1: Sum of PID2 and PID5.

Subsequently, long tracks, i.e., tracks originating from the vertex and reaching the calorimeter, are analyzed. The identification of the particles associated with these tracks is provided by the PID values, explained in subsection 3.3.2. The sum of PID2 and PID5 provides a clear distinction between hadrons and leptons. This is shown in figure 5.1. Negative PID values correspond to signals from hadrons, while positive values originate from lepton signals. For a clean selection of leptons the sum of the PID values is required to be higher than 2, as indicated by the vertical line.

From the sample of detected leptons, the particle with highest momentum is selected. The track and vertex probability are required to be larger than 0.01, in agreement with the studies presented in [102]. Additionally, the z-coordinate of the vertex, z_{vert}, is restricted to 0 cm $< z_{vert} < 25$ cm to exclude interactions originating from other sources than the hydrogen target, in particular the collimator.

In order to avoid that the selected lepton hits one or more inactive detector components, resulting in incorrectly reconstructed kinematics, fiducial volume cuts are applied to the lepton track. They are presented in table 5.1. In addition, to ensure a reliable identification of the lepton, the electromagnetic shower generated by the lepton in the calorimeter, needs to be contained inside this detector. The supplementary constraints involved can also be found in table 5.1.

Finally, kinematic restrictions are applied on the lepton. The first constraint involves the energy transfer to the proton, ν. It is limited to 24 GeV when the trigger threshold in the calorimeter is set to 3.5 GeV. To be insensitive to fluctuations in trigger threshold, originating from the non-optimized preliminary calibration of the calorimeter used during data taking, and consequently to avoid normalization problems in the measurement of the beam-helicity asymmetry, the upper value of ν is restricted to 22 GeV. Secondly, in order to select the deep-inelastic regime, a lower limit of 4 GeV^2 is necessary for the square of the invariant mass of the photon-nucleon system. A lower limit of 9 GeV^2 is, however, applied in order to reduce

fiducial volume cuts	
septum plate	$\lvert 181 * y_s + y_p \rvert > 7$
rear field clamps[2] for front track	$\lvert 383 * y_s + y_p \rvert < 54$
front field clamps for front track	$\lvert 172 * x_s + x_p \rvert < 31$
rear field clamps for back track	$\lvert 108 * x'_s + x'_p \rvert < 100$
rear field clamps for back track	$\lvert 108 * y'_s + y'_p \rvert < 54$
requirements on shower containment	
horizontally	$\lvert 463 * x'_s + x'_p \rvert < 175$
vertically	$\lvert 463 * y'_s + y'_p \rvert > 30$
	$\lvert 463 * y'_s + y'_p \rvert < 108$

Table 5.1: Applied fiducial-volume and calorimeter-related cuts on the DIS lepton. All quantities are expressed in cm. The variables $x_{s[p]}$ and $y_{s[p]}$ ($x'_{s[p]}$ and $y'_{s[p]}$) represent, respectively, the x and y coordinates of the track slope [position] at the location of FC1 (BC4), projected to $z = 0$ cm ($z = 275$ cm).

the contribution from background processes to the exclusive sample [103]. Lastly, to ensure the validity of the factorization theorem, one needs $Q^2 \gg M_h^2$, with M_h being the mass of the final hadronic state: the proton mass in case of elastic DVCS and the Δ^+ mass in case of the study of associated DVCS with the recoil detector. Limited by statistics, this condition is, however, relaxed to $Q^2 > 1$ GeV[23].

The leptons satisfying all of the above mentioned constraints are called DIS leptons, and the corresponding events DIS events.

It has to be noted that at this stage no requirement is imposed on the charge of the DIS lepton. The presented data selection can never entirely guarantee that the selected lepton is the original scattered beam lepton. However, the probability to misidentify a lepton as such is independent of its charge. The number of, in the present case, electrons identified as scattered beam leptons gives a good estimate for the number of misidentified positrons. The kinematic distributions, presented in the following, are restricted to events that contain a DIS lepton of the correct charge. For the extraction of the asymmetries, events with DIS electrons are assigned a negative weight. This procedure allows to correct for events in which the positron is erroneously identified as the scattered beam lepton. This correction has, however, only a very small effect: the ratio of the number of negatively charged DIS leptons to the number of positively charged DIS leptons amounts to 0.6%; for DVCS events, this ratio falls below 0.05%.

5.2.2 Selection of photons

Now the selection of single-photon events is considered. For this category of events the detection of exactly 1 DIS lepton and 1 untracked cluster in absence of detection of any other

---

[2]The choice of the rear field clamps instead of the front field clamps results in a more restrictive constraint on the lepton track.

[3]This condition is not adequate, and is adjusted, for the study of associated DVCS. For the selection of DIS events, which are used for the normalization of the associated-DVCS sample, this condition is, however, sufficient.
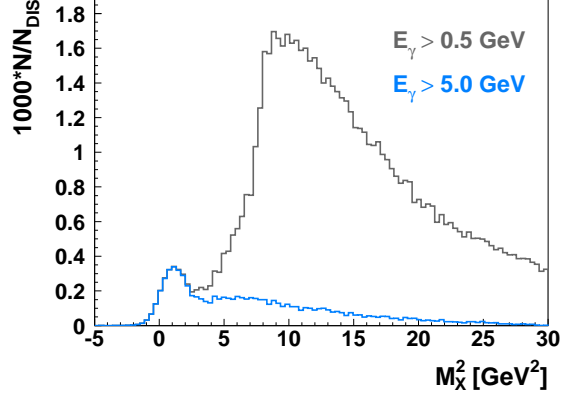
Figure 5.2: Influence of the photon-energy restriction on the missing-mass distribution. The blue curve represents the missing-mass distribution for single-photon events containing a photon with energy above 5 GeV; for the gray curve this constraint on the photon energy is released.

particle in the spectrometer is required.

The detected photon has to satisfy certain criteria in order to ensure a correct reconstruction of its kinematics. For the determination of its energy, the signal it generates in the preshower, E_{presh}, is restricted to $1\,\text{MeV} < E_{presh} < 110\,\text{MeV}$. The lower cut rejects photons that do not convert in the preshower, as their energy can not be reconstructed reliably [103], while the upper cut ensures that the preshower ADC is not in overflow [66]. This is mandatory, because the energy of a photon is reconstructed from the energy it deposits in the calorimeter and in the preshower. The proper expression for the parametrization of the photon energy in terms of these two energy depositions is based on the study of lepton signals [104]. As photons that convert in the preshower show the same shower characteristics as leptons, the parametrization developed for leptons can be adopted for the reconstruction of the photon energy. In order for this reconstruction to be reliable, one has to in addition make certain that the shower generated by the photon is well contained inside the calorimeter. This restricts the photon's energy-weighted position in the detector along the y axis, y_{calo}, to $33\,\text{cm} < |y_{calo}| < 105\,\text{cm}$. The lower limit also ensures that the photon does not intersect the spectrometer septum plate. In order to avoid the rear field clamps the photon has to satisfy the constraint:

$$\left| \frac{y_{calo} - y_{vert}}{z_{calo} - z_{vert}} (383 - z_{vert}) + y_{vert} \right| < 54\,\text{cm}, \tag{5.1}$$

where y_{vert} (z_{vert}) represents the y (z) component of the vertex, as determined from the lepton track, and z_{calo} ($= 729\,\text{cm}$) represents an effective shower depth inside the calorimeter, defined with respect to $z = 0\,\text{cm}$. This effective shower depth, obtained also from the analysis of lepton signals, corresponds to the z position that, on average, results in the most precise
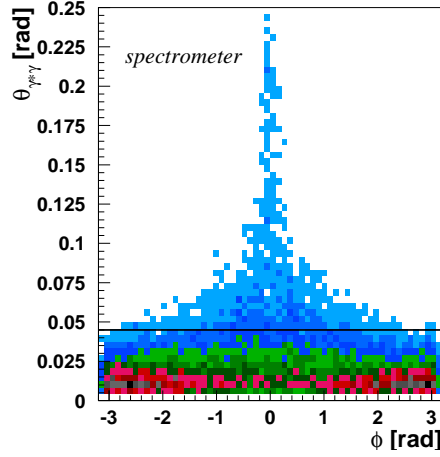
105

Figure 5.3: Photon opening angle $\theta_{\gamma^*\gamma}$, with $\theta_{\gamma^*\gamma} > 5$ mrad, as a function of the angle ϕ for single-photon events selected with the spectrometer in the exclusive missing-mass region.

reconstruction of the photon's polar angle at energies characteristic for DVCS events [105][4]. Finally, the location of the front field clamps restricts the energy-weighted x position in the calorimeter, x_{calo}, to $|x_{calo}| < 125$ cm.

For correctly reconstructed photons, an additional constraint is imposed in order to improve the purity of the sample of exclusive events. A large fraction of background events is eliminated by restricting the photon energy to values above 5 GeV. This is illustrated in figure 5.2. The figure shows the missing-mass distribution for all events containing 1 DIS lepton and 1 properly reconstructed photon. For the events represented by the gray curve no additional restriction, other than the one implemented in HRC, is imposed on the cluster energy; the blue curve only represents events for which the cluster energy exceeds 5 GeV. As can be seen, the exclusive region, with missing mass around 1 GeV^2, is unaffected by the introduction of a 5 GeV threshold, while a large fraction of background located at higher missing mass is rejected.

5.2.3 Selection of exclusive events

In order to obtain the sample of exclusive events, additional requirements need to be fulfilled. They concern, among others, the angle between the virtual and real photon, $\theta_{\gamma^*\gamma}$. This angle is shown in figure 5.3 as a function of the azimuthal angle between the lepton scattering plane and the photon production plane, ϕ, for single-photon events in the exclusive missing-mass region, i.e., in a missing-mass range around the proton mass (see further). As can be seen, only for small values of $\theta_{\gamma^*\gamma}$ all values of ϕ are covered. To ensure a full acceptance in ϕ,

---

[4]The measurement presented in reference [105] is based on a different alignment of the spectrometer components, in particular of the calorimeter, and preliminary studies have shown that this value needs to be optimized [106]. This is at present under more detailed investigation.

needed for a proper extraction of the asymmetries, an upper limit on $\theta_{\gamma^*\gamma}$ of 70 mrad is proposed in reference [107]. Studies presented in reference [103] revealed that a reduction of this lower limit to 45 mrad not only improves the uniformity of the acceptance, but also reduces the contribution from the background processes. Accordingly, this upper limit, indicated by the horizontal line in figure 5.3, is also used in the present analysis. This constraint needs to be supplemented with a restriction on the minimum value of $\theta_{\gamma^*\gamma}$, since the angle ϕ is not defined for $\theta_{\gamma^*\gamma} = 0$ mrad. The appropriate lower limit for which $\theta_{\gamma^*\gamma}$ is larger than 0 mrad within its resolution is determined to be 5 mrad in reference [105] from the resolutions of all variables entering the calculation of $\theta_{\gamma^*\gamma}$, and adopted subsequently.

In order for the factorization theorem to be valid, the magnitude of the squared four-momentum transfer to the nucleon, t, needs to be much smaller than Q^2. In addition, as elastic DVCS events are centered around low values of $|t|$, a constraint on this variable is useful for the rejection of background, in particular for the rejection of semi-inclusive DIS events, which are distributed at even higher $|t|$ values than are associated DVCS events. However, as the recoiling proton is not detected when solely using information from the forward spectrometer, this variable can only be calculated from the reconstructed lepton and photon kinematics. Here, the limited photon-energy measurement restricts the resolution in t to 0.11 GeV^2 [103]. The dependence of t on the photon energy can be eliminated, and the resolution for elastic DVCS events improved by an order of magnitude if, instead of using t, one introduces the quantity t_c:

$$t_c = \frac{-Q^2 - 2\nu(\nu - \sqrt{\nu^2 + Q^2}\cos\theta_{\gamma^*\gamma})}{1 + \frac{1}{M_p}(\nu - \sqrt{\nu^2 + Q^2}\cos\theta_{\gamma^*\gamma})}, \tag{5.2}$$

which is obtained through the replacement of the missing mass M_X by the proton mass M_p in equation 2.51, in combination with the expression for t in terms of the reconstructed photon energy. The two above given arguments for a restriction on t translate to an upper limit on $|t_c|$ of 0.7 GeV^2 [103].

Restrictions are also imposed on Q^2 and x_B; they read 1 GeV$^2 < Q^2 < 10$ GeV^2 and $0.03 < x_B < 0.35$. These restrictions only remove very few events, and are solely applied in order to define the covered phase space [108].

Finally, a constraint is placed on the squared missing mass, M_X^2. The distribution is shown in figure 5.4 for experimental data (red curve) and for Monte-Carlo data (gray curve), with the latter additionally subdivided into the contributions from elastic BH (green) and from background processes (blue). An explanation about the Monte-Carlo simulation for the analysis of DVCS follows in section 5.4. The experimental data and the simulated data are each normalized to the respective number of DIS events. The M_X^2 distribution obtained from experimental data is shifted by -0.462 GeV^2; the origin of this shift is explained in the following subsection. As the photon energy enters the calculation of the missing mass, a relatively wide distribution, extending to negative values, is observed. The difference between the width of the exclusive peak from the Monte-Carlo simulation and from experimental data is related to the photon-energy correction, discussed in section 4.3 and in the subsequent subsection. This correction is applied to experimental data, but not to the simulated data. The excess of exclusive events ($\sim 20\%$) in the simulation is not yet clarified. A partial explanation might be related to the absence of radiative effects in the Monte-Carlo simulation; these would smear events from the exclusive region into the higher-M_X^2 region, which is itself
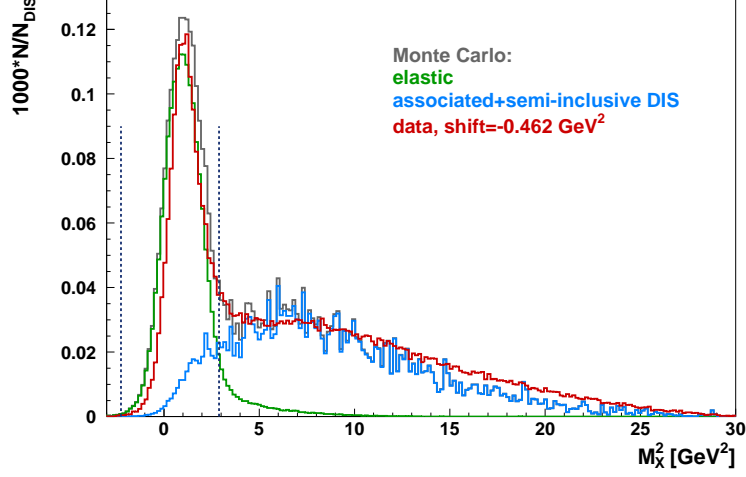
Figure 5.4: Missing-mass distribution for exclusive events selected from experimental and Monte-Carlo data. The distributions are normalized to the respective number of DIS events.

slightly underestimated by the present simulation. On the other hand, since the Monte-Carlo simulation only contains the BH processes, but not the DVCS processes, the inclusion of these latter would lead to an increase of events in the exclusive peak. Another reason for the discrepancy in yield between both distributions might be found in the restrictions imposed on the track and vertex probability, explained in section 5.2.1. It has namely been observed that the occupancy at low probability values is higher for experimental data than for Monte-Carlo data [109]. The applied constraints on the vertex and track probability would thus reject less events for the simulated data. Detailed studies are, however, needed.

The choice for the restrictions imposed on M_X^2 finds its motivation in figure 5.4. An upper limit is set at the M_X^2 value that corresponds to the point where the amount of signal and background are equal, in agreement with reference [107]. The choice for a lower limit on M_X^2 is more arbitrary. It has also been taken in accordance with reference [107]. Both boundaries are indicated by the vertical lines in figure 5.4. For the experimental (Monte-Carlo) data they correspond to $-1.79\,(-2.25)\,\text{GeV}^2$ and $3.35\,(2.89)\,\text{GeV}^2$.

5.2.4 Photon-energy correction

The mean position of the squared missing-mass distribution varies over time. This is shown by the open symbols in figure 5.5. Each point in this figure represents the fit mean of the exclusive M_X^2 distribution[5] for data collected over a certain time period. As the main reason for the observed variation over time is believed to lie in the calorimeter calibration, the time periods are chosen so that they each correspond to one calorimeter-calibration period, i.e.,

---

[5]The range for the fit to M_X^2 is adjusted iteratively for each time period; it is taken around the fit mean value, μ, as: $\mu - 3.34\,\text{GeV}^2 < M_X^2 < \mu + 0.91\,\text{GeV}^2$.
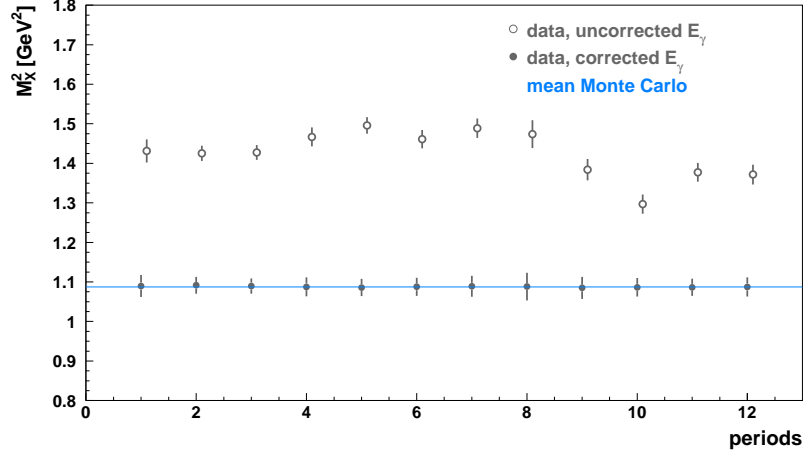
Figure 5.5: Fit mean value of the M_X^2 distribution over time. The definition of the different time periods can be found in appendix D. The open symbols represent the observed mean value without the inclusion of individual photon-energy correction factors; the closed symbols show the mean values after the implementation of the time-dependent correction.

the time-dependent calibration factors for the various calorimeter blocks are determined over that same time period. The run ranges corresponding to each time period can be found in appendix D.

In order to eliminate the time dependence of the missing mass, a simple correction to the reconstructed photon energy in the form of a multiplicative factor was determined for each individual period. This method is preferred over a shift of the exclusive missing-mass window, separately for each time period, as the photon energy enters, e.g., also the calculation of the missing transverse momentum, described in the next section. For the determination of the photon-energy correction factor, the fit mean value of the M_X^2 distribution from the Monte-Carlo simulation is chosen as a reference. The values of the individual correction factors can be found in appendix D. The result of the correction on the M_X^2 distribution is shown in figure 5.5, as represented by the closed symbols; the mean value from the Monte-Carlo simulation is indicated by the horizontal line. A flat distribution over time can be observed. However, the width of the distribution shows a slight increase from 0.806 ± 0.006 GeV^2, without correction, to 0.816 ± 0.006 GeV^2, with correction. In order to improve the resolution of the missing mass, an additional photon-energy correction factor constant over time is considered. The effect of the introduction of a global scale factor on the width of the distribution is shown in figure 5.6 for different values of this scale factor. The minimum of the curve, at a value of the scale factor of 0.98, corresponds to a slightly improved resolution of 0.800 ± 0.006 GeV^2. Consequently, this global correction factor, in combination with the individual correction factors, is adopted for the correction of the photon energy.
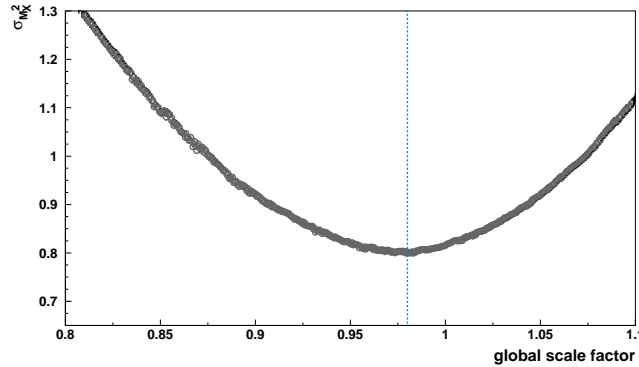
Figure 5.6: Width of the fit M_X^2 distribution as a function of various values of the global photon-energy correction factor. The vertical line indicates the chosen global scale factor, which corresponds to the highest resolution in M_X^2.

5.3 Event selection with the recoil detector

A more refined selection of elastic DVCS events is possible through the inclusion of additional information provided by the recoil detector. The increase in purity is, however, accompanied by a decrease in statistics due to, among others, the reduced acceptance. The additional requirements imposed on the exclusive sample, described previously, are explained in following. The first part treats more specifically the selection of protons and summarily the rejection of events in which photons are present; the last part describes the imposed kinematic constraints.

5.3.1 Proton selection

A very basic constraint is placed on the number of detected charged particles, namely, the detection by the recoil tracking detectors of exactly 1 positively charged particle in the absence of detection of negatively charged particles is required. The event selection had been cross-checked up to this point in an independent analysis. The cross-check resulted in a perfect agreement for a sample of 126439 DIS events out of which 73 events satisfying the presently treated exclusive constraints were selected.

As described in section 3.4, several track parametrizations, corresponding to different track hypotheses, can be provided for a reconstructed particle with positive charge. To determine the order in which the provided hypotheses need to be considered for an optimal tracking resolution, the generated and reconstructed momentum of protons from the exclusive sample are compared. This comparison is shown in figure 5.7. For the selection procedure presented on the left-hand side of figure 5.7, first the proton hypothesis is favored; if this hypothesis is not acceptable, with the χ^2 of the fit to the track restricted to values smaller than 100, the stopped-proton hypothesis is considered; in the absence of the latter, the track parameters provided for the pion hypothesis are chosen; finally, if also the pion hypothesis
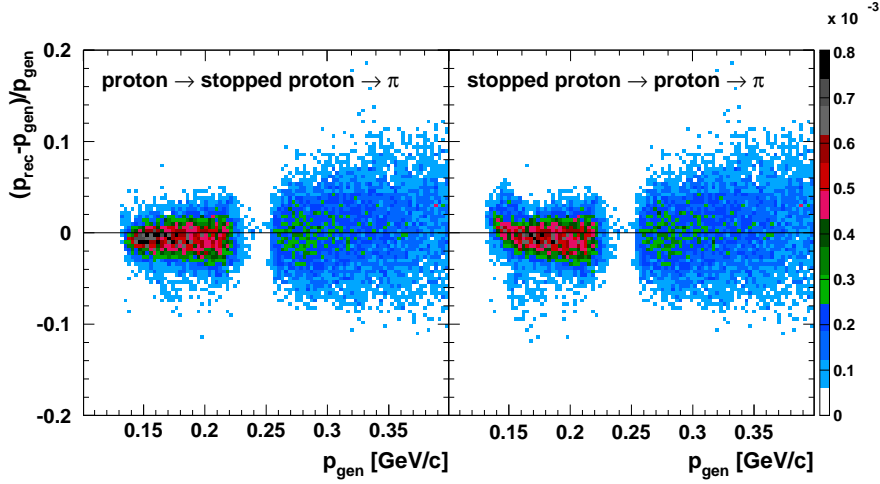
Figure 5.7: Comparison of the reconstructed and generated momentum for two sequences of track-hypothesis selection. For more details, see text.

is not acceptable, the event is rejected. For the other selection sequence, shown on the right-hand side, the stopped-proton hypothesis is considered before the proton hypothesis. As can be seen, the first selection sequence results in a superior track reconstruction, and is thus adopted subsequently.

What can also be observed in figure 5.7, is the absence of events for momenta around ~ 0.24 GeV/c. This finds its origin in the track-reconstruction algorithm. Protons with momenta below 0.24 GeV/c are stopped in material located in front of the scintillating-fiber tracker, i.e., in the target cell, the silicon-strip detector or the scattering chamber. Protons with momenta above 0.26 GeV/c reach the outer barrel of the scintillating-fiber tracker. Protons in the intermediate momentum range leave a signal in the silicon-strip detector and possibly in the inner barrel of the scintillating-fiber tracker, but not in the outer barrel. Because the two layers of the silicon-strip detector are separated by a small distance from each other, but located at a large distance from the scintillating-fiber tracker, 2 space points in the silicon-strip detector originating from the same particle can easily be combined with a space point from the inner barrel of the scintillating-fiber tracker to form a track. As during the track reconstruction it is impossible to determine with certainty if the space point from the scintillating-fiber tracker indeed is associated with the signals in the silicon-strip detector, two tracks are reconstructed: one track is reconstructed from the signals in the silicon-strip detector only, while the other track also includes the space point from the scintillating-fiber tracker. Because of the restriction imposed on the number of detected particles, these events are discarded from the sample.

However, studies on the Monte-Carlo simulation have revealed that for more than 96% of the exclusive events in which exactly 2 positively charged particles are reconstructed, only 1 particle is actually present. This finding is visualized as a function of the particle's momen-

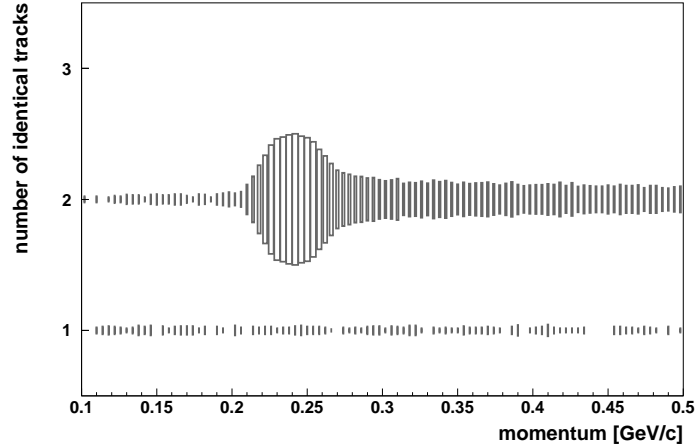Figure 5.8: Distribution of events that contain 2 tracks associated with the same generated particle (number of identical tracks = 2) and that contain 2 tracks each associated with a different particle (number of identical tracks = 1), as a function of the momentum of one of the reconstructed particles.

tum in figure 5.8. The figure represents the distribution of events in which the same particle is reconstructed twice (number of identical tracks = 2) and in which only one track is reconstructed per particle (number of identical tracks = 1), as a function of the momentum of one of the reconstructed particles [6]. As can be seen, for the majority of events at momenta of ∼ 0.24 GeV/c only 1 particle is present, while 2 tracks are reconstructed. This is also observed at higher momenta. For momenta below 0.21 GeV/c, 2-track events in which 1 or 2 particles are generated are equally distributed. For more than 96% of the erroneously reconstructed 2-track events, the pion and proton hypothesis are provided for one particle, while for the other particle only the proton hypothesis [7] is supplied. The latter particle reconstruction corresponds to a track formed of 2 space points in the silicon-strip detector only, while the former represents a track of 3 space point, i.e., including also the space point from the inner scintillating-fiber tracker. On the other hand, for less than 18% of the events in which 2 positively charged particles are generated, this same configuration of track hypotheses is observed. Thus, provided that the appropriate track-hypothesis configuration is present, one can include the events in which 2 positively charged particles are reconstructed to the exclusive sample. This increases the statistics for exclusive events in which 1 proton is present by 15%, while the contamination of 2-particle events to the total sample lies below 0.1%.

---

[6]The difference in momentum between 2 reconstructed particles that are associated with the same generated particle is on average centered around 0. As such, the reconstructed momentum is representative for both tracks. The same assertion is valid for the polar and azimuthal angle. For events in which 2 particles are generated, evidently no statement can be made.

[7]The stopped-proton hypothesis might also be provided, but as stated above, the proton hypothesis is favored over the stopped-proton hypothesis.
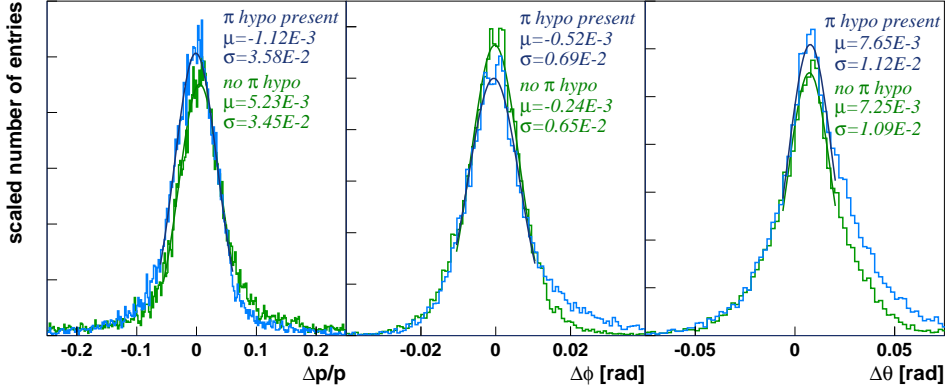
Figure 5.9: Comparison between the Monte-Carlo generated and reconstructed momentum of particles with tracks formed of 2 (green) and 3 space points (blue) for events in which 2 positively charged particles are reconstructed. The given values for μ and σ represent the result of the indicated fit of a Gauss distribution.

For these 2-track events, the appropriate selection of track parameters is determined from the distributions shown in figure 5.9. Here, the generated and reconstructed momentum, polar angle and azimuthal angle from the proton hypotheses are compared for protons reconstructed from 2 space points (green) and from 3 space points (blue). Based on the mean and width of the distributions, the parameters from the tracks with 3 space points are chosen and subsequently used.

The effect on the momentum distribution of the here described treatment of 2-track events is shown in figure 5.10, with on the left-hand side the momentum distribution for experimental data collected in 2006, in the center the reconstructed-momentum distribution for the Monte-Carlo simulation, and on the right-hand side the corresponding generated-momentum distribution. The blue curve represents single-track events, the green curve represents the events in which 2 positively charged particles are reconstructed with the appropriate aforementioned track hypotheses, and the gray curve represents the sum of both. In accordance with figure 5.8, the majority of recovered 2-track events are located at momenta around 0.24 GeV/c and higher, while only a very small fraction is located at momenta below 0.21 GeV/c. Comparing the distributions for the generated and reconstructed tracks from the Monte-Carlo simulation, it is clear that there is still room for improvement. Nevertheless, the presented procedure is acceptable for a preliminary study. The recovered 2-track events will be denoted in the following as 1-track events.

It has to be noted that the momentum distribution for the experimental data collected in 2007 shows a different behavior, because it stems from an older data production with a track-reconstruction algorithm that differs in certain aspects. No discontinuity is observed in the momentum distribution for 1-track events, and the statistics gained by the inclusion of 2-track events is negligible. Nevertheless, the same procedure is applied for the selection of data collected in 2007.

113
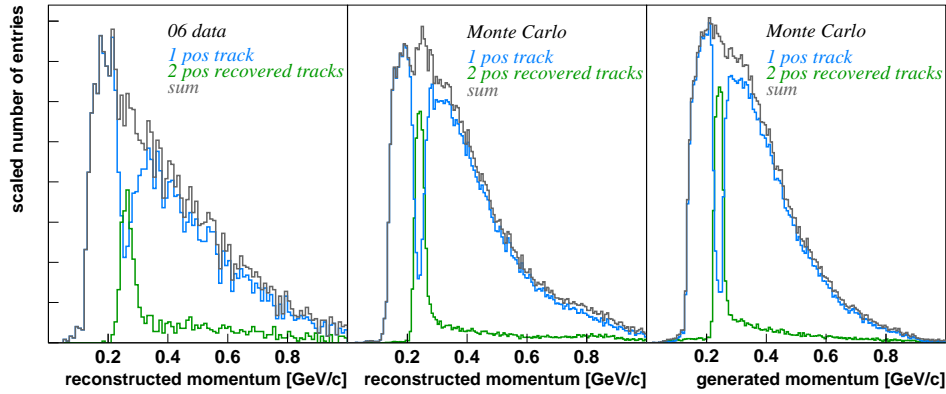
Figure 5.10: Momentum distribution for events in which 1 positively charged particle (blue) and 2 positively charged particles with appropriate track hypothesis (green) are reconstructed; the sum of both distributions is represented in gray. The distribution is shown for reconstructed tracks from experimental data collected in 2006 (left), reconstructed tracks from the Monte-Carlo simulation (center), and for the generated Monte-Carlo particles (right).

Finally, protons can be identified using particle-identification information provided by the silicon-strip detector and the scintillating-fiber tracker. The PID distributions for various momentum ranges are shown in figure 5.11 for the presently selected particles from the Monte-Carlo simulation (left) and from experimental data (right). As can be seen, the PID distribution for data is shifted towards negative values, as was already shown in figure 4.54. However, the different event configuration and aimed purpose allow now for a momentum-independent PID cut, which for data is chosen at -2, while for the Monte-Carlo simulation it is set to 0. Studies on the Monte-Carlo simulation have shown that a higher threshold for the PID value does not result in a significant increase in purity. Indeed, varying the PID threshold from 0 to 5 only increases the fractional amount of protons from 98.89% to 99.03%. The remaining 1% corresponds in majority to unidentified particles [8], while a very small fraction ($< 0.03\%$) can be attributed to signals from pions and kaons. On the other hand, for PID values smaller than 0, 92% pions and 5% protons are found, while another 2% stems from unidentified particles.

5.3.2 Rejection of photons

The algorithm for the identification by the photon detector of signals originating from neutral particles is described in section 4.12, and is put to use for the selection of elastic DVCS events. Any event in which at least 1 neutral particle is detected is excluded from the exclusive sample. The performance of the photon detector for the presently described event sample is

---

[8]The unknown identity of these particles is only a result of the algorithm used to link a reconstructed track with a generated particle, and points either to tracks reconstructed from signals generated by different particles, or to tracks formed of 2 space points of which one originates from the scintillating-fiber tracker (see also subsection 4.12.2).
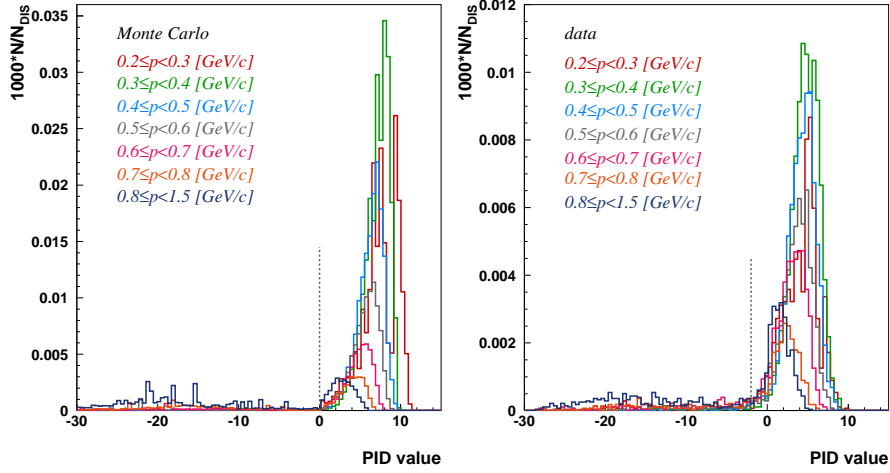
Figure 5.11: PID distribution for particles from the exclusive sample detected in the recoil detector for the Monte-Carlo simulation (left) and for experimental data (right). The various represented distributions correspond to the different momentum ranges indicated in the figure; the vertical line indicates the PID cut for the selection of protons.

treated in the next section.

5.3.3 Imposed kinematic constraints using the recoil detector

The reconstruction of the proton, in addition to the scattered lepton and radiated photon, allows to further enhance the fractional contribution from elastic DVCS. To this effect two additional constraints are proposed in reference [110], and included in the present analysis. Both constraints relate to transverse components only, as the resolution in the plane transverse to the beam line is superior to the resolution in the longitudinal direction. The first proposed constraint is placed on the azimuthal angle $\phi_{miss,p}$ between the transverse missing momentum reconstructed from the information provided by the forward spectrometer ($\vec{p}_{t,miss}$) and the transverse momentum of the proton reconstructed by the recoil detector ($\vec{p}_{t,p}$). The second requirement concerns the ratio of the norm of the two transverse-momentum components, i.e., $p_{t,miss}/p_{t,p}$. The distributions of both quantities are shown in figure 5.12 for the events selected from the Monte-Carlo simulation (gray) and from experimental data. The distributions obtained from data are shown without the photon-energy correction discussed in subsection 5.2.4 (light blue), with the time-dependent correction only (dark blue), and with the time-dependent and global correction (red). The results of a Gaussian fit within a window of 0.15 around the mean are also given for the $p_{t,miss}/p_{t,p}$ distribution. As can be seen, the total photon-energy correction has a small but beneficial influence, whereas the application of the time-dependent correction only results in a increased spread of the distribution, as is

115
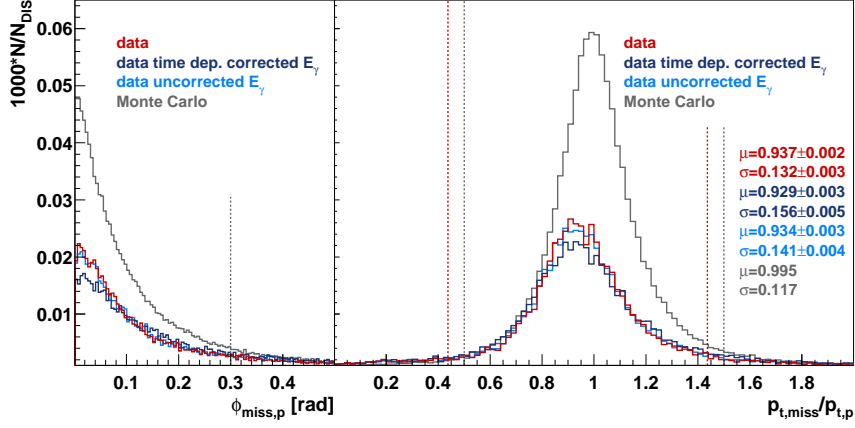
Figure 5.12: Distributions in $\phi_{miss,p}$ (left) and $p_{t,miss}/p_{t,p}$ (right) for Monte-Carlo data (gray) and for experimental data (blue and red). The vertical lines delimit the range of allowed values, according to the proposal from reference [110]. The parameters μ and σ correspond to the parameters of a Gaussian fit in a window of 0.15 around μ.

also observed for the missing-mass distribution. However, it is clear that the distributions from the Monte-Carlo simulation and from data differ in width, mean position and statistics. The latter point will be addressed further; for the other points, a possible explanation might be found in the misalignment of the recoil detector with respect to the forward spectrometer. This forms at present a subject of study.

The constraints proposed in reference [110] restrict $\phi_{miss,p}$ to values below 0.3 rad, as indicated by the vertical line in figure 5.12 (left), and $p_{t,miss}/p_{t,p}$ to values between 0.5 and 1.5, indicated by the gray vertical lines in figure 5.12 (right). Because of the observed shift in mean position for the latter distribution from data, the allowed range for $p_{t,miss}/p_{t,p}$ is adjusted accordingly to 0.437 for the lower limit and 1.437 for the upper limit. This adjustment is indicated in figure 5.12 (right) by the red vertical lines. The constraint on $\phi_{miss,p}$ for the experimental data is left unaltered.

It has to be noted that the proposed constraints and potentially their values do not necessarily represent the optimal choice, and that (with a better understanding of the detectors) improvement is possible, e.g., via the implementation of kinematic fitting as a method to select elastic DVCS events. This approach is currently under development, and has shown to give good results on Monte-Carlo data [111]. For the application on experimental data, the estimation of the errors on the kinematic parameters remains at present an open point [112].

Table 5.2 summarizes the constraints imposed on the kinematic variables for the selection of DIS events, single-photon events, and exclusive events using information from the forward spectrometer and the recoil detector.

DIS events	$\nu < 22\,\text{GeV}$
	$W^2 > 9\,\text{GeV}^2$
	$Q^2 > 1\,\text{GeV}^2$
single-photon events	$E_\gamma > 5\,\text{GeV}$
exclusive events	$5\,\text{mrad} < \theta_{\gamma^*\gamma} < 45\,\text{mrad}$
	$-t_c < 0.7\,\text{GeV}^2$
	$Q^2 < 10\,\text{GeV}^2$
	$0.03 < x_B < 0.35$
	$-1.79\,\text{GeV}^2 < M_X^2 < 3.35\,\text{GeV}^2$
recoil detector	$\phi_{miss,p} < 0.3\,\text{rad}$
	$0.437 < p_{t,miss}/p_{t,p} < 1.437$

Table 5.2: Cuts on kinematic variables applied for the selection of DIS events, single-photon events, and exclusive events using the forward spectrometer and the recoil detector. For the selection of events on Monte-Carlo data, the constraints on M_X^2 and $p_{t,miss}/p_{t,p}$ are slightly modified (see text).

5.4 Monte-Carlo studies

This section first gives a short explanation on the Monte-Carlo simulation used for the analysis of DVCS. Then studies on Monte-Carlo data are presented and compared to experimental data in order to gain insight into the extracted exclusive sample.

5.4.1 Monte-Carlo simulation

For all Monte-Carlo studies shown in the present chapter, two generators are of importance: one for the simulation of semi-inclusive neutral-meson production, and one for the simulation of elastic and associated BH and elastic DVCS. Other exclusive processes, with exclusive π^0 production forming the dominant contribution, are not included in the present Monte-Carlo simulation. This may affect the estimates of the signal-to-background ratios. The overall contribution from exclusive π^0 production, however, was estimated in reference [113] to be $0.4 \pm 0.4\%$ for the exclusive DVCS sample selected with information from the forward spectrometer only.

The gmc_dvcs generator [105] is used for the simulation of BH and DVCS events. The modeling of the elastic BH process is built on the Mo–Tsai formalism [114]. For the associated BH production, the Brasse parametrization [115] is used to calculate the inclusive cross section $\frac{d\sigma_{\gamma^*p}}{dWdQ^2}$. Up to the $\Delta(1232)$ resonance single-meson production is simulated. The separation of the inclusive cross section into the single-meson sub-processes is based on MAID [116]. For the higher resonance region, the remaining inclusive cross section is attributed to multi-meson production. An isotropic angular distribution of the decay products is here assumed; for the single-meson production MAID provides the angular dependence of the decay.

The simulation of elastic DVCS is based on 5 different GPD models discussed in reference [43]. These models include the GPDs H, $\tilde{H}$ and E, relevant for DVCS on an unpolarized

117

target. The parametrization of the GPDs is taken from reference [35]. For the comparison of kinematic distributions from the Monte-Carlo simulation and from experimental data it is preferable not to include the elastic DVCS process in the simulation, because of the uncertainties arising from the model dependence. The simulation of elastic DVCS is, however, used at HERMES for the study of systematic uncertainties entering the extraction of asymmetries. This point is not addressed in the present work, and thus the elastic DVCS process is not considered in the Monte-Carlo simulation.

Currently only very little is known about associated DVCS. Because of the absence of proper estimates for this process at HERMES, it is not simulated in the Monte Carlo.

The generation of semi-inclusive DIS events is performed by gmc_disng. This generator is based on LEPTO [117], which simulates complete events for deep-inelastic leptoproduction off unpolarized nucleons. The modeling of the fragmentation process and of the decay of unstable particles is done by JETSET [118], a program using the LUND string model [119]. JETSET was originally tuned to results of high-energy experiments, but was adapted to the energy scale of HERMES [120]. Although radiative processes are also simulated in gmc_disng through RADGEN [121], a better agreement between experimental data and the Monte-Carlo simulation is obtained when only using gmc_disng to simulate semi-inclusive contributions and gmc_dvcs to simulate the elastic and associated BH processes [105].

The subsequent treatment by the HERMES Monte Carlo of the various generated particles has been addressed in section 4.3.

5.4.2 Comparison between experimental and simulated data

In the following a comparison between the kinematic distributions obtained from experimental data and from the Monte-Carlo simulation is presented. The Monte-Carlo data are herewith divided into the different contributions from elastic BH, associated BH, and semi-inclusive DIS. The main contributions to semi-inclusive photon production stem from semi-inclusive π^0 ($> 80\%$) and η ($\sim 15\%$) production [103], where either one photon escapes the HERMES acceptance or the spatial resolution of the calorimeter does not allow to individually distinguish both decay photons. The kinematic distributions are presented for exclusive events selected with the forward spectrometer only and for exclusive events selected with the additional recoil-detector information. The constraints on the missing mass and on $p_{t,miss}/p_{t,p}$ are adjusted separately for data and Monte Carlo, as explained previously. The normalization of the Monte-Carlo data is adjusted in order to allow for a better visual comparison of the distributions, except for the missing-mass distribution. This distribution is also not restricted to the exclusive missing-mass range but shown over a larger interval.

The distributions for the exclusive event sample selected with the forward spectrometer only are shown in figure 5.13. Apart from the discrepancy in yield, a good agreement between experimental data and Monte-Carlo data is observed. The disagreement for the ϕ distribution is expected, since the Monte-Carlo simulation does not include the DVCS processes.

From the distributions in x_B and Q^2, it is clear that the cuts imposed on these two quantities ($0.03 < x_B < 0.35$ and 1 GeV$^2 < Q^2 < 10$ GeV^2) reject a negligible fraction of valuable data. The same is true for the constraint on E_γ, as DVCS photons mainly have energies above 5 GeV.

While for the t_c distribution experimental data and Monte-Carlo data agree, a relative shift
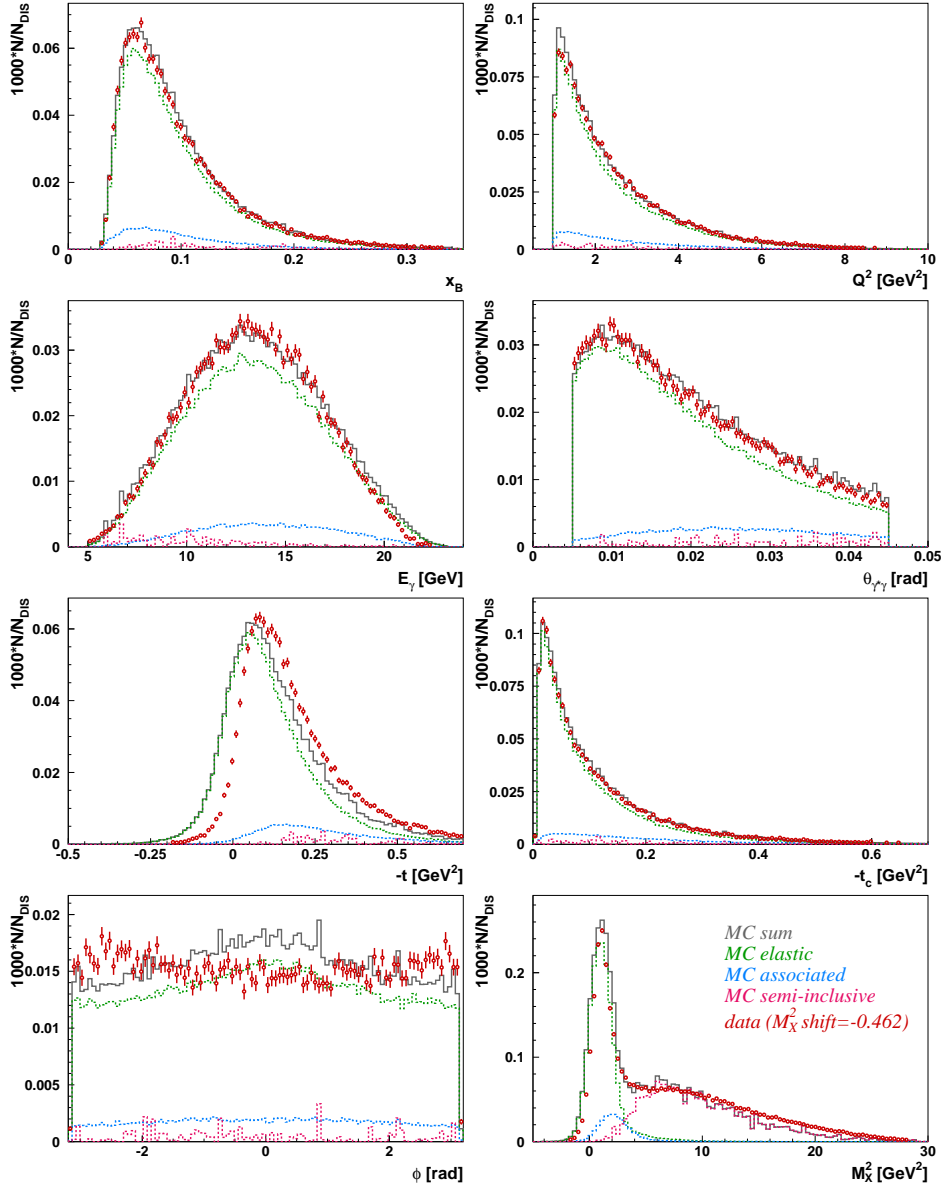
Figure 5.13: Kinematic distributions for exclusive events obtained from experimental data and from the Monte-Carlo simulation. The normalization of the Monte-Carlo simulation is adjusted for a better comparison, except for the missing-mass distribution. The latter distribution is also not restricted to the exclusive missing-mass range but shown over a larger interval.

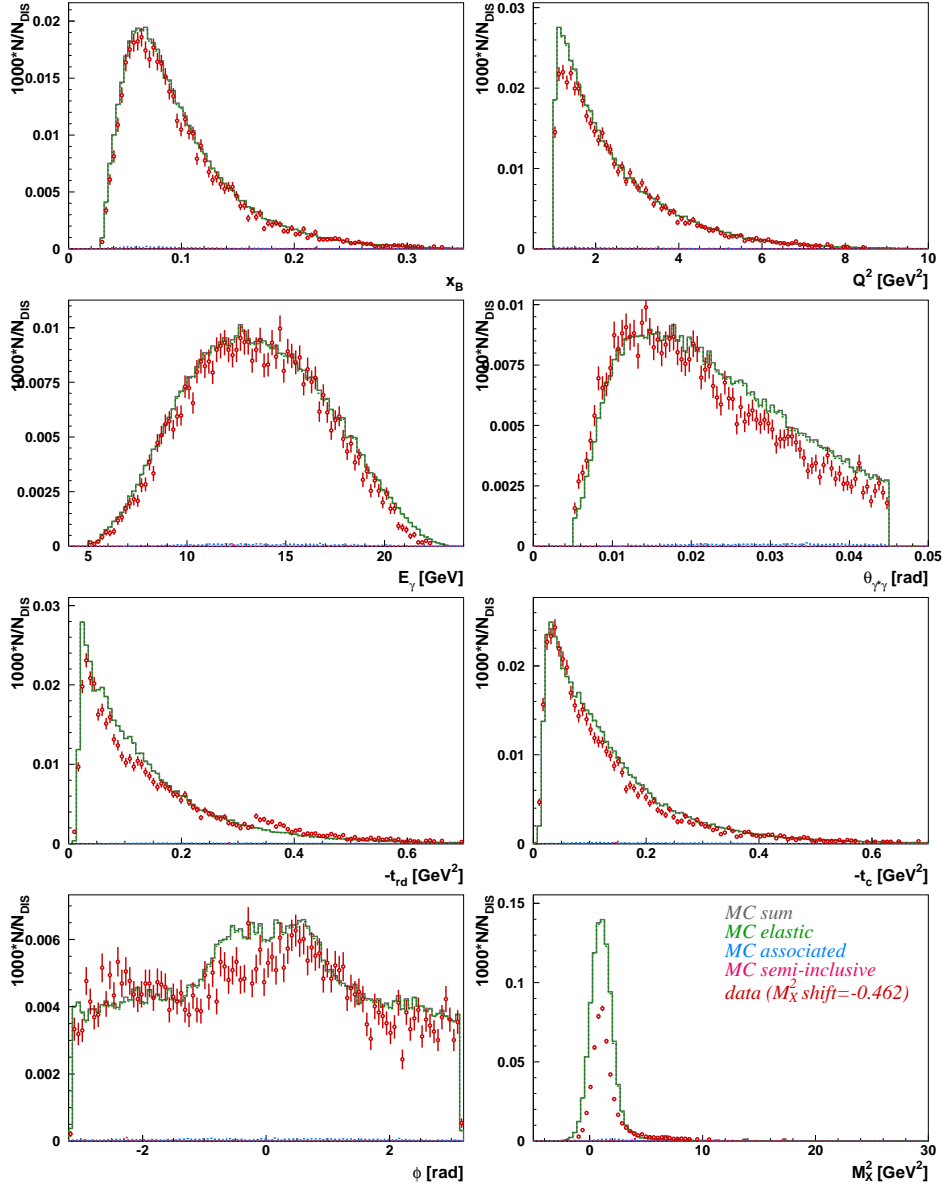Figure 5.14: Kinematic distributions for exclusive events obtained from experimental data and from the Monte-Carlo simulation using additional information provided by the recoil detector. The normalization of the Monte-Carlo simulation is adjusted for a better comparison, except for the missing-mass distribution. The latter distribution is also not restricted to the exclusive missing-mass range but shown over a larger interval.

is observed for t. This can be attributed to the photon-energy reconstruction. The limited resolution of this reconstruction causes the distribution in $-t$ to extend down to negative values, both for experimental and simulated data. From the simulated distribution it can be observed that the associated BH and semi-inclusive DIS events are located at higher values in $-t$ than the elastic BH events. The assumption on M_X introduced for the calculation of t_c does, however, systematically shift the background distributions to lower values in $-t_c$.

Finally, the missing-mass distribution is shown. While most of the semi-inclusive background is located at high M_X^2 values, it is clear that the limited resolution does not allow for the separation of associated production, i.e., associated BH and associated DVCS, at low M_X^2 values.

The comparison between experimental and simulated data for exclusive events selected with the inclusion of the recoil-detector information described in section 5.2 is shown in figure 5.14. In general a less good agreement between experimental and Monte-Carlo data is observed. Also, the overestimate in yield by the Monte-Carlo simulation is larger for the present event selection than for the event selection involving only the forward spectrometer. One obvious cause is inefficiencies of recoil-detector components, which apart from the deactivation of the n-sides of the two outer silicon-strip sensors from quadrant 2, are not accounted for in the Monte-Carlo simulation. Additionally, noise hits in the photon detector are not simulated, leading thus to a reduced event rejection for the Monte-Carlo data.

Figure 5.14 shows that the imposed constraints on x_B, Q^2, and E_γ are also suited for the selection of exclusive events with the recoil detector. The constraint imposed on $\theta_{\gamma^*\gamma}$ might be reconsidered, since the justification for the upper limit on this variable partially finds its origin in the rejection of background. The background contribution is now drastically reduced, as can be seen from the presented distributions. This point is more explicitly addressed further. Examining, in analogy to figure 5.3, $\theta_{\gamma^*\gamma}$ as a function of ϕ for single-photon events in the exclusive missing-mass region with the additional requirement that a proton is detected in the recoil detector shows that increasing the upper limit on $\theta_{\gamma^*\gamma}$ is not beneficial for the uniformity of the acceptance. The distribution is shown in figure 5.15. It is less peaked at $\phi = 0$ compared to data selected with the forward spectrometer only, because of the reduction in background. However, the upper limit on $\theta_{\gamma^*\gamma}$ of 45 mrad remains an appropriate choice in view of the uniformity of the acceptance.

Compared to the data sample selected with the forward spectrometer only, the distribution in $-t_c$ is slightly shifted towards higher values, i.e., from 0.12 GeV^2 to 0.13 GeV^2. This can be related to the detection threshold for protons in the recoil detector, which amounts to 0.13 GeV/c in momentum. This detection threshold results in a lower limit on the absolute value of the squared four-momentum transfer to the nucleon of 0.017 GeV^2. In the comparison between data selected with the forward spectrometer only and data selected with the inclusion of recoil-detector information, the influence of the background contributions, located at higher values in $|t_c|$, should also not be forgotten. Indeed, the Monte-Carlo simulation indicates that for pure elastic BH events selected with the spectrometer, the mean $-t_c$ amounts to 0.10 GeV^2. The inclusion of the recoil detector results in a mean of 0.13 GeV^2, the value obtained from experimental data. Finally, the modified acceptance can also have an influence on the $-t_c$ distribution obtained using recoil-detector information.

With the detection of the recoil proton, the squared four-momentum transfer to the proton can be calculated directly from the momentum reconstructed by the recoil detector. This
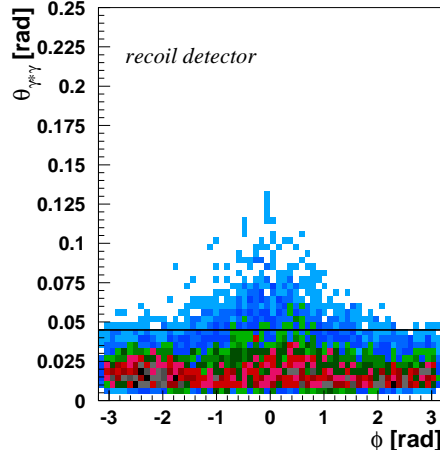
Figure 5.15: Photon opening angle $\theta_{\gamma^*\gamma}$, with $\theta_{\gamma^*\gamma} > 5$ mrad, as a function of the angle ϕ for single-photon events in the exclusive missing-mass region for which in addition a proton is detected by the recoil detector.

quantity, denoted as t_{rd}, has a higher resolution than t_c for values above $-0.2\,\mathrm{GeV}^2$, while for smaller values t_c is reconstructed more precisely [122]. In view of the Ji relation, discussed in chapter 2, the use of t_{rd} is thus preferable. However, to allow for a direct comparison between events selected with and without the recoil detector, the variable t_c is used in the following. In order to satisfy the factorization theorem the constraint imposed on this variable is not altered. The distribution in t_{rd} is also shown in figure 5.14. The discontinuity in the distribution for experimental data at $-t_{rd} \approx 0.35\,\mathrm{GeV}^2$ originates from the sample of data collected in 2007; it is related to the omission of energy losses in inactive detector material for the reconstruction of protons with momenta above 0.6 GeV/c. The small dip at $-t_{rd} \approx 0.045\,\mathrm{GeV}^2$ and subsequent shoulder are attributed to the special treatment of 2-track events in the recoil detector, which affects momenta around 0.21 GeV/c, as discussed in subsection 5.3.1.

The recoil detector slightly favors values of $\phi = 0$ compared to events selected with the spectrometer only. This enhancement can be understood on the level of detector acceptance knowing that for DVCS and BH events at HERMES the real photon is emitted in a cone around the virtual photon, and mainly observed at the inner edges of the calorimeter, spread around the beam line. For low values of Q^2, corresponding to azimuthal angles of $\pm\pi/2$ for the virtual photon and scattered lepton, values of $\phi = 0$ are slightly disfavored, while for high Q^2 values, with the virtual photon and scattered lepton located along the diagonal in the transverse plane, values of $\phi = 0$ are slightly favored. Because of the active detection of protons by the diamond-shaped silicon-strip detector and the scintillating-fiber tracker, an enhancement of events with virtual photons along the diagonal, thus with $\phi \approx 0$, is expected. This is indeed observed in figure 5.14. However, for the interpretation of the distribution obtained from experimental data, the inefficiencies of the recoil detector also need to be taken into account. The azimuthal angle of the proton reconstructed by the recoil detector is shown

122
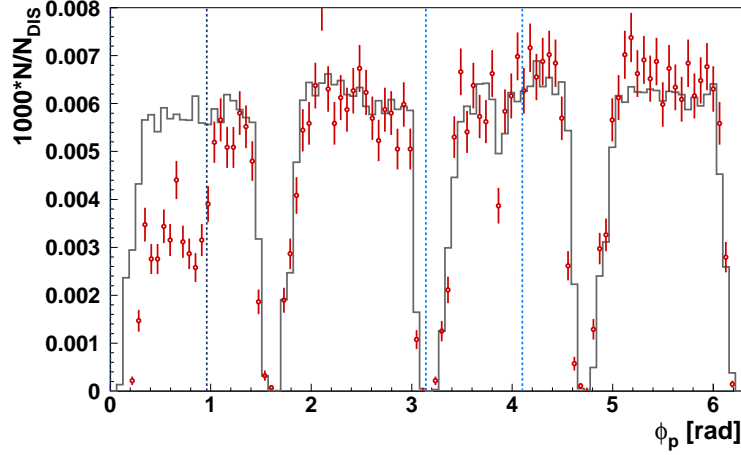
Figure 5.16: Distribution in the azimuthal angle of protons detected by the recoil detector for experimental data (red) and Monte-Carlo data (gray). The normalization of the Monte-Carlo data is adjusted for a better comparison.

in figure 5.16 for experimental data (open symbols) and Monte-Carlo data (histogram). The effect of the inefficiencies in the first half of quadrant 2, i.e., for azimuthal angles below 1 rad, on the detection of protons is clearly visible. The range in ϕ covered by protons detected in this quadrant half is shown in figure 5.17 (top), as represented by the dark blue symbols. Protons detected in the first half of quadrant 4, indicated by the light blue vertical lines in figure 5.16, cover the same range in ϕ, and are also shown in figure 5.17, represented by the light blue symbols. Comparing the range in ϕ covered by protons detected in these quadrant halves with the range in ϕ covered by protons detected in the remaining part of the recoil detector, shown in the bottom panel of figure 5.17, gives some clarification on the observed ϕ distribution. The first halves of quadrant 2 and 4 cover ranges in ϕ centered around -0.8 rad and 2.3 rad. These can be related to the decrease in statistics observed for the ϕ distribution in figure 5.14.

5.4.3 Impact of the recoil detector on the selection of DVCS events

According to the Monte-Carlo simulation, the recoil detector can reduce the background contribution to the sample of exclusive events to below 1%. The effect of various requirements imposed on particles detected in the recoil detector is summarized in table 5.3. The first row indicates the contributions from elastic BH, associated BH and semi-inclusive DIS to the total exclusive sample selected with information provided by the forward spectrometer. Associated BH forms, with 11%, the dominant background contribution. The detection of exactly one charged particle identified as a proton (2nd row) reduces this contribution down to 5%. If in addition the absence of neutral particles is required (3rd row), associated BH contributes only 2%. This reduction in background is of the same magnitude as the requirement that a proton
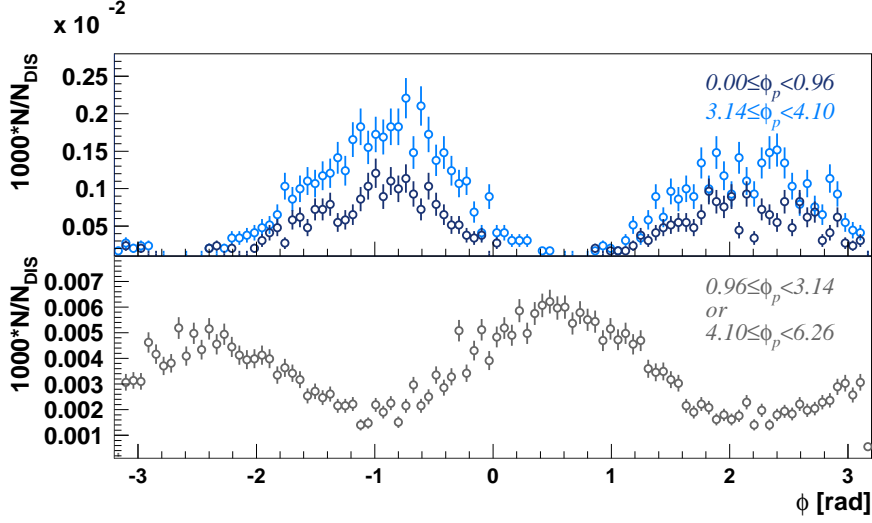
Figure 5.17: Regions in ϕ covered by the various recoil-detector parts indicated in figure 5.16: first half of quadrant 2 (top, light blue) and 4 (top, dark blue), and the remaining recoil-detector area (bottom, gray).

is detected and that it satisfies the restrictions imposed on $\phi_{miss,p}$ and $p_{t,miss}/p_{t,p}$ (4th row). The combination of these constraints (5th row) finally reduces the total background contribution down to less than 1%. The last row in table 5.3 indicates that particle identification has a small but beneficial influence on the rejection of background events: solely requiring the detection of a positively charged particle, without actively identifying it as a proton, brings the background contribution above 1%. With the reduction in background to below 1% the recoil detector satisfies the originally proposed requirements for the analysis of DVCS [110].

The asymmetries are eventually extracted in 4 bins of $-t_c$, x_B, and Q^2. The fractional contributions from the subprocesses in each of these bins is given for the exclusive sample selected with the forward spectrometer only in table 5.4 and for the exclusive sample se-

	el. BH	as. BH	SIDIS
spec.	$86.20 \pm 0.30\%$	$11.12 \pm 0.07\%$	$2.70 \pm 0.30\%$
1 p	$94.60 \pm 0.10\%$	$4.98 \pm 0.05\%$	$0.38 \pm 0.10\%$
1 p & no γ	$97.90 \pm 0.08\%$	$1.93 \pm 0.03\%$	$0.17 \pm 0.07\%$
1 p & copl.	$97.80 \pm 0.08\%$	$2.09 \pm 0.03\%$	$0.11 \pm 0.08\%$
1 p, no γ & copl.	$99.06 \pm 0.03\%$	$0.92 \pm 0.02\%$	$0.02 \pm 0.02\%$
1 'p', no γ & copl., no PID	$98.65 \pm 0.05\%$	$1.29 \pm 0.03\%$	$0.06 \pm 0.04\%$

Table 5.3: Fractions of elastic BH, associated BH and semi-inclusive DIS events for various criteria on the data selection. For the explanation of the outer left column, see text.

	el. BH	as. BH	SIDIS
$-t_c$			
$0.00 - 0.06$	$93.52 \pm 0.43\%$	$5.18 \pm 0.06\%$	$1.30 \pm 0.45\%$
$0.06 - 0.14$	$86.35 \pm 0.60\%$	$10.73 \pm 0.12\%$	$2.93 \pm 0.67\%$
$0.14 - 0.30$	$78.31 \pm 0.67\%$	$17.43 \pm 0.20\%$	$4.26 \pm 0.80\%$
$0.30 - 0.70$	$67.34 \pm 0.74\%$	$27.58 \pm 0.39\%$	$5.08 \pm 0.97\%$
x_B			
$0.03 - 0.07$	$89.01 \pm 0.32\%$	$10.20 \pm 0.09\%$	$0.79 \pm 0.35\%$
$0.07 - 0.10$	$86.32 \pm 0.74\%$	$10.60 \pm 0.13\%$	$3.08 \pm 0.82\%$
$0.10 - 0.15$	$85.29 \pm 0.55\%$	$12.08 \pm 0.14\%$	$2.64 \pm 0.62\%$
$0.15 - 0.35$	$79.67 \pm 0.89\%$	$13.15 \pm 0.21\%$	$7.18 \pm 1.02\%$
Q^2			
$1.0 - 1.5$	$89.50 \pm 0.70\%$	$8.40 \pm 0.11\%$	$2.11 \pm 0.76\%$
$1.5 - 2.3$	$86.93 \pm 0.53\%$	$10.75 \pm 0.12\%$	$2.31 \pm 0.58\%$
$2.3 - 3.5$	$84.51 \pm 0.57\%$	$12.34 \pm 0.14\%$	$3.16 \pm 0.64\%$
$3.5 - 10.0$	$81.56 \pm 0.43\%$	$14.71 \pm 0.16\%$	$3.72 \pm 0.48\%$

Table 5.4: Fractional contributions from elastic BH (el. BH), associated BH (as. BH), and semi-inclusive DIS (SIDIS) for data selected with information from the forward spectrometer only. The variables $-t_c$ and Q^2 are expressed in GeV^2.

	el. BH	as. BH
$-t_c$		
$0.00 - 0.06$	$99.84 \pm 0.02\%$	$0.16 \pm 0.02\%$
$0.06 - 0.14$	$99.29 \pm 0.03\%$	$0.71 \pm 0.03\%$
$0.14 - 0.30$	$98.52 \pm 0.10\%$	$1.39 \pm 0.06\%$
$0.30 - 0.70$	$97.06 \pm 0.14\%$	$2.94 \pm 0.14\%$
x_B		
$0.03 - 0.07$	$99.20 \pm 0.04\%$	$0.81 \pm 0.04\%$
$0.07 - 0.10$	$99.15 \pm 0.04\%$	$0.85 \pm 0.04\%$
$0.10 - 0.15$	$99.06 \pm 0.05\%$	$0.94 \pm 0.05\%$
$0.15 - 0.35$	$98.53 \pm 0.18\%$	$1.29 \pm 0.08\%$
Q^2		
$1.0 - 1.5$	$99.36 \pm 0.04\%$	$0.64 \pm 0.04\%$
$1.5 - 2.3$	$99.12 \pm 0.04\%$	$0.88 \pm 0.04\%$
$2.3 - 3.5$	$98.99 \pm 0.05\%$	$1.01 \pm 0.05\%$
$3.5 - 10.0$	$98.58 \pm 0.13\%$	$1.30 \pm 0.06\%$

Table 5.5: Fractional contributions from elastic BH (el. BH) and associated BH (as. BH) for data selected with the inclusion of recoil-detector information. The variables $-t_c$ and Q^2 are expressed in GeV^2.

lected with the inclusion of recoil-detector information in table 5.5. Because of the restricted amount of statistics generated for the simulation of semi-inclusive DIS, the fractional contribution from this process is not explicitly given for the data sample involving the recoil detector. For events selected with the forward spectrometer, the fractional contribution from associated BH rises strongly with $-t_c$; for the semi-inclusive DIS contribution this rise is softer. A positive correlation between the fractional contributions from the two categories of background processes and the kinematic variables x_B and Q^2 also exists, but it is less pronounced. A similar dependence of the associated-BH contribution on the kinematic variables is also observed for data selection involving the recoil detector, except that the rise as a function of $-t_c$ is steeper.

The enhanced purity of the exclusive sample using the recoil detector, however, is accompanied by a significant loss in statistics. Table 5.6 shows the effect of the various requirements presented in table 5.3 on the fractional amount of collected statistics with respect to data selected with the spectrometer only. The second column represents the fractions for the Monte-Carlo simulation, the third column gives the results for experimental data, and the last column compares the fraction of experimental data with respect to Monte-Carlo data. According to the Monte-Carlo simulation, less than 50% of the original exclusive sample remains after the application of all constraints related to the recoil detector. Already solely the detection of a proton reduces the event yield by more than 40%. The situation for experimental data is at present different. Here, less than 30% of the original data sample satisfies all imposed constraints. The requirement of 1 charged particle identified as a proton already leads to a further reduction compared to the Monte-Carlo simulation. Even when excluding the less efficient quadrants, the comparison between experimental and Monte-Carlo data does not improve significantly, e.g., the ratio increases from 56% to 60% for the requirement involving only the detection of exactly 1 positively charged particle. Comparing the distribution in number of tracks reconstructed by the recoil detector for exclusive events from the Monte-Carlo simulation and the experimental data, a small excess of 2-track and 3-track

	MC wrt. spec.	data wrt. spec.	data wrt. MC
spec.	100%	100%	$79.2 \pm 0.5\%$
1 p	$57.1 \pm 0.2\%$	$40.0 \pm 0.2\%$	$55.5 \pm 0.5\%$
1 p & no γ	$54.9 \pm 0.2\%$	$35.1 \pm 0.2\%$	$50.6 \pm 0.4\%$
1 p & copl.	$49.2 \pm 0.2\%$	$32.3 \pm 0.2\%$	$52.0 \pm 0.5\%$
1 p, no γ & copl.	$48.3 \pm 0.2\%$	$29.2 \pm 0.2\%$	$48.0 \pm 0.4\%$
1 'p', no γ & copl., no PID	$48.7 \pm 0.2\%$	$29.6 \pm 0.2\%$	$48.2 \pm 0.4\%$

Table 5.6: Fractional yield of events after the application of various recoil-detector related constraints with respect to the number of exclusive events selected with the forward spectrometer only. The fractions obtained for Monte-Carlo data are given in the 2nd column, those determined for experimental data are presented in the 3rd column. The last column gives the ratio of the normalized number of exclusive events from experimental data to the normalized number of exclusive events from Monte-Carlo data. For the explanation of the outer left column, see text.

events as well as an excess of 0-track events is observed for experimental data. However, for a solid understanding detailed studies are needed. The excess of events rejected by the photon detector in experimental data is related to the presence of noise hits. These are not simulated in the Monte-Carlo simulation. Finally, the misalignment of the recoil detector could account for the surplus of discarded events when considering the constraints on the transverse momentum components.

Performance of the photon detector on the selection of elastic DVCS events

The requirement on the absence of detection of neutral particles by the photon detector rejects, according to the Monte-Carlo simulation, $0.57 \pm 0.02\%$ of elastic BH, $62.7 \pm 0.5\%$ of associated BH, and $57 \pm 16\%$ of semi-inclusive DIS events from the sample of exclusive events reconstructed by the spectrometer and containing 1 detected proton. According to the simulation, the photon detector has thus a negligible impact on the rejection of valuable data. However, as already alluded and shown in the last section of this chapter, the fraction of rejected elastic events is larger for experimental data. As can be seen from table 5.6 this is still at an acceptable level.

In order to understand the amount of rejected background, one needs to take into account the acceptance covered by the photon detector, the shower probability of generated photons, and the lower threshold placed on the energy deposition. Only the fraction of associated BH is analyzed, since the statistics generated for semi-inclusive DIS events does not allow a detailed study. From the associated BH events in which minimum 1 neutral pion is generated, $75.9 \pm 0.4\%$ contain a decay photon that lies in the acceptance of the photon detector; only $63.8 \pm 0.5\%$ contain a photon that effectively generates a signal in the detector, corresponding to a 84% shower probability. Finally, for $60.0 \pm 0.5\%$ of the events, the photons generate a signal above 1 MeV. From these latter events $98.9 \pm 0.1\%$ are rejected by the photon detector. Thus the algorithm proposed in section 4.12 proves to be sufficient for the selection of elastic DVCS. The remaining 3% of associated BH events rejected by the photon detector originate mainly from the detection of a neutron or a positively charged pion.

5.5 Extraction of beam-helicity asymmetries

This section presents the beam-helicity asymmetries measured from experimental data. First the extraction method is described; subsequently the obtained asymmetries are shown for exclusive events reconstructed with the forward spectrometer and for events reconstructed with the inclusion of recoil-detector information.

5.5.1 Extraction method

The asymmetries are extracted using the extended maximum likelihood (EML) method. This method and its application to the present analysis are first briefly explained.

Suppose a set of m unknown parameters $\theta = (\theta_1, \theta_2, ..., \theta_m)$ needs to be estimated from a set of N independently measured quantities $(\mathbf{x}_1, \mathbf{x}_2, ..., \mathbf{x}_N)$, with $\mathbf{x}_i$ distributed according to the probability density function normalized to unity, $f(\mathbf{x}; \theta)$, of which the functional form

is known. The parameters θ are estimated by maximizing the likelihood function $\mathbf{L}(\theta)$:

$$\mathbf{L}(\theta) = \prod_{i=1}^{N} f(\mathbf{x}_i; \theta), \tag{5.3}$$

thus solving the equation $\partial \mathbf{L}(\theta)/\partial \theta_i = 0$, for $i = 1, ..., m$. This forms the basis of the maximum likelihood (ML) method.

If one wishes to incorporate information not only on the shape of the expected distribution in $\mathbf{x}$, but also on its magnitude, the EML method applies. This might be of interest, e.g., for the present study. Indeed, as events are collected over a certain time period, but the number of collected events is not fixed, the inclusion of the total observed number of events as additional information can result in an improved constraint on the estimation of the parameters. The likelihood function $\mathbf{L}(\theta)$ can be adapted accordingly as:

$$\mathbf{L}(\theta) = \frac{[\mathbb{N}(\theta)]^N}{N!} e^{-\mathbb{N}(\theta)} \prod_{i=1}^{N} f(\mathbf{x}_i; \theta) \tag{5.4}$$

$$= \frac{e^{-\mathbb{N}(\theta)}}{N!} \prod_{i=1}^{N} F(\mathbf{x}_i; \theta), \tag{5.5}$$

obtained from considering the number of observed events as Poisson distributed with mean $\mathbb{N}(\theta) = \int d\mathbf{x}\, F(\mathbf{x}; \theta)$. Here $F(\mathbf{x}; \theta)$ represents the extended probability density function, related to $f(\mathbf{x}; \theta)$ via $F(\mathbf{x}; \theta) = \mathbb{N}(\theta) f(\mathbf{x}; \theta)$. Another, more instructive, derivation of the EML function can be found in [123]. If $\mathbb{N}$ depends on the parameters to be estimated, the EML method offers the obvious advantage of an additional constraint. In the opposite case, the maximization of $\mathbf{L}(\theta)$ with respect to the parameters θ reduces to the previously described ML method. Usually for the estimation of the parameters one maximizes $\ln \mathbf{L}(\theta)$ (or equivalently minimizes $-\ln \mathbf{L}(\theta)$), which has the advantage that the exponentials reduce to normal factors and the product is transformed into a simple sum.

The extended probability density function $F(\mathbf{x}, P; \theta)$ for the extraction of the beam-helicity asymmetries can be written as:

$$F(\mathbf{x}, P; \theta) = \mathcal{L}(P)\epsilon(\mathbf{x}, P)\sigma_{UU}(\mathbf{x})[1 + PA_{LU}(\mathbf{x}; \theta)]. \tag{5.6}$$

Here P represents the beam polarization, $\mathcal{L}(P)$ the integrated luminosity, $\epsilon(\mathbf{x}, P)$ the detection efficiency, $\sigma_{UU}(\mathbf{x})$ the cross section for an unpolarized beam and unpolarized target, $A_{LU}(\mathbf{x}; \theta)$ the beam-helicity asymmetry, and $\mathbf{x} = (x_B, t, Q^2, \phi)$. Since $\mathcal{L}(P), \epsilon(\mathbf{x}, P)$ and $\sigma_{UU}(\mathbf{x})$ are independent of θ, they can be omitted from the expression of $F(\mathbf{x}, P; \theta)$ with regard to the differentiation of $\mathbf{L}(\theta)$. One thus needs to minimize:

$$-\ln \mathbf{L}(\theta) = \mathbb{N}(\theta) - \sum_{i=1}^{N} \ln \left[1 + PA_{LU}(\mathbf{x}; \theta)\right]. \tag{5.7}$$

For the determination of $\mathbb{N}(\theta)$ detection inefficiencies are currently not considered. Regarding the forward spectrometer, this assumption is proven justified for the extraction of

asymmetries on previously collected data [108], but needs to be verified for the here analyzed data sample. No statement can at present be made concerning the influence of the recoil detector.

With $\epsilon(\mathbf{x}, P) = 1$, and substituting for $\mathcal{L}(P)$ the equivalent number of DIS events, the expression for $\mathbb{N}(\theta)$ simplifies to:

$$\mathbb{N}(\theta) = N_{DIS} \sum_{i=1}^{N} K(P)[1 + \langle P \rangle A_{LU}(\mathbf{x_i}; \theta)], \tag{5.8}$$

with N_{DIS} the total number of observed DIS events and $\langle P \rangle$ the net polarization. The quantity K(P) is given by:

$$K(P) = \begin{cases} \frac{1}{\overrightarrow{N}_{DIS}} \left(1 - \frac{\langle \overrightarrow{P} \rangle}{\langle P \rangle}\right)^{-1} & \text{if } P > 0, \\ \frac{1}{\overleftarrow{N}_{DIS}} \left(1 - \frac{\langle \overleftarrow{P} \rangle}{\langle P \rangle}\right)^{-1} & \text{if } P < 0. \end{cases} \tag{5.9}$$

The superscript $\rightarrow (\leftarrow)$ indicates the integration over the positive (negative) beam-polarization state.

From the expression for $K(P)$, it can be seen that if the net polarization is zero, or if the θ dependence vanishes after integration over the entire kinematic range, the extraction method is equivalent to the ML method. In the present case $\langle P \rangle = 11.2\%$, and the chosen fit function, defined below, does not eliminate the dependence of $\mathbb{N}(\theta)$ on the parameters to be estimated[9].

The fit function chosen for $A_{LU}(\mathbf{x}; \theta)$ is of the form:

$$A_{LU}(\phi; \theta) = \sum_{n=1}^{2} A_{LU}^{\sin(n\phi)} \sin(n\phi) + \sum_{n=0}^{1} A_{LU}^{\cos(n\phi)} \cos(n\phi). \tag{5.10}$$

For simplicity the dependence on kinematic variables other than ϕ is not explicitly written. The coefficients with physics meaning are $A_{LU}^{\sin(\phi)}$ and $A_{LU}^{\sin(2\phi)}$. The amplitude $A_{LU}^{\sin(\phi)}$ is related to the coefficients $s_1^{\mathcal{I}}$ and s_1^{DVCS} appearing in equation (2.45), and the amplitude $A_{LU}^{\sin(2\phi)}$ is related to $s_2^{\mathcal{I}}$, with the twist-3 coefficients s_1^{DVCS} and $s_2^{\mathcal{I}}$ suppressed with respect to the twist-2 coefficient $s_1^{\mathcal{I}}$. The $\cos(n\phi)$ modulations are not expected from theory, but are included as a verification of the stability of the obtained $\sin(n\phi)$ amplitudes.

In addition to the extraction of the asymmetries with the EML method, the least squares method is also used as a consistency check. This method relies on the minimization of the

---

[9]Based on reference [124], if $\sigma_{UU}(\mathbf{x})$ from equation (5.6) is even in ϕ in the acceptance and only $\sin\phi$ modulations enter the expression of $A_{LU}(\mathbf{x}; \theta)$, then $\mathbb{N}(\theta)$, obtained after complete integration over ϕ, becomes independent of θ. On the contrary, a constant fit term or a $\cos\phi$ modulation in combination with the $\cos\phi$ dependence of $\sigma_{UU}(\mathbf{x})$ results in a dependence on θ. Examining this for the present analysis, the fit results obtained for $A_{LU}(\mathbf{x}; \theta) = \sum_{n=1}^{2} A_{LU}^{\sin(n\phi)} \sin(n\phi)$ are compatible with each other when considering or omitting $\mathbb{N}(\theta)$ for events reconstructed with forward-spectrometer information only. For data selected with in addition the recoil detector the leading amplitude remains unaltered, but a deviation from zero by 1σ is observed for $A_{LU}^{\sin(2\phi)}$ when discarding $\mathbb{N}(\theta)$. The inclusion of $\cos(n\phi)$ terms in the fit function yields large discrepancies between the method that omits and includes $\mathbb{N}(\theta)$.

quantity χ^2:

$$\chi^2 = \sum_{i=1}^{N'} \frac{(A_{LU}^i - A_{LU}(\phi_i;\theta))^2}{\sigma_i^2},$$ (5.11)

where the sum runs over the N' bins in ϕ. The quantity A_{LU}^i is taken in accordance with references [103] and [107] as:

$$A_{LU}^i = \frac{1}{|P|} \frac{\frac{\overrightarrow{N}}{\overrightarrow{N}_{DIS}} - \frac{\overleftarrow{N}}{\overleftarrow{N}_{DIS}}}{\frac{\overrightarrow{N}}{\overrightarrow{N}_{DIS}} + \frac{\overleftarrow{N}}{\overleftarrow{N}_{DIS}}}(\phi_i),$$ (5.12)

with $\overrightarrow{N}$ ($\overleftarrow{N}$) and $\overrightarrow{N}_{DIS}$ ($\overleftarrow{N}_{DIS}$) representing, respectively, the number of exclusive events and the number of DIS events collected with positive (negative) beam polarization. The polarization value $|P|$ is taken as the average over the absolute values of both polarization states: $(|\overrightarrow{P}| + |\overleftarrow{P}|)/2$. With in the present case $\overrightarrow{P} = +40.17\%$ and $\overleftarrow{P} = -39.44\%$, this results in a value of $|P| = 39.80\%$. The error σ_i in equation (5.11) is calculated from A_{LU}^i by propagating the errors on $\overrightarrow{N}$ and $\overleftarrow{N}$, but omitting the uncertainties on the other quantities, which are usually included as systematic uncertainties. The fit function $A_{LU}(\phi_i;\theta)$ is taken of the form defined in equation (5.10).

The EML method is preferred over the least squares method, since contrary to the least squares method, it is not binned in ϕ. On the other hand, the least squares method offers the advantage of an easy estimate for the quality of the fit.

5.5.2 Results

Using the above described methods, the asymmetries are extracted for the exclusive events selected with the forward spectrometer only and for the events selected with in addition recoil-detector information. The former data sample consists of 41878 exclusive events; the latter contains 12249 exclusive events. The average of the respective kinematic variables of both samples are similar:

$$\langle -t_{c,spec} \rangle = 0.12 \text{ GeV}^2 \qquad \langle -t_{c,rec} \rangle = 0.13 \text{ GeV}^2$$
$$\langle x_{B,spec} \rangle = 0.10 \qquad \langle x_{B,rec} \rangle = 0.10$$
$$\langle Q^2_{spec} \rangle = 2.48 \text{ GeV}^2 \qquad \langle Q^2_{rec} \rangle = 2.52 \text{ GeV}^2,$$ (5.13)

where the subscript rec ($spec$) refers to the data selected with (without) recoil-detector information. As already pointed out, care should be taken of the difference in background contributions when interpreting these results in terms of detector acceptance, and conversely for the interpretation of the background contributions, the modified acceptance can influence the kinematic coverage, and consequently the asymmetries.

The asymmetry defined in equation (5.12) is represented in figure 5.18 as a function of ϕ for the exclusive sample selected with the forward spectrometer only (left), and for data selected with the inclusion of recoil-detector information (right). The results of the fit based on the EML method and the least squares method are also indicated. Both methods generate
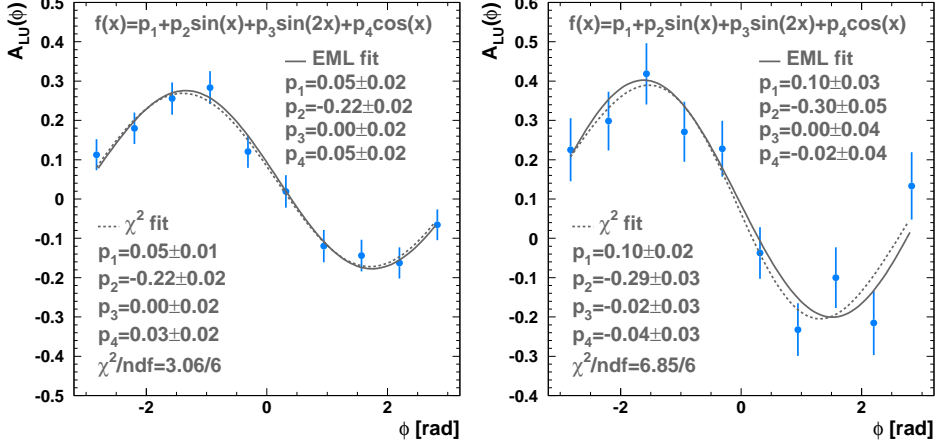
Figure 5.18: Extracted asymmetries as a function of ϕ for data selected with the spectrometer (left) and with in addition the recoil detector (right). The fit results from the EML method and least squares method are indicated as well.

results in agreement with each other. These results are also consistent with previous analyses, see, e.g., references [103, 122].

The leading azimuthal amplitude, i.e., $A_{LU}^{\sin(\phi)}$, differs significantly from zero, and increases from -0.22 ± 0.02 for the data selection disregarding the recoil detector to -0.30 ± 0.05 for the data selection involving the recoil detector. As just explained, this can reflect the enhanced background suppression, but also the influence of a modified acceptance. The $A_{LU}^{\sin(2\phi)}$ amplitude is in both cases compatible with zero, in agreement with the suppression expected from theory. In disagreement with theory, however, is the significant non-zero result for the constant term. This points to a non-optimal normalization. It has been noted in reference [113] that a time-dependent adjustment of the position of the exclusive missing-mass window, which is in principle equivalent to the here applied correction on the photon energy, has a beneficial influence on the reduction in magnitude of the $A_{LU}^{\cos(0\phi)}$ amplitude. Although the magnitude of $A_{LU}^{\cos(0\phi)}$ decreases when adjusting the missing-mass window, its value remains non-zero, in particular for the sample of data collected in 2007. This can point either to a remaining effect of the reconstruction of the photon energy or to another source. At present studies on the improvement of the calorimeter calibration are in progress. Also the $A_{LU}^{\cos(\phi)}$ shows unexpectedly a small non-zero value, in particular for data selected with the spectrometer only. This can be caused by experimental limitations, e.g., inefficiencies, or is just the result of statistical fluctuations. It was checked that the omission of the $\cos(n\phi)$ terms from the fit function does not alter the extracted values of the $\sin(n\phi)$ amplitudes, nor does it influence significantly the uncertainty on these quantities.

To show that the asymmetry vanishes for non-exclusive events, the leading amplitude is represented in figure 5.19 as a function of the squared missing mass, M_X^2, for data se-
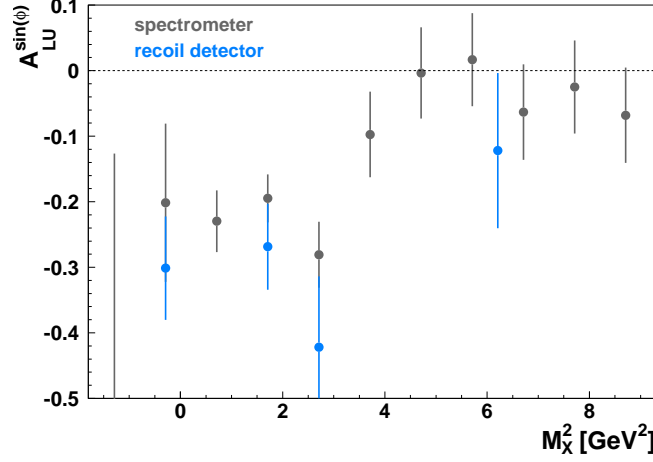
Figure 5.19: Leading amplitude $A_{LU}^{\sin(\phi)}$ as a function of the squared missing mass, M_X^2, for exclusive events selected with the spectrometer only (gray) and for exclusive events selected with the inclusion of recoil-detector information (blue).

lected with the spectrometer (gray) and with in addition the recoil detector (blue). As can be observed, $A_{LU}^{\sin(\phi)}$ shows a significant and constant non-zero value inside the exclusive missing-mass region, while at higher M_X^2 values it reduces to zero.

Finally, the physics amplitudes as a function of $-t_c$, x_B, and Q^2, whereby two of the variables other than the one considered are integrated over, are compared in figure 5.20 for data selected with the spectrometer only (gray) and with the inclusion of the recoil detector (blue). The numerical results of the extracted amplitudes are also given in table 5.7. Within the statistical uncertainty, no dependence of the amplitudes on the kinematic variables can be observed, neither for $A_{LU}^{\sin(\phi)}$ nor for $A_{LU}^{\sin(2\phi)}$. Also, within the uncertainty no clear relation is discerned between the ratios of the leading amplitudes extracted with and without recoil-detector information and the fractional background contributions from tables 5.4 and 5.5 as a function of the kinematic variables. A more appropriate comparison between the two extracted asymmetries would include the determination of acceptance effects. Additionally, a small correction for the semi-inclusive DIS contribution, and its asymmetry[10], would isolate the effect from associated DVCS and BH. Finally, as already stated previously, the influence of inefficiencies needs to be understood and possibly corrected for.

5.6 Study of associated deeply virtual Compton scattering

In this section the study of events assumed to originate from the associated DVCS and associated BH process $ep \rightarrow e\Delta^+\gamma$, in the following commonly referred to as associated DVCS,

---

[10]The values of the extracted amplitudes for semi-inclusive π^0 production given in reference [103] amount to $A_{LU}^{\sin(\phi)} = -0.03 \pm 0.19$ and $A_{LU}^{\sin(2\phi)} = 0.33 \pm 0.20$. The considered event sample is reconstructed with the forward spectrometer only.
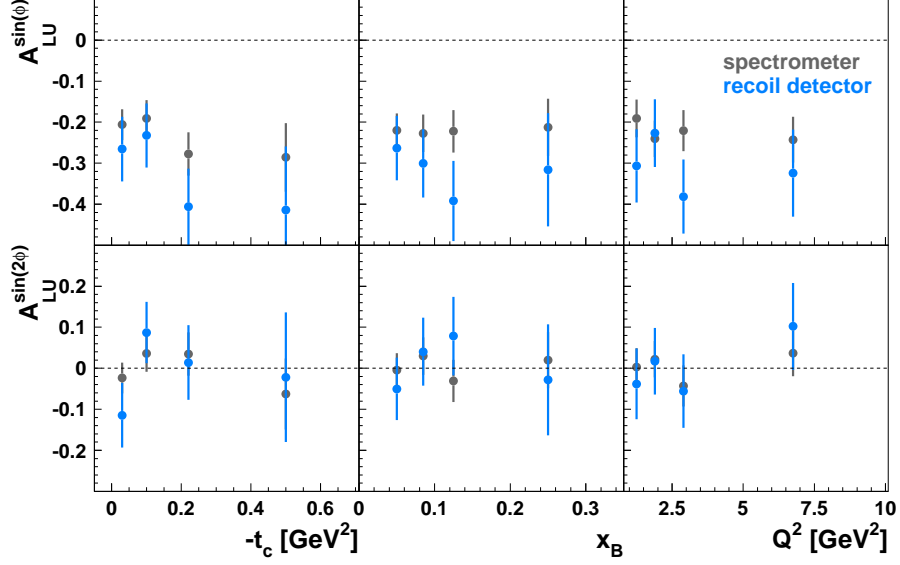
Figure 5.20: Amplitudes $A_{LU}^{\sin(\phi)}$ and $A_{LU}^{\sin(2\phi)}$ as a function of $-t_c$ (left), x_B (center), and Q^2 (right) for exclusive events selected with the spectrometer only (gray) and with the inclusion of recoil-detector information (blue). The uncertainties are statistical only.

	$A_{LU}^{\sin\phi}$		$A_{LU}^{\sin 2\phi}$	
	spec.	rec. det.	spec.	rec. det.
$0.00 \leq -t_c < 0.06$	-0.21 ± 0.04	-0.27 ± 0.08	-0.02 ± 0.04	-0.11 ± 0.08
$0.06 \leq -t_c < 0.14$	-0.19 ± 0.05	-0.23 ± 0.08	0.04 ± 0.04	0.09 ± 0.07
$0.14 \leq -t_c < 0.30$	-0.28 ± 0.05	-0.41 ± 0.09	0.03 ± 0.05	0.01 ± 0.09
$0.30 \leq -t_c < 0.70$	-0.29 ± 0.08	-0.41 ± 0.16	-0.06 ± 0.09	-0.02 ± 0.16
$0.03 < x_B < 0.07$	-0.22 ± 0.04	-0.26 ± 0.08	0.00 ± 0.04	-0.05 ± 0.08
$0.07 \leq x_B < 0.10$	-0.23 ± 0.05	-0.30 ± 0.08	0.03 ± 0.05	0.04 ± 0.08
$0.10 \leq x_B < 0.15$	-0.22 ± 0.05	-0.39 ± 0.10	-0.03 ± 0.05	0.08 ± 0.10
$0.15 \leq x_B < 0.35$	-0.21 ± 0.07	-0.32 ± 0.14	0.02 ± 0.07	-0.03 ± 0.14
$1.0 < Q^2 < 1.5$	-0.19 ± 0.05	-0.31 ± 0.09	0.00 ± 0.05	-0.04 ± 0.09
$1.5 \leq Q^2 < 2.3$	-0.24 ± 0.04	-0.23 ± 0.08	0.02 ± 0.04	0.02 ± 0.08
$2.3 \leq Q^2 < 3.5$	-0.22 ± 0.05	-0.38 ± 0.09	-0.04 ± 0.05	-0.06 ± 0.09
$3.5 \leq Q^2 < 10.0$	-0.24 ± 0.06	-0.32 ± 0.11	0.04 ± 0.06	0.10 ± 0.11

Table 5.7: Amplitudes $A_{LU}^{\sin(\phi)}$ and $A_{LU}^{\sin(2\phi)}$ extracted in 4 bins of $-t_c$, x_B, and Q^2 for exclusive events selected with the spectrometer only and with the inclusion of recoil-detector information. The variables $-t_c$ and Q^2 are expressed in GeV^2. The uncertainties are statistical only.

is described. According to the previously presented Monte-Carlo simulation, the photon detector successfully identifies signals from photons. This is now further investigated on Monte-Carlo and experimental data for the analysis of associated DVCS. Here the channel $\Delta^+ \to p\pi^0$ is examined.

The selection criteria, determined mainly from Monte-Carlo studies, are described first; subsequently the events selected from experimental data are presented and compared with the simulation; finally, the asymmetry extracted from this data sample is shown.

5.6.1   Event selection

The selection procedure adopted for the analysis of associated DVCS is for the major part analogous to the procedure developed for the identification of exclusive events described in the previous sections. The same final state particles need to be reconstructed by the forward spectrometer, i.e., a positron and a photon, while in the recoil detector the detection of exactly 1 proton and 1 or 2 photons in the absence of detection of any other particle is required.

The detection of photons by the photon detector relies on the identification of untracked clusters, as explained in section 4.12. Since events in which 2 photons generate a signal in the photon detector constitute a small subsample only of the events in which at least 1 photon is detectable, the analysis of the appropriate event selection concentrates on the identification of events containing minimum 1 photon. The suppression of 2-photon events results from a convolution of the photon-detector acceptance, the shower probability (amounts to 84% and is energy dependent), and the threshold imposed on the energy deposition in the photon detector. When considering the sample of simulated associated BH events that satisfy all subsequently described constraints related to the spectrometer and that contain in addition a detected proton and at least one photon in the photon-detector acceptance, $43 \pm 1\%$ of these events are found to have both decay photons in the acceptance. The same comparison, but now for photons that effectively generate a signal above 1 MeV results in an outcome of $20 \pm 1\%$.

For the identification by the photon detector of associated DVCS events, the detection of minimum 1 or minimum 2 untracked clusters originating from a different layer is required, with the constraint that each of the involved layers contains maximum 2 untracked clusters[11]. Indeed, as can be seen in figure 5.21, π^0-decay photons from events satisfying the selection criteria related to the analysis of associated DVCS generate most of the time a signal in 1 or 2 layers. The former group of photons have, according to the Monte-Carlo simulation, a mean energy of 120 MeV; for the latter the mean energy amounts to 160 MeV. Photons generating a shower that passes through all tungsten layers have average energies of 220 MeV. The event selection requiring the presence of at least 1 untracked cluster has the advantage of larger statistics, whereas the other offers the benefit of a reduced contribution from background processes. For the selected events, the energy deposition associated with the untracked clus-

---

[11]Subsequently, when referring to 1, 2, or 3 untracked clusters, it is implicitly assumed that the photon-detector layer from which they originate does not contain more than 2 untracked clusters. Additionally, when requiring the detection of minimum 2 or 3 untracked clusters, these clusters are not allowed to belong to the same layer. The former condition rejects a small percentage of events (2–5%) which potentially are not clean. However, it also can reject events in which various reconstructed clusters originate from the same photon. This is at present not investigated in more detail.
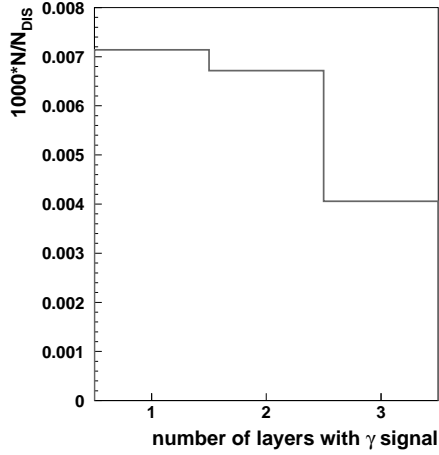
Figure 5.21: Monte-Carlo simulation of the number of photon-detector layers in which a signal above 1 MeV is generated by a π^0-decay photon.

ters needs in addition to lie above a certain threshold, which amounts to 2.5 MeV or 3.5 MeV depending on the event topology. This requirement originates from the presence of noise in experimental data, and is discussed in more detail in the subsequent subsection.

Regarding the constraints imposed on the kinematic variables reconstructed from information provided by the forward spectrometer, the restrictions on x_B and E_γ are unaltered; the modifications related to the other variables are discussed in the following.

As already explained, the squared mass of the final hadronic state needs to be much smaller than Q^2 in order to ensure the validity of the factorization theorem. With the mass of the Δ^+ amounting to 1.232 GeV, a minimum value of 1.5 GeV^2 is required for Q^2, where the limited amount of available statistics does not allow for a stronger restriction. The condition $Q^2 < 10\,\mathrm{GeV}^2$ is not modified.

The upper limit on the angle between the virtual and real photons, $\theta_{\gamma^*\gamma}$, also needs to be reconsidered; the lower limit remains unchanged. The imposed restriction on the maximum value of $\theta_{\gamma^*\gamma}$ finds its justification for the analysis of elastic DVCS with the forward spectrometer in the reduction of background and in the uniformity of the acceptance; for events selected with in addition recoil-detector information the uniformity of the acceptance forms the dominant argument. Indeed, as can be seen in figure 5.22 (left), which represents the opening angle for single-photon events restricted to the exclusive missing-mass region and containing in addition 1 detected proton, a reconsideration of this upper limit in view of background reduction seems, according to the simulation, justified. However, an increase of the presently imposed upper limit is not beneficial for the acceptance uniformity, as was shown in figure 5.15.

Also shown in figure 5.22 is the opening angle for single-photon events in the exclusive missing-mass region adjusted for the analysis of associated DVCS (see further), with $Q^2 > 1.5\,\mathrm{GeV}^2$, and in which in addition to the proton, minimum 1 (center) or 2 (right) photon
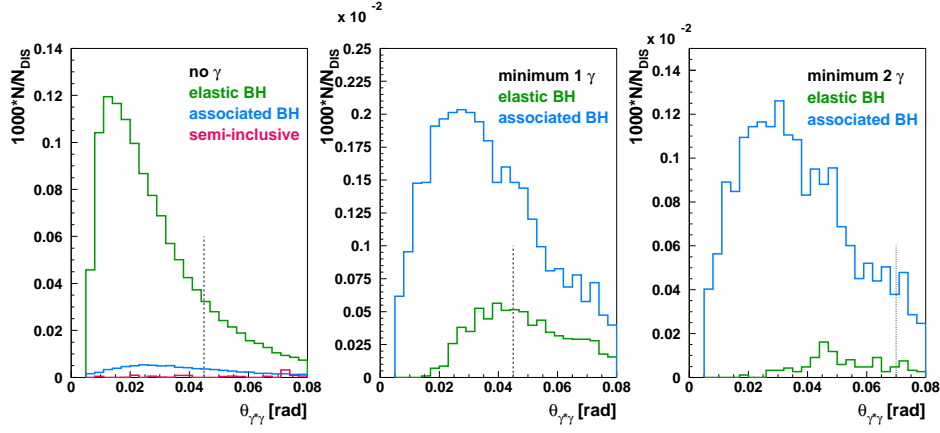
Figure 5.22: Photon opening angle $\theta_{\gamma^*\gamma}$, with $\theta_{\gamma^*\gamma} > 5$ mrad, for simulated single-photon events in the exclusive missing-mass region containing 1 proton (left), and minimum 1 (center) or 2 (right) photon clusters. The exclusive missing-mass window and the lower limit on Q^2 are modified for the event sample considering photons (see text). The vertical dashed (dotted) line indicates the imposed upper limit of 45 mrad (70 mrad) on $\theta_{\gamma^*\gamma}$.

clusters are reconstructed by the recoil detector. Because of the small amount of generated statistics, the semi-inclusive DIS contribution is not represented. As can be observed, the elastic-BH distribution is located at higher values of $\theta_{\gamma^*\gamma}$ in comparison with the distribution obtained in the analysis of elastic DVCS. It is the requirement of photon detection in the recoil detector that is responsible for this shift. Additionally, it can be seen that the contribution from elastic BH is strongly reduced when the minimum required number of photon clusters is increased from 1 to 2. Especially for the latter event selection, an increase of the imposed upper limit on $\theta_{\gamma^*\gamma}$ seems advantageous in order to gain statistics.

Table 5.8 compares the fractional contributions from associated BH, elastic BH, and semi-inclusive DIS for single-photon events that satisfy the hitherto described constraints and are located in the appropriate missing-mass region with detection of minimum 1 or 2 photon

	minimum 1 γ cluster		minimum 2 γ clusters	
	$\theta_{\gamma^*\gamma} < 45$	$\theta_{\gamma^*\gamma} < 70$	$\theta_{\gamma^*\gamma} < 45$	$\theta_{\gamma^*\gamma} < 70$
as. BH	$79.2 \pm 3.4\%$	$75.5 \pm 2.5\%$	$86.7 \pm 5.3\%$	$85.7 \pm 4.1\%$
el. BH	$12.4 \pm 0.7\%$	$16.4 \pm 0.7\%$	$2.4 \pm 0.3\%$	$4.7 \pm 0.4\%$
SIDIS	$8.5 \pm 3.8\%$	$8.1 \pm 3.0\%$	$10.9 \pm 5.5\%$	$9.7 \pm 4.3\%$

Table 5.8: Fractional contributions from associated BH (as. BH), elastic BH (el. BH), and semi-inclusive DIS (SIDIS) for events satisfying the selection criteria for the analysis of associated DVCS, with the omission of the constraint on t. The influence of a modified upper limit on $\theta_{\gamma^*\gamma}$ [mrad] is presented for events containing at least 1 or 2 untracked clusters.
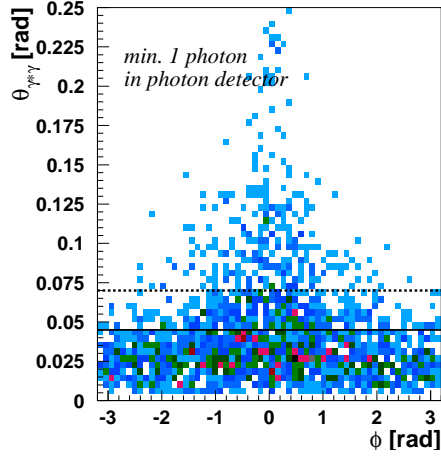
Figure 5.23: Photon opening angle $\theta_{\gamma^*\gamma}$, with $\theta_{\gamma^*\gamma} > 5$ mrad, for single-photon events in the exclusive missing-mass region of the associated-DVCS analysis, for which 1 proton and minimum 1 photon cluster are reconstructed by the recoil detector.

clusters, for either an upper limit on $\theta_{\gamma^*\gamma}$ of 45 mrad or of 70 mrad. For events containing minimum 1 photon cluster the main background contribution originates from elastic BH, whereas for events with at least 2 photon clusters semi-inclusive DIS forms the dominant contribution. The influence of a modified upper limit on $\theta_{\gamma^*\gamma}$ seems more pronounced for events in which at least 1 photon cluster is detected.

However, a revision of the requirement on $\theta_{\gamma^*\gamma}$ is only justified if the uniformity of the acceptance is guaranteed. Figure 5.23 shows the photon opening angle as a function of ϕ for the here considered type of single-photon events selected from experimental data. At least 1 photon cluster is here reconstructed by the photon detector. The sharp peak at $\phi = 0$ corresponds, according to the Monte-Carlo simulation, to semi-inclusive DIS events. The full line indicates the upper limit of 45 mrad; the dashed horizontal line designates the region where $\theta_{\gamma^*\gamma} = 70$ mrad. Although an upper limit of 70 mrad slightly degrades the uniformity of the acceptance, it increases, according to the Monte-Carlo simulation, the amount of associated BH events by $39 \pm 2\%$ ($37 \pm 1\%$) in case the presence of minimum 2 (1) untracked clusters is required in the photon detector. In view of this substantial gain in statistics, an upper limit of 70 mrad is adopted for the event selection requiring minimum 2 photon clusters.

The approach used in the analysis of elastic DVCS for the determination of the squared four-momentum transfer to the nucleon is not of application for the study of associated production. Instead, the squared four-momentum transfer, t, reconstructed from the energy of the photon detected in the forward spectrometer is considered. The distribution of this quantity is shown in figure 5.24 (left) for events from a Monte-Carlo simulation satisfying all constraints related to the analysis of associated DVCS with the omission of the requirement on the detection of untracked clusters in the photon detector. Only the distributions originating from elastic and associated BH are shown, with each distribution normalized individually. Because
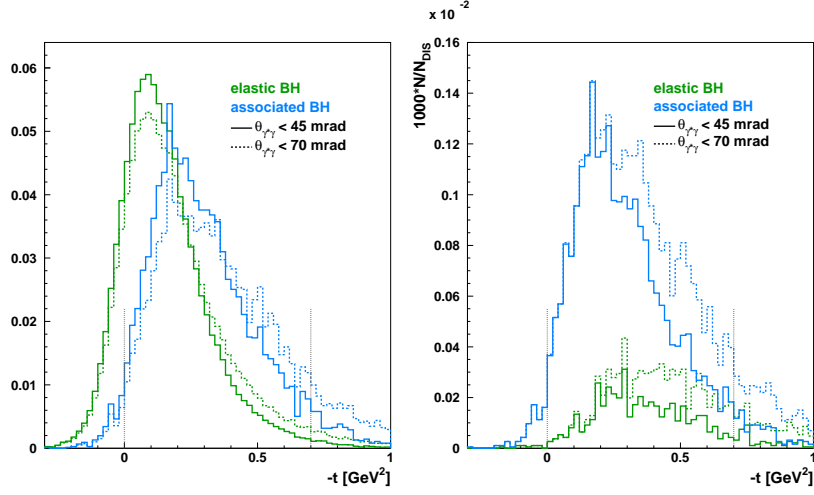
Figure 5.24: Distribution in $-t$ for elastic BH (green) and associated BH (blue) events selected for the analysis of associated DVCS with the omission of photon-cluster detection (left) and with the requirement on the presence of at least 1 untracked cluster (right). The vertical lines delimit the allowed range in $-t$.

of the calorimeter resolution, the distributions extend to negative, unphysical, values, as already mentioned previously. This is more pronounced for elastic BH events, which are on average centered around lower values in $|t|$. In the present analysis of associated DVCS, no final results are presented as a function of t. If, however, the t dependence of observables were shown, a simple (yet not optimal) approach for its presentation would consist in the rejection of events with negative $-t$ values. In accordance with this approach, it was chosen to discard events in the unphysical t region. In view of the analysis of associated DVCS, this constraint seems beneficial. However, as already observed for the distribution in $\theta_{\gamma^*\gamma}$, the requirement of the detection of an untracked cluster in the photon detector moves the elastic-BH distribution towards higher values. This is shown in figure 5.24 (right). Since $\theta_{\gamma^*\gamma}$ and $-t$ are correlated, it is not surprising that the same effect is observed for both variables. As can be seen in the figure, allowing $\theta_{\gamma^*\gamma}$ values of up to 70 mrad shifts the distribution in $-t$ to higher values. The increase of the upper limit on the opening angle does, however, not modify the relative proportion of background and signal significantly. An appropriate upper limit on $-t$ of 0.7 GeV^2 was estimated from the Monte-Carlo simulation, resulting from a compromise between a minimal loss of data and an acceptable signal-to-background ratio, and at the same time ensuring the validity of the factorization theorem. The imposed constraint on t reduces the gain in statistics obtained by releasing the upper limit on $\theta_{\gamma^*\gamma}$ from 45 mrad to 70 mrad. Nevertheless, the gain in statistics still amounts to $26 \pm 1\%$ for the events containing minimum 2 untracked clusters. Since the distribution in t from the experimental data is shifted (and altered in shape) with respect to the distribution obtained from the Monte-Carlo simulation, because of the difference in the reconstruction of the high-energetic
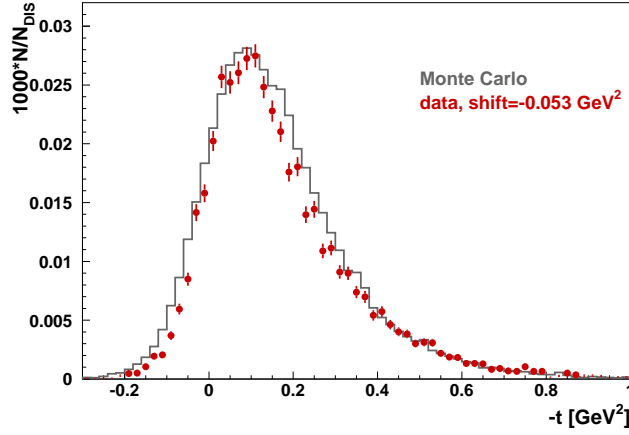
Figure 5.25: Distribution in $-t$ for events from experimental data (red) and Monte-Carlo data (gray) that satisfy the selection criteria related to the analysis of associated DVCS with the omission of the requirement on photon detection in the recoil detector. The normalization of the Monte-Carlo simulation is adjusted for a better comparison.

photon, the imposed restrictions are adjusted for experimental data. The comparison between experimental data and Monte-Carlo data is shown in figure 5.25. The event samples satisfy all selection criteria related to the analysis of associated DVCS with, in view of larger statistics, the omission of the requirement on the presence of photons in the recoil detector. The distribution from experimental data is here shifted by -0.053 GeV^2, corresponding to an upper limit of $-t < 0.753$ GeV^2. The lower limit is left unaltered, since this constraint is only present because of the limited resolution in t, and does not reject additional background neither from elastic BH nor from semi-inclusive DIS, both located at higher values in $-t$.

Finally, the missing mass reconstructed from experimental data is restricted to the window -0.538 GeV$^2 < M_X^2 < 3.262$ GeV^2, resulting again from a compromise between a sample with high purity and a minimal loss in statistics[12]. For the simulated data, the upper and lower limit are reduced by -0.462 GeV^2. The distribution in M_X^2 is shown in the following subsection.

The contributions from associated BH, elastic BH, and semi-inclusive DIS for the events satisfying all requirements related to the analysis of associated DVCS is presented in table 5.9. Several event topologies are considered. They are classified by the minimum number of untracked clusters present in the photon detector, i.e., at least 1, 2 or 3, where as explained previously, for the latter two event configurations the clusters need to originate from a different layer. For the requirement on the presence of minimum 1 cluster, $\theta_{\gamma^*\gamma}$ is restricted to

---

[12]In view of the limited amount of statistics available for the Monte-Carlo simulation, these restrictions as well as those imposed on some of the other kinematic variables might possibly be improved when carrying out a new analysis based on a larger data sample.

values below 45 mrad; for the other two topologies this upper limit is released to 70 mrad. As can be concluded from the table, in combination with the results from table 5.8, the number of required untracked clusters has manifestly a substantial influence on the purity of the sample: the fractional contribution from associated BH varies from $\sim 80\%$ to $\sim 95\%$ with increasing number of untracked clusters, but is accompanied by a large loss in statistics, on the order of 75%.

	as. BH	el. BH	SIDIS
min. 1 γ cluster	$79.7 \pm 3.6\%$	$12.1 \pm 0.7\%$	$8.3 \pm 4.1\%$
min. 2 γ clusters	$87.8 \pm 4.6\%$	$4.1 \pm 0.4\%$	$8.1 \pm 4.8\%$
3 γ clusters	$95.4 \pm 2.6\%$	$2.0 \pm 0.4\%$	$2.7 \pm 2.6\%$

Table 5.9: Fractional contributions from associated BH (as. BH), elastic BH (el. BH), and semi-inclusive DIS (SIDIS) for the events satisfying the selection criteria related to the analysis of associated DVCS.

Regarding the requirement on the detection of 2 untracked clusters originating from the same photon-detector layer, the purity of the sample is not enhanced. Indeed, the fractional contribution from associated BH amounts to 80.7 ± 11.0. It has not been analyzed if these two clusters correspond to different photons or if they relate to the same photon.

In order to gain statistics, the asymmetries are also extracted from the event sample for which the constraint on the lower limit of Q^2 is released to $1 \, \text{GeV}^2$. This slightly complicates the theoretical interpretation of the data, but increases the size of the selected sample by $\sim 50\%$. The contributions from the individual processes corresponding to this event selection are summarized in table 5.10. Within the statistical precision no variation in the fractional contributions from elastic and associated BH and semi-inclusive DIS is observed compared to the data selected with the restriction $Q^2 > 1.5 \, \text{GeV}^2$.

	as. BH	el. BH	SIDIS
min. 1 γ cluster	$82.4 \pm 2.9\%$	$11.1 \pm 0.6\%$	$6.5 \pm 3.3\%$
min. 2 γ clusters	$90.2 \pm 3.5\%$	$3.7 \pm 0.3\%$	$6.0 \pm 3.7\%$
3 γ clusters	$96.5 \pm 1.9\%$	$1.5 \pm 0.3\%$	$2.0 \pm 1.9\%$

Table 5.10: Fractional contributions from associated BH (as. BH), elastic BH (el. BH), and semi-inclusive DIS (SIDIS) for the events satisfying the selection criteria related to the analysis of associated DVCS. The restriction on Q^2 is released to $Q^2 > 1.0 \, \text{GeV}^2$.

Table 5.11 summarizes the constraints on kinematic variables and on the energy of photon-detector clusters applied on the single-photon event sample for the analysis of associated DVCS. Cuts related to the selection of single-photon events are given in table 5.2.

kinematic variables	
x_B	$[0.03, 0.35]$
Q^2	$[1.5, 10]$ or $[1.0, 10]$ GeV^2
$\theta_{\gamma^*\gamma}$	$[5, 45]$ or $[5, 70]$ mrad
$-t$	$[0.0, 0.753]$ GeV^2
M_X^2	$[-0.538, 3.262]$ GeV^2
photon-detector cluster energy [MeV]	
min. 1 cluster	> 3.5 (A layer)
	> 2.5 (B & C layer)
min. 2 clusters	> 2.5

Table 5.11: Constraints on kinematic variables and photon-detector cluster energies of single-photon events for the analysis of associated DVCS. Cuts applied on kinematic variables for the selection of single-photon events can be found in table 5.2.

5.6.2 Comparison between experimental and simulated data

Energy deposition by photons

As pointed out in the previous section, the energy of photon-detector clusters associated with neutral particles is required to lie above a certain threshold value in order for an event to be considered a candidate event from associated DVCS. This condition is related to the suppression of noise hits. It was explained in section 4.10 that a minimal energy deposition of 1 MeV is sufficient to this effect. For the analysis of associated DVCS this condition needs to be revised, as outlined in the following. Figure 5.26 shows the energy of untracked clusters from the photon-detector A layer for single-photon events with $\theta_{\gamma^*\gamma} > 5$ mrad and with the restriction on the energy of the untracked calorimeter cluster released. In the recoil detector the detection of minimum 1 positive particle in addition to the detection of photon clusters is required. The distributions represented by a full line are the result of the Monte-Carlo simulation; the distributions represented by the closed symbols originate from experimental data. The various colors are indicative for the different types of constraints imposed on the photon-detector clusters: either the presence of at least 1 untracked cluster is required in the photon-detector layer (green), or this condition is restricted to the detection of exactly 1 untracked cluster (blue), possibly with the additional requirement that an untracked cluster is also reconstructed in one of the other photon-detector layers (red). A strong disagreement between experimental data and simulated data is visible at low energy depositions, especially for the first considered category. This discrepancy corresponds to noise hits in the photon detector, present for experimental data, but not modeled in the Monte-Carlo simulation. For experimental data the difference at low cluster energies between the first type of constraints and the second type of constraints is dominated by noise hits. The restriction on the detection of exactly 1 untracked cluster in the A layer and at least 1 untracked cluster in the B or C layer reduces the number of noise hits to an imperceptible level. The remaining discrepancy between experimental data and Monte-Carlo data results from the incorrect simulation of the energy deposition in the photon detector, as described in section 4.3, and from the imperfect
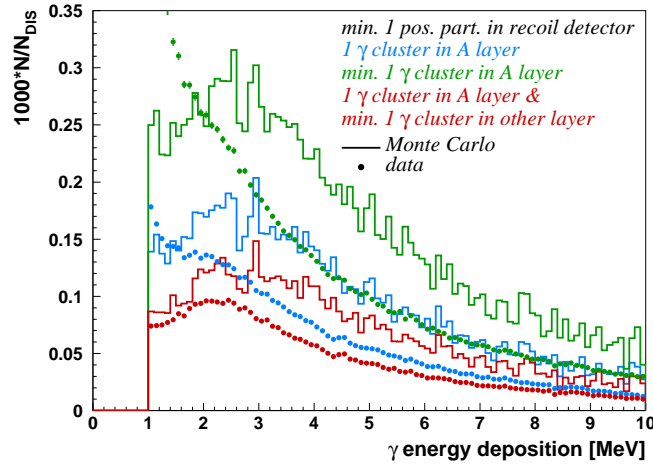
141

Figure 5.26: Energy of untracked photon-detector A-layer clusters for single-photon events satisfying revised requirements (see text). Distributions from Monte-Carlo data (full line) and experimental data (closed symbols) are presented for 3 event categories: events containing at least 1 untracked cluster (green), exactly 1 untracked cluster (blue), and exactly 1 untracked cluster with in addition an untracked cluster in the B or C layer (red).

calibration of the photon-detector strips from quadrant 2. Discarding this quadrant shifts the small peak around ~ 2 MeV to higher values. In view of the recoil-detector inefficiencies, a larger contamination of misidentified untracked clusters in experimental data can also not be excluded.

The same type of distributions, but now for exclusive events selected with the forward spectrometer and containing in addition 1 proton and at least 1 untracked cluster reconstructed by the recoil detector, are shown in figure 5.27. On the left-hand side of the figure the distributions for events containing minimum 1 (green) and exactly 1 (blue) untracked cluster without considering the other photon-detector layers are presented; for the distributions shown on the right-hand side the requirement on detection of untracked clusters in one of the other layers is incorporated. Restricting the data sample to exclusive events results in a relatively more prominent presence of noise hits compared to the data sample shown in figure 5.26, since the number of events that contain a neutral particle is suppressed. Yet, also for the here examined event selection the consideration of the other layers reduces the noise level considerably, but does not eliminate it. In order to discard noise hits from the event sample, a restrictive energy threshold is imposed on the cluster energy. For events in which the presence of minimum 1 untracked cluster is required the energy threshold is set to 3.5 MeV for the A layer and to 2.5 MeV for the other layers, which are less affected by noise hits. When requiring minimum 2 untracked clusters, the energy threshold is reduced for the A layer to 2.5 MeV.
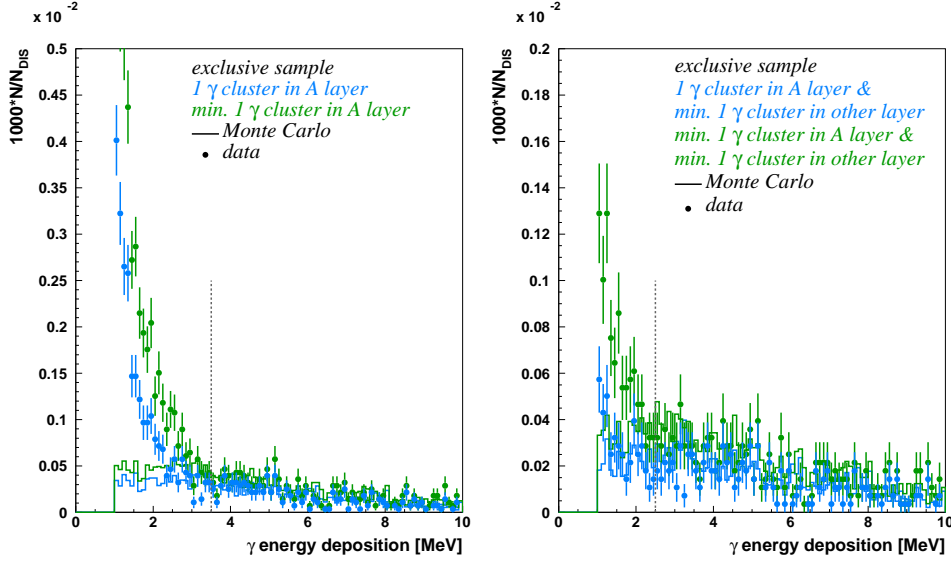
Figure 5.27: Energy of untracked photon-detector A-layer clusters for exclusive events in which 1 proton in addition to untracked photon-detector clusters is detected. Distributions from Monte-Carlo data (full line) and experimental data (closed symbols) are shown for events containing at least 1 untracked cluster (green), exactly 1 untracked cluster (blue), with omission (left) or consideration (right) of the presence of untracked clusters in the B or C layer. The vertical lines indicate the lower energy limit.

Missing-mass distribution

The constraint imposed on the missing-mass distribution remains to be clarified. To this effect the squared missing-mass distribution for the events satisfying the selection criteria related to the analysis of associated DVCS with detection of at least 1 untracked photon-detector cluster is shown over an extended range in figure 5.28 for experimental and simulated data. The sample selected from the Monte-Carlo simulation is subdivided into the different contributing processes: associated BH (blue), elastic BH (green), their sum (gray), and semi-inclusive DIS (magenta). The distribution from experimental data (red) is again shifted by $-0.462 \, \mathrm{GeV}^2$. A good agreement is observed between the Monte-Carlo simulation and the experimental data, with a peak centered around the square of the Δ^+-resonance mass. The presence of elastic BH, concentrated around the squared proton mass, and semi-inclusive DIS, mainly located at higher M_X^2 values, broadens the measured distribution with respect to the associated-BH distribution. It has to be noted that the normalization of the simulation is not adjusted. Since the requirement of proton detection results in a deficit of events from experimental data in comparison with simulated data, the present situation corresponds effectively to an excess of events from experimental side. The constraint imposed on M_X^2 for the analysis of associated DVCS is indicated in the figure by the blue vertical lines. It was chosen as a compromise between the number of selected events and the suppression of the background contributions.
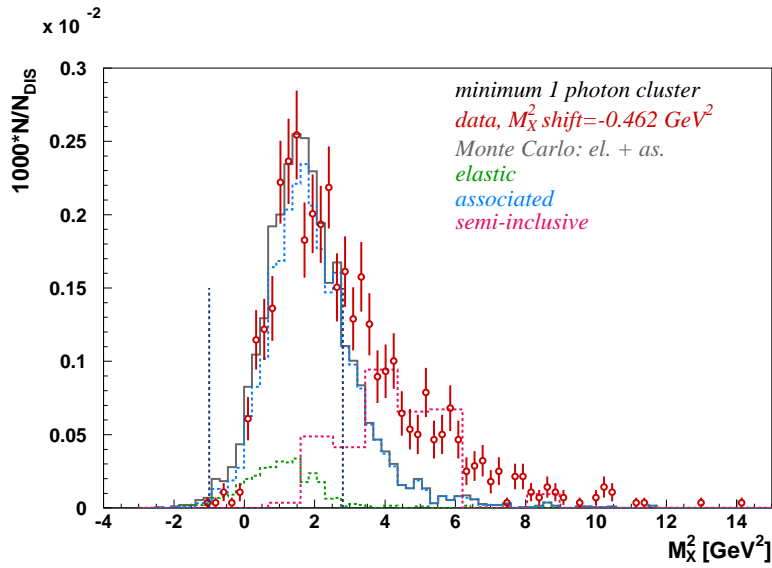
143

Figure 5.28: Squared missing-mass distribution for events satisfying the selection criteria related to the analysis of associated DVCS. In the photon detector the reconstruction of at least 1 untracked cluster is required. The distributions from experimental (red symbols) and Monte-Carlo data are presented. They are normalized to the respective number of DIS events. The distribution obtained from experimental data is shifted by $-0.462\,\mathrm{GeV}^2$. The vertical lines indicate the selected missing-mass range.

As presented in table 5.9, more restrictive requirements on the number of untracked clusters allow for a further suppression of the background, but lead also to a substantial loss in statistics. A small indication for the reduction in background seems visible in the missing-mass distribution. This is shown in figure 5.29 for events containing at least 2 (left) or 3 (right) untracked photon-detector clusters. For the former event sample a slight shift, in comparison with the distribution from figure 5.28, of the left-hand side of the peak towards higher M_X^2 values, indicating the suppression of elastic BH, can be distinguished; for the distribution obtained when requiring 3 untracked clusters, the reduction from the semi-inclusive DIS contribution, present at higher M_X^2 values, seems more pronounced.

Kinematic distributions

Figure 5.30 presents the comparison between the kinematic distributions obtained from experimental and simulated data for events satisfying the selection criteria related to the analysis of associated DVCS. The events considered here are required to contain at least 1 untracked photon-detector cluster. A relatively good agreement is observed between the Monte-Carlo simulation and the experimental data. The distribution in x_B is slightly shifted towards higher values in comparison with the data sample selected for the analysis of elastic production, see figures 5.13 and 5.14. This shift is related to the correlation between x_B and Q^2, with Q^2 re-
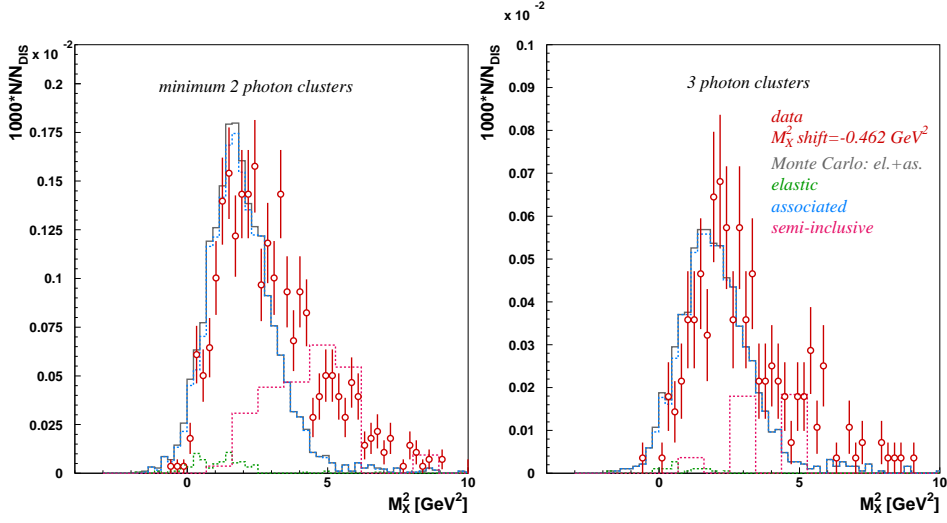
144

Figure 5.29: Squared missing-mass distribution for events satisfying the selection criteria related to the analysis of associated DVCS. In the photon detector the reconstruction of at least 2 (left) or 3 (right) untracked clusters is required. The distributions from experimental (red symbols) and Monte-Carlo data are presented. They are normalized to the respective number of DIS events. The distribution obtained from experimental data is shifted by $-0.462 \, \text{GeV}^2$.

stricted at present to values above $1.5 \, \text{GeV}^2$. Independently of this, the distribution in $\theta_{\gamma^*\gamma}$ is also concentrated around larger values with a shape that differs from what is observed for the previously studied category of exclusive events. The four-momentum transfer $-t$ is increased as well, which can for a small fraction only be attributed to the imposed constraint on Q^2. The distribution in ϕ shows, at least for the Monte-Carlo simulation, a smoother behavior in comparison with the sample obtained in the analysis of elastic DVCS using recoil-detector information. Here the requirement on Q^2 slightly centers the distribution around $\phi = 0$.

Lastly, an estimate for the variation with $-t_c$ of the background contribution to the event sample selected for the analysis of elastic DVCS is compared for experimental and simulated data. As shown in tables 5.4 and 5.5, the Monte-Carlo simulation predicts a substantial rise of the associated-BH contribution as a function of $-t_c$. In order to verify this experimentally, exclusive events reconstructed with the forward spectrometer and containing in addition 1 proton and at least 2 untracked clusters detected by the recoil detector are compared to the sample of events satisfying the same requirements except for the explicit detection of untracked photon-detector clusters. The ratio of the respective numbers of observed events as a function of $-t_c$ is presented in table 5.12 for experimental data (exp) and Monte-Carlo data (MC). For the simulated data, also the contribution from associated BH is given, where the event sample obtained with (without) consideration for the presence of untracked clusters is labeled $s_{2\gamma}$ (s_{excl}). The ratio of the fractions from experimental and Monte-Carlo data (exp/MC) is included as well. An increase with $-t_c$ in the fractional number of exclusive events containing untracked clusters is observed both for simulated and for experimental
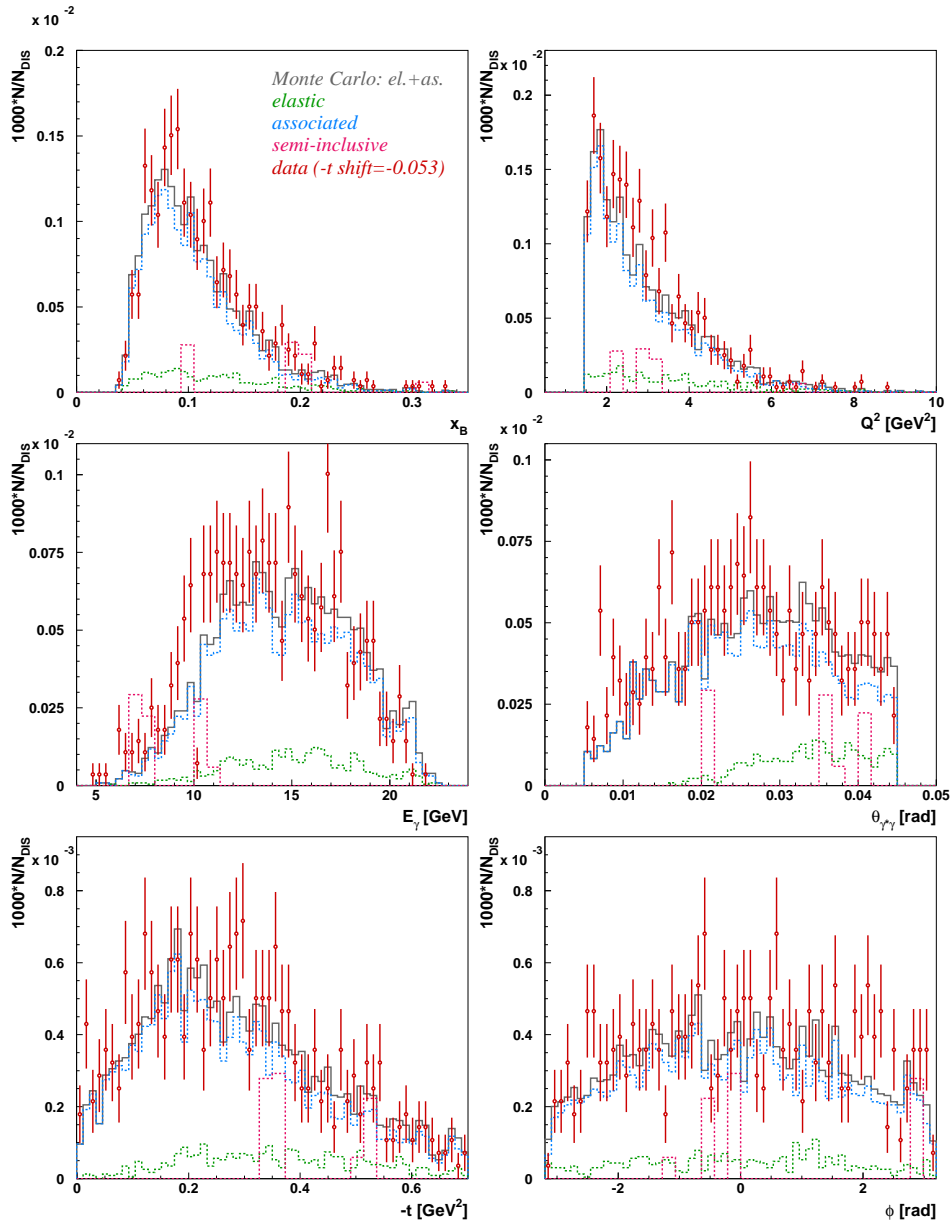
Figure 5.30: Kinematic distributions for events satisfying the constraints related to the analysis of associated DVCS with the requirement of the presence of minimum 1 untracked photon-detector cluster. The distributions obtained from experimental data (red symbols) and from the Monte-Carlo simulation are presented. They are normalized to the respective number of DIS events.

data. Since the contribution from associated BH to the sample $s_{2\gamma}$ is predicted to decrease with $-t_c$, some caution is required in the interpretation of these results. Although the rate at which the fractional contribution from $s_{2\gamma}$ increases is relatively similar for experimental and Monte-Carlo data, the experimental data overestimates the Monte-Carlo simulation by $\sim 50\%$. This can be related to experimental limitations, the absence of associated DVCS in the simulation, or uncertainties in the modeling of the associated-BH contribution.

$-t_c$	exp	MC	exp/MC	$s_{2\gamma}$	s_{excl}
$0.00 - 0.06$	1.18 ± 0.14	0.84 ± 0.04	1.40 ± 0.18	100.0 ± 0.00	2.46 ± 0.06
$0.06 - 0.14$	2.33 ± 0.20	1.18 ± 0.04	1.97 ± 0.19	99.63 ± 0.21	3.99 ± 0.08
$0.14 - 0.30$	3.76 ± 0.29	2.75 ± 0.32	1.37 ± 0.19	82.35 ± 9.72	6.89 ± 0.12
$0.30 - 0.70$	6.09 ± 0.63	4.60 ± 0.27	1.32 ± 0.16	85.44 ± 4.43	12.66 ± 0.26

Table 5.12: Fractional number (in %) of exclusive events reconstructed with the spectrometer in which 1 proton and at least 2 untracked photon-detector clusters are detected ($s_{2\gamma}$) with respect to the event sample satisfying the same requirements, but discarding photon-detector information (s_{excl}). The fractions are given for experimental (exp) and simulated (MC) data as a function of $-t_c$ [GeV^2]. Also the ratio of the fractions from experimental and simulated data (exp/MC) is presented. The last 2 columns contain the fractional contributions (in %) from associated BH, according to the Monte-Carlo simulation, for the 2 event samples $s_{2\gamma}$ and s_{excl}.

5.6.3 Extraction of the beam-helicity asymmetry

Although the analysis as well as the number of collected events is very limited, the asymmetry defined in equation (5.12) is extracted for the events satisfying the constraints related to the analysis of associated DVCS, in particular for these events in which minimum 1 and 2 untracked photon-detector clusters are observed. For the former sample 604 events are extracted; for the latter 360 events are found. The asymmetries are also presented for the data samples that contain events with Q^2 values down to 1 GeV^2. The corresponding number of collected events amounts to 849 and 530, respectively. The kinematic coverage for the events containing at least 1 untracked photon-detector cluster averages to:

$$\langle -t_{high} \rangle = 0.33 \text{ GeV}^2 \qquad \langle -t_{low} \rangle = 0.29 \text{ GeV}^2$$
$$\langle x_{B,high} \rangle = 0.11 \qquad \langle x_{B,low} \rangle = 0.10$$
$$\langle Q^2_{high} \rangle = 2.97 \text{ GeV}^2 \qquad \langle Q^2_{low} \rangle = 2.48 \text{ GeV}^2, \qquad (5.14)$$

where the subscript $high$ (low) refers to a lower limit on Q^2 of 1.5 GeV^2 (1.0 GeV^2). For the data sample with Q^2 restricted to 1 GeV^2, the average kinematics in x_B and Q^2 are similar to those from the analysis of elastic DVCS. The more constraining limit on Q^2, i.e., 1.5 GeV^2, shifts both variables to higher values. As already stated in the preceding subsection, a large difference is observed for the average kinematic coverage in t. For the analysis of elastic DVCS using recoil-detector information $\langle -t \rangle$ amounts to 0.19 GeV^2, while here values on the order of 0.30 GeV^2 are observed.
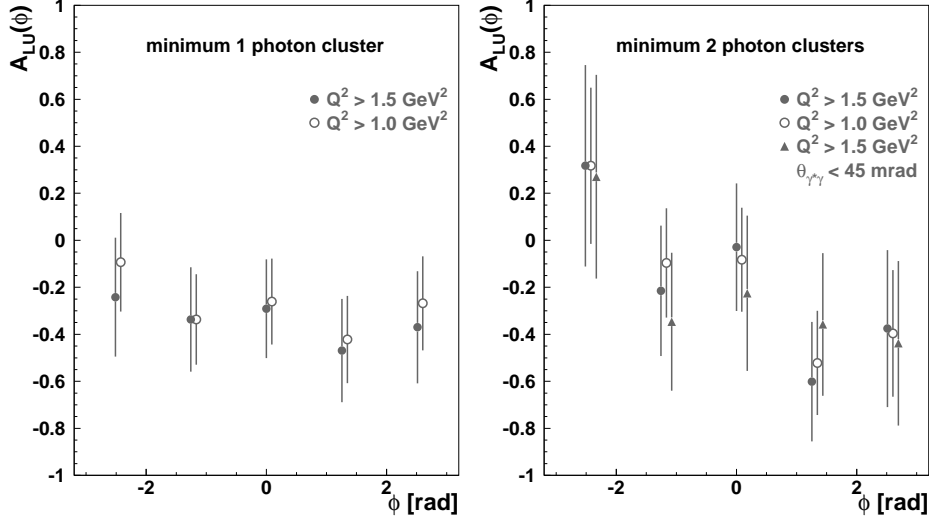
Figure 5.31: Asymmetries extracted from the sample of events satisfying the constraints related to the selection of associated DVCS. The asymmetries are shown for events containing at least 1 untracked cluster (left) and minimum 2 untracked clusters (right).

The asymmetries are presented in figure 5.31 for events containing at least 1 (left) and 2 untracked clusters (right). Here the asymmetries extracted from the data sample for which the lower limit on Q^2 is set to $1.5\,\mathrm{GeV}^2$ ($1.0\,\mathrm{GeV}^2$) are represented by the closed (open) symbols. For the events containing at least 2 untracked clusters the asymmetries are also extracted with the restriction on $\theta_{\gamma^*\gamma}$ reduced to 45 mrad (triangles) in order to investigate the influence of a change in kinematic distribution. The asymmetry amplitudes obtained from the fit, based on the EML method, of the function defined in equation (5.10) are given in table 5.13.

	$A_{LU}^{\cos(0\phi)}$	$A_{LU}^{\sin(\phi)}$	$A_{LU}^{\sin(2\phi)}$	$A_{LU}^{\cos(\phi)}$
	minimum 1 γ cluster			
$Q^2 > 1.5\,\mathrm{GeV}^2$	-0.28 ± 0.13	-0.13 ± 0.19	-0.04 ± 0.18	0.02 ± 0.19
$Q^2 > 1.0\,\mathrm{GeV}^2$	-0.24 ± 0.11	-0.08 ± 0.16	0.01 ± 0.16	0.00 ± 0.16
	minimum 2 γ clusters			
$Q^2 > 1.5\,\mathrm{GeV}^2$	-0.14 ± 0.19	-0.27 ± 0.25	0.05 ± 0.25	-0.10 ± 0.26
$\theta_{\gamma^*\gamma} < 45$ mrad	-0.16 ± 0.20	-0.10 ± 0.27	0.23 ± 0.27	-0.14 ± 0.29
$Q^2 > 1.0\,\mathrm{GeV}^2$	-0.11 ± 0.15	-0.24 ± 0.21	0.14 ± 0.21	-0.05 ± 0.21

Table 5.13: Asymmetry amplitudes extracted from the fit to the events satisfying the requirements related to the selection of associated DVCS. Various constraints are applied on the kinematic variables Q^2 and $\theta_{\gamma^*\gamma}$, as explained in the text and as indicated in figure 5.31. The given uncertainties are statistical only.

The modified requirements on Q^2 do not result in a significant change of the extracted asymmetry values. Although within the statistical uncertainty the data points are compatible with each other, the more restrictive constraint on $\theta_{\gamma^*\gamma}$ for the event sample containing at least 2 untracked clusters seems to modify the asymmetry in the direction of a constant, as observed for the asymmetry extracted from the data sample containing minimum 1 untracked photon-detector cluster. The presence of a constant offset can be related to an imperfect normalization, as discussed in section 5.5.2, describing the analysis of elastic DVCS. Within the uncertainty no statement can be made about the presence or absence of a non-zero asymmetry.

6. Summary and conclusion

In the present dissertation the commissioning of the HERMES recoil photon detector and its performance have been reported. The photon detector is the outer-lying component of the HERMES recoil detector. The other recoil-detector components are the silicon-strip detector, installed directly around the HERMES target cell, and the scintillating-fiber tracker. The recoil detector was constructed in order to reduce the background contribution to the sample of events selected at the HERMES experiment for the study of deeply virtual Compton scattering (DVCS). The main background contribution to the selected event sample originates from associated DVCS, where the proton does not stay in its ground state but is excited to a Δ^+ resonance. This Δ^+ decays, with a branching ratio of 67%, into a proton and a neutral pion, with the latter decaying into two photons, and, with a branching ratio of 33%, into a neutron and a positively charged pion.

The silicon-strip detector and the scintillating-fiber tracker are able to reconstruct and identify charged particles, namely protons and negatively and positively charged pions. The photon detector is also sensitive to these particles, but its main purpose lies in the detection of photons. The photon detector consists of 3 cylindrical tungsten-scintillator layers. The scintillator layers are subdivided into 2 cm wide strips, oriented parallel to the HERA beam line for the inner layer, and oriented under an angle of respectively $+45.6°$ and $-46.2°$ for the following two layers.

Prior to its installation in the HERMES experiment the recoil detector was placed in a test area, where signals from cosmic particles were collected. These data allowed to gain insights in the photon detector (and the other two recoil-detector components), and to obtain a rough calibration as well as a preliminary determination of the photon-detector efficiency. Based on the collected data, the photon detector was also implemented in the digitization routine of the HERMES Mont Carlo.

Beginning of 2006 the recoil detector was installed in the HERMES experiment. The recoil detector was completely operational starting from September 2006 and collected then data over a period of 10 months. Data were accumulated by scattering a longitudinally polarized positron beam, with positive and negative helicity, off an unpolarized hydrogen and deuterium target. A total of 28 M DIS events on hydrogen target and 7 M DIS events on deuterium target were collected.

Using pion tracks reconstructed from this data set, the photon detector was then aligned with respect to the recoil tracking detectors. In a next step, the photon detector was calibrated, again using signals from charged pions. Data production based on this calibration allowed to subsequently control the quality of the calibration and to measure the efficiency of the

photon-detector strips. Regarding these two aspects, the results are satisfactory: the response of the photon detector is stable in time and the efficiency for the detection of protons and pions amounts to 95% and 92%, respectively. Also, it was shown that the photon detector can contribute to the identification of protons and pions. It needs to be mentioned, however, that the quality of the calibration, and consequently of the measured strip efficiencies, in one quadrant of the photon detector is insufficient. This is related to problems with the track reconstruction, more specifically with inefficiencies in the two tracking detectors. However, at present the quality of the reconstructed tracks has improved and is proven sufficient for a reliable calibration of the photon detector. Once a new production, with corrected photon-detector calibration, is available, it can be checked if the strips located in this problematic quadrant have a higher efficiency. Regardless of this aspect, a new iteration of the photon-detector calibration is mandatory because of cross-talk corrections at the level of the PMT-clustering routine.

For the identification of photons, an algorithm was developed that controls if signals in the photon-detector layers can be or can not be associated with a reconstructed track. This algorithm was subsequently used in the analysis of DVCS on a hydrogen target. According to the Monte-Carlo simulation, this algorithm is very efficient: it correctly identifies 99% of the associated DVCS events in which a photon generates a signal above threshold, i.e., 1 MeV, in the photon detector. The total efficiency of the photon detector to reject events from associated DVCS lies however lower, namely around 63%. This is due to a combination of the photon-detector acceptance, the shower probability of photons (which lies around 84%), and the imposed 1 MeV threshold, which aims at the rejection of noise. Still according to the Monte-Carlo simulation, the recoil detector as a whole is able to reduce the total background contribution from 14% to < 1%, in agreement with its design performance. Solely the requirement of proton detection by the recoil tracking detectors reduces the background contribution down to 5%. Kinematic restrictions on this proton further reduce the background contribution down to 2%. Finally, the inclusion of the photon detector limits the background contribution to below 1%. This simulation does, however, not yet take into account detector inefficiencies, which have been shown to strongly affect track reconstruction in a part of the above mentioned problematic recoil-detector quadrant. The missing-mass distribution shows that also for experimental data the recoil detector largely reduces the background contribution. However, the recoil detector also rejects 20% more events for experimental data in comparison with simulated data. Here, 2% are rejected by the photon detector. The latter can be explained by the presence of noise, which is not simulated in the Monte Carlo, with signal values above 1 MeV. Additionally, it can not be excluded that a fraction of signals identified as photon signals originate from charged particles that are not reconstructed by the tracking detectors.

In a last step, events from associated DVCS were selected. In order to eliminate remaining noise signals, the threshold value for photon detection was set to minimum 2.5 MeV. According to the Monte-Carlo simulation an event sample can be selected that contains $80 \pm 4\%$, $88 \pm 5\%$, or $95 \pm 3\%$ associated DVCS events, depending on the selection criteria. More severe conditions lead to a sample with higher purity, but also drastically reduce the number of selected events. The reconstructed missing-mass distribution for the events selected from experimental data corresponds to the mass distribution of the Δ^+ resonance, with a shape that is in very good agreement with the simulation.

152

From the above stated, one can conclude that the photon detector works reliably. Regarding its main purpose, namely the rejection of photons, the simulation indicates that the photon detector contributes to a further reduction in background of 1%, in comparison with a detector system consisting solely of the silicon-strip detector and the scintillating-fiber tracker. This simulation does, however, not yet take into account detector inefficiencies. The photon detector rejects 3% (1%) of the events from experimental (simulated) data, selected for the analysis of DVCS using the recoil tracking detectors. Active detection of photon signals allowed to successfully select associated DVCS events. The collected statistics is, however, insufficient for the extraction of the beam-helicity asymmetry.

Appendix A. Alignment parameters of the photon detector

layer	x [cm]	y [cm]	ϕ [deg]
A	0.12 ± 0.01	0.00 ± 0.01	-1.74 ± 0.02
B	0.28 ± 0.01	0.20 ± 0.01	-4.03 ± 0.02
C	-0.11 ± 0.01	0.35 ± 0.01	0.24 ± 0.02

Table A.1: Alignment parameters of the photon-detector layers determined using negatively charged pions.

layer	x [cm]	y [cm]	ϕ [deg]
A	0.18 ± 0.02	0.03 ± 0.02	-2.23 ± 0.04
B	0.36 ± 0.01	-0.06 ± 0.02	-4.76 ± 0.03
C	0.00 ± 0.02	0.44 ± 0.01	0.00 ± 0.04

Table A.2: Alignment parameters of the photon-detector layers determined using positively charged pions.

Appendix B. Calculation of the most probable energy deposition

The most probable energy, E_{mpv}, deposited by a charged particle crossing a medium is given by [97, 98]:

$$
\begin{aligned}
E_{mpv} &= \xi(\lambda_{mp} + 1 - \gamma_E + \ln\frac{2m_e c^2 \beta^2 \xi}{I^2(1-\beta^2)} - \beta^2 - \delta) \\
&= \xi(0.200 + \ln\frac{2m_e c^2 \beta^2 \xi}{I^2(1-\beta^2)} - \beta^2 - \delta),
\end{aligned}
\tag{B.1}
$$

where $\lambda_{mp} = -0.2228$ is the value for which the Landau function $\Phi(\lambda)$ reaches its maximum, $\gamma_E = 0.577$ is Euler's constant, $m_e c^2 = 0.511$ MeV is the electron mass, β the relativistic speed, I the mean excitation energy, and δ the correction for the density effect. The variable ξ is given by:

$$
\xi = \frac{K}{2}\frac{Z}{A}\frac{1}{\beta^2}\rho x,
\tag{B.2}
$$

with $K/(2A) = 0.1535/A$ MeV cm^2/g (see [71]) and x [cm] the distance traveled by the charged particle inside the medium. The variable A represents the atomic mass of the medium ($A = 6.2374$ g/mol for the photon-detector strips), Z its atomic number ($Z = 3.38$), and ρ its density ($\rho = 1.032$ g/cm^3).

The value of I for a composite material, like the photon-detector strips, can be obtained with Bragg's formula [99]:

$$
N \ln I = \sum_i N_i \ln I_i,
\tag{B.3}
$$

with N_i being the number density of electrons associated to element i. The base material of the photon-detector strips consists of hydrogen and carbon, with N_i values [77]: $N_H = 5.23\,10^{22}$ cm^{-3}, $N_C = 28.44\,10^{22}$ cm^{-3}, and $N = 33.67\,10^{22}$ cm^{-3} for the composite material. As the chemical bindings affect the mean excitation energy, one has to take the physical state of the elements into account for the value of I_i. The carbon and hydrogen atoms form unsaturated compounds; the values for I_C and I_H are taken accordingly from reference [99]: $I_H = 14.8$ eV and $I_C = 75.1$ eV, resulting in $I = 58.1$ eV. The use of Bragg's formula should not induce an error in stopping power larger than $\pm 1\%$.

B. Calculation of the most probable energy deposition
_____

The reduction in stopping power due to the polarization of the medium in response to the electric field of the impinging particle, the density effect, is taken into account by δ. Usually Sternheimer's parametrization is used for the value of δ [99]:

$$\delta = \begin{cases} 0, & X < X_0 \\ 4.606X + C + a(X_1 - X)^3, & X_0 \leq X \leq X_1 \\ 4.606X + C, & X_1 < X, \end{cases} \qquad (B.4)$$

where $X = log(\beta/\sqrt{1-\beta^2})$, $C = -2\ln(I/\hbar\omega_p) - 1$, $a = -(C + 4.606X_0)/(X_1 - X_0)^3$, and $X_0 = 0.2$ and $X_1 = 2.0$ in the present case. The plasma energy $\hbar\omega$ is given by [71]: $\hbar\omega = 28.816\sqrt{\rho Z/A} = 21.549$ eV. This yields a value for $C = -2.985$ and $a = 0.354$. The use of Sternheimer's parametrization results in a maximum error of $\pm 2\%$ in stopping power.

According to [99], the above given formula for E_{mpv} is valid if $\xi/w_m < 0.01$, with $w_m = 2m_ec^2\beta^2/(1-\beta^2)$. Thus, for a charged pion crossing the photon-detector strips, the formula is only valid for higher-momentum pions, above 500 MeV/c.

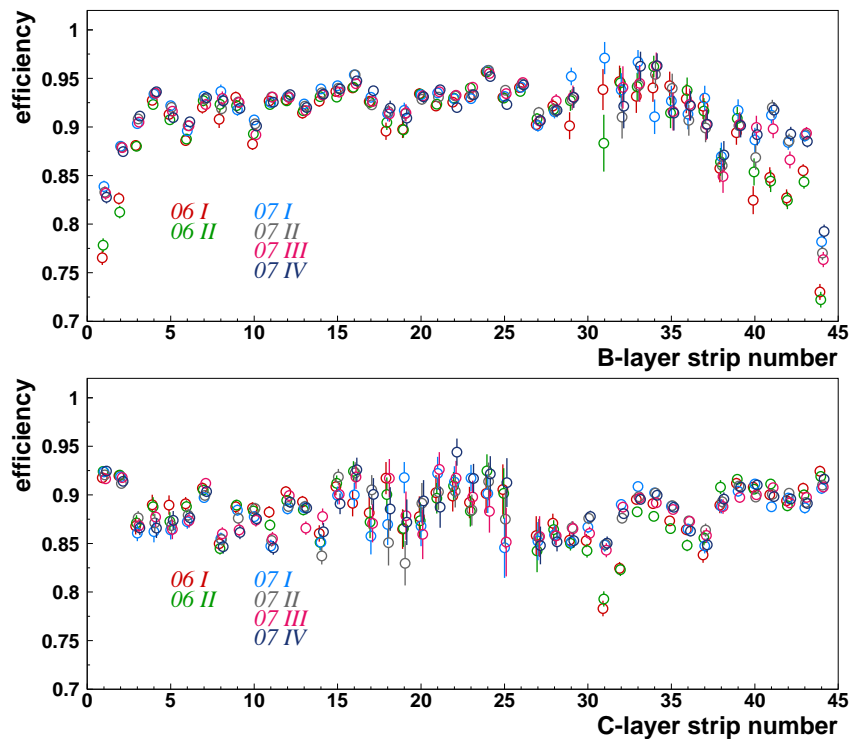# Appendix C. Time dependence of the photon-detector efficiency

Figure C.1: Time dependence of the photon-detector B-layer (top) and C-layer (bottom) strips.

Figure C.1 shows the time dependence of the efficiencies of the B- and C-layer strips. The data collected in 2006 are subdivided into 2 time periods; the data collected in 2007 are subdivided into 4 time periods.

Appendix D. Correction factors to the photon energy

The tables given below contain the multiplicative correction factors that need to be applied to the photon energy, for each of the indicated periods individually, in order to eliminate the time dependence of the missing mass. The correction factors are obtained from the examination of the mean of the fit, μ, to the M_X^2 distribution inside the range: $\mu - 3.34\,\mathrm{GeV}^2 < M_X^2 < \mu + 0.91\,\mathrm{GeV}^2$. For an optimal resolution in M_X^2 an additional global correction factor of 0.98 needs to be applied to the photon energy.

period	run (06e)	scale factor
1	27934–31000	1.01410
2	31001–37000	1.01580
3	37001–43000	1.01545
4	43001–48195	1.01683

Table D.1: Individual correction factors valid for the indicated run ranges of the 06e μDST production.

period	run (07c)	scale factor
5	1–5000	1.01830
6	5001–10000	1.01680
7	10001–15000	1.01680
8	15001–20000	1.01660
9	20001–25000	1.01315
10	25001–30000	1.00924
11	30001–35000	1.01215
12	35001–40515	1.01257

Table D.2: Individual correction factors valid for the indicated run ranges of the 07c μDST production.

Bibliography

[1] J.Ashman et al., Phys. Lett. B **206**, 364, 1988; Nucl. Phys. **B 328**, 1, 1989.

[2] A.V. Radyushkin, Phys. Rev. D **56**, 5524, 1997.

[3] X. Ji and J. Osborne, Phys. Rev. D **58**, 094018, 1998.

[4] J. C. Collins and A. Freund, Phys. Rev. D **59**, 074009, 1999.

[5] M. Burkardt, hep-ph/9611416, 1996.

[6] M. Diehl, Phys. Rep. **388**, 41, 2003.

[7] A. V. Belitsky and D. Müller, Phys. Lett. B **417**, 129, 1998.

[8] L. Mankiewicz, et al., Phys. Lett. B **425**, 186, 1998.

[9] A. V. Belitsky et al., Nucl. Phys. B **629**, 323, 2002.

[10] N. Kivel and L. Mankiewicz, Nucl. Phys. B **672**, 357, 2003.

[11] N. Kivel and L. Mankiewicz, Eur. Phys. J. C **21**, 621, 2001.

[12] X. Ji, J. Phys. G **24**, 1181, 1998.

[13] M. Diehl, Eur. Phys. J. C **19**, 485, 2001.

[14] R. Enberg, et al., Eur. Phys. J. C **47**, 87, 2006.

[15] M. El Beiyad, et al., to appear in the proceedings of 18th International Workshop on Deep-Inelastic Scattering and Related Subjects, Florence, Italy, 2010. (Preprint hep-ph/10060740)

[16] D. Müller, et al., Fortschr. Phys. **42**, 101, 1994.

[17] X. Ji, Phys. Rev. D **55**, 7114, 1997.

[18] J. Bümlein et al., Nucl. Phys. B **560**, 283, 1999.

[19] A. V. Belitsky and D. Müller, Nucl. Phys. B **537**, 397, 1998.

[20] A. V. Belitsky, et al., Nucl. Phys. B **574**, 347, 2000.

[21] V. N. Gribov and L. N. Lipatov, Sov. J. Nucl. Phys. **15**, 438, 1972.

[22] L. N. Lipatov, Sov. J. Nucl. Phys. **20**, 94, 1975.

[23] G. Altarelli and G. Parisi, Nucl. Phys. B **126**, 298, 1977.

[24] Y. L. Dokshitzer, Sov. Phys. JETP **46**, 641, 1977.

[25] A. V. Efremov and A. V. Radyushkin, Phys. Lett. B **94**, 245, 1980.

[26] G. P. Lepage and S. J. Brodsky, Phys. Lett. B **87**, 359, 1979.

[27] K. Goeke, et al., Prog. Part. Nucl. Phys. **47**, 401, 2001.

[28] F. D. Aaron et al. [H1 Collaboration and ZEUS Collaboration], JHEP **01**, 109, 2010.

[29] D. de Florian et al., Phys. Rev. Lett. **101**, 072001, 2008.

[30] M. Anselmino et al., Phys. Rev. D **75**, 054032, 2007.

[31] M. Burkardt, Phys. Rev. D **62**, 071503, 2000.

[32] M. Burkardt, Int. J. Mod. Phys. A **18** 173, 2003.

[33] X. Ji, Phys. Rev. Lett. **78**, 610, 1997.

[34] R. L. Jaffe and A. Manohar, Nucl. Phys. B **337**, 509, 1990.

[35] M. Vanderhaeghen, et al., Phys. Rev. D **60**, 094017, 1999.

[36] A. V. Radyushkin, Phys. Rev. D **59**, 014030, 1999.

[37] I. V. Musatov and A. V. Radyushkin, Phys. Rev. D **61**, 074027, 2000.

[38] M. V. Polyakov and C. Weiss, Phys. Rev. D **60**, 114017, 1999.

[39] V. Y. Petrov et al., Phys. Rev. D **57**, 4325, 1998.

[40] M. Diehl et al., Eur. Phys. J. C **39**, 1, 2005.

[41] M. Guidal and M. Vanderhaeghen, Phys. Rev. Lett. **90**, 012001, 2003.

[42] P. Mergell, et al., Nucl. Phys. A **596**, 367, 1996.

[43] V. A. Korotkov and W.-D. Nowak, Eur. Phys. J. C **23**, 455, 2002.

[44] P. A. M. Guichon et al., Phys. Rev. D **68**, 034018, 2003.

[45] L. L. Frankfurt, et al., hep-ph/9808449.

[46] L. L. Frankfurt, et al., Phys. Rev. Lett. **84**, 2589, 2000.

[47] A. Airapetian et al., Phys. Rev. Lett. **87**, 182001, 2001.

[48] A. Airapetian et al, Phys. Rev. D **75**, 011103, 2007.

[49] A. Airapetian et al, JHEP **11**, 083, 2009.

[50] A. Airapetian et al, JHEP **06**, 066, 2008.

[51] A. Airapetian et al, JHEP **06**, 019, 2010.

[52] G.-A. Voss and B. H. Wiik, Annu. Rev. Nucl. Part. Sci. **44**, 413, 1994.

[53] A. A. Sokolov and I. M. Ternov, Sov. Phys. Dokl. **8**, 1203, 1964.

[54] M. Beckmann et al., Nucl. Instrum. Meth. A **479**, 334, 2002.

[55] J. Buon and K. Steffen, Nucl. Inst. Meth. A **245**, 248, 1986.

[56] D. P. Barber et al., Nucl. Instrum. Meth. A **329**, 79, 1993.

[57] A. Airapetian et al., internal report POL2000-2007-001, DESY, 2007.

[58] I. Lehmann et al., HERMES Internal Report 06-080, DESY, 2006.

[59] Target group, Unpolarized Gas Feed System — Shift crew operation manual, HERMES internal, 2006.

[60] W. Wander, Reconstruction of high-energy scattering events in the HERMES experiment, Ph.D. thesis, Friedrich-Alexander Universität Erlangen, 1996.

[61] A. Kisselev, HTC status report, HERMES tracking meeting, DESY, September 4, 2008.

[62] A. Kisselev, HTC Monte-Carlo X-check, HERMES collaboration meeting, DESY, September 22–26, 2008.

[63] J. Ely, HERMES Internal Report 01-056, DESY, 2001.

[64] J. Wendland, HERMES Internal Report 01-067, DESY, 2001.

[65] M. Feuerstack-Raible, Nucl. Instr. and Meth. A **447**, 35, 2000.

[66] A. Vandenbroucke, Exclusive π^0 Production at Hermes: Detection—Simulation—Analysis, Ph.D. thesis, Universiteit Gent, 2006.

[67] A. Mussgiller, http://www-hermes.desy.de/groups/rcoilgrp/recoil/Plots/2009/ dEE_deuteron_lepton.eps.

[68] S. Yaschenko, Recoil tracking status, HERMES collaboration meeting, DESY, June 2–6, 2008.

[69] X.-G. Lu, The HERMES Recoil Detector: Particle Identification and Determination of Detector Efficiency of the Scintillating Fiber Tracker, diploma thesis, Univeristät Hamburg, 2009.

[70] A. Borysenko et al., Status of the Recoil Photon Detector, HERMES internal, 2002.

[71] Particle Data Group, J. Phys. G **33**, 2006.

[72] http://physics.nist.gov/PhysRefData/Xcom/html/xcom1.html.

[73] M.J. Berger and S.M. Seltzer, Tables of Energy Losses and Ranges of Electrons and Positrons, National Aeronautics and Space Administration Report NASA-SP-3012 (Washington DC 1964).

[74] B. Rossi, High Energy Particles, Prentice-Hall, Inc., Englewood Cliffs, NJ, 1952.

[75] C. Fabjan, Calorimetry in high-energy physics, from Experimental techniques in High Energy Physics, ed. T. Ferbel (Addision-Wesley, Menlo Park CA 1987).

[76] G. F. Knoll, Radiation and Measurement, John Wiley and Sons, New York, 1979.

[77] http://www.detectors.saint-gobain.com/uploadedFiles/SGdetectors/Documents/Product_Data_Sheets/BC400-404-408-412-416-Data-Sheet.pdf.

[78] C. Zorn, Plastic and Liquid Organic Scintillators, from Instrumentation in High Energy Physics, ed. F. Sauli (World Scientific, 1992).

[79] J. B. Birks and A. Hallam, J. Phys. B **11**, 18, 1978.

[80] R. Brun et al., GEANT detector description and simulation tool (long writeup W5013), CERN-CN Application Software Group, Geneva, 1994.

[81] H. Fesefeldt, RWTH Aachen report PITHA 85/2, 1985.

[82] http://www.detectors.saint-gobain.com/uploadedFiles/SGdetectors/Documents/Brochures/Scintillating-Optical-Fibers-Brochure.pdf.

[83] T. Förster, Zwischenmolekulare Energiewanderung und Fluoreszenz, Ann. Physik **2**, 55, 1948.

[84] D. Clark, Nucl. Instrum. Methods **117**, 295, 1974.

[85] R. J. Potter, J. Opt. Soc. Am. A **51**, 10, 1960.

[86] http://sales.hamamatsu.com/index.php?id=13199677&language=2.

[87] Y. Van Haarlem, The HERMES recoil photon detector and nuclear p_t-broadening at HERMES, Ph.D. Thesis, University Gent, Sep 2007.

[88] M. Tytgat, PD HDC, HERMES Recoil Meeting, DESY, March 17, 2006.

[89] M. Tytgat, Photon Detector Clustering routines, HERMES Recoil Software Meeting, DESY, November 3, 2005.

[90] M. Tytgat, PMT Pixel Clustering for the Photon Detector, HERMES Recoil Meeting, DESY, July 1, 2005.

[91] M. Tytgat, Clustering Routines for the Photon Detector, HERMES Recoil Software Meeting, DESY, October 17, 2005.

[92] A. Martínez de la Ossa, The Photon Detector Clustering, Hermes Technical Recoil Meeting, DESY, September 17, 2008.

[93] E.H. Bellamy et al., Nucl. Instrum. Methods A **339**, 468, 1994.

[94] G. P. Capitani, private communication.

[95] W. Benecke, Ergebnisse der Einmessung des PD mit dem Lasertracker, HERMES internal, February 7, 2006.

[96] U. Fano, Ann. Rev. Nucl. Sci. **13**, 1, 1963.

[97] H. Bichsel, Rev. Mod. Phys. **60**, 3, 1988.

[98] D. H. Wilkinson, Nucl. Instrum. Methods A **383**, 513, 1996.

[99] S. P. Ahlen, Rev. Mod. Phys. **52**, 1, 1980.

[100] Saint-Gobain (Ceramics and Plastics), Detector Application Information Note, charged particle detection.

[101] H. Jo, Photon Detector noise studies status, HERMES Recoil Meeting, DESY, April 25, 2008.
H. Jo, Photon Detector noise studies, HERMES Recoil Meeting, DESY, August 1, 2008.

[102] J. Bowles, HTC probability cut study, HERMES exclusive week, DESY, February 22–26, 2010.

[103] F. Ellinghaus, Beam-Charge and Beam-Spin Azimuthal Asymmetries in Deeply-Virtual Compton Scattering, Ph.D. thesis, Humboldt University of Berlin, 2003.

[104] E. Avetisyan, Calorimeter photon energy, HERMES collaboration meeting, DESY, June 15–19, 2009.

[105] B. Krauss, Deeply Virtual Compton Scattering and the HERMES-Recoil Detector, Ph.D. thesis, Physikalisches Institut II, FAU Erlangen-Nürnberg, February 2005.

[106] E. Avetisyan, Study of Shower Depth in the Calorimeter, HERMES DVCS/Recoil Meeting, DESY, December 1, 2009.

[107] J. Ely, Measurement of the single spin azimuthal asymmetry in the predominantly exclusive electroproduction of photons from the proton, Ph.D. thesis, University of Colorado, 2002.

[108] D. Zeiler, Deeply Virtual Compton Scattering off an Unpolarized Hydrogen Target at the HERMES experiment, Ph.D. thesis, University Erlangen-Nuremberg, 2009.

[109] A. Kisselev, documentation provided with the code that extracts HTC information: ucode-1.3, HERMES internal, 2010.

[110] HERMES collaboration, The HERMES Recoil Detector: Technical Design Report, HERMES internal, 02–003, 2002.

[111] S. Yashenko, Kinematic fitting for DVCS, Exclusive—DVCS week, DESY, October 29, 2009.

[112] S. Yashenko, News on kinematic fitting for exclusive proceses, HERMES collaboration week, Glasgow, April 12, 2010.

[113] J. Burns, Analysis of Deeply Virtual Compton Scattering on the Proton, HERMES release report Version 2.2, February 11, 2010.

[114] L.W. Mo and Y. Tsai, Rev. Mod. Phys. **41**, 205, 1969.

[115] F. W. Brasse et al., Nucl. Phys. B **110**, 413, 1976.

[116] D. Drechsel et al., Nucl. Phys. A **645**, 145, 1999.

[117] G. Ingelman, A. Edin, J. Rathsman, Comput. Phys. Commun. **101**, 108-134, 1997.

[118] T. Sjöstrand, Comput. Phys. Commun. **82**, 74, 1994.

[119] B. Andersson, et al., Phys. Rept. **97**, 31 (1983).

[120] A. Hillenbrand, Measurement and Simulation of the Fragmentation Process at HERMES, Ph.D. thesis, Friedrich-Alexander Universität Erlangen, 2005.

[121] I. Akushevich, et al., RADGEN 1.0: Monte Carlo generator for radiative events in DIS on polarized and unpolarized targets, talk presented at the Workshop "Monte Carlo generators for HERA physics", DESY, Hamburg, 1999. (hep-ph/9906408)

[122] W. Yu, Beam-Helicity Azimuthal Asymmetry measured with the Recoil Detector in exclusive electroproduction of real photons at HERMES, Ph.D. thesis, Justus-Liebig Universität, Giessen, 2009.

[123] R. Barlow, Extended maximum likelihood, Nucl. Instrum. Methods A **297**, 496, 1990.

[124] A. Miller, Maximum Likelihood, HERMES collaboration meeting, DESY, June 19–23, 2006.

Samenvatting

Het hier voorgestelde werk levert een bijdrage tot het onderzoek naar de oorsprong van de spin van het nucleon (proton of neutron). Nucleonen bestaan uit elementaire fermion deeltjes, de quarks, die met elkaar interageren via de uitwisseling van gluonen, de ijkbosonen van de sterke wisselwerking, welke beschreven is door de theorie kwantumchromodynamica. Een proton (neutron) bestaat uit 2 (1) up quarks en 1 (2) down quark. Deze quarks worden valentiequarks genoemd. Ze staan in voor statische eigenschappen van het nucleon, zoals zijn lading en andere kwantumgetallen. De uitgewisselde gluonen kunnen opsplitsen in quark-antiquark paren en deze quarks, genaamd zeequarks, kunnen dan weer annihileren in gluonen. Het nucleon kan dus gezien worden als bestaande uit valentiequarks omgeven door een zee van quarks die voortdurend annihileren in gluonen en ontstaan uit de splitsing van gluonen. Die elektrisch geladen (quarks) en elektrisch neutrale (gluonen) bouwstenen van het nucleon worden ook wel partonen genoemd.

Oorspronkelijk werd gedacht dat de enige bijdrage tot de spin van het nucleon afkomstig was van de spins van de valentiequarks. In 1988 toonden metingen uitgevoerd aan het EMC experiment te CERN in Geneve (Zwitserland) echter aan dat de spins van de (valentie- en zee-)quarks slechts een kleine bijdrage leveren, namelijk $14 \pm 9 \pm 21\%$ [1]. Daaropvolgend werden een reeks nieuwe experimenten opgestart, waaronder het HERMES experiment te DESY in Hamburg (Duitsland), om de oorsprong van de spin van het nucleon nader te onderzoeken. Deze experimenten bevestigden het eerder gemeten resultaat van het EMC experiment met grotere precisie. Daarenboven kon ook informatie over de individuele spinbijdrage van verschillende quark types, namelijk van het up, down en strange (anti-)quark verzameld worden. Eerste metingen met betrekking tot gluonen wijzen op een eerder geringe bijdrage van de spins van deze deeltjes. Verwacht wordt dus dat de bijdrage van het baanimpulsmoment van de partonen aanzienlijk is.

De bijdrage van het totaal impulsmoment van de quarks wordt door de Ji relatie in verband gebracht met veralgemeende partondistributies [33]. Kennis van deze fenomenologische distributies leidt dan tot de bepaling van het baanimpulsmoment van de quarks, gezien hun spin-bijdrage gekend is.

Veralgemeende partondistributies verschaffen informatie over de structuur van het nucleon. Zij vormen, zoals de naam al doet vermoeden, een veralgemening van de standaard partondistributiefuncties. De partondistributiefuncties kunnen geïnterpreteerd worden als de waarschijnlijkheidsdichtheid om partonen te vinden in het nucleon als functie van de longitudinale impulsfractie die ze dragen. Hierbij wordt het nucleon gezien als zich bevindend in een snel bewegend referentiestelsel. De spin-onafhankelijke partondistributies houden geen

rekening met de spin-toestand van de betrokken deeltjes, terwijl de spin-afhankelijke distributies het aantal quarks (of gluonen) met spin parallel en anti-parallel aan de spin van het nucleon vergelijken. Hierbij is de spin georiënteerd volgens de bewegingsrichting van het nucleon.[1] Behalve het verschaffen van informatie over de (spin-afhankelijke) longitudinale impulsdistributie van de partonen, beschrijven de veralgemeende partondistributies ook de (spin-afhankelijke) transversale positie van de partonen in het nucleon [32].

Het theoretisch eenvoudigste proces dat toegang verschaft tot veralgemeende partondistributies is diep-virtuele Compton verstrooiing (DVCS)[2]. In dit proces interageert een lepton met een quark in het proton via de uitwisseling van een hoog-virtueel foton. Dit foton wordt door het quark geabsorbeerd en vervolgens zendt dit quark een reëel foton uit, waarna het terugkeert naar het proton. Hierbij blijft het proton intact maar bekomt het een nieuwe impuls. DVCS werd reeds verscheidene jaren aan het HERMES experiment bestudeerd. Het HERMES experiment ligt aan de HERA versneller te DESY in Hamburg. Het verzamelde gegevens van 1995 tot en met 30 juni 2007, datum waarop de HERA versneller definitief werd stilgelegd. In de HERA versneller werden elektronen en positronen versneld tot een energie van 27.6 GeV. Initieel was de bundel ongepolariseerd. Omwille van een asymmetrie in de kleine spin-flip amplitude in de emissie van synchrotron straling, het Sokolov-Ternov effect [53], bouwde zich na verloop van tijd een transversale polarisatie op. Door middel van spin-rotatoren, geplaatst voor en achter het HERMES experiment, werd de spinoriëntatie van de bundeldeeltjes 90° gedraaid, zodat de leptonenbundel bij doorgang door het HERMES experiment longitudinaal gepolariseerd was. In het HERMES experiment werden de bundeldeeltjes verstrooid aan gasvormige trefdeeltjes. Deze deeltjes werden geïnjecteerd in een trefcel die integraal deel uitmaakt van de leptonenbundellijn. Doorheen de jaren werd gebruik gemaakt van transversaal en longitudinaal gepolariseerd waterstofgas, longitudinaal gepolariseerd deuterium- en heliumgas en ongepolariseerde zwaardere gassen, zoals krypton, neon en xenon. Ook de gepolariseerde trefgassen werden soms in ongepolariseerde toestand gebruikt. Data werden verzameld voor de studie van processen in diep-inelastische verstrooiing (DIS). Bij dit soort processen, waartoe DVCS behoort, is de vierimpuls van het virtueel foton, dat uitgewisseld wordt tussen het bundellepton en het trefdeeltje, voldoende groot zodat dit foton de interne structuur van het nucleon kan ontrafelen.

Aan het HERMES experiment wordt DVCS bestudeerd via de extractie van asymmetrieën. Onder andere de bundel-spin asymmetrie werd geanalyseerd. Deze telt het verschil in aantal genormaliseerde DVCS events waarbij de spin van de bundelleptonen parallel en anti-parallel georiënteerd is aan de bundel-bewegingsrichting, als functie van de hoek tussen het vlak gedefinieerd door het bundellepton en het verstrooid lepton en het vlak gedefinieerd door het virtueel en het reëel foton. De beschikbaarheid van elektronen en positronen als bundeldeeltjes verschaft de unieke mogelijkheid voor het meten van de ladingsasymmetrie, namelijk de asymmetrie die het verschil in het genormaliseerd aantal DVCS events, verzameld met elektronen en positronen, telt. De verscheidene polarisatietoestanden van het waterstof trefgas lieten toe om informatie omtrent verschillende soorten veralgemeende par-

---

[1]Daarnaast bestaan ook partondistributies die de structuur van een nucleon met transversaal-gerichte spin beschrijven.

[2]In tegenstelling tot de standaard partondistributies zijn veralgemeende partondistributies niet direct toegankelijk, maar verschijnen ze in de verstrooiingsamplitude in convolutie met de harde interactie van het virtueel foton met het actieve quark.

tondistributies te verzamelen. Daarenboven kon ook informatie over DVCS aan het neutron verzameld worden door de gegevens gemeten aan de waterstof trefcel en aan de deuterium trefcel met elkaar te vergelijken, en kon de afhankelijkheid van DVCS aan het massagetal onderzocht worden dankzij de metingen met de zwaardere trefgassen.

Voor de studie van DVCS aan het HERMES experiment werden het reëel foton en het verstrooid lepton gereconstrueerd door de HERMES spectrometer, die een voorwaartse geometrie vertoont. Omwille van de lage energie en de hoekverdeling van het teruggestoten proton kon dit deeltje echter niet gedetecteerd worden in het experiment. Dankzij de reconstructie van zijn ontbrekende massa kon toch de nodige informatie verzameld worden. De ontbrekende-massa resolutie van de HERMES spectrometer is echter onvoldoende om DVCS events individueel te identificeren en af te scheiden van events waar bijvoorbeeld het proton niet in zijn grondtoestand blijft maar geëxciteerd is tot een Δ^+-resonantie. Dit soort proces wordt geassocieerde DVCS genoemd. De bijdrage van geassocieerde DVCS events tot de sample events geselecteerd voor de studie van DVCS waarbij het proton in zijn grondtoestand blijft, in oppositie met geassocieerde DVCS ook wel elastische DVCS genoemd, is geschat op 11%. Daarenboven is er nog een kleine bijkomende contaminatie, $\sim 3\%$, van andere DIS processen. De voornaamste bijdrage is hier afkomstig van processen waarbij een energetisch neutraal pion gecreëerd wordt, maar waarbij enkel één van zijn vervalfotonen gedetecteerd wordt door de spectrometer.

De Δ^+-resonantie vervalt voor $\sim 67\%$ in een proton en een neutral pion, waarbij dit laatste deeltje zelf in 2 fotonen vervalt, en voor 33% in een neutron en een positief geladen pion. Om geassocieerde DVCS events, alsook de overige achtergrond events, uit de data sample te verwijderen, werd in 2006 een recoil detector geïnstalleerd rond de HERMES trefcel. Deze detector bestaat uit 3 actieve detectordelen die omgeven zijn door een 1 T supergeleidende magneet. De binnenste detectorcomponent is een siliciumdetector. Deze detector bevindt zich in de vacuümkamer. Dit maakt de detectie van laag-energetische protonen mogelijk, hetgeen wenselijk is met het oog op de Ji relatie. Rond de siliciumdetector bevindt zich, buiten het HERA vacuüm, een spoordetector bestaande uit scintillator vezels. Beide detectordelen staan in voor de reconstructie en identificatie van geladen deeltjes, meer specifiek protonen en positief en negatief geladen pionen. De buitenste detectorcomponent, geplaatst rond de spoordetector, is de fotondetector. Deze detector staat in voor de detectie van fotonen en is eveneens gevoelig voor geladen deeltjes. De fotondetector is omwille van zijn constructie niet in staat de energie van de fotonen te reconstrueren. Hij bestaat uit drie cilindrische lagen, waarbij elke laag op zichzelf bestaat uit een laag wolfraam gevolgd door een laag scintillator materiaal. Fotonen kunnen interageren in de wolfraam laag en de daaruitvolgend gecreëerde geladen deeltjes worden vervolgens gedetecteerd in de scintillator laag. De scintillator laag is 1 cm dik en onderverdeeld in 2 cm brede strips. De strips van de binnenste scintillator laag liggen evenwijdig aan de bundellijn, terwijl in de twee volgende scintillator lagen de strips geplaatst zijn onder een hoek van respectievelijk $+45.6°$ en $-46.2°$.

Een groot deel van het hier voorgestelde werk bestaat uit het opstellen en in gebruik nemen van de fotondetector. Vooreerst werd deze detector, samen met de andere recoil detectoren, opgesteld in een testruimte. Hier werden signalen van kosmische deeltjes verzameld. Het triggersignaal voor het uitlezen van de recoil detectorcomponenten werd geleverd door de fotondetector. De analyse van deze gegevens liet een ruwe kalibratie van de fotondetector toe, evenals een eerste bepaling van de efficiëntie van de scintillator strips. Aan de

hand van deze gegevens werd de fotondetector eveneens in de 'digitization' routine van de HERMES Monte Carlo (HMC) simulatie geïmplementeerd. HMC is gebaseerd op GEANT, een systeem van detector en fysica simulatie routines ontworpen door CERN. In GEANT kunnen verscheidene detectorvolumes gedefinieerd worden. Generatoren, verschillend naar gelang het te bestuderen fysisch proces, genereren deeltjes waarvan de doorgang doorheen de detectoren gesimuleerd wordt. In een tweede stap worden deze gegevens verwerkt door de digitization routine. GEANT veronderstelt namelijk dat de detector een ideaal detectiesysteem is. In werkelijkheid dragen talrijke factoren bij tot een verminderde detectieresolutie. Deze vermindering in resolutie werd voor de fotondetector in rekening gebracht aan de hand van de gegevens verzameld in de testruimte.

Eind 2005 en begin 2006 werd de recoil detector geïnstalleerd in het HERMES experiment. Vanaf september 2006 waren alle onderdelen van de recoil detector operationeel en werden gegevens verzameld tot eind juni 2007. Gedurende deze 10 maanden was de trefcel alternerend gevuld met ongepolariseerd waterstof en ongepolariseerd deuterium. De bundellijn was hierbij gevuld met positronen, met positieve en negatieve polarisatie. Voor beide spin-toestanden bedroeg de polarisatie gemiddeld 40%. In totaal werden 28 M DIS events verzameld met waterstof en 7 M DIS events met deuterium.

De allereerste geïdentificeerde deeltjessignalen in de fotondetector waren afkomstig van elastisch verstrooide protonen. De selectie van deze protonen is relatief eenvoudig. Het berustte enkel op de ADC signalen van de fotondetector en de reconstructie van het verstrooid lepton door de voorwaartse spectrometer. Vervolgens werd aan de hand van geladen pionen, gereconstrueerd door de silicium- en spoordetector, de oriëntatie van de scintillator strips uit de twee buitenste fotondetector lagen gemeten evenals de positie en oriëntatie van elke fotondetector laag. In een volgende stap werd de fotondetector gekalibreerd, eveneens door middel van signalen afkomstig van geladen pionen. Eenmaal de verwerking van gegevens berustend op deze kalibratie beschikbaar was, kon de kwaliteit van de kalibratie worden nagegaan en kon de efficiëntie van de fotondetector strips opgemeten worden. Met betrekking tot deze twee aspecten zijn de bekomen resultaten voldoeninggevend. De response van de fotondetector is stabiel in tijd en de efficiëntie voor de detectie van protonen en geladen pionen bedraagt, respectievelijk, 95% en 92%. Eveneens werd aangetoond dat de fotondetector kan bijdragen tot het onderscheiden van protonen en geladen pionen. Evenwel dient opgemerkt te worden dat in een kwadrant van de fotondetector de gekalibreerde signalen tot 25% lager liggen, hetgeen ook de strip efficiëntie beïnvloedt. Dit is te wijten aan problemen in de spoorreconstructie, meer bepaald aan niet-operationele en inefficiënte onderdelen van de twee detectoren die instaan voor de spoorreconstructie. De kwaliteit van de spoorreconstructie is thans verbeterd en voldoende voor een betrouwbare kalibratie[3]. Eenmaal een nieuwe productie van de gegevens, met verbeterde fotondetector kalibratie, beschikbaar is, kan worden nagegaan of de fotondetector strips gelegen in dit kwadrant eveneens een hogere efficiëntie vertonen.

Voor de identificatie van fotonsignalen werd een algoritme ontwikkeld dat voor elk signaal gemeten in de fotondetector nagaat of het wel of niet in verband kan gebracht worden met een gereconstrueerd spoor. Dit algoritme werd dan gebruikt voor de selectie van DVCS events. Studies van gesimuleerde gegevens tonen aan dat het algoritme zelf 99% efficiënt is in

---

[3]Dit werd aangetoond door de analyse van fotondetector signalen afkomstig van kosmische deeltjes, verzameld in tussenperiodes over de jaren 2006 en 2007. De selectie van deze deeltjes gebeurt onafhankelijk van de silicium- en spoordetector.

het identificeren van signalen afkomstig van fotonen. Evenwel wordt een kleinere fractie ge-associeerde DVCS events geïdentificeerd. De verklaring hiervoor ligt deels in het feit dat niet alle fotonen in het geometrisch detectiebereik van de fotondetector liggen. Van de fotonen die wel in het detectiebereik liggen, genereren slechts 84% een signaal in de fotondetector. Daarenboven moet dit signaal boven de 1 MeV drempelwaarde liggen. Deze drempelwaarde staat in voor het verwerpen van ruissignalen aanwezig in de fotondetector.

Volgens de analyse van gesimuleerde data is de recoil detector in staat om de bijdrage van achtergrond events te herleiden van 14% naar $< 1\%$. Voor events waarin een proton gereconstrueerd is door de silicium- en spoordetector, bedraagt de bijdrage van achtergrond events 5%. Wordt daarenboven geëist dat dit proton aan bepaalde kinematische voorwaarden voldoet, dan wordt de bijdrage van achtergrond events verminderd tot 2%. Tenslotte herleidt de fotondetector deze bijdrage tot $< 1\%$. Deze simulatie brengt tot op heden de inefficiënties van de verscheidene detectorcomponenten echter niet in rekening. Deze inefficiënties hebben een grote invloed op de spoorreconstructie in een deel van het problematische detectorkwa-drant. De ontbrekende-massa distributie toont duidelijk aan dat de recoil detector ook voor de experimentele gegevens zorgt voor een sterk verminderde bijdrage van de achtergrond events. Evenwel worden voor de experimentele gegevens ook 20% meer events verworpen door de recoil detector in vergelijking met de simulatie. De fotondetector draagt hierin 2% bij. Dit laatste kan verklaard worden door de aanwezigheid van ruis (hetgeen niet geïmplementeerd is in de simulatie) met signaalwaarde boven 1 MeV. Ook valt niet uit te sluiten dat sporen van geladen deeltjes niet gereconstrueerd zijn, met als gevolg dat de fotondetector deze deeltjes identificeert als fotonen.

In een laatste stap werden geassocieerde DVCS events geselecteerd. Ter verwijdering van resterende ruissignalen werd de drempelwaarde in de fotondetector verhoogd tot 2.5 MeV. Volgens de Monte Carlo simulatie kan een sample geassocieerde DVCS events met een zui-verheid van $80 \pm 4\%$, $88 \pm 5\%$ of $95 \pm 3\%$ geselecteerd worden, afhankelijk van de selec-tiecriteria. Striktere voorwaarden leiden tot een verhoogde zuiverheidsgraad maar ook tot een aanzienlijke vermindering in statistiek. De gereconstrueerde ontbrekende-massa distributie stemt overeen met de massadistributie van de Δ^+-resonantie, met een goede overeenkomst tussen experimentele en gesimuleerde gegevens.

In conclusie is de fotondetector een goed werkende detector. In verband met zijn hoofd-functie, namelijk het verwerpen van events in dewelke fotonen aanwezig zijn, toont de Monte Carlo simulatie aan dat de fotondetector voor de analyse van DVCS bijkomend 1% van de achtergrondbijdrage verwerpt, in vergelijking met een detectorsysteem dat enkel uit de silicium- en spoordetector bestaat. Deze simulatie brengt echter detector inefficiënties niet in rekening. Van deze werd aangetoond dat ze een grote invloed hebben op de spoorreconstruc-tie in een deel van het problematische recoil detectorkwadrant. De fotondetector verwerpt 3% (1%) van de experimentele (gesimuleerde) events geselecteerd voor de analyse van elastis-che DVCS. Actieve detectie van fotonsignalen laat toe om met succes geassocieerde DVCS events te selecteren, maar het verkregen aantal events is echter onvoldoende voor de extractie van de bundel-spin asymmetrie.

176

Acknowledgments